ISSN 2959-0663 (Print)
ISSN 2959-0671 (Online)
ISSN-L 2959-0663

EURASIAN JOURNAL OF CHEMISTRY

2024. Vol. 29 No. 3(115)

Special Issue

Nano- and Photo- Catalysis in Current Chemistry: Possibilities and Challenges

Guest Editors:
Prof. Xintai Su, Prof. Gulzhian I. Dzhardimalieva, Prof. Murzabek I.Baikenov

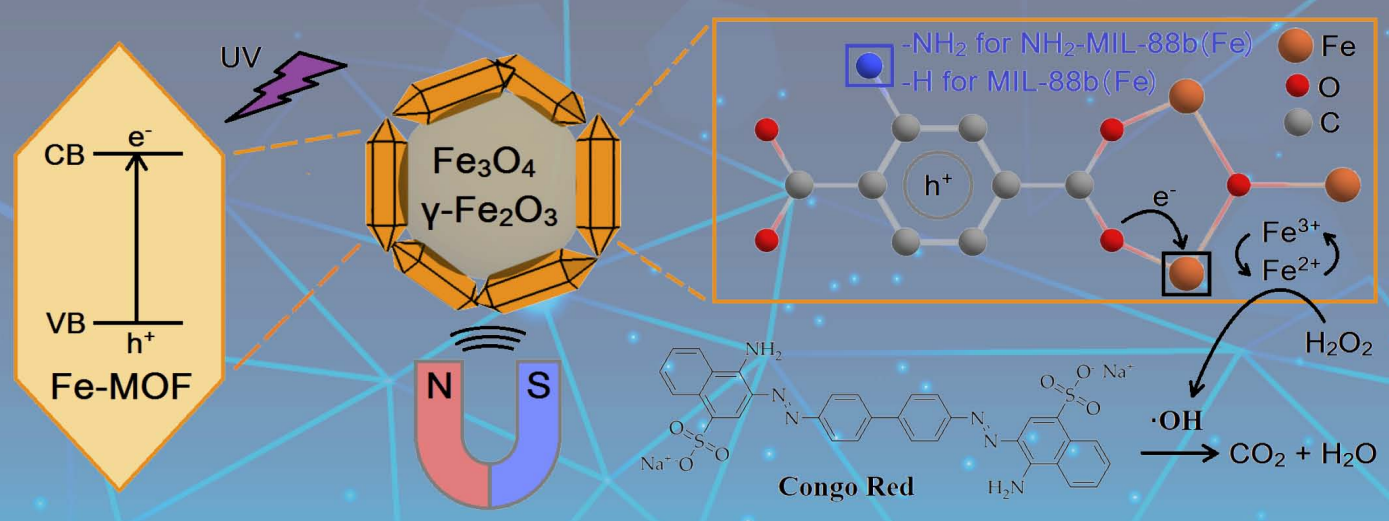

ISSN 2959-0663 (Print)
ISSN 2959-0671 (Online)
ISSN-L 2959-0663

EURASIAN JOURNAL OF CHEMISTRY

2024

No. 3(115)

Special Issue

Nano- and Photo- Catalysis in Current Chemistry: Possibilities and Challenges

Guest Editors: ***Prof. Xintai Su, Prof. Gulzhian I. Dzhardimalieva, Prof. Murzabek I.Baikenov***

July–August–September

September 30th, 2024

Founded in 1996

Published 4 times a year

Karaganda, 2024

Publisher: **Karagandy University of the name of academician E.A. Buketov**
Postal address: 28, University Str., Karaganda, 100024, Kazakhstan
E-mail: chemistry.vestnik@ksu.kz; irina.pustolaikina@ksu.kz; ipustolaikina@gmail.com
Tel./fax: +7(7212) 34-19-40.
Web-site: http://chemistry-vestnik.ksu.kz

Eurasian Journal of Chemistry. — 2024. — No. 3(115). Special Issue "Nano- and Photo- Catalysis in Current Chemistry: Possibilities and Challenges". — 170 p.
ISSN 2959-0663 (Print). ISSN 2959-0671 (Online). ISSN-L 2959-0663
Proprietary: NLC "Karagandy University of the name of academician E.A. Buketov".
Registered by the Ministry of Information and Social Development of the Republic of Kazakhstan. Re-registration certificate No. KZ95VPY00063697 dated 30.01.2023.
Signed in print 27.09.2024. Format 60×84 1/8. Offset paper. Volume 21,25 p.sh. Circulation 200 copies. Price upon request. Order № 98.
Printed in the Publishing house of NLC "Karagandy University of the name of acad. E.A. Buketov".
28, University Str., Karaganda, 100024, Kazakhstan. Tel.: +7(7212) 35-63-16. E-mail: izd_kargu@mail.ru
Front Cover Image featured from the Graphical Abstract of the article: Sidorov, V.L., Baimuratova, R.K., Korchagin, D.V., Ivanov, A.V., Kydralieva, K.A., & Dzhardimalieva, G.I. (2024). Magnetically Separable Fe_3O_4/γ-Fe_2O_3@MIL-88b(Fe) and Fe_3O_4/γ-Fe_2O_3@NH_2-MIL-88b(Fe) Composites for the Photocatalytic Degradation of Congo Red Dye. *Eurasian Journal of Chemistry.* https://doi.org/10.31489/2959-0663/3-24-5

CONTENTS

PREFACE

NANO- AND PHOTO- CATALYSIS IN CURRENT CHEMISTRY: POSSIBILITIES AND CHALLENGES

How to Cite: Su, X., Dzhardimalieva, G.I., & Baikenov, M.I. (2024) Special Issue Foreword from Guest Editors. *Eurasian Journal of Chemistry, 29, 3(115), 4-6.* https://doi.org/10.31489/2959-0663/3-24-3

PREFACE

Preface

Received: 23 September 2024 | Published online: 26 September 2024

https://doi.org/10.31489/2959-0663/3-24-3

Xintai Su[1]*, Gulzhian I. Dzhardimalieva[2,3], Murzabek I. Baikenov[4]

[1]*South China University of Technology, Guangzhou, Guangdong, China;*
[2]*Federal Research Center of Problems of Chemical Physics and Medicinal Chemistry, Russian Academy of Sciences, Chernogolovka, Moscow region, Russia;*
[2]*Moscow Aviation Institute (National Research University), Moscow, Russia;*
[4]*Karaganda Buketov University, Karaganda, Kazakhstan*

Special Issue Foreword from Guest Editors

Dear Colleagues,

We are pleased to present this Special Issue *"Nano- and Photo- Catalysis in Current Chemistry: Possibilities and Challenges"* focused on current trends and innovation in catalysis. Catalysis plays a crucial role in current chemistry and about 90 % of the volume of modern chemical production is based on catalytic processes. Catalysts speed up chemical reactions by reducing activation energy, while the catalysts themselves remain unchanged throughout the reaction. This is especially important in industry, where catalysts increase process efficiency, reduce production costs, and enable chemical transformations that would not normally occur. Additionally, catalysis promotes the development of environmentally friendly technologies by minimizing harmful emissions. As a result, the chemical industry becomes more sustainable and environmentally friendly.

In this Special Issue, authors from countries such as China, Russia, Czech Republic, Azerbaijan, Uzbekistan and Kazakhstan share their 14 papers in the field of catalysis with readers of the *Eurasian Journal of Chemistry*.

The article by Professor **Xintai Su** from *South China University of Technology (Guangzhou, China) "Thermal Catalytic Production of Potassium Humate Fertilizer from Tobacco Straw and Its Performance in Wheat Hydroponics"* focuses on the production of artificial humic acid from waste biomass and considers its contribution to agricultural productivity. In this study, potassium humate was obtained from agricultural waste tobacco straw by thermal catalysis using environmentally friendly Fe_2O_3 as a catalyst. This study provides a green and simple technology for the resourceful utilization of tobacco straw to produce high value-added potassium humate, and enriches the source of raw materials for potassium humate, expanding its application in the field of crop growth.

Professor **Gulzhian I. Dzhardimalieva** (*Federal Research Center of Problems of Chemical Physics and Medicinal Chemistry, Russian Academy of Sciences, Chernogolovka, Moscow region, Russia*), professor **Kamila A. Kydralieva** (*Moscow Aviation Institute, Moscow, Russia*) and coauthors presented research paper «A Statistical Design Approach for an Effective Catalyst in the Fenton Reaction in Case of Fe_3O_4-MOF MIL-88b (Fe) in Methylene Blue Degradation Kinetics», in which composites containing metal-organic framework MIL88b(Fe), nanoparticles magnetite (Fe_3O_4) or maghemite (γ-Fe_2O_3) modified by humic acids or ascorbic acid were synthesized and tested in the decomposition reaction of methylene blue. The prognostic model based on multivariate correlation analysis was used by the authors. It was shown that only the total concentration of released iron ions is a significant factor influencing the kinetics of the Fenton reaction.

Professor **Murzabek I. Baikenov** from *Karaganda Buketov University (Karaganda, Kazakhstan)* with co-authors determined the optimal conditions for demetallization of the heavy fraction of coal tar from

Shubarkol Komir JSC by means of full factorial experiment. It was established that the optimal conditions for demetallization are equal to 0.04 ratio of the "Coal shale" catalytic additive to the heavy fraction of coal tar with boiling point above 300 °C, process temperature in the range of 420–430 °C, duration from 20 to 30 minutes and initial pressure between 3 and 5 MPa. Experiments conducted under these conditions showed a degree of demetallization of 87–89 %.

A mini-review by Professor **Sarkyt E. Kudaibergenov** *(Institute of Polymer Materials and Technology, Almaty, Kazakhstan)* briefly discusses the catalytic properties of polyampholytes, polyampholyte-metal complexes, polyampholyte-metal nanoparticles and polyampholyte-catalase conjugates. Special focus is given to amphoteric hydrogels and cryogels that encapsulate metal nanoparticles or enzymes. Additionally, the review explores the potential of light-driven hydrogen and oxygen evolution reactions from water, facilitated by metal nanoparticles within amphoteric hydrogels in the presence of photosensitizers.

Professor **Abduali Bayeshov** from *National Center on Complex Processing of Mineral Raw Materials of the Republic of Kazakhstan (Almaty, Kazakhstan)* with co-authors summarized the results of their pioneering research using the redox Ti (IV)-Ti (III) system, which demonstrates a catalytic effect on the cathodic reduction of selenium (VI), copper (II), platinum (IV), palladium (IV), bismuth, arsenic (V) ions, uranium (VI), as well as manganese dioxide suspension. It was demonstrated that in the presence of the redox Ti (IV)-Ti (III) system, hard-to-reduce selenate ions can be reduced at room temperature. The catalytic action of the Ti(IV)-Ti(III) redox system was demonstrated and the reaction mechanism was established.

The article "Effects of Selenite Ions on a Luminescence Enzymatic System" by Professor **Nadezhda S. Kudryasheva** (*Siberian Federal University, Krasnoyarsk, Russia*) and coauthors is focused on the biochemical and physicochemical aspects of toxicity of a redox-active compound in live organisms. Sodium selenite (Na_2SeO_3) was chosen as a model redox-active compound; a coupled enzymatic system from luminous marine bacteria was applied to imitate a biochemical process. It was demonstrated that Na_2SeO_3 suppressed bioluminescence of the enzyme system; the effective inhibition concentration was 10^{-2} M.

Researchers from *Lomonosov Moscow State University, Moscow, Russia* (Doctor **Gennadii A. Badun**) and from *Siberian Federal University, Krasnoyarsk, Russia* (Professors **Grigoriy N. Churilov**, **Nadezhda S. Kudryasheva** with others) studied radioprotective properties of fullerenol $C_{60,70}O_y(OH)_x$, ($x+y$ = 24–28), a water-soluble polyhydroxylated fullerene derivative with an electron-deficient aromatic carbon structure. Tritium, a radionuclide of low decay energy, was selected to simulate an exposure to low-dose irradiation (< 0.05 Gy), and luminous marine bacteria *Photobacterium phosporeum* was used as a model cellular object to monitor radiation bioeffects; the bioluminescence intensity of the bacteria was used as a tested biological parameter. It was found, what tritium activated the bacterial luminescence; the addition of fullerenol ($< 3\cdot10^{-3}$ g/L) "mitigated" the activation, thus revealing the radioprotective capacity of fullerenol for the marine microorganism.

Authors from *Institute of Catalysis and Inorganic Chemistry named after acad. M. Nagiyev of Ministry of Science and Education of Republic of Azerbaijan, Baku, Azerbaijan* (Professor **Yuriy N. Litvishkov** and Drs. **Nargalam M. Hasanguliyeva, Ninel V. Shakunova**) studied the activity of mono- and di-substituted cobalt and nickel ferrites prepared by microwave solid-phase synthesis was studied in the reaction of liquid-phase oxidation of m-xylene to m-toluic acid. It was established that among the tested samples, the di-substituted ferrites of spinel structure with the composition of $Ni_{0,6}Co_{0,4}Fe_2O_4$ have the shortest induction period and the highest initial rate of oxygen absorption.

Professor **Gulzhian I. Dzhardimalieva** (*Federal Research Center of Problems of Chemical Physics and Medicinal Chemistry, Russian Academy of Sciences, Chernogolovka, Russia*) and coauthors studied rational synthesis of UiO-66 and its application in the hydrogenation reaction of p-chloronitrobenzene. The effects of reaction temperature, linker volume concentration and solvent type on the specific surface area and thermal properties were evaluated. The composition, structure and physicochemical properties of the obtained compounds by IR spectroscopy, TGA and XRD analysis were also studied.

Synthesis and electrocatalytic activity of copper nanoparticles supported on nickel ferrite were studied by Professor **Nina M. Ivanova** *(LLP "Institute of Organic Synthesis and Coal Chemistry of Kazakhstan Republic", Karaganda, Kazakhstan)* and coauthors. Cu(x)/$NiFe_2O_4$(y) magnetic composites with different component ratios were prepared by chemical reduction of copper cations in the presence of sonicated nickel ferrite and characterized by X-ray diffraction spectroscopy and scanning electron microscopy. The electrocatalytic activity of Cu(x)/$NiFe_2O_4$(y) composites deposited on a cathode was investigated in the electrohydrogenation of acetophenone (APh). It was shown that the electrocatalytic activity of these composites appears starting from the percentage ratio of their components x:y = 40:60.

Preparation and characterization of copper nanoparticles stabilized by poly(vinyl alcohol) for catalytic oxidation of 1-propanol were studied by the authors from *Institute of Polymer Materials and Technology, Almaty, Kazakhstan* (Professors **Sarkyt E. Kudaibergenov**, **Dina N. Akbayeva)** with coauthors from Al-Farabi Kazakh National University, *Almaty, Kazakhstan.* The aqueous solution of copper (II) complex of poly(vinyl alcohol) (PVA-Cu(II)) was characterized by conductimetric titration, UV-Vis spectroscopy and FTIR. The optimum catalyst mass and reaction time were found for the conversion of 1-propanol to propionaldehyde with yields ranging from 61.4 % to 87.8 %.

Professor **Kamila A. Kydralieva** (*Moscow Aviation Institute, Moscow, Russia*) and coauthors presented study of magnetically separable Fe_3O_4/γ-Fe_2O_3@MIL-88b(Fe) and Fe_3O_4/γ-Fe_2O_3@NH_2-MIL-88b(Fe) composites for the photocatalytic degradation of Congo Red dye. These composites were characterized by elemental analysis, FTIR spectra, XRD patterns, magnetization curves, TGA profiles, nitrogen adsorption-desorption isotherms. Using ultraviolet-visible spectroscopy and Congo Red anionic azo dye as organic pollutant, composites' adsorption kinetics were observed and their photocatalytic activities were studied. As a result, Fe_3O_4/γ-Fe_2O_3@MIL-88b(Fe) and Fe_3O_4/γ-Fe_2O_3@NH_2-MIL-88b(Fe) were both capable photocatalysts for generating hydroxyl radicals from hydrogen peroxide (H_2O_2) through Fenton-like reaction with removal efficiencies of CR dye approaching 89 % and 95 %, respectively.

Associate Professor **Gulsym K. Burkeyeva** from *Karaganda Buketov University, Karaganda, Kazakhstan* with coauthors presented synthesis and investigation of catalytic properties of metal-polymer nanocomposites based on copolymers of polypropylene glycol fumarate phthalate and polypropylene glycol maleate phthalate, using acrylic acid and immobilized cobalt metal particles as catalysts. A classical reaction of the electrocatalytic hydrogenation of pyridine to piperidine was applied. SEM and dynamic light scattering were used to investigate the average size and dispersity of cobalt metal nanoparticles. The results of the studies indicated high catalytic activity of metal-polymer nanocomposites based on p-PGMPh–AA–Co^0 and p-PGFPh–AA–$Co^{0.}$

The team of authors led by Professor **Xintai Su** (*South China University of Technology, Guangzhou, Guangdong, China*) reported about construction of a series of Ag/AgCl@MIL-53(Fe) samples with different Fe:Ag ratios by hydrothermal methods and their use in the photocatalytic water oxidation reactions. XRD characterization showed the successful preparation of Ag/AgCl@MIL-53(Fe) heterostructure catalysts. The reaction results showed that sample AAM-2 (Fe:Ag=5:1) had the best photocatalytic water oxidation performance, with the highest TOF value of 0.14 mmol/(g·s) and quantum efficiency of 39.0 % under the conditions of catalyst mass of 1 mg and pH=9.0 for boric acid-borax buffer solution.

Dear Readers! In this Special Issue «*Nano- and Photo- Catalysis in Current Chemistry: Possibilities and Challenges»* you will find 14 papers in the field of catalysis involving researchers from China, Russia, Czech Republic, Azerbaijan, Uzbekistan and Kazakhstan. The Guest Editors of this Special Issue have invited new authors with interesting topics and hope that the collected articles will attract reader interest and expand the audience of the *Eurasian Journal of Chemistry*!

*Information about Guest Editors**

**The editors' names are presented in the following order: First Name, Middle Name and Last Name*

Xintai Su — Professor, School of Environment and Energy, Guangdong Provincial Key Laboratory of Solid Wastes Pollution Control and Recycling, South China University of Technology, 510006, Guangzhou, Guangdong, PR China; e-mail: suxintai@scut.edu.cn; https://orcid.org/0000-0001-6615-5273

Gulzhian Iskakovna Dzhardimalieva — Doctor of Chemical Sciences, Head of Laboratory of Metallopolymers, Federal Research Center of Problems of Chemical Physics and Medicinal Chemistry, Russian Academy of Sciences, Chernogolovka, Moscow region, 142432, Russia; e-mail: dzhardim@icp.ac.ru; https://orcid.org/0000-0002-4727-8910

Murzabek Ispolovich Baikenov — Doctor of Chemical Sciences, Professor, Karaganda Buketov University, Universitetskaya street, 28, 100024, Karaganda, Kazakhstan; e-mail: murzabek_b@mail.ru; https://orcid.org/0000-0002-8703-0397

How to Cite: Li, Q., Li, J., Zhao, Y., Zhu, Y., Baikenov, M.I., Liu, X., & Su, X. (2024) Thermal Catalytic Production of Potassium Humate Fertilizer from Tobacco Straw and its Performance in Wheat Hydroponics. *Eurasian Journal of Chemistry, 29, 3(115), 7-15.* https://doi.org/10.31489/2959-0663/3-24-12

Article

Received: 2 July 2024 | Revised: 31 August 2024 |
Accepted: 13 September 2024 | Published online: 23 September 2024

UDC 544.42+519.242.7

https://doi.org/10.31489/2959-0663/3-24-12

Qianqian Li[1], Jinlin Li[1], Yinqiao Zhao[1], Yingjie Zhu[1],
Murzabek I.Baikenov[2], Xiaofei Liu[3], Xintai Su[1]*

[1]*School of Environment and Energy, Guangdong Provincial Key Laboratory of Solid Wastes Pollution Control and Recycling, South China University of Technology, Guangzhou, Guangdong, China;*
[2]*Karaganda Buketov University, Karaganda, Kazakhstan;*
[3]*College of Chemistry and Chemical Engneering, Xinjiang Agricultural University, Urumqi, China*
*(*Corresponding author's e-mail: suxintai@scut.edu.cn)*

Thermal Catalytic Production of Potassium Humate Fertilizer from Tobacco Straw and Its Performance in Wheat Hydroponics

Production of artificial humic acid (AHA) from waste biomass will contribute to environmental protection and agricultural productivity. However, there is still a lack of a faster, more efficient and eco-friendly way for sustainable production. In this study, potassium humate was prepared from agricultural waste tobacco straw by thermal catalysis using environmentally friendly Fe_2O_3 as a catalyst. The yield of potassium humate was successfully increased to 68.77 %. In the present study, using characterization methods such as TG-DTG and UV, it was found that the potassium humate prepared from tobacco straw had lower aromaticity, smaller molecular weight, as well as better solubility and better quality. In addition, the effect of potassium humate fertilizer on wheat biomass was also investigated in this experiment by wheat hydroponics. The results showed that the germination rate of wheat increased by 17 % and the fresh and dry weights increased by 6.94 % and 19.31 %, respectively, with the addition of potassium humate prepared with iron catalyst. This study provides a green and simple technology for the resourceful utilization of tobacco straw to produce high value-added potassium humate, and enriches the source of raw materials for potassium humate, expanding its application in the field of crop growth.

Keywords: Tobacco straw, potassium humate, wheat growth, wheat hydroponics, artificial humic acid (AHA), biomass, tobacco straw, thermal catalysis, fertilizer.

Introduction

Agricultural production is the second largest contributor of greenhouse gases (19.9 percent), after the energy sector (68.1 percent). A large amount of solid waste is generated annually from agricultural production [1]. Common agricultural wastes include rice straw, tobacco straw, wheat straw, corn stover and bagasse, etc. In total, about 998 million tons of agricultural waste are generated globally each year, of which about 110 million tons of agricultural waste are generated annually in Europe, China, Japan, and India, and 240 million tons of agricultural waste are generated annually in the United States [2–3]. These agricultural wastes mainly contain cellulose, hemicellulose, lignin and starch, and are rich in high value components and bioactive compounds such as dietary fibre, polysaccharides, proteins and fatty acids [4]. It also contains other polar organic functional groups such as ethers, phenols, carboxyl groups, ketones, aldehydes and alcohols [5]. Humus is produced by microbial degradation of dead biomass (e.g. lignin), which is difficult to break down further. The properties and structure of humic substances depend on the specific conditions under

which they are extracted from water or soil. Although humic substances come from different sources, their properties are very similar [6]. In soils and sediments, humic substances can be divided into three main fractions: humic acid (HA), fulvic acid (FA) and humin (HM). The main elements are carbon (C), hydrogen (H), oxygen (O), nitrogen (N) and sulphur (S), and it also contains many reactive groups and a large variety of reactive functional groups, such as hydroxyl, alcohol hydroxyl, phenol hydroxyl, quinone group, carbonyl group, and a small amount of methoxyl, amino group, alkenyl group and so on. These functional groups are capable of forming coordination compounds or other biochemical reactions with a variety of substances such as metal ions, and are used in many fields such as industry and environmental protection.

In addition, Fe-based catalysts applied to the synthesis of AHS have gained increasing attention due to the excellent biocompatibility and environmental friendliness. The addition of Fe catalysts to establish the Fenton reaction promoted the lignin macromolecular structure formation for the artificial synthesis of humic-like substances and an increase in the yield of AHA. Additionally, Fe can be used in biomass pyrolysis to catalyze lignin depolymerization. This indicates the great potential of Fe catalysts in supporting biomass structural transformation. As one of the typical Fe catalysts, iron oxyhydroxide (FeOOH) has a high density of hydroxyl radicals on its surface and exhibits acid-base bifunctional catalytic activity with excellent catalytic performance, which makes it a reliable choice for promoting the artificial humification process. FeOOH, similar to other metal hydroxides, can be used in many aspects, such as photocatalysis, electrocatalysis and coal liquefaction, and has a very high application value. However, FeOOH's role in abiotic humification has not been explored, and its effect on each part of AHS has not been investigated.

Although HA from mineral sources is easy to obtain, the humus content of mineral sources such as lignite and weathered coal is low, and the preparation of HA with higher molecular weights and lower yields is still a problem that needs to be solved urgently. The preparation of biochemical HA from biomass waste has become an efficient way to utilize agricultural resources, and it is also one of the main sources of HA preparation. After a series of physical treatments, the straw is hydrolyzed, catalyzed and oxidized into HA by chemical reagents, and then biochemical HA is obtained by filtration, washing, drying, crushing and grinding. The biochemical HA obtained by this method has a low molecular weight, is rich in oxygen-containing functional groups, and is highly active. Therefore, due to the non-renewable nature of coal, the raw material for HA, as well as its high price and transport costs, a new and efficient HA production technology has been developed from existing, renewable and inexpensive materials. Some researchers have proposed methods to convert biomass solid waste into HA-like substances by modeling the humus formation process in nature. For example, some chemicals obtained modified humic acid-based cross-linked composite pre-tuned to the sorbed copper ion. Such tuning forms adsorption centers in the polymer network of the composite, which can repeatedly and highly specifically interact with the template, and highly selectively extract target molecules from solution, leading to significant increase in sorbent capacity [7]. Some chemicals accelerated the humification process and synthesized HA with a structure similar to that of natural HA by using black soil and leaves as precursors and hydrothermal treatment at 200 °C for 24 h [8]. Some chemicals converted food waste into artificial HA under hydrothermal conditions, which resulted in a HA yield of 43.5 % after only 1 h of treatment, and also produced mineral-like HA with similar structure and composition [9]. Therefore, it is feasible to prepare HA-like substances from biomass. However, since the disadvantages of hydrothermal conversion are its duration and low yield, as well as the high equipment requirement, there is an urgent need to find a simple and efficient HA extraction method. In this study, potassium humate was prepared by thermal catalysis using tobacco straw as a waste biomass feedstock and environmentally friendly Fe_2O_3 as a catalyst. Fe_2O_3 can also modulate the properties of AHS by changing the content and nature of AHA (Artificial Humic Acid) and AFA (Artificial Fulvic Acid). The main results of this work were: 1) The yield of potassium humate was successfully increased to 68.77 % at a roasting temperature of 225 °C, a roasting time of 2 h, and an iron catalyst dosage of 1 % (relative to the mass fraction of tobacco straw); 2) Using characterization methods such as TG-DTG and UV, it was found that the potassium humate prepared from tobacco straw has a lower aromaticity, a smaller molecular weight and better solubility and better quality; 3) It can be proved by comparing the results of TG-DTG, UV and other characterization methods that the addition of Fe_2O_3 catalyst contributed to the increase of xanthic acid content and oxygen-containing functional group content in potassium humate. In addition, the effect of potassium humate fertilizer on wheat biomass was also investigated in this experiment by wheat hydroponics. The results showed that the germination rate of wheat increased by 17 % and the fresh and dry weights increased by 6.94 % and 19.31 %, respectively, with the addition of potassium humate prepared with iron catalyst. This study provides a green and simple technology for the resourceful utilization of tobacco straw to produce high value-added potassium humate, and enriches the

source of raw materials for potassium humate, expanding its application in the field of crop growth. Overall, the main objective of this study is to provide a new and sustainable pathway for the accelerated production of AHS from waste biomass, thus effectively utilizing a large amount of waste biomass.

Experimental

Tobacco straw is a lignocellulosic raw material that is abundant, inexpensive and easily available. Tobacco straw was used as a typical waste biomass in this study. Potassium humate was prepared by weighing a certain amount of tobacco straw and crushing it through a 200 mesh sieve. The experiment was divided into two groups, the first group mixed 10g of tobacco straw powder and catalyst Fe_2O_3 in the ratio of 1:0.01 by mass and added to 30 % KOH solution; the second group added 10g of tobacco straw powder only to 30 % KOH solution. Equal amount of 30 ml of deionised water was added to the two groups of mixtures and fully dissolved after sonication. The two groups of mixtures were transferred into an oven and then dried at 70 °C. Then the two mixtures were completely ground, transferred into a crucible, wrapped with tin paper, transferred to a high-temperature blast drying oven, and roasted for 120 min at 225 °C. After roasting, the product obtained was quenched by adding deionised water. After standing for some time, the product was transferred to a beaker and dissolved in water, the soluble organic substances were completely dissolved by ultrasonication, and the solid-liquid separation was achieved by filtration. The solid and liquid were transferred to an oven and dried at 70 °C to obtain potassium humate samples, which were weighed. The sample obtained without catalyst addition was named S-HLS-K and the sample prepared with catalyst addition was named CS-HLS-K.

The test crop was wheat, potassium humate was extracted with KOH as leaching agent to obtain potassium humate and then adjusted the pH to pH 6.5–7.5 (the pH range suitable for wheat growth), the experiment was conducted in April 2024 in the laboratory of the School of Environment and Energy, South China University of Technology, Guangzhou, China. Wheat seeds were provided by Guangdong Academy of Agricultural Sciences. The prepared S-HLS-K and CS-HLS-K potassium humate fertilizers were added to the experimental groups, and clean water was used as the control group, which was uniformly placed in the laboratory for cultivation. Seedlings were raised in a hydroponic potting apparatus (the potting apparatus is divided into two parts, with a planting basket on the upper part and a transparent bottle on the lower part, and the planting basket has a uniform gap on the side to facilitate the absorption of nutrients by the growing down root system) on 11 April 2024. The experiment was carried out in an environment with an average day and night temperature of 23–25 °C, relative humidity of 50–65 % and natural light conditions. The water was replenished regularly every morning and evening, and 50 wheat seeds were born in each planting basket, evenly and randomly arranged. After one week of wheat growth, wheat seedlings were harvested on 18 April 2024 and the growth of wheat seedlings was determined. Each treatment was repeated three times to ensure the accuracy of the experiment.

Analytical Methods

In this experiment, based on the specific steps of the titration method of ammonium ferrous sulphate in the national standard GB/T 34765-2017, the xanthate content of the prepared potassium humate was determined and compared with that of the commercial mineral source potassium humate.

In order to investigate in depth, the detailed chemical composition of the produced potassium humate versus that of the commercial mineral source potassium humate, a series of elemental analytical characterization techniques were employed in this study to determine the content of five key elements, namely carbon, hydrogen, oxygen, nitrogen and sulphur, in the samples. These detailed elemental analytical data provided a revealing characterization of the elemental composition of the samples. In addition, based on the measured H/C and O/C atomic ratios, the degree of aromatization and the number of oxygen-containing functional groups of the samples can be further deduced. In this experiment, a high-precision Vario EL cube type elemental analyzer (Elementar, Germany) was used to ensure the accuracy and reliability of the data.

UV-1800PC model UV-visible spectrophotometer manufactured by Shanghai Meppan Instruments Co was used for the UV-Vis absorption spectroscopy analysis and detection of substances. First, a 0.05 mol/L sodium bicarbonate solution was configured using a 250 mL volumetric flask. Subsequently, 5 mg of S-HLS-K and CS-HLS-K samples were weighed and each dissolved in the previously configured sodium bicarbonate solution, and the solution was fixed using a 50 mL volumetric flask to ensure homogeneity and then allowed to stand. During the detection stage, the scanning wavelength range was set to 200–900 nm and the samples were detected sequentially. Special attention was paid to the absorbance ratio at wavelengths 465 nm and 665 nm, i.e., E_4/E_6.

Fourier infrared spectroscopy plays an important role in the study of compositional and structural characteristics of HA, which can accurately detect the relative content of functional groups in the sample and their existence patterns, providing reference data for the analysis of HA. Nicolet iN 10 Fourier infrared spectrometer (Thermo Fisher Scientific) was used for this experiment. To ensure the accuracy of the experimental results, the instrumental resolution of 0.06 cm^{-1} was set and 32 scans were performed. Also, the scanning the range was set between 600 and 4000 cm^{-1} for this experiment to fully analyze the infrared spectral properties of the powder samples.

Scanning electron microscope SEM SU8010 model (Hitachi, Japan) was used to observe the main microstructural morphology of the sample and the size of the material from different angles. It was adjusted by magnification to observe the surface microstructural characteristics of the material.

Results and Discussion

Fig. 1 shows the scanning electron microscope (SEM) photographs of commercial iron oxide, from which it can be seen that the commercial iron oxide consists of irregular particles of different sizes, and the particle size is mainly distributed in the 500 nanometres or so.

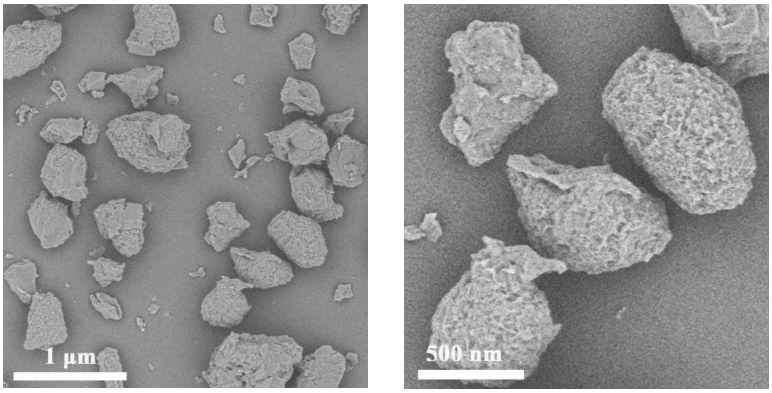

Figure 1. SEM images of commercial Fe_2O_3 catalysts

The effect of addition of iron catalyst on the yield of potassium humate and the content of xanthate and humic acid in the catalytic roasting process was investigated. The results have shown that under the conditions of roasting temperature of 225 °C, roasting time of 2 h, and the amount of iron catalyst of 1 % as a percentage of the mass of the raw material, tobacco straw), the yield of potassium humate can be effectively increased to 68.77 %. It was 3.87 % higher than the yield of potassium humate 64.90 % obtained without adding iron catalyst under the same conditions. The effect of FeOOH on the composition of AHS was investigated by separating and quantifying the residues (RS), AHA and AFA in both AHS. Fig. 2(*a*) and 2(*b*) present the amount of each component in the AHS before and after addition of iron catalyst, respectively. As it can be seen from the comparison of the content of each component (Fig. 2), Fe catalyst increased significantly the AFA content in AHS from 11.5 wt% to 26.4 wt% and decreased the RS from 56.9 wt% to 52.8 wt%. These changes indicate that the Fe catalyst improved the composition and properties of AHS by increasing AFA with smaller molecular weight and water solubility, which imply that the activity and plant uptake of AHS would be enhanced.

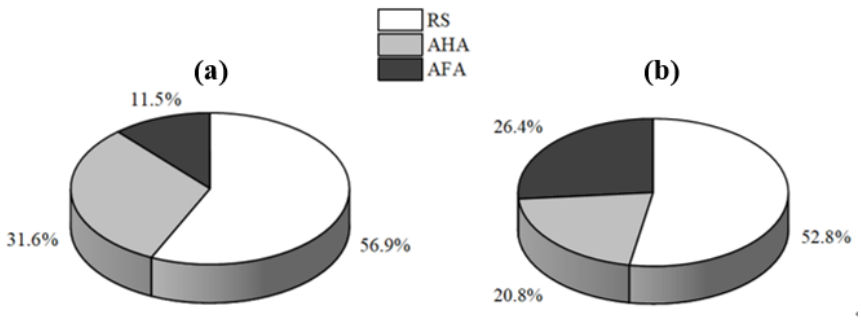

Figure 2. Changes in AHS composition with the addition of iron catalysts

The elemental content and elemental ratios of biomass during the conversion process were determined and calculated by elemental analysis techniques. As shown in Table 1, both HAK and specific samples exhibited high carbon content, this suggests that HA preparation promotes carbon sequestration. The elemental ratios implied that some chemical reactions took place: both H/C and O/C ratios of HAK were lower than those of tobacco straw, indicating that dehydration and decarboxylation reactions occurred during pyrolysis. Low H/C and O/C ratios are often associated with high aromaticity of the material, suggesting that the pyrolysis process promotes the production of more aromatic substrates, which in turn enhances the potential for HA synthesis in this way, allowing the biomass to be transformed into forms such as peat and lignite.

The O/C ratio usually reflects the contribution of carbohydrates and carboxylic acids to artificial HA (AHA) formation. Therefore, a higher O/C ratio implies that AHA contains a higher proportion of compounds such as carboxylic acids and furans. The increase in O/C ratio with the use of Fe catalyst further indicates the positive role of Fe catalyst in promoting the formation of carboxylic acids, furans and other carbohydrates. A higher N/C ratio, on the other hand, is often regarded as one of the characteristics of natural HA in peat or soil, and the high N/C value exhibited by AHA in this experiment not only indicates that its properties are similar to those of natural HA, but also reflects its high degree of humification and plant origin.

Table 1

Organic Elemental Content and Elemental Ratio of Samples

Specimens	Elemental composition (wt.%)					Atomic ratio		
	N	C	H	S	O	N/C	H/C	O/C
Tobacco straw	0.94	43.49	6.92	0.00	49.55	0.02	1.90	0.85
HAK	2.62	57.16	4.12	0.35	35.75	0.05	0.86	0.47
HAK-Fe	2.83	57.07	4.14	0.29	35.67	0.05	0.87	0.47
AHA	3.04	61.17	5.03	0.51	30.25	0.05	0.98	0.37
AHA-Fe	3.22	55.96	4.85	0.00	35.97	0.06	1.04	0.48

Table 2 shows the E_4, E_6 and E_4/E_6 ratios measured using UV-Vis spectrophotometer. In order to investigate the effect of catalyst on the degree of humification and functional groups of AHA and AFA, the ratio of absorption values of AHA and AFA at 465 nm and 665 nm was further analyzed. The results showed that AHA displayed a higher E_{465}/E_{665} ratio compared to C-HA. This ratio is usually used as an indicator to assess the degree of aromaticity and aromatic carbon condensation, with higher ratios being associated with lower aromaticity. Thus, the AHAs and AFAs prepared in this experiment have lower aromaticity compared to C-HA. Meanwhile, the E_{465}/E_{665} ratio of AHA-2 was higher than that of AHA-1, which indicates that the addition of Fe catalyst had an effect on the aromaticity of HA, i.e., more aromatic rings were broken during the catalysis. Low aromaticity represents high hydrophilicity, which also coincides with the fact that FA exhibits stronger hydrophilicity. Thus, the catalysts altered the properties of AHA and AFA to have lower aromaticity, smaller molecular weight and higher hydrophilicity, which is consistent with the results of the above analyses.

Table 2

E_4/E_6 ratio for S-HLS-K, CS-HLS-K and M-HA-K

	AHA-1	AHA-2	C-HA
E_{465}	0.406	0.416	0.370
E_{665}	0.164	0.123	0.153
E_4/E_6	2.476	3.382	2.418

The results of the IR spectral characterization of the three potassium humates are shown in Fig. 3. The positions of the characteristic peaks in the IR spectra of different potassium humates are almost the same, indicating that they contain very similar functional groups. 3281.2 cm^{-1} represents the stretching and bending vibrations of -OH and N-H. The characteristic peaks at 1558.9 cm^{-1} are due to the stretching of C=C in the aromatic ring [10], and the peaks at 1393.1 and 1052.8 cm^{-1} represent C–O vibrations in the aromatic ring and ether, respectively. The lower characteristic peaks of CS-HLS-K near 1558.9 cm^{-1}, 1393.1 cm^{-1} and

1052.8 cm^{-1} indicate that CS-HLS-K has lower aromaticity, which is consistent with the analysis of the results of the UV-determined E_4/E_6 ratio.

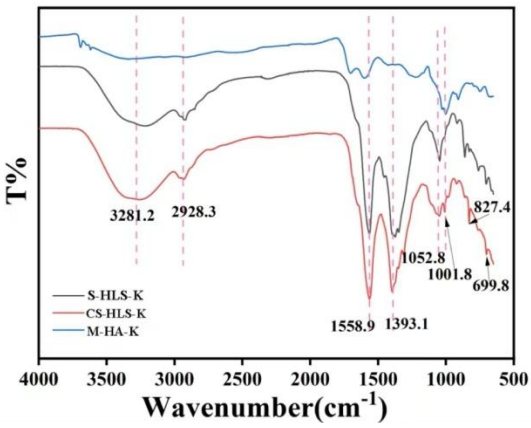

Figure 3. Infrared spectra of S-HLS-K, CS-HLS-K and M-HA-K

Figure 4 shows the TG-DTG analysis performed in N_2 atmosphere, which was used to monitor the changes in tobacco straw during heat treatment. The weight loss of tobacco straw was gradual, with the fastest rate of weight loss occurring at 283 °C. The weight loss of the tobacco straw was also observed in the heat treatment process. From room temperature to 150 °C, the weight loss of tobacco straw was attributed to the evaporation of adsorbed and crystalline water or the partial release of some light volatiles. At temperatures above 150 °C, the fibers begin to degrade rapidly. The first important stage of thermal decomposition occurs between 150 and 350 °C, during which the glucosyl and glycosidic bonds break, releasing small amounts of gases such as carbon dioxide and methane. At this stage, the mass loss of tobacco straw reaches 38.3 %, indicating that the biomass structure undergoes a large transformation in this temperature range. A second stage of mass loss of tobacco straw was observed in the range of 350–550 °C, which was caused by a richer structure of aromatic compounds. Typically, cellulose and hemicellulose undergo significant transformation at temperatures below 300 °C, whereas lignin is relatively stable with only minor changes. Initial interaction and pyrolysis of hemicellulose, cellulose and lignin occurs during a mild pyrolysis process at 200–300 °C. At this stage, some hemicellulose and a small amount of lignin were degraded. The mild pyrolysis process promotes the onset of lignocellulose depolymerization and further destroys the structure of lignocellulose.

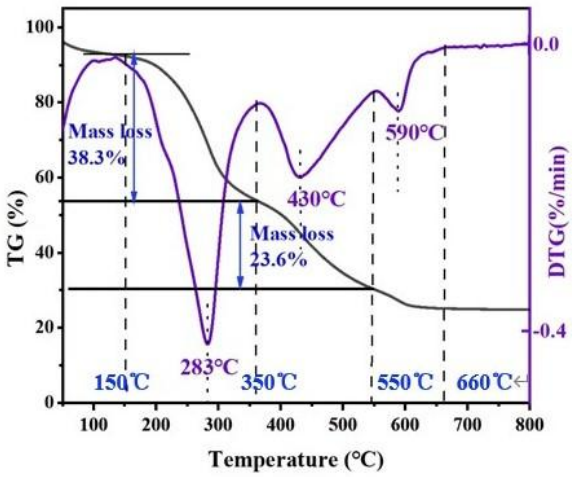

Figure 4. TG-DTG curves of pyrolysis of tobacco straw under N_2 atmosphere

The growth conditions of the three groups of wheat seeds in water and after spraying with different kinds of potassium humate solutions for 1 week are shown in Fig. 5. As can be seen from the figure, the

growth difference of wheat plants above ground and the growth difference of roots were both large. Compared with the control group (Fig. 5B(*a*)), the addition of CS-HLS-K solution (Fig. 5B(*c*)) promoted the growth of wheat more obviously.

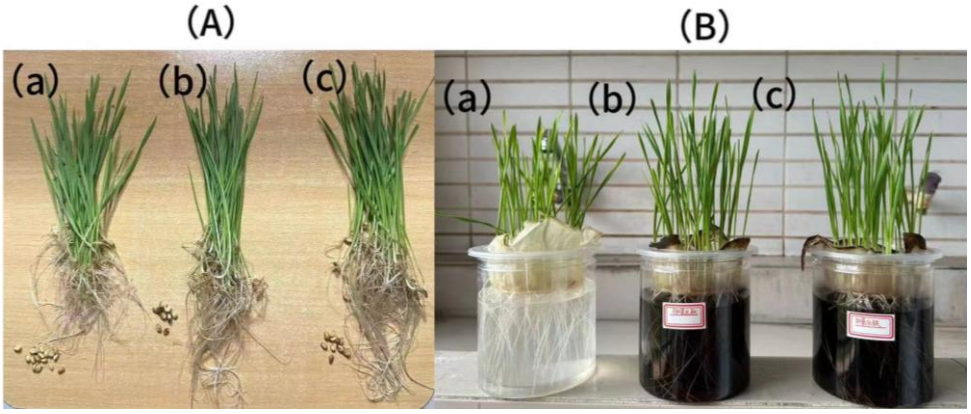

Figure 5. (A) Wheat plant laying after one week of hydroponics (B) Wheat plant growth after one week of hydroponics (*a*) Clear water group; (*b*) 10 mg/L S-HLS-K solution; (*c*) 10 mg/L CS-HLS-K solution

Each biomass of wheat plants (germination rate, total fresh and dry weight of wheat plants) was determined and after three replications, the effect of different potassium humates on germination rate of wheat seeds is shown in Fig. 6, and the effect on the average aboveground and root length of wheat plants, fresh and dry weight of wheat plants is shown in Fig. 7. It can be seen from Fig. 6 that the germination rate of treatment group 3 increased by 17 % compared to that of the fresh water control group, and that the germination rate of treatment group 3 increased by 6 % compared to that of treatment group 2, indicating that the promotion of wheat germination was more pronounced in treatment group 3 compared to that of treatment group 2. As can be seen from Fig. 7, the fresh and dry weight of wheat plants increased by 6.94 % and 19.31 %, respectively, in comparison with fresh water control group. Compared with the fresh water control group, all parameter of 2 and 3 treatments increased, which proves that the addition of potassium humate can have a certain promoting effect on the growth of wheat. Based on the data of the indexes, it was estimated that the growth promotion effect of different potassium humate solutions was CS-HLS-K > S-HLS-K. The wheat with CS-HLS-K solution had the highest germination rate, the best root growth and the greatest increase in the fresh and dry weights, and the growth promotion effect of CS-HLS-K was the most significant, which might be due to the addition of catalysts to increase the oxygen-containing functional groups of the material C =O, O–C–O, as well as the content of nitrogen, potassium and other elements required for the plant growth, thus effectively promoting the growth of all parts of wheat. In addition, CS-HLS-K's lower aromaticity, less molecular weight, and better solubility and quality are also conducive to the promotion of crop growth.

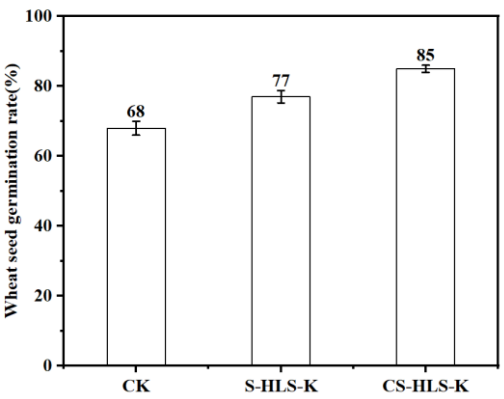

Figure 6. Germination rate of wheat seeds

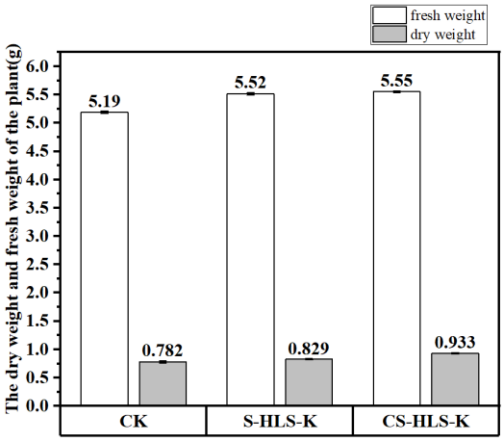

Figure 7. Fresh and dry weight of wheat plants

Conclusions

The green and clean Fe_2O_3 was used as a catalyst for the catalytic preparation of potassium humate analogues. Under the thermal catalysis condition of 225 °C, time of 2 h and catalyst amount of 1 % (mass percentage of raw tobacco straw), the quality measurement results have shown that the catalytically prepared CS-HLS-K had lower aromaticity, smaller molecular weight, better solubility and superior quality as compared to M-HA-K. The addition of catalyst promoted the macromolecular humification process and the carbonation and oxygenation process of tobacco straw. It also increased the number of oxygen-containing functional groups in potassium humate. The results of plant growth experiments have shown that CS-HLS-K increased the germination rate of wheat by 17 % and the fresh and dry weights by 6.94 % and 19.31 %, respectively, compared to that of the clear water control group, indicating that CS-HLS-K had a more significant growth promotion effect on wheat compared to M-HA-K. The study in this article not only provides a direction for the resourceful utilization of agricultural waste to prepare potassium humate with better performance, but also offers a certain recommendations for the green production of potassium humate materials and its application in promoting plant growth.

Funding

This work is supported by the project of the Xinjiang Science and Technology Department (2022B01042, 2022E01051, 2022E02098), the Yili State Science and Technology Bureau Project (YZ2023A7, YZD2024A16, YZ2023A11), and the Project of Changji Science and Technology Bureau (2023Z04)

*Author Information**

**The authors' names are presented in the following order: First Name, Middle Name and Last Name*

Qianqian Li — Undergraduate of Environmental Engineering, South China University of Technology, 510006, Guangzhou, Guangdong, China; e-mail: lqq12180517@gmail.com; https://orcid.org/0009-0002-2755-4292

Jinlin Li — Undergraduate of Environmental Engineering, South China University of Technology, 510006, Guangzhou, Guangdong, China; e-mail: 1347565531@qq.com

Yinqiao Zhao — Undergraduate of Environmental Engineering, South China University of Technology, 510006, Guangzhou, Guangdong, China; e-mail: 2924160897@qq.com

Yingjie Zhu — Undergraduate of Environmental Engineering, South China University of Technology, 510006, Guangzhou, Guangdong, China; e-mail: 205834545@qq.com

Murzabek Ispolovich Baikenov — Doctor of Chemical Sciences, Professor, Karaganda Buketov University, Universitetskaya street, 28, 100024, Karaganda, Kazakhstan; e-mail: murzabek_b@mail.ru; https://orcid.org/0000-0002-8703-0397

Xiaofei Liu — Associate Processor, College of Chemistry and Chemical Engneering, Xinjiang Agricultural University, 311 East Nongda Road, 830052, Urumqi, China; e-mail: 1136887541@qq.com; https://orcid.org/0009-0000-9199-2989

Xintai Su (*corresponding author*) — Professor, School of Environment and Energy, Guangdong Provincial Key Laboratory of Solid Wastes Pollution Control and Recycling, South China University of Technology, 510006, Guangzhou, Guangdong, PR China; e-mail: suxintai@scut.edu.cn; https://orcid.org/0000-0001-6615-5273

Author Contributions

The manuscript was written through contributions of all authors. All authors have given approval to the final version of the manuscript. CRediT: **Qianqian Li** conceptualization, data curation, investigation, methodology, resources, writing-original draft, writing-review & editing; **Jinlin Li** conceptualization, supervision, writing-review & editing; **Yinqiao Zhao** conceptualization, supervision, writing-review & editing; **Yingjie Zhu** writing-review & editing; **Murzabek Ispolovich Baikenov** writing-review & editing; **Xiaofei Liu** writing-review & diting; **Xintai Su** writing-review & editing.

Acknowledgments

Authors thank *South China University of Technology* for access to library facilities.

Conflicts of Interest

The authors declare no conflict of interest.

References

1 Kamusoko, R., Jingura, R. M., Parawira, W., & Chikwambi, Z. (2021) Strategies for valorization of crop residues into biofuels and other value-added products. *Biofuels, Bioproducts and Biorefining*, *15*(6), 1950–1964. https://doi.org/10.1002/bbb.2282

2 Lamers, P., Searcy, E., Hess, J. R., & Stichnothe, H. (2016) *Developing the global bioeconomy: Technical, market, and environmental lessons from Bioenergy*, Academic Press is an imprint of Elsevier.

3 Cao, L., Zhang, C., Chen, H., Tsang, D. C. W., Luo, G., Zhang, S., & Chen, J. (2017) Hydrothermal liquefaction of Agricultural and Forestry Wastes: State-of-the-art review and future prospects. *Bioresource Technology*, *245*, 1184–1193. https://doi.org/10.1016/j.biortech.2017.08.196

4 Bhatia, S. K., Joo, H. -S., & Yang, Y. -H. (2017) Biowaste-to-bioenergy using biological methods — a mini-review. *Energy Conversion and Management*, 177, 640–660. https://doi.org/10.1016/j.enconman.2018.09.090

5 Bhujbal, S. K., Ghosh, P., Vijay, V. K., Rathour, R., Kumar, M., Singh, L., & Kapley, A. (2022) Biotechnological potential of rumen microbiota for sustainable bioconversion of lignocellulosic waste to biofuels and value-added products. *Science of The Total Environment*, 814, 152773. https://doi.org/10.1016/j.scitotenv.2021.152773

6 Fong, S. S., Seng, L., Chong, W. N., Asing, J., Nor, M. F., & Pauzan, A. S. (2006) Characterization of the coal derived humic acids from Mukah, Sarawak as soil conditioner. *Journal of the Brazilian Chemical Society*, 17(3), 582–587. https://doi.org/10.1590/s0103-50532006000300023

7 Muldakhmetov, Z.M., Gazaliev, A.M., Zhakina, A.Kh., Vassilets, Ye.P., & Arnt, O.V. (2022) Synthesis of a Composite Based on Humic Acid Tuned to Sorbed Copper Ion. Bulletin of the University of Karaganda Chemistry, 108(4), 182–189. https://doi.org/10.31489/2022Ch4/4-22-14

8 Yang, F., Zhang, S., Cheng, K., & Antonietti, M. (2019). A hydrothermal process to turn waste biomass into artificial fulvic and humic acids for soil remediation. *Science of The Total Environment*, *686*, 1140–1151. https://doi.org/10.1016/j.scitotenv.2019.06.045

9 Chen, P., Yang, R., Pei, Y., Yang, Y., Cheng, J., He, D., Huang, Q., Zhong, H., & Jin, F. (2022) Hydrothermal synthesis of similar mineral-sourced humic acid from food waste and the role of protein. *Science of The Total Environment*, 828, 154440. https://doi.org/10.1016/j.scitotenv.2022.154440

10 Qi, Y., Zhu, J., Fu, Q., Hu, H., Rong, X., & Huang, Q. (2017) Characterization and CU sorption properties of humic acid from the decomposition of Rice Straw. *Environmental Science and Pollution Research*, 24(30), 23744–23752. https://doi.org/10.1007/s11356-017-9999-9

How to Cite: Saman, D., Bondarenko, L.S., Baimuratova, R.K., Dzeranov, A.A., Dzhardimalieva, G.I., Tropskaya, N.S., & Kydralieva, K.A. (2024) A Statistical Design Approach for an Effective Catalyst in the Fenton Reaction in Case of Fe_3O_4-MOF MIL-88b (Fe) in Methylene Blue Degradation Kinetics. *Eurasian Journal of Chemistry, 29, 3(115), 16-29.* https://doi.org/10.31489/2959-0663/3-24-15

Article

Received: 19 June 2024 | Revised: 2 August 2024 |
Accepted: 12 August 2024 | Published online: 13 September 2024

UDC 544.4+519.242

https://doi.org/10.31489/2959-0663/3-24-15

Daniel Saman[1], Lyubov S. Bondarenko[1,2*], Rose K. Baimuratova[3], Artur A. Dzeranov[1,2,3], Gulzhian I. Dzhardimalieva[1,3], Nataliya S. Tropskaya[1,2], Kamila A. Kydralieva[1]

[1]*Moscow Aviation Institute (National Research University), Moscow, Russia;*
[2]*Sklifosovsky Research Institute for Emergency Medicine, Moscow, Russia;*
[3]*Federal Research Center of Problems of Chemical Physics and Medicinal Chemistry, Russian Academy of Sciences, Chernogolovka, Moscow region, Russia*
*(*Corresponding author's e-mail: l.s.bondarenko92@gmail.com)*

A Statistical Design Approach for an Effective Catalyst in the Fenton Reaction in Case of Fe_3O_4-MOF MIL-88b (Fe) in Methylene Blue Degradation Kinetics

In this paper composites containing metal-organic framework MIL88b(Fe), nanoparticles magnetite (Fe_3O_4) or maghemite (γ-Fe_2O_3) modified by humic acids or ascorbic acid were synthesized and tested in the decomposition reaction of methylene blue. Analysis of predictive model based on multi-factor correlation analysis «physical-chemical properties — concentration of methylene blue after degradation» showed that in a line of selected parameters (initial iron concentration in sample, elemental cell parameter, Fe^{2+}/Fe^{3+} ion ratio on sample surface, total iron ion released concentration, surface area specific, surface charge), a significant factor influencing Fenton reaction kinetics, is only the total concentration of the released iron ions (p-value = 0.0162). The influence of separate Fe^{2+} and Fe^{3+} ions and reaction time on the Fenton reaction kinetics was evaluated by multi-factor analysis. The results demonstrated that concentrations of released iron ions are statistically significant, with a square of the concentration of ions Fe^{2+} and the result of the reaction time to the concentration of ions Fe^{3+}. A comparison of the sign and the coefficient values shows that an increase in ion concentration results in a reduction in methylene blue concentration, thereby accelerating the Fenton reaction rate, with Fe^{2+} ion concentration affecting more than Fe^{3+}. The resulting model is proposed as a means of selecting a sample with the maximum Fenton reaction rate at a given point in time.

Keywords: Fenton reaction, MOFs, methylene blue, degradation kinetics, MIL-88b (Fe), heterogeneous catalysts, predictive model, multivariate correlation analysis.

Introduction

The Fenton reaction is widely used for the oxidation of organic compounds and is characterized by the occurrence of a series of radical chain reactions during the interaction of iron ions and hydrogen peroxide [1, 2]. The most significant contribution to the oxidation process is made by the formation of hydroxyl radicals with the participation of a divalent iron cation according to Equation 1 [3]:

$$Fe^{2+} + H_2O_2 \longrightarrow Fe^{3+} + OH^- + \dot{O}H, \quad (1)$$

Despite the absence of restrictions associated with mass transfer, and the relatively high rates of homogeneous Fenton processes, there are a number of disadvantages. These include the need to strictly maintain the pH of the process (pH 2.8–3.5) [4, 5] to achieve optimal catalytic activity, and the formation of a larger amount of ferrous sludge (iron hydroxides/oxides) [6,7]. To overcome these disadvantages, current research has largely focused on the development of heterogeneous Fenton catalysts [8]. The leaching of metal ions from heterogeneous Fenton reaction catalysts is typically slow, resulting in minimal precipitation during the oxidation process [9]. The reusability and wide pH range performance of most heterogeneous catalysts also make these systems more attractive for advanced oxidation processes with highly active hydroxyl radicals) [10, 11]. Surface ions of divalent and trivalent iron serve as a source of formation of hydroxyl radicals in heterogeneous catalysts for the Fenton reaction [12]. A variety of iron minerals such as hematite, goethite, magnetite, ferrihydrite, pyrite, etc. have already been used in heterogeneous Fenton processes for the degradation of a multitude organic pollutants [13–15]. Porous iron materials are of greatest interest, since the sorption of organic compounds subject to oxidation increases the rate of decomposition [6]. The immobilisation of iron compounds using a ~~wide~~ range of traditional porous materials including alumina, carbon black, sili-

con dioxide, zeolite, fibers, biosorbents, hydrogels, etc. is common approach [16–19]. More recently, innovative porous materials known as metal-organic frameworks (MOFs) have been used as heterogeneous Fenton catalysts [20–22].

MOFs are a class of porous materials constructed from metal ions or their clusters connected to each other via organic linkers [23]. The principal advantages of these porous materials are their uniform pore distribution, high surface areas and the possibility of designing the porous structure [24–27]. The pore diameter of these materials can be controlled by varying the nature of the structure-forming element (type of metal and its chelate environment) and the organic bridging linker and its size. Furthermore the possibility of hierarchically combining several coordination polymers into one material, allows for the control, selectivity towards the adsorbate and, in general, functional properties [28–32]. In particular, iron-containing MOF structures, Fe-MOFs, have demonstrated the most significant achievements in the photodegradation of organic pollutants both under visible light and through the Fenton reaction due to the presence of iron-oxo clusters in the structure, as well as high specific surface area values [33]. Such clusters demonstrate their inherent absorption in the visible range and can transfer electrons from O^{2-} to Fe^{3+} [34]. This facilitates the oxidation of organic compounds via the photo-Fenton process [35]. Among all known Fe-MOFs, MIL-88b was previously shown to be the most efficient heterogeneous Fenton catalyst [36], while also exhibiting the highest photocatalytic activity in visible light [37] и biocompatibility [38]. The porous structure of MIL-88b is an organic-inorganic network with rhombic and hexagonal cavities, in the nodes of which iron oxo clusters are evenly distributed [39–41]. Electron-rich organic terephthalic acid ligands included in the MIL-88b structure typically act as electron donors for the reduction of Fe(III) to Fe(II) [42]. It is also known that MIL-88b does not have sufficient chemical stability [43], but this fact is even useful for the sacrificial release of iron ions during the Fenton process [44].

The combination of MOFs with magnetic particles (MPs) is considered more promising, as it offers the potential to combine the advantageous properties of both MOFs and MPs. This could result in enhanced chemical stability of the material and the additional possibility of precise positioning with rapid and easy release under the influence of an external magnetic field [45, 46]. A comprehensive examination of the Fenton reactivity of diverse iron-based materials can be found in the existing literature. It is observed that the most significant factors determining the reaction rate are crystallinity, specific surface area, oxygen vacancies and valence states of iron, as well as the redox potential of the transformation reaction Fe^{3+}/Fe^{2+} [6, 21, 22, 37, 47]. However, there is currently no effective tool based on machine learning methods that can be used to predict the catalytic activity of iron-containing materials in the processes of decomposition of organic pollutants using the Fenton reaction.

In this study, a predictive model based on multivariate correlation analysis was proposed to enable the prediction of the effectiveness of the pro-oxidant properties of the resulting iron-containing materials. The concentration of methylene blue (MB) after decomposition is considered as an indicator of the rate of the Fenton reaction. The scientific novelty of this study also lies in the preparation of iron-containing Fe-MOFs magnetic composites with enhanced pro-oxidant properties for inducing ROS under model conditions due to additional functionalization of the structure with humic acids (HA) or ascorbic acid (AA) as chelating agents. It is known that HA, which is part of the magnetically active catalyst, also serves as a stabilizer of magnetite nanoparticles (NP) [48]. In addition, magnetite NP modified with HA or AA exhibit anti/pro-oxidant properties due to the presence of donor-acceptor groups. Therefore, in this paper MOF and silane-based composites (in particular, tetraethoxysilane and 3-aminopropyltriethoxysilane copolymer, TA) containing magnetite (Fe_3O_4) or maghemite (γ-Fe_2O_3), as well as the stabilizer HA/prooxidant AA were synthesized and tested in the decomposition reaction of MB. We think that this study can clarify the structure-activity relationships of different iron minerals in heterogeneous Fenton processes and inspire the development of new heterogeneous Fenton catalysts based on MOFs and silanes.

Experimental

Synthesis Fe-MOFs Composites

In this study, a rational method for the synthesis of **MOFs** was used to target iron-carboxylate MOFs such as MIL-88b [49]. To synthesize the coordination polymer of the MIL-88b series, 5 g of terephthalic acid and 7.35 g of Fe_3OAcetate were dissolved in 100 mL of dimethylformamide with stirring on a magnetic stirrer (300 rpm) for 30 min. Fe_3OAcetate ($[Fe_3O(C_8H_4O_4)_3(H_2O)_3]Cl$) was synthesized according to a previously published method [43]. The resulting composites were isolated using a Buchner funnel, washed multiple times with distilled water subsequently, and dried in a vacuum (10^{-3} Torr, 50 °C, 12 h). The yield was 6.82 g.

In a typical synthesis of a series of such composites, Fe^{2+} to Fe^{3+} chlorides were added at a rate to produce magnetite of 25 wt % in the final composite (**MOF-Fe_3O_4**). At the first stage, the synthesis of magnetite was carried out according to the Elmore method [50]. Then, terephthalic acid and Fe_3OAcetate were added to the resulting reaction mixture. The synthesis was maintained with constant stirring at 900 rpm in an argon atmosphere for 60 min. The remaining steps, including precipitation and purification, were similar to those used in the preparation of MOFs. The yield was 4.6 g.

The **MOF-HA-Fe_3O_4** or **MOF-AA-Fe_3O_4** complex was prepared in a manner similar to MOF-Fe_3O_4, with the addition of HA or AA after the magnetite or maghemite suspension preparation stage. The amount added of AA and HA was 200 mg (10 wt % based on MOF). At the first stage, the synthesis of magnetite was carried out according to the Elmore method [50]. Then 200 mg of the stabilizer HA or pro-oxidant AA was added to the reaction system and the resulting mixture was kept for 5 min with stirring 800–1200 rpm at the pH≈7. Subsequently, terephthalic acid ($C_8H_6O_4$, 1.4 g, 0.084 mol) and Fe_3OAcetate (2.07 g, 0.0028 mol) were added to the resulting reaction mixture for *in situ* synthesis MOF. The reaction mixture was maintained under stirring (800–1200 rpm) on an overhead stirrer for 60 min. The remaining steps, including precipitation and purification, were similar to those used in the preparation of MOF. The yield was 4.5 and 3.5 g for MOF-HA-Fe_3O_4 and MOF-AA-Fe_3O_4 respectively.

Synthesis Fe-TA Composites

The **TA** is a silica gel functionalized with 3-aminopropyl fragments obtained by the interaction of tetraethoxysilane (T) and 3-aminopropyltriethoxysilane (A). To obtain TA, 10 mL of tetraethoxysilane and 4.2 mL of 3-aminopropyltriethoxysilane (T:A ratio = 1:0.5, mol/mol) were mixed with 150 mL of deionized water. The mixture was continuously stirred on an overhead stirrer (600 rpm, for 10 min) and then shaken on a laboratory shaker (150 rpm, for 24 h) at room temperature. The resulting precipitate was washed with distilled water pH~8 and centrifuged (3000 rpm, 10 min, 4 cycles). The sample was lyophilized and dried in a freeze dryer at –37 °C. The yield was 4.57 g.

In order to obtain the **TA-HA-Fe^{3+}** (1:0.1:0.5 wt/wt/wt), complex (1:0.1:0.5 wt/wt/wt), the iron salts were weighed based on the amount of Fe in 1 g of magnetite per 2 g of TA. Portions of 1.562 g $FeCl_3 \cdot 6H_2O$ and 0.2 g HA (sodium salt of humic acids, Powerhumus, Humintech, Germany; 5 $mmol \cdot g^{-1}$ of COOH and OH-groups, Mw=8 kD) were weighed and dissolved in 200 mL of deionized water. The solution was then dispersed in an ultrasonic bath for 10 min. Subsequently the TA particles were poured into the solution and redispersed in an ultrasonic bath for 10 min. The solutions were stirred on a laboratory shaker (170 rpm) for 18 h. The resulting precipitate was separated using a centrifuge (3000 rpm, 10 min) and dried in air at room temperature. The yield was 2.7 g.

The preparation of magnetically active **TA-HA-Fe_2O_3** (1:0.1:0.5, wt/wt/wt) composites was carried out in several stages. For this purpose, 2 g of TA and 0.2 g of HA were mixed with 200 mL of degassed distilled water in a non-inert atmosphere. The mixture was stirred at 1400-1500 rpm for 30 min. Then, weighed amounts of salts were added: 2.7 g of $FeCl_3 \cdot 6H_2O$, 0.99 g $FeCl_2 \cdot 4H_2O$ and 6 mL 25 % NH_4OH, calculated per 1 g of Fe_3O_4. The mixture was stirred at 1400–1500 rpm for 10 min. The remaining stages, including precipitation and purification, were similar to those used in the preparation of TA-HA-Fe^{3+}. The yield was 2.85 g.

The **TA-AA-Fe_3O_4** (1:0.1:0.5 wt/wt/wt) complex was obtained by following the same procedure as that used for the synthesis of the TA-HA-Fe_3O_4, with the exception that the same amount of AA was added instead of HA. The salt samples were dissolved in degassed distilled water in an argon atmosphere at 1400–1500 rpm. Then 6 m 25 % NH_4OH were added and stirred for 30 min. The resulting Fe_3O_4 precipitate was separated using a magnet (0.3 T) and washed once with 200 mL of degassed distilled water. Then AA was dissolved in 70 mL of a solution containing magnetite, 200 mL of 96 % C_2H_5OH (pH=7-8) were added with constant stirring (1200 rpm) and 2 g of TA. The solution was stirred on an overhead stirrer (1000 rpm) for 60 min. The remaining steps, including precipitation and purification, were similar to those used in the preparation of MOFs. The yield was 2.66 g.

X-ray Diffraction Analysis (XRD)

The phase composition and primary particle size of the samples were determined by XRD analysis using the Bragg-Brentano geometry on a Philips X'Pert diffractometer (Philips Analytical, Eindhoven, The Netherlands). Cu-K_α radiation (λ = 1.5406 Å) was used as the X-ray source. The collected data were smoothed using the Savitzky-Golay algorithm [51]. The measurements were performed at room temperature, covering an angular range of $10° < 2\Theta < 110°$ with a step size of 0.025° and a dwell time of 1 second per step.

Low-Temperature Nitrogen Adsorption Analysis

The specific surface area and porous structure characteristics of the samples were determined by N_2 adsorption-desorption analysis using a Quantachrome instrument. Prior to analysis, the samples were degassed and subjected to vaporization. They were then "thermally trained" by heating in a stream of inert N_2 gas under vacuum at 150 °C for 30 min. The adsorption isotherms were obtained by measuring the volume of N_2 gas adsorbed by the sample surface as a steady flow of a He-N_2 gas mixture with varying N_2 concentration (0 to approximately 1 volume fraction) was passed through the sample at liquid nitrogen temperature (77 K).

Desorption isotherms were obtained by measuring the volume of N_2 desorbed from the sample surface as the N_2 concentration in the gas mixture was decreased from approximately 1 to 0 volume fraction. The specific surface area and characteristics of the porous structure were calculated from the obtained adsorption-desorption isotherms using the Brunauer-Emmett-Teller (BET) and Barret-Joyner-Halenda (BJH) methods.

Elemental Analysis

The content of C, H, N was determined on an elemental analyzer "VarioMicrocube" (ElementarGmbH, Germany) using the classical Dumas-Preglia method — by burning the sample in the presence of an oxidant in an inert gas current. The Fe content was determined on the atomic absorption spectrometer "AAS-3" (Zeiss, Germany). The identification of functional groups of the obtained compounds was carried out on a Perkin-Elmer Spectrum 100 Fourier transform infrared spectrometer (USA, 2006) equipped with an attachment for broken total internal reflection (TIR) with a diamond prism of single reflection. The penetration depth for a medium with a sufficiently deep refractive index (2.43) at 1000 cm^{-1} is 1.66 microns. FT-IR-ATR spectra were taken in the range of 360–4000 cm^{-1} at room temperature using 24 scans and a resolution of 2 cm^{-1}. The baseline of the obtained spectra was corrected in the OPUS program.

X-ray Photoelectron Spectroscopy (XPS)

The surface layer of the samples was investigated by X-ray photoelectron spectroscopy. The XPS system was equipped with a dual anode (Al, Mg) X-ray source (SPECS XR50) and a hemispherical analyzer (SPECS Phoibos 150). The measurements were performed using Al K-α radiation (excitation energy: 1486.61 eV). The XPS data were analyzed using the CasaXPS software package. The peaks were deconvoluted using a Shirley-type background and a combination of Gaussian (50 %) and Lorentzian (50 %) functions. The half-heights of the C1s and O1s peaks were recorded during the analysis.

Dynamic and Electrophoretic Light Scattering (DLS, ELS)

The surface charge of the NPs, known as the zeta potential, was determined using ELS. This analysis was performed on a NanoBrook Omni particle analyzer (Brookhaven Instruments Corporation, Holtsville, NY, USA) at a specific wavelength of 633 nm. The instrument uses a solid-state He-Ne laser as a light source and measures scattered light at an angle of 173 degrees. All measurements were performed at a controlled temperature of 25 °C. Prior to analysis, each sample was diluted to a concentration of 0.1 g L^{-1} with an appropriate solvent. A standardized procedure was followed to ensure consistent measurement conditions. The diluted sample was dispersed in an ultrasonic bath for 10 seconds to break up any particle aggregates. After dispersion, the sample was allowed to rest for a further 100 seconds to reach equilibrium prior to measurement. All measurements were performed at a controlled temperature of 25±0.1 °C to minimize thermal fluctuations and ensure reproducibility. The pH of the suspension was adjusted to a range of 3 to 10 using either dilute NaOH or HCl. The pH was measured using a combination pH electrode for accurate control.

The results of the studies are presented in Table 1.

Table 1

Physicochemical characteristics of composites

Sample	Lattice parameter[a]	SSA[b]	Elemental analysis data	XPS data[c]	Zeta potential[d]	References
	Å	$m^2 g^{-1}$	Fe, %	Fe^{2+}/Fe^{3+}	mV	
MOF	–	220	18.5	0.66	–8.0	[44]
MOF-Fe_3O_4	8.378	197	33.9	1.02	+4.7	[44]
MOF-HA-Fe_3O_4	8.387	83	43.2	–	–9.1	–
MOF-AA- Fe_3O_4	8.389	174	44.4	1.59	–3.2	[44]
TA-HA-Fe^{3+}	–	237	15.8	1.08	–25	–
TA-HA-Fe_2O_3	8.301	208	20.2	–	+29.5	–
TA-AA-Fe_3O_4	8.381	116	32.5	–	–2.5	[52]

Notes: [a]The lattice cell parameter was calculated using XRD data; [b]SSA — specific surface area determined by low-temperature nitrogen adsorption; [c]The Fe^{3+}/Fe^{2+} ratio is calculated using XPS data; [d]Zeta potential determined by ELS at pH=4.6 in deionized water.

Results and Discussion

Evaluation of the Prooxidant Ability of selected Promising Samples in the Fenton Reaction

To evaluate the prooxidant activity of the obtained iron-containing preparations in the Fenton reaction, the well-known reaction of decolorization of MB in the presence of hydroxyl radicals •OH was used. The hydroxyl radicals as a result of the disproportionation reaction of 100 mM H_2O_2, catalyzed by selected promising NP, at pH 4.5, close to the pH of the tumor [53], and 37 °C, lead to the discoloration of the MB solution to colorless cation-free MB. The rate of bleaching of MB was assessed 0, 30, 90 and 180 min after preparation of the suspension by the change in optical density at a wavelength of 652 nm using UV-Vis-spectroscopy. The interaction of MB with iron-containing compounds can be described by three processes occurring both in parallel and sequentially: (1) sorption of MB on the surface of NP, (2) photodegradation of MB, and (3) degradation of MB in the presence of H_2O_2 as a result of the Fenton reaction. Hernandez et al. [54] showed that sorption and photodegradation of MB can be considered as two sequential processes, at the same time, 150 min after the start of interaction of the dye with magnetite NP, the concentration of MB in the supernatant decreases by half from 20 to 10 mg L^{-1}. This was attributed by the authors to photodegradation of the product as determined by mass spectrometry. Hydrogen peroxide was then added to initiate the Fenton reaction, which would increase the rate of dye decomposition. However it is difficult to estimate the concentration of MB undergoing separate sorption or photodegradation or degradation during the Fenton reaction due to the complexity of the processes occurring, a comparison was conducted between the rate of change in the optical density of the solution in the presence/absence of H_2O_2 (during sorption/degradation during the Fenton reaction).

An assessment of the degradation of MB in sorption experiments (in the absence of H_2O_2) and the Fenton reaction (in the presence of H_2O_2) showed that all preparations, with the exception of TA-AA-Fe_3O_4, demonstrate a decrease in MB concentration by 60 % or more within 180 min (Fig. 1*a*).

The insufficient activity of the TA-AA-Fe_3O_4 sample can probably be associated with the low concentration of both released ions Fe^{3+} and Fe^{2+} (Fig. 1*b*, *c*). Thus, the TA-AA-Fe_3O_4 sample is considered unpromising and is excluded from further sampling.

The next step is to assess the role of the Fenton reaction as a source of hydroxyl radicals in the reduction of the MB in the supernatant. In Fig. 2 shows the difference between the concentrations of MB subjected to sorption and decomposition under the influence of H_2O_2 for the remaining four promising samples.

The data obtained indicates that, the decrease in the concentration of MB in the supernatant for the MOF-HA-Fe_3O_4 sample is a result of the sorption processes, rather than the Fenton reaction. This obsevation leads to the conclusion that the MOF-HA-Fe_3O_4 sample can be excluded from the list of promising samples. The high sorption capacity of MOF-HA-Fe_3O_4 is probably due to the presence of HA in its composition together with MOF. One can assume a competitive mechanism of sorption and degradation, as a result of which sorption processes occur faster due to the greater availability of MB in solution.

At the next stage, the evaluation of promising samples was carried out based on the reaction rate and reaction rate constant. Thus, an assessment of the reaction rate showed that the preparations TA-HA-Fe_2O_3 and TA-HA-Fe^{3+} demonstrate a maximum reaction rate (both sorption and Fenton reaction) 30 min after the start of the experiment, while the reaction in the presence of MOF-AA-Fe_3O_4 reaches its maximum 90 min after the start of the experiment, indicating a prolonged effect of the NP. A comparison shows that the rate of the Fenton reaction decreases in the series: TA-HA-Fe^{3+} > MOF-AA-Fe_3O_4 > TA-HA-Fe_2O_3. This correlates with the release patterns of both Fe^{3+} and Fe^{2+}: TA-HA-Fe^{3+} and TA-HA-Fe_2O_3 released 9 % and 0.1 % Fe^{3+} after 30 min, while the concentration of Fe^{2+} released by the MOF-AA-Fe_3O_4 only increased within three hours and reached 0.45 %.

The pronounced activity of the TA-HA-Fe^{3+} sample is associated with the release of Fe^{3+} from the complex, the rate of which is higher than that of samples with iron oxide NP. This is consistent with the results of Wang et al. [55] who found that at low pH values (pH < 4.2), iron ions Fe(II, III) released from the complexes predominantly participate in the formation of •OH hydroxyl radicals salts, while at neutral pH values the formation of •OH occurs mainly due to the catalytic decomposition of H_2O_2 by surface iron (which is at least 50 times more effective than dissolved iron ions) [56], which determines the choice of NP as ion sources gland. At the same time, [57, 58] found that the rate of generation of •OH radicals using free Fe^{2+} is higher than with the participation of Fe^{2+} on the surface of Fe_3O_4 NP.

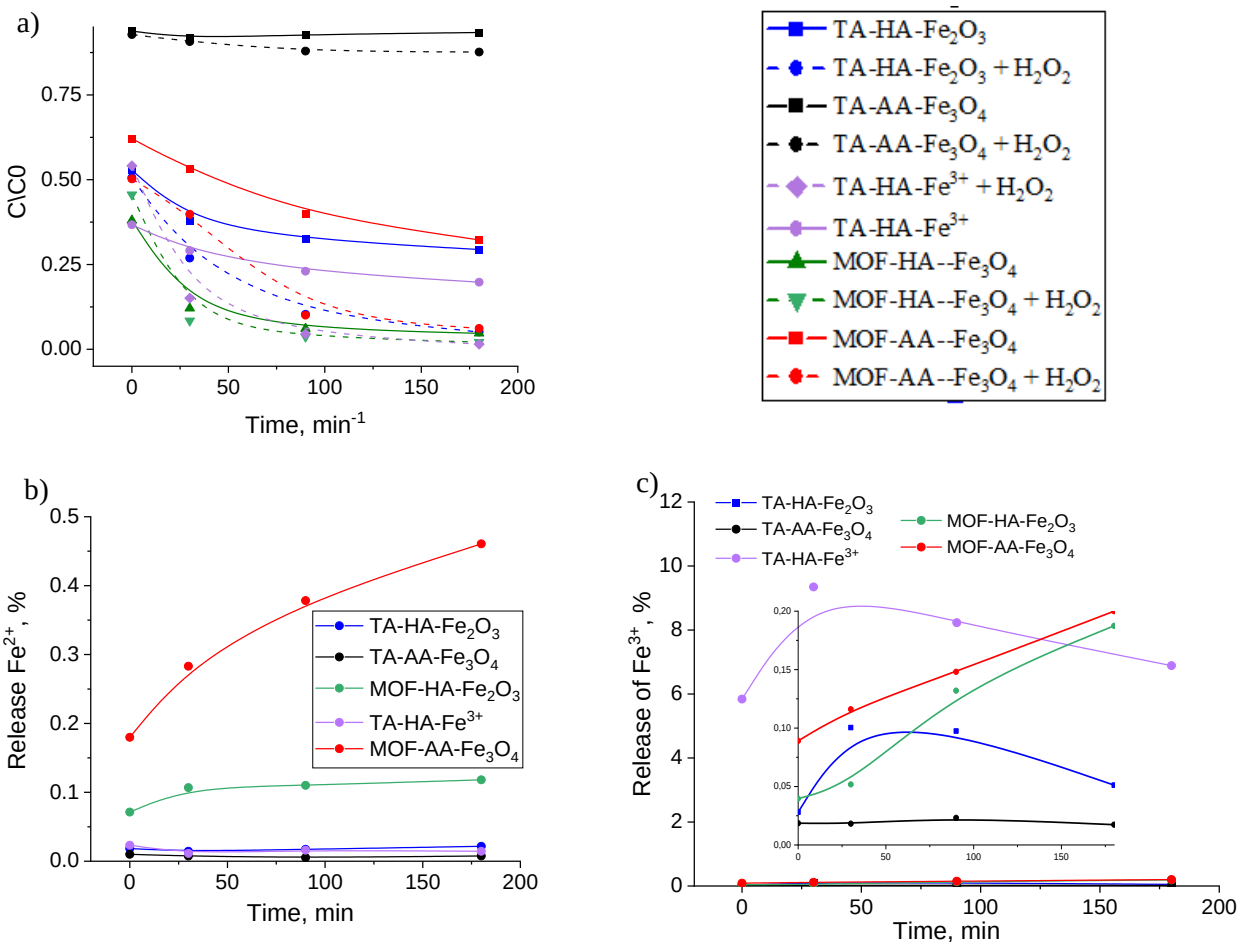

Figure 1. (*a*) Catalytic degradation of MB by samples (MB concentration = 11 mg L^{-1}; H_2O_2 concentration = 100 mM; and sample dosage = 1 g L^{-1}, 0.1 M NaAc buffer pH = 4.5; 37 °C). Solid lines show MB adsorption without H_2O_2; dotted lines show a decrease in the MB concentration with H_2O_2. (*b*) Kinetics of the Fe^{2+} release. (*c*) Kinetics of the Fe^{3+} release. Data normalized to the iron content

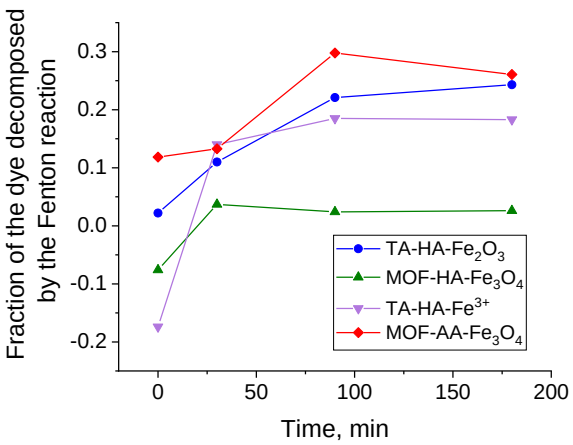

Figure 2. Fraction of the dye decomposed by the Fenton reaction for the four perspective samples

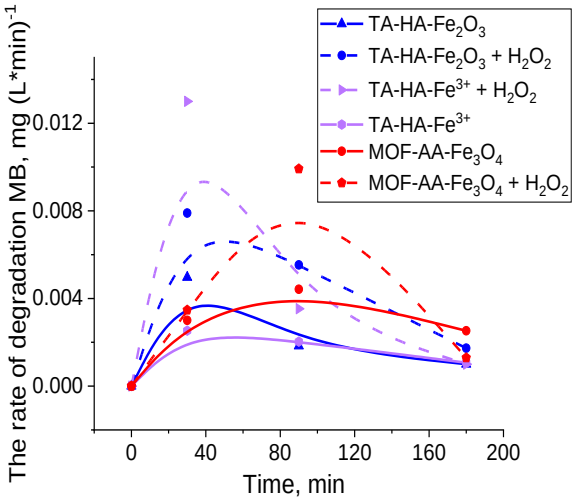

Figure 3. The rate of decomposition of MB versus time

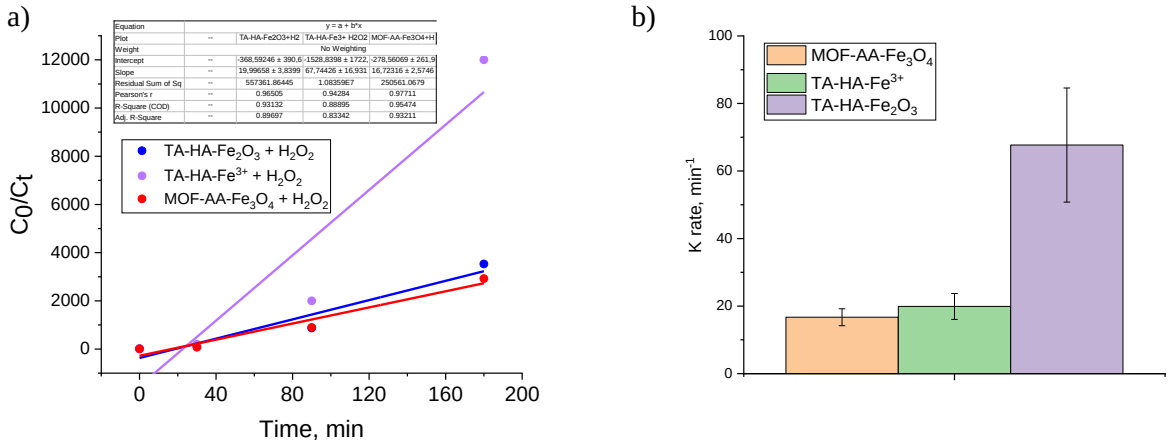

Figure 4. (*a*) Kinetic curve of pseudo-second-order MB degradation and values of degradation rate constants (0.1 M NaAc buffer pH=4.5; 100 mM H_2O_2; 0-180 min; 37 °C; concentration of NPs=10 g L^{-1}; concentration of MB=11 mg L^{-1}) (*b*) Constants of the reaction's rate

An assessment of the reaction rate kinetics showed that the Fenton reactions in the presence of three promising samples can be classified as pseudo-second order reactions (R^2 values are presented in the table) with rate constants of 16.7±2.5 s^{-1}, 19.9±3.8 s^{-1} and 67.7±19.3 s^{-1} for MOF-AA-Fe_3O_4, TA-HA-Fe_2O_3 and TA-HA-Fe^{3+}, respectively (Fig. 4*a*, *b*). It is obvious that the highest value of the reaction rate constant in the presence of TA-HA-Fe^{3+} is due to the highest rate of release of Fe^{3+}.

Regression Models

In order to comprehend the mechanism through which the nature of NP exerts its influence on their pro-oxidant properties, a predictive model was constructed on the basis of a multivariate correlation analysis of the relationship between "physicochemical properties and concentration of MB after degradation". The presence of iron ions is the most obvious catalyst for the Fenton reaction, however our objective was to ascertain whether other physicochemical characteristics of the samples would affect the rate of the Fenton reaction. In this case, the concentration of MB after degradation is an indicator of the rate of the Fenton reaction, and therefore the effectiveness of the pro-oxidant properties of the resulting samples. The initial concentration of iron in the preparation, the unit cell parameter (for oxides), the ratio of Fe^{2+}/Fe^{3+} on the surface, specific surface area, zeta potential, and the concentration of released Fe^{2+} and Fe^{3+} were used as physicochemical characteristics. At the first stage, a regression model was built to assess the influence of selected six parameters (initial iron concentration, unit cell parameter, ratio of Fe^{2+}/Fe^{3+} on the surface, specific surface area, zeta potential, concentration of released Fe^{2+} and Fe^{3+} in total) on the concentration of MB for five promising samples, as well as MOF and Fe_3O_4-MOF which had been previously studied. The zeta potential parameters and the concentration of the released Fe^{2+} and Fe^{3+}, as well as the concentration of MB after the Fenton reaction, were selected as the initial experimental variables and were observed over a five-minute period.

An assessment of the coefficient of determination (adjusted R^2 = 0.9343) and p-value = 0.0433 shows that a linear model can be used to describe the dependence of the result (MB concentration) on the output parameters. The adjusted R^2 value indicates that the linear model can account for more than 93 % of the total variability while the remaining values cannot be described by it.

The results of an analysis based on the methodology of surface response made it possible to compose the following second order equation:

$$Y = 0.0995 + 0.0063\ A + 0.0314\ B - 0.1338\ C + 0.151125\ D - 0.0109\ F - 0.0591\ E,$$

where Y is the concentration of MB in the Fenton reaction (mg L^{-1}), A is the initial concentration of iron in the sample (%), B is the unit cell parameter (A), C is the ratio of Fe^{2+}/Fe^{3+} on the surface of the sample, D is the total concentration of released iron ions (Fe^{2+} and Fe^{3+}, %), F is the specific surface area (m^2 g^{-1}), E is surface charge (mV).

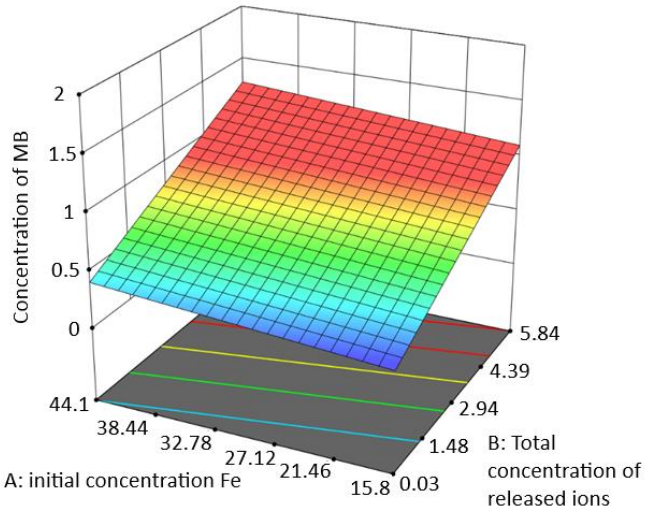

Figure 5. Effect of initial iron concentration and total concentration of released Fe^{2+}/Fe^{3+} on MB degradation

The equation permitted the evaluation of the influence of a particular factor and the interaction between the six factors on the concentration of MB. The sign of the coefficient in the equation indicates the direction of the trend in the results: negative and positive coefficients show negative and positive effects, respectively. A positive sign and therefore a positive effect indicate that the response changes in direct proportion to a change in the level of the factor, and a negative effect with an inverse change in the level of the factor. As evidenced by the derived equation (1), the effects of A, B and D on the concentration of MB are positive, whereas those of C, F and E are negative. However, the p-value indicates that only the total concentration of released iron ions is a significant factor (p-value = 0.0162, parameters with a p-value < 0.05 are considered significant, Fig. 5). Thus, the concentration of released iron ions is the only parameter selected that affects the kinetics of the Fenton reaction.

It was of interest to evaluate the influence of separately Fe^{2+} and Fe^{3+} and reaction time on the kinetics of the Fenton reaction. To this end, a regression model was also built with three parameters (reaction time, concentration of released Fe^{2+} and concentration of released Fe^{3+}) and response (concentration of MB in the supernatant after the Fenton reaction). The predicted R^2 value of 0.7800 is in the agreement with the adjusted R^2 value of 0.9111 with a difference of less than 0.2. Adeq Precision, indicating the signal-to-noise ratio, is 17.702, which is significantly greater than 4, indicating adequate signal and the ability to use the model to predict the kinetics of the Fenton reaction (Fig. 6). The model's F-value of 31.89 and p-value < 0.0001 indicate that the model is significant. There is only a 0.01 % chance that such a large F value could arise from noise. Furthermore, there is a strong correlation between the predicted and experimental values.

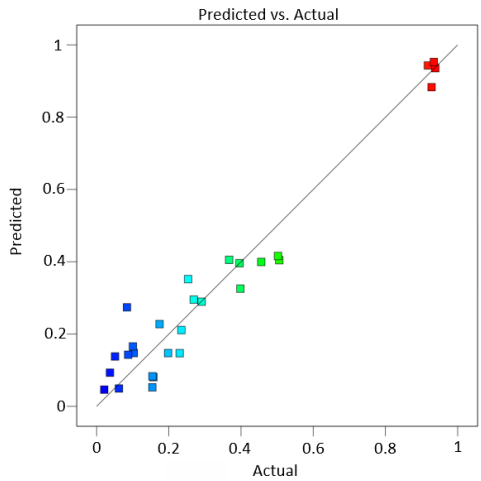

Figure 6. Dependence of predicted values on predicted values

Based on the obtained coefficients, a quadratic regression equation was compiled:

$$Y = -2.24626 - 0.1317\,A - 2.7981\,B - 2.5506\,C - 0.0832\,AB + \\ + 0.0779\,AC - 2.928\,BC + 0.1318\,A^2 + 0.1392\,B^2 - 0.1642\,C^2,$$

where Y is the concentration of MB in the Fenton reaction (%), A is the reaction time (min), B is the concentration of released Fe^{2+} (%), C is the concentration of released Fe^{3+} (%).

According to the p-value parameters (Table 2), the concentrations of released iron ions, the square of the Fe^{2+} ion concentration, and the product of the reaction time and the Fe^{3+} concentration are statistically significant.

Table 2

Data of ANOVA for quadratic model

Source	Sum of Squares	df	Mean Square	F-value	p-value	
Model	2.11	9	0.2342	31.89	< 0.0001	significant
A-Time	0.0244	1	0.0244	3.33	0.0848	
B-Fe^{2+}	0.0627	1	0.0627	8.54	0.0091	
C-Fe^{3+}	0.0486	1	0.0486	6.61	0.0192	
AB	0.0107	1	0.0107	1.46	0.2425	
AC	0.0206	1	0.0206	2.81	0.1111	
BC	0.0662	1	0.0662	9.01	0.0077	
A^2	0.0743	1	0.0743	10.12	0.0052	
B^2	0.0200	1	0.0200	2.72	0.1163	
C^2	0.0183	1	0.0183	2.49	0.1323	
Residual	0.1322	18	0.0073			
Cor Total	2.24	27				

Comparison of the sign and magnitude of the coefficients shows that an increase in ion concentration leads to a decrease in the concentration of MB. This implies that the rate of the Fenton reaction increases, with the concentration of Fe^{2+} exerting a greater influence than Fe^{3+}. This is consistent with the fact that the Fenton reaction initiated by Fe^{2+} is significantly faster ($k = 63\ M^{-1}\cdot S^{-1}$) than the reaction occurring during the reduction of Fe^{3+} to Fe^{2+} ($k = 0.001–0.02\ M^{-1}\cdot S^{-1}$) [36]. Notably, the effect of time on the reaction is indirect, and occurs in combination with the concentration of Fe^{3+}.

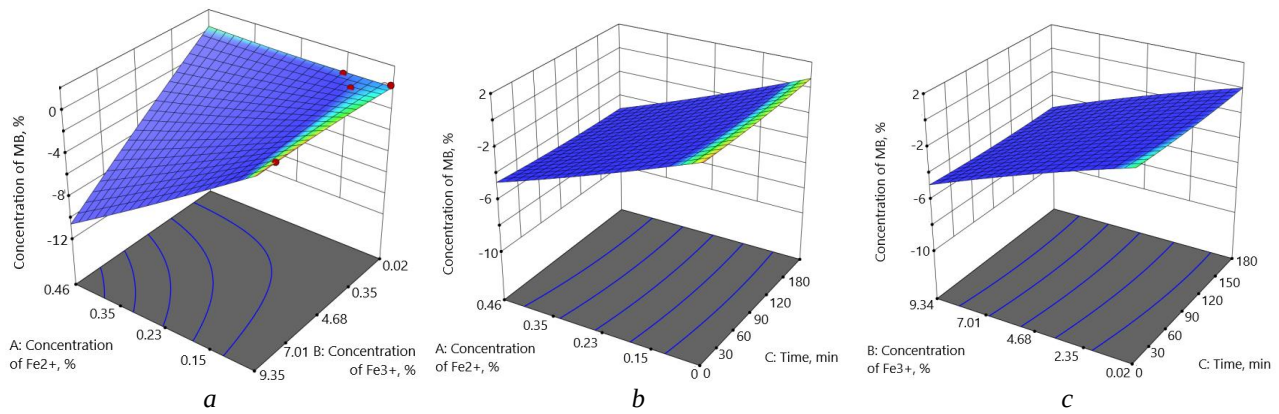

Figure 7. Response surfaces for the MB degradation value for different combinations of factors: concentration of released Fe^{3+} and Fe^{2+} (*a*), concentration of released Fe^{2+} and time (*b*) and concentration of released Fe^{3+} and time (*c*)

It can be demonstrated that the maximum reaction rate can be achieved at different times by controlling the concentration of released iron ions. For example, in some cases, a rapid effect of the sample in the first minutes of its administration is required. Then, to achieve the maximum effect (MB concentration in the supernatant should be 0 % 5 min after administration), 0.13 % Fe^{2+} and 1.78 % Fe^{3+} are required (Fig. 7*a*). Therefore, if we assume that the relationship between the concentration of the initial sample and the ions released by it is linear, then using the MOF-AA-Fe_3O_4 sample as an example, to achieve the maximum reaction

rate in 5 min, it is necessary to introduce 47.6 g L^{-1} of the sample. On the other hand, when the concentration of released Fe^{2+} is reduced to 0.12 %, the concentration of Fe^{3+} released to degrade the entire MB within 5 min is 1.41 % (Fig. 7*c*). Thus, the use of TA-HA-Fe^{3+} would allow achieving such a reaction rate using only 1.6 g L^{-1} of the sample. Thus, it is more rational to use the sample MOF-AA-Fe_3O_4 to achieve a prolonged prooxidant effect 3 h after insertion, and TA-HA-Fe^{3+} to achieve its maximum effect within the first 30 min after insertion.

To test the model, samples of MOF, MOF-Fe_3O_4, Fe_3O_4-MOF [43, 44] and Fe_3O_4-SiO_2 were selected and the degradation of methylene blue, as well as the release of Fe^{2+} and Fe^{3+} 60 minutes after the start of the experiment, were assessed (Supplementary Materials, Table S1, Fig. S1). The experimental data values correlate with the theoretical ones, the value of the corrected determination coefficient R^2 was 0.87. Thus, the obtained model can be successfully used to predict the degradation of methylene blue in kinetic experiments based on the concentration of released Fe^{2+} and Fe^{3+} ions. The limitation is the difficulty in extrapolating the model when using data that are outside the ranges of the input parameters.

Conclusions

This paper presents the synthesis and testing of composites containing the metal-organic framework MIL88b(Fe), as well as nanoparticles of magnetite (Fe_3O_4) or maghemite (γ-Fe_2O_3) modified by humic acids or ascorbic acid in the decomposition reaction of methylene blue. The proposed predictive model based on multi-factor correlation analysis of "physical-chemical properties — methylene blue concentration after degradation" showed that in a line of selected parameters (initial iron concentration in sample, elemental cell parameter, Fe^{2+}/Fe^{3+} ion ratio on sample surface, total iron ion released concentration, surface area specific, surface charge), a significant factor influencing Fenton reaction kinetics, is only the total concentration of the released iron ions (p-value = 0.0162). Evaluation of the influence of separate Fe^{2+} and Fe^{3+} ions and reaction time to the Fenton reaction kinetics by multi-factor analysis showed that concentrations of released iron ions are statistically significant, with the concentration of Fe^{2+} ions affecting more than Fe^{3+}. The developed model is proposed for forecasting the prooxidant properties of preparations.

Supporting Information

The Supporting Information is available free at https://ejc.buketov.edu.kz/index.php/ejc/article/view/141/101

Funding

This research was supported by the Russian Science Foundation (project № 22-73-10222).

*Author Information**

**The authors' names are presented in the following order: First Name, Middle Name and Last Name*

Daniel Saman — MD Student, Moscow Aviation Institute (National Research University), 125993, Moscow, Russia; e-mail: saman_d@mail.ru

Lyubov Sergeevna Bondarenko (*corresponding author*) — Candidate of Chemical Sciences, Associate Professor, Department 903 "Advanced Materials and Technologies for Aerospace Engineering", Moscow Aviation Institute (National Research University), 125993, Moscow, Russia; e-mail: l.s.bondarenko92@gmail.com; https://orcid.org/0000-0002-3107-0648

Rose Kurmangalievna Baimuratova — Candidate of Chemical Sciences, Junior Researcher, Federal Research Center of Problems of Chemical Physics and Medicinal Chemistry, Russian Academy of Sciences, 142432, Chernogolovka, Moscow region, Russia; e-mail: roz_baz@mail.ru; https://orcid.org/0000-0002-8389-6871

Artur Albertovich Dzeranov — 4th year PhD Student, Department 903 "Advanced Materials and Technologies for Aerospace Applications", Moscow Aviation Institute (National Research University), 125993, Moscow, Russia; e-mail: arturdzeranov99@gmail.com; https://orcid.org/0000-0003-3240-9321

Gulzhian Iskakovna Dzhardimalieva — Doctor of Chemical Sciences, Head of Laboratory of Metallopolymers, Federal Research Center of Problems of Chemical Physics and Medicinal Chemistry, Rus-

sian Academy of Sciences, Chernogolovka, Moscow region, 142432, Russia; e-mail: dzhardim@icp.ac.ru; https://orcid.org/0000-0002-4727-8910

Nataliya Sergeevna Tropskaya — Doctor of Biological Sciences, Head of the Department of Experimental Damage Laboratory, Sklifosovsky Research Institute for Emergency Medicine, 129090, Moscow, Russia; e-mail: ntropskaya@mail.ru; https://orcid.org/0000-0001-5870-9483

Kamila Asylbekovna Kydralieva — Doctor of Chemical Sciences, Department 903 "Advanced Materials and Technologies for Aerospace Applications", Moscow Aviation Institute (National Research University), 125993, Moscow, Russia; e-mail: kydralievaka@mai.ru; https://orcid.org/0000-0002-4596-4140

Author Contributions

The manuscript was written through contributions of all authors. All authors have given approval to the final version of the manuscript. CRediT: **Daniel Saman** — investigation; **Lyubov Sergeevna Bondarenko** — methodology, validation, writing-original draft, writing-review & editing; **Rose Kurmangalievna Baimuratova** writing-original draft, — investigation; **Artur Albertovich Dzeranov** — investigation; **Gulzhian Iskakovna Dzhardimalieva** — data curation, conceptualization; **Nataliya Sergeevna Tropskaya** — formal analysis, resources; **Kamila Asylbekovna Kydralieva** — data curation, conceptualization, writing-original draft, writing-review & editing.

Acknowledgments

Low-temperature nitrogen adsorption were carried out in accordance with the state tasks, state registration 124013000757-0 using the equipment of the Multi-User Analytical Center of FRC PCP and MC RAS.

Conflicts of Interest

The authors declare no conflict of interest.

References

1 Jain, B., Singh, A. K., Kim, H., Lichtfouse, E., & Sharma, V. K. (2018). Treatment of organic pollutants by homogeneous and heterogeneous Fenton reaction processes. *Environmental Chemistry Letters*, *16*(3), 947–967. https://doi.org/10.1007/s10311-018-0738-3

2 Sreeja, P. H., & Sosamony, K. J. (2016). A Comparative Study of Homogeneous and Heterogeneous Photo-fenton Process for Textile Wastewater Treatment. *Procedia Technology*, *24*, 217–223. https://doi.org/10.1016/j.protcy.2016.05.065

3 Clarizia, L., Russo, D., Di Somma, I., Marotta, R., & Andreozzi, R. (2017). Homogeneous photo-Fenton processes at near neutral pH: A review. *Applied Catalysis B: Environmental*, *209*, 358–371. https://doi.org/10.1016/j.apcatb.2017.03.011

4 Wang, C., Liu, H., Sun, Z., Huang, J., & Liao, Y. (2012). Supported Nanosized α-FeOOH Improves Efficiency of Photoelectro-Fenton Process with Reaction-Controlled pH Adjustment for Sustainable Water Treatment. *International Journal of Photoenergy*, *2012*, 1–7. https://doi.org/10.1155/2012/689807

5 Kremer, M. L. (2003). The Fenton Reaction. Dependence of the Rate on pH. *The Journal of Physical Chemistry A*, *107*(11), 1734–1741. https://doi.org/10.1021/jp020654p

6 Nidheesh, P. V. (2015). Heterogeneous Fenton catalysts for the abatement of organic pollutants from aqueous solution: A review. *RSC Advances*, *5*(51), 40552–40577. https://doi.org/10.1039/C5RA02023A

7 Litter, M. I., & Slodowicz, M. (2017). An overview on heterogeneous Fenton and photoFenton reactions using zerovalent iron materials. *Journal of Advanced Oxidation Technologies*, *20*(1), 20160164. https://doi.org/doi:10.1515/jaots-2016-0164

8 Hussain, S., Aneggi, E., & Goi, D. (2021). Catalytic activity of metals in heterogeneous Fenton-like oxidation of wastewater contaminants: a review. *Environmental Chemistry Letters*, *19*(3), 2405–2424. https://doi.org/10.1007/s10311-021-01185-z

9 Azfar Shaida, M., Verma, S., Talukdar, S., Kumar, N., Salim Mahtab, M., Naushad, Mu., & Haq Farooqi, I. (2023). Critical analysis of the role of various iron-based heterogeneous catalysts for advanced oxidation processes: A state of the art review. *Journal of Molecular Liquids*, *374*, 121259. https://doi.org/10.1016/j.molliq.2023.121259

10 Li, N., He, X., Ye, J., Dai, H., Peng, W., Cheng, Z., Yan, B., Chen, G., & Wang, S. (2023). H2O2 activation and contaminants removal in heterogeneous Fenton-like systems. *Journal of Hazardous Materials*, *458*, 131926. https://doi.org/10.1016/j.jhazmat.2023.131926

11 Zhu, Y., Xie, Q., Deng, F., Ni, Z., Lin, Q., Cheng, L., Chen, X., Qiu, R., & Zhu, R. (2023). The differences in heterogeneous Fenton catalytic performance and mechanism of various iron minerals and their influencing factors: A review. *Separation and Purification Technology*, *325*, 124702. https://doi.org/10.1016/j.seppur.2023.124702

12 Pereira, M. C., Oliveira, L. C. A., & Murad, E. (2012). Iron oxide catalysts: Fenton and Fentonlike reactions — a review. *Clay Minerals*, 47(3). https://doi.org/10.1180/claymin.2012.047.3.01

13 Garrido-Ramírez, E. G., Theng, B. K. G., & Mora, M. L. (2010). Clays and oxide minerals as catalysts and nanocatalysts in Fenton-like reactions—A review. *Applied Clay Science*, *47*(3), 182–192. https://doi.org/10.1016/j.clay.2009.11.044

14 Munoz, M., de Pedro, Z. M., Casas, J. A., & Rodriguez, J. J. (2015). Preparation of magnetite-based catalysts and their application in heterogeneous Fenton oxidation — A review. *Applied Catalysis B: Environmental*, *176–177*, 249–265. https://doi.org/10.1016/j.apcatb.2015.04.003

15 Lai, L., He, Y., Zhou, H., Huang, B., Yao, G., & Lai, B. (2021). Critical review of natural iron-based minerals used as heterogeneous catalysts in peroxide activation processes: Characteristics, applications and mechanisms. *Journal of Hazardous Materials*, *416*, 125809. https://doi.org/10.1016/j.jhazmat.2021.125809

16 Hartmann, M., Kullmann, S., & Keller, H. (2010). Wastewater treatment with heterogeneous Fenton-type catalysts based on porous materials. *Journal of Materials Chemistry*, 20(41). https://doi.org/10.1039/c0jm00577k

17 Jin, Q., Kang, J., Chen, Q., Shen, J., Guo, F., & Chen, Z. (2020). Efficiently enhanced Fenton-like reaction via Fe complex immobilized on silica particles for catalytic hydrogen peroxide degradation of 2,4-dichlorophenol. *Applied Catalysis B: Environmental*, *268*, 118453. https://doi.org/10.1016/j.apcatb.2019.118453

18 González-Bahamón, L. F., Hoyos, D. F., Benítez, N., & Pulgarín, C. (2011). New Fe-immobilized natural bentonite plate used as photo-Fenton catalyst for organic pollutant degradation. *Chemosphere*, 82(8). https://doi.org/10.1016/j.chemosphere.2010.11.071

19 Noorjahan, M., Durga Kumari, V., Subrahmanyam, M., & Panda, L. (2005). Immobilized Fe(III)-HY: An efficient and stable photo-Fenton catalyst. *Applied Catalysis B: Environmental*, *57*(4), 291–298. https://doi.org/10.1016/j.apcatb.2004.11.006

20 Cen, S., Lv, X., Jiang, Y., Fakhri, A., & Gupta, V. K. (2020). Synthesis and structure of iron–copper/hollow magnetic/metal–organic framework/coordination sites in a heterogeneous catalyst for a Fenton-based reaction. *Catalysis Science & Technology*, 10(19). https://doi.org/10.1039/D0CY01027H

21 Cheng, M., Lai, C., Liu, Y., Zeng, G., Huang, D., Zhang, C., Qin, L., Hu, L., Zhou, C., & Xiong, W. (2018). Metal-organic frameworks for highly efficient heterogeneous Fenton-like catalysis. *Coordination Chemistry Reviews*, *368*, 80–92. https://doi.org/10.1016/j.ccr.2018.04.012

22 Lu, S., Liu, L., Demissie, H., An, G., & Wang, D. (2021). Design and application of metal-organic frameworks and derivatives as heterogeneous Fenton-like catalysts for organic wastewater treatment: A review. *Environment International*, *146*, 106273. https://doi.org/10.1016/j.envint.2020.106273

23 Batten, S. R., Champness, N. R., Chen, X. -M., Garcia-Martinez, J., Kitagawa, S., Öhrström, L., O'Keeffe, M., Paik Suh, M., & Reedijk, J. (2013). Terminology of metal–organic frameworks and coordination polymers (IUPAC Recommendations 2013). *Pure and Applied Chemistry*, *85*(8), 1715–1724. https://doi.org/10.1351/PAC-REC-12-11-20

24 Zhang, M., Bosch, M., Gentle Iii, T., & Zhou, H.-C. (2014). Rational design of metal–organic frameworks with anticipated porosities and functionalities. *CrystEngComm*, *16*(20), 4069–4083. https://doi.org/10.1039/C4CE00321G

25 Silva, P., Vilela, S. M. F., Tomé, J. P. C., & Almeida Paz, F. A. (2015). Multifunctional metal–organic frameworks: From academia to industrial applications. *Chemical Society Reviews*, *44*(19), 6774–6803. https://doi.org/10.1039/C5CS00307E

26 Zhinzhilo, V. A., Litvinova, A. Yu., Lyamina, V. M., Dzhardimalieva, G. I., & Uflyand, I. E. (2022) Coordinating Polymers Based on Nickel(II) and Cobalt(II) Trimesinates as Promising Adsorbents of Organic Dyes. *Bulletin of the University of Karaganda — Chemistry*, *107*(3), 239–253. https://doi.org/10.31489/2022Ch3/3-22-20

27 Dzhardimalieva, G., Zhinzhilo, V., & Uflyand, I. (2022). Advances in the chemistry of composites of metal-organic frameworks. *Russian Chemical Reviews*, *91*(10), 5055–5055. https://doi.org/10.57634/RCR5055

28 Si, J., Xia, H. -L., Zhou, K., Li, J., Xing, K., Miao, J., Zhang, J., Wang, H., Qu, L. -L., Liu, X. -Y., & Li, J. (2022). Reticular Chemistry with Art: A Case Study of Olympic Rings-Inspired Metal–Organic Frameworks. *Journal of the American Chemical Society*, *144*(48), 22170–22177. https://doi.org/10.1021/jacs.2c09832

29 Furukawa, H., Kim, J., Ockwig, N. W., O'Keeffe, M., & Yaghi, O. M. (2008). Control of Vertex Geometry, Structure Dimensionality, Functionality, and Pore Metrics in the Reticular Synthesis of Crystalline Metal−Organic Frameworks and Polyhedra. *Journal of the American Chemical Society*, *130*(35), 11650–11661. https://doi.org/10.1021/ja803783c

30 O'Keeffe, M. (2009). Design of MOFs and intellectual content in reticular chemistry: A personal view. *Chemical Society Reviews*, *38*(5), 1215. https://doi.org/10.1039/b802802h

31 Dybtsev, D. N., Yutkin, M. P., Peresypkina, E. V., Virovets, A. V., Serre, C., Férey, G., & Fedin, V. P. (2007). Isoreticular Homochiral Porous Metal−Organic Structures with Tunable Pore Sizes. *Inorganic Chemistry*, *46*(17), 6843–6845. https://doi.org/10.1021/ic7009226

32 Baimuratova, R. K., Andreeva, A. V., Uflyand, I. E., Shilov, G. V., Bukharbayeva, F. U., Zharmagambetova, A. K., & Dzhardimalieva, G. I. (2022). Synthesis and Catalytic Activity in the Hydrogenation Reaction of Palladium-Doped Metal-Organic Frameworks Based on Oxo-Centered Zirconium Complexes. *Journal of Composites Science*, *6*(10), 299. https://doi.org/10.3390/jcs6100299

33 Wang, D., Huang, R., Liu, W., Sun, D., & Li, Z. (2014). Fe-Based MOFs for Photocatalytic CO_2 Reduction: Role of Coordination Unsaturated Sites and Dual Excitation Pathways. *ACS Catalysis*, *4*(12), 4254–4260. https://doi.org/10.1021/cs501169t

34 Laurier, K. G. M., Vermoortele, F., Ameloot, R., De Vos, D. E., Hofkens, J., & Roeffaers, M. B. J. (2013). Iron(III)-Based Metal–Organic Frameworks As Visible Light Photocatalysts. *Journal of the American Chemical Society*, *135*(39), 14488–14491. https://doi.org/10.1021/ja405086e

35 Du, C., Zhang, Y., Zhang, Z., Zhou, L., Yu, G., Wen, X., Chi, T., Wang, G., Su, Y., Deng, F., Lv, Y., & Zhu, H. (2022). Fe-based metal organic frameworks (Fe-MOFs) for organic pollutants removal via photo-Fenton: A review. *Chemical Engineering Journal*, 431, 133932. https://doi.org/10.1016/j.cej.2021.133932

36 Zhang, H., Chen, S., Zhang, H., Fan, X., Gao, C., Yu, H., & Quan, X. (2019). Carbon nanotubes-incorporated MIL-88B-Fe as highly efficient Fenton-like catalyst for degradation of organic pollutants. *Frontiers of Environmental Science & Engineering*, *13*(2), 18. https://doi.org/10.1007/s11783-019-1101-z

37 Laurier, K. G. M., Vermoortele, F., Ameloot, R., De Vos, D. E., Hofkens, J., & Roeffaers, M. B. J. (2013). Iron(III)-Based Metal–Organic Frameworks As Visible Light Photocatalysts. *Journal of the American Chemical Society*, *135*(39), 14488–14491. https://doi.org/10.1021/ja405086e

38 Baati, T., Njim, L., Neffati, F., Kerkeni, A., Bouttemi, M., Gref, R., Najjar, M. F., Zakhama, A., Couvreur, P., Serre, C., & Horcajada, P. (2013). In depth analysis of the in vivo toxicity of nanoparticles of porous iron(III) metal–organic frameworks. *Chemical Science*, *4*(4), 1597. https://doi.org/10.1039/c3sc22116d

39 Serre, C., Mellot-Draznieks, C., Surblé, S., Audebrand, N., Filinchuk, Y., & Férey, G. (2007). Role of Solvent-Host Interactions That Lead to Very Large Swelling of Hybrid Frameworks. *Science*, 315(5820). https://doi.org/10.1126/science.1137975

40 Serre, C., Millange, F., Surblé, S., & Férey, G. (2004). A Route to the Synthesis of Trivalent Transition-Metal Porous Carboxylates with Trimeric Secondary Building Units. *Angewandte Chemie International Edition*, 43(46), 6285–6289. https://doi.org/10.1002/anie.200454250

41 Baimuratova, R. K., Zhinzhilo, V. A., Uflyand, I. E., Dmitriev, A. I., Zhidkov, M. V., Ovanesyan, N. S., Kugabaeva, G. D., & Dzhardimalieva, G. I. (2023). Low-Temperature Synthesis of Metal–Organic Coordination Polymers Based on Oxo-centered Iron Complexes: Magnetic and Adsorption Properties. *Russian Journal of Physical Chemistry A*, *97*(4), 735–748. https://doi.org/10.1134/S0036024423040064

42 He, J., Zhang, Y., Zhang, X., & Huang, Y. (2018). Highly efficient Fenton and enzyme-mimetic activities of NH2-MIL-88B(Fe) metal organic framework for methylene blue degradation. *Scientific Reports*, *8*(1), 5159. https://doi.org/10.1038/s41598-018-23557-2

43 Bondarenko, L., Baimuratova, R., Reindl, M., Zach, V., Dzeranov, A., Pankratov, D., Kydralieva, K., Dzhardimalieva, G., Kolb, D., Wagner, F. E., & Schwaminger, S. P. (2024). Dramatic change in the properties of magnetite-modified MOF particles depending on the synthesis approach. *Heliyon*, e27640. https://doi.org/10.1016/j.heliyon.2024.e27640

44 Bondarenko, L., Baimuratova, R., Dzeranov, A., Pankratov, D., Kicheeva, A., Sushko, E., Kudryasheva, N., Valeev, R., Tropskaya, N., Dzhardimalieva, G., & Kydralieva, K. (2024). Fenton reaction-driven pro-oxidant synergy of ascorbic acid and iron oxide nanoparticles in MIL-88B(Fe). *New Journal of Chemistry*, 10.1039.D4NJ00963K. https://doi.org/10.1039/D4NJ00963K

45 Zhang, C.-F., Qiu, L.-G., Ke, F., Zhu, Y.-J., Yuan, Y.-P., Xu, G.-S., & Jiang, X. (2013). A novel magnetic recyclable photocatalyst based on a core–shell metal–organic framework Fe3O4@MIL-100(Fe) for the decolorization of methylene blue dye. *Journal of Materials Chemistry A*, *1*(45), 14329. https://doi.org/10.1039/c3ta13030d

46 Yadav, S., Dixit, R., Sharma, S., Dutta, S., Solanki, K., & Sharma, R. K. (2021). Magnetic metal–organic framework composites: Structurally advanced catalytic materials for organic transformations. *Materials Advances*, *2*(7), 2153–2187. https://doi.org/10.1039/D0MA00982B

47 Rahim Pouran, S., Abdul Raman, A. A., & Wan Daud, W. M. A. (2014). Review on the application of modified iron oxides as heterogeneous catalysts in Fenton reactions. *Journal of Cleaner Production*, *64*, 24–35. https://doi.org/10.1016/j.jclepro.2013.09.013

48 Dzhardimalieva, G. I., Irzhak, V. I., Bratskaya, S. Yu., Maiorov, V. Yu., Privar, Yu. O., Kasymova, E. D., Kulyabko, L. S., Zhorobekova, Sh. Zh., & Kydralieva, K. A. (2020). Stabilization of Magnetite Nanoparticles in Humic Acid Medium and Study of Their Sorption Properties. *Colloid Journal*, *82*(1), 1–7. https://doi.org/10.1134/S1061933X20010032

49 Sapianik, A. A., Kiskin, M. A., Kovalenko, K. A., Samsonenko, D. G., Dybtsev, D. N., Audebrand, N., Sun, Y., & Fedin, V. P. (2019). Rational synthesis and dimensionality tuning of MOFs from preorganized heterometallic molecular complexes. *Dalton Transactions*, *48*(11), 3676–3686. https://doi.org/10.1039/C8DT05136D

50 Elmore, W. C. (1938). Ferromagnetic Colloid for Studying Magnetic Structures. *Physical Review*, *54*(4), 309–310. https://doi.org/10.1103/PhysRev.54.309

51 Savitzky, A., & Golay, M. J. E. (1964). Smoothing and Differentiation of Data by Simplified Least Squares Procedures. *Analytical Chemistry*, *36*(8), 1627–1639. https://doi.org/10.1021/ac60214a047

52 Dzeranov, A., Pankratov, D., Bondarenko, L., Telegina, L., Dzhardimalieva, G., Saman, D., & Kydralieva, K. (2024). Humic acids-modified mesoporous silica encapsulating magnetite: Crystal and surface characteristics. *CrystEngComm*. https://doi.org/10.1039/D4CE00281D

53 Ma, B., Wang, S., Liu, F., Zhang, S., Duan, J., Li, Z., Kong, Y., Sang, Y., Liu, H., Bu, W., Li, L. (2018). Self-assembled copper-amino acid nanoparticles for in situ glutathione "and" H_2O_2 sequentially triggered chemodynamic therapy, *Journal of the American Chemical Society*, *141*, 849–857. https://doi.org/10.1021/jacs.8b08714

54 Hernandez, J. S. T., Aragón-Muriel, A., Corrales Quintero, W., Castro Velásquez, J. C., Salazar-Camacho, N. A., Pérez Alcázar, G. A., & Tabares, J. A. (2022). Characterization of Fe_3O_4 Nanoparticles for Applications in Catalytic Activity in the Adsorption/Degradation of Methylene Blue and Esterification. *Molecules*, *27*(24). https://doi.org/10.3390/molecules27248976

55 Wang, B., Yin, J.-J., Zhou, X., Kurash, I., Chai, Z., Zhao, Y., & Feng, W. (2013). Physicochemical Origin for Free Radical Generation of Iron Oxide Nanoparticles in Biomicroenvironment: Catalytic Activities Mediated by Surface Chemical States. *The Journal of Physical Chemistry C*, *117*(1), 383–392. https://doi.org/10.1021/jp3101392

56 Voinov, M. A., Pagán, J. O. S., Morrison, E., Smirnova, T. I., & Smirnov, A. I. (2011). Surface-Mediated Production of Hydroxyl Radicals as a Mechanism of Iron Oxide Nanoparticle Biotoxicity. *Journal of the American Chemical Society*, *133*(1), 35–41. https://doi.org/10.1021/ja104683w

57 Hermanek, M., Zboril, R., Medrik, I., Pechousek, J., & Gregor, C. (2007). Catalytic Efficiency of Iron(III) Oxides in Decomposition of Hydrogen Peroxide: Competition between the Surface Area and Crystallinity of Nanoparticles. *Journal of the American Chemical Society*, *129*(35), 10929–10936. https://doi.org/10.1021/ja072918x

58 Wang, F., Pauletti, G. M., Wang, J., Zhang, J., Ewing, R. C., Wang, Y., & Shi D. (2013). Dual surface functionalized janus nanocomposites of polystyrene/Fe_3O_4@SiO_2 for simultaneous tumor cell targeting and stimulus-induced drug release. *Advanced Materials*, *25*, 3485–3489. https://doi.org/10.1002/adma.201301376

How to Cite: Baikenov, M.I., Izbastenova, D.S., Su, X., Tusiphan, A., Akanova, Z.B., Balpanova, N.Zh., Baikenova, G.G., Zhao, Zh., & Li, W. (2024) Optimal Conditions for Demetallization of the Heavy Fraction of Low-Temperature Coal Tar of Shubarkol Komir JSC in the Presence of "Coal Shale" Catalytic Additive. *Eurasian Journal of Chemistry, 29, 3(115), 30-41.* https://doi.org/10.31489/2959-0663/3-24-11

Article

Received: 2 June 2024 | Revised: 8 August 2024 |
Accepted: 13 August 2024 | Published online: 23 September 2024

UDC 665.666.022

https://doi.org/10.31489/2959-0663/3-24-11

Murzabek I. Baikenov[1], Dariya S. Izbastenova[1*], Xintai Su[2], Almas Tusiphan[1], Zeinep B. Akanova[1], Nazerke Zh. Balpanova[1], Gulzhan G. Baikenova[3], Zhen Zhao[4], Wencui Li[4]

[1]*Karaganda Buketov University, Karaganda, Kazakhstan;*
[2]*School of Environment and Energy, Guangdong Provincial Key Laboratory of Solid Wastes Pollution Control and Recycling, South China University of Technology, Guangzhou, Guangdong, China;*
[3]*Karaganda University of Kazpotrebsoyuz, Karaganda, Kazakhstan;*
[4] *College of Chemistry & Chemical Engineering Shenyang Normal University, Shenyang, Liaoning, China*
*(*Corresponding author's e-mail: dom_dariya@mail.ru)*

Optimal Conditions for Demetallization of the Heavy Fraction of Low-Temperature Coal Tar of Shubarkol Komir JSC in the Presence of "Coal Shale" Catalytic Additive

The optimal conditions for demetallization of the heavy fraction of coal tar from Shubarkol Komir JSC were determined by means of full factorial experiment. Optimal conditions for demetallization of the aforementioned fraction were found to be a proportion of "Coal shale" catalytic additive to the heavy fraction of coal tar with boiling point above 300 °C equal to 0.04, process temperature in the range of 420–430 °C, duration from 20 to 30 minutes and initial pressure between 3 and 5 MPa. Experiments conducted under these conditions demonstrated the demetallization rates of 87–89 %. Conversion of the heavy fraction of coal tar in hydrogen medium at pressure of 4.0 MPa and temperature of 420 °C was examined, with and without the use of the "Coal Shale" catalytic additive. The findings demonstrate that the incorporation of the "Coal Shale" catalytic additive is associated with a notable enhancement in the production of liquid hydrogenate, reaching up to 57 %. Atomic emission spectral analysis was used to investigate the content of rare and dispersed elements including Ge, Ga, Y, Yb, Zr, Nb the ash of the heavy fraction of coal tar and the "Coal shale" catalytic additive, as well as in the solid product of demetallization of the heavy fraction of coal tar using the catalytic additive. The results showed that the use of "Coal shale" as the catalytic additive leads to an increase in the content of Ga, Yb, Y elements by 3-3.8 times, and Zr — by 7.5 times compared to the initial heavy fraction of coal tar in the absence of the catalytic additive.

Keywords: full factorial experiment, coal shale, coal tar, rare trace elements, dispersed trace elements, ash, optimal conditions, demetallization, heavy fraction.

Introduction

It is evident that solid and heavy hydrocarbon raw materials, including coal, shale, heavy petroleum residues and coal tar represent a promising source of essential elements such as germanium, gallium, tungsten, nickel, molybdenum and rare earth elements [1–5]. Solid and heavy hydrocarbon raw materials, low-temperature coal tar and coal shale and their processing products are distinguished by an exceptional diversity of trace element composition [2]. Since to date, 84 elements of the periodic system have been identified in solid fossil fuels, of which most are trace elements, that is, their content does not exceed 0.1 %.

These sources, in addition to low-temperature coal tar and coal shale, stand out for their unique trace element composition. The latest research has revealed that solid fossil fuels contain [6, 7] up to 84 elements of the periodic table, the majority of which are classified as trace elements with a concentration below 0.1 %. This discovery highlights the potential of hydrocarbon raw materials as an alternative source for the extraction of rare metals, which could have a significant impact on the development of the metallurgical and chemical industries.

Oil shale is characterized by a high level of ash content, reaching 30-80 %, which limits their direct use in the energy and chemical industries. Nevertheless, they can be of great interest as catalytic additives and hydrogen donors for the processing of heavy hydrocarbons. The study [8] shows the possibility of using coal

shale as hydrogen donors in the thermal dissolution of brown coal. A considerable quantity of hydrogen is present in oil shales, and the mineral part acts as a source of valuable trace elements [7].

Trace elements contained in solid and heavy hydrocarbon raw materials, in most cases, exceed or are commensurate with their quantitative purposefully extracted from ore raw materials [4]. The review [2] shows that work was carried out on the extraction of germanium from oil shale and coal tar fraction, and the inexpediency of extracting trace elements separately from complex and multicomponent raw materials has been established. In this regard, special attention is paid to technologies for concentrating metals [9-10] contained in oil shale and in the heavy fraction of coal tar into a solid phase by demetallization. Currently, the demetallization method is used for demetallization of heavy hydrocarbon feedstocks, in particular for heavy oil residues and heavy oils [10]. A review of the literature revealed that demetallization of solid fuels and coal tar is a relatively unsystematic process. Therefore, is crucial to identify the conditions that facilitate the concentration of trace elements in the solid phase through demetallization and to predict the most optimal methods for their processing. Additionally, it is essential to assess the feasibility of obtaining concentrates of these valuable metals.

The purpose of this study is to determine the optimal conditions for demetallization of the heavy fraction of low-temperature coal tar and coal shale from Shubarkol Komir JSC, and to investigate the impact of the "Coal Shale" catalytic additive on the qualitative and quantitative composition of the light and middle fraction obtained from the hydrogenation process.

Experimental

The heavy fraction of coal tar from Shubarkol Komir JSC, with boiling point above 300 °C, was selected for the study as a result of fractionation of low-temperature coal tar at atmospheric pressure. The elemental composition of the heavy fraction of coal tar of Shubarkol Komir JSC is presented in [11]. The catalytic additive used in this study was coal shale from Shubarkol Komir JSC (which will henceforth be referred to as the "Coal Shale" catalytic additive.

The original coal shale was subjected to grinding in a shek mill, then screened on *Sieve Shaker OBRK-SA, manufactured by Changzhou Oubeiruike Instrument and Equipment CO LTD, 2022*, with particles smaller than 0.1 and 0.1 mm, then stored in polyethylene bags.

The experimental conditions were selected on the basis of existing literature on catalytic hydrogenation of coal tar [10] and on the basis of our previous studies [12–15]. Demetallization experiments were performed in a high pressure reactor with a 0.3 L stirrer (PRC production). The initial hydrogen pressure is 3–5 MPa, the weight of the heavy fraction of coal tar with the catalytic addition of shale is 35–45 grams, the duration is from 20 to 60 minutes, the heating temperature is from 380 to 420 °C, the ratio of the catalytic addition of shale to the heavy fraction of tar with a boiling point above 300 °C varied in the range of 0.00–0.15.

During demetallization of the heavy fraction of coal tar with boiling point above 300 °C, Shubarkol Komir JSC obtained a hydrogenate, which was subjected to fractionation at atomospheric pressure: a light fraction of 100–200 °C and a middle fraction of 200–300 °C.

The solid phase of hydrogenation and the residue of hydrogenate fractionation with boiling point above 300 °C were ashed, and the concentration of 30 trace elements in the resulting ash was determined using the atomic emission spectral method. This method is based on the combustion of the sample in an electric arc discharge on a diffraction spectrograph 8 which is equipped with a multichannel analyzer of atomic emission spectra (MAES).

The results of the ash analysis were recalculated in relation to the heavy fraction of coal tar and the "Coal shale" catalytic additive, taking into account ash content by formula [16]:

$$C\left(\frac{g}{t}\right) = C_a * A / 100, \quad (1)$$

where C — is the concentration of element in the heavy fraction of coal tar and coal shale, C_a — is the concentration of the element in ash, A — is the ash content (%).

In order to study the possibility of using coal shale as the catalytic additive for demetallization of the heavy fraction of coal tar of Shubarkol Komir JSC, experiments were carried out without using the "Coal Shale" catalytic additive.

The experiment "Without catalytic additive" was carried out in a high-pressure reactor with stirring device at the temperature of 420 °C, initial hydrogen pressure of 4.0 MPa, and duration of 60 minutes.

Liquid products were also subjected to fractional distillation at atmospheric pressure with selection of the light fraction fraction 100–200 °C and the middle fraction 200–300 °C.

The individual chemical composition of the demetallization products of the heavy fraction of low-temperature coal tar of Shubarkol Komir JSC was determined using an Agilent 7890A gas chromatograph with an Agilent 5975C mass-selective detector. Column parameters Rxi-5ms: length — 30 m, diameter — 0.25 mm, column adsorbent thickness — 0.25 microns, column heating rate 8 °C/min, carrier gas — helium; gas pressure in the column 1.38×10^5 Pa; sample volume 2×10^{-4} cm^3; input mode — split, library — NIST08. The composition of the fractions was determined semi-quantitatively by peak area. The data were processed using the GSMSD Data Analysis program.

The elemental composition of the "Coal shale" catalytic additive comprising carbon, hydrogen and sulfur was determined using a CHNOS element analyzer Vario El Cube (Elementer Analysen System GmbH).

The texture characteristics of the catalyst additive were determined by physical nitrogen adsorption using a TriStar II 3020 (USA) instrument. The samples were heated under nitrogen current at 200°C for 1 hour before analysis. The BET specific surface area was calculated from the amount of nitrogen adsorbed in the range of relative pressures 0.05–0.30. The total pore volume was calculated from the amount of nitrogen adsorbed at a relative pressure close to unity ($P/P_0 = 0.874$), assuming that all available pores were filled with condensed nitrogen in the normal liquid state. The micropore volume was calculated using the t-method.

The composition and texture characteristics of the "Coal shale" catalytic additive are given in Table 1.

Table 1

Composition and textural characteristics of the catalytic additive

Sample	Ash content Ad	Content, wt.%			Textural characteristics		
		S	H	C	S_{sp}, m^2/g	V_{pores}, cm^3/g	$V_{micropores}$, cm^3/g
"Coal shale" catalytic additive	50–70	0.93	6.83	66.2	18.5348	0.053782	0.000485

In order to determine the optimal conditions for demetallization of the heavy fraction of coal tar of Shubarkol Komir JSC in the presence of the "Coal Shale" catalytic additive, we used a full factorial experiment (FFE). FFE is an experiment in which all possible, repeated combinations of factor levels are realized [17].

Results and Discussion

The effect of FFE on the degree of demetallization of the heavy fraction of coal tar with a boiling point above 300 °C and coal shale (y, %) was investigated. Coal shale is a source of trace elements, and also acts as the catalytic additive in the process of demetallization of mixture of the heavy fraction of coal tar and coal shale. The effects of four factors were studied: the ratio of the catalytic additive to the heavy fraction of coal tar above 300 °C (X_1) in the range of 0.00–0.15, temperature (X_2) 380–420 °C, process duration (X_3) 20–60 minutes, and initial hydrogen pressure (X_4) 3.0–5.0 MPa.

The FFE planning stages are as follows:

1. Factor coding;
2. Drawing up a matrix plan, $N = 2^4$, where N is the number of experiments, two levels of factor variation — upper and lower, factor coding +1, –1;
3. Checking the homogeneity of the dispersions of parallel experiments, their reproducibility;
4. Calculation of regression equation coefficients, their errors and significance;
5. Model adequacy testing.

The planning matrix with generating relationship $X_4 = X_1, X_2, X_3$ is shown in Table 2.

The levels of variable factors and their ranges are presented in Table 3.

Table 2

Half-replica from FFE with generating ratios $X_4 = X_1, X_2, X_3$, where X_4 — is the initial hydrogen pressure factor

Experiment No.	Factors on a dimensionless scale					Degree of demetallization *Y*, %
	X_0	X_1	X_2	X_3	X_4	
1	+1	+1	+1	+1	+1	88.3
2	+1	–1	–1	+1	+1	64.0
3	+1	–1	+1	+1	–1	67.4
4	+1	+1	–1	+1	–1	56.7
5	+1	+1	+1	–1	–1	87.9
6	+1	–1	–1	–1	–1	66.2
7	+1	–1	+1	–1	+1	80.8
8	+1	+1	–1	–1	+1	75.0

Table 3

Levels of variable factors and intervals of variation

Level of factors	Factor code value				Natural values of factors			
	X_1	X_2	X_3	X_4	Ratio of tar fraction to the "Coal Shale" catalytic additive	T, ºC	τ, duration, min	*P*, initial hydrogen pressure, MPa
Basic level	0	0	0	0	0.11	400	40.0	3.0
Variation interval	1	1	1	1	0.04	20.0	20.0	2.0
Upper level	1	1	1	1	0.15	420	60.0	5.0
Lower level	–1	–1	–1	–1	0.11	380	20.0	3.0

Regression equation with coefficients:

$$\hat{y} = b_0 + b_1x_1 + b_2x_2 + b_3x_3 + b_4x_4 . \quad (2)$$

The coefficients of the regression equation were calculated using the following formulas:

$$b_0 = \frac{1}{8}\sum_{1}^{8} x_0 y_i = 73.3 ; \quad (3)$$

$$b_1 = \frac{1}{8}\sum_{1}^{8} x_1 y_i = 3.69 ; \quad (4)$$

$$b_2 = \frac{1}{8}\sum_{1}^{8} x_2 y_i = 7.88 ; \quad (5)$$

$$b_3 = \frac{1}{8}\sum_{1}^{8} x_3 y_i = 4.19 ; \quad (6)$$

$$b_4 = \frac{1}{8}\sum_{1}^{8} x_4 y_i = 3.74 ; \quad (7)$$

$$\hat{y} = 77.3 + 3.69x_1 + 7.88x_2 + 4.19x_3 + 3.74x_4 . \quad (8)$$

The variability in the adequacy of the optimization parameter and the assessment of the significance of the coefficients in accordance with the Student's criterion [17] were calculated:

$$S_{var}^2 = \frac{\sum_1^3 \left(y_1^0 - \bar{y}_0\right)^2}{2} = 0.97 ; \quad (9)$$

$$S_{var} = 0.94 ; \quad (10)$$

$$S_{bj} = \frac{0.94}{\sqrt{8}} = 0.33 ; \quad (11)$$

$$t_0 = \frac{73.3}{0.33} = 222.08 ; \quad (12)$$

$$t_1 = \frac{3.69}{0.33} = 11.17\,; \tag{13}$$

$$t_2 = \frac{7.88}{0.33} = 23.84\,; \tag{14}$$

$$t_3 = \frac{4.19}{0.33} = 12.7\,; \tag{15}$$

$$t_4 = \frac{3.74}{0.33} = 11.33\,. \tag{16}$$

Three additional parallel experiments were conducted in the center of the matrix design (Table 2) and the following values of the degree of demetallization *y*, %, were obtained:

$$y_1^0 = 86.4\,; \tag{17}$$

$$y_2^0 = 88.3\,; \tag{18}$$

$$y_3^0 = 87.8\,; \tag{19}$$

$$\bar{y}_0 = \frac{\sum_{n=1}^{3} y_i^0}{3} = 87.5\,; \tag{20}$$

$$S_{res}^2 = \frac{\sum_{i=1}^{8}(y_i - \bar{y}_0)^2}{N-e} = \frac{(88.3-92.84)^2 + (64.0-69.6)^2 + (67.4-78.4)^2}{3} = 57.66\,. \tag{21}$$

We evaluate the significance of the coefficients in equation (8) according to the Student's criterion [17]. Since we have the number of parallel experiments is three, according to the tabulated values of the Student's criterion, for the significance level $n = 0.05$ and the number of degrees of freedom $f = 3–1 = 2$, then $t_r = 4.3$.

The adequacy of the obtained equation is checked by Fisher's criterion:

$$F = S_{res}^2 \Big/ S_{rep}^2 = \frac{57.7}{0.94} = 7.9\,. \tag{22}$$

The adequacy of the linear model was validated using F-test: $F_{calc} \le F_{tab}$, $F_{tab} = 19.3$.

Based on the matrix data and the regression equation, the following conclusions are made:

1. The greatest influence on the degree of demetallization of heavy fraction of coal tar above 300 °C in the presence of the “Coal Shale” catalytic additive is exerted by factors: X_2 — process temperature (ºC), X_3 — process duration (min) and X_4 — initial hydrogen pressure.

2. The least effect on the degree of demetallization of the heavy fraction of the coal tar above 300 °C in the presence of the “Coal shale” catalytic additive is exerted by the factor X_1 — the ratio of the catalytic additive of oil shale to the heavy fraction of the coal tar above 300 °C.

The rate of molecular hydrogen consumption per unit of organic mass in the mixture was — 1.75 %. Hydrogen consumption was determined on the basis of the mixture, hydrogenate, solid residue and gas phase.

Thus, the optimal conditions for the hydrodemetallization process of the mixture: the ratio of the catalytic additive (“Coal shale”) to the heavy fraction of the coal tar above 300 °C is 0.04, the 420–430 °C temperature, the duration is 20–30 minutes, the initial pressure is 3–5 MPa. Carrying out the process under optimal conditions showed the degree of demetallization 87–89 %.

Table 4 presents the qualitative and quantitative composition of the light and middle fraction of hydrogenates obtained in the presence of the catalytic additive “Coal shale”, as well as in its absence.

Figure 1 illustrates the component composition of the 100–200 °C light fraction and 200–300 °C middle fraction of the hydrogenate of the heavy fraction of coal tar of Shubarkol Komir JSC “Without catalytic additive” and using the “Coal shale” catalytic additive at the temperature of 420 °C, the initial hydrogen pressure of 4 MPa and the duration of 60 minutes.

The yield of liquid hydrogenate of the 100–200 °C light fraction without a catalytic additive is 5.2 %, while the yield of liquid hydrogenate of the 200–300 °C middle fraction is 9.0 %. The addition of the “Coal shale” catalytic additive, derived from the heavy fraction of coal tar with the boiling point above 300 °C, resulted in a significant increase in the yield of the liquid hydrogenate of the light fraction of 100–200 °C to 43.5 %, and a notable enhancement in the yield of the middle fraction of (200–300 °C) to 13.4 %.

Table 4

Individual chemical composition of light and middle hydrogenate fractions (experimental conditions: 420 °C, 60 min, 4 MPa, ratio 0.13)

№	Class of compounds	Compounds	Area without and with catalytic additive "Coal shale", %			
			100–200 °C Light fraction		200–300 °C Middle fraction	
			Without	With	Without	With
1	2	3	4	5	6	7
1	Paraffinic hydrocarbons	Pentane, 3-ethyl-2,2-dimethyl-	–	0.33	–	–
		Hexane, 2,5-dimethyl-	0.59	0.37	–	–
		Hexane, 3-ethyl-2,5-dimethyl-	–	0.46	–	–
		Heptane	2.09	–	–	–
		Heptane, 3-methyl-	2.88	–	–	–
		Heptane, 3-ethyl-2-methyl-	0.86	–	–	–
		Octane, 3-methyl-	0.33	–	–	–
		Octane, 2,3- dimethyl -	–	1.23	–	–
		Octane, 2,6-dimethyl-	0.75	0.87	–	–
		Octane, 3,5-dimethyl-	–	1.04	–	–
		Nonane, 2-methyl-	4.05	–	–	–
		Decane, 2,6,8-trimethyl-	5.0	–	–	–
		Decane, 2,6,7-trimethyl-	0.23	–	–	–
		Decane, 2,6,6-trimethyl-	–	4.72	–	–
		Decane, 2,5,9-trimethyl-	–	0.82	1.02	0.35
		Undecane, 3,6-dimethyl-	4.77	–	–	2.7
		Undecane, 4,6-dimethyl-	0.27	0.63	1.91	–
		Undecane, 2,5-dimethyl-	–	5.11	–	–
		Undecane, 2,6-dimethyl-	–	2.98	–	1.51
		Dodecane, 2,6,11-trimethyl-	13.2	–	3.54	–
		Dodecane, 2,7,10-trimethyl-	–	6.6	–	–
		Dodecane, 2-methyl-	0.26	–	–	–
		Pentadecane	3.06	3.02	3.83	3.34
		Heptadecane, 2,6-dimethyl-	–	2.08	–	–
		Heptadecane	5.1	–	2.75	11.9
		Eicosane	3.46	0,88	14.2	6.58
		Heneicosane	–	0.51	2.37	–
		Heptacosane	–	–	6.64	–
2	Aromatic hydrocarbons	Benzene, 1,3,5-triethyl-	0.27	–	0,51	–
		Benzene, 1-ethyl-2-methyl-	3.24	–	–	–
		Benzene, 1-methyl-3-propyl-	0,34	0.35	–	–
		Benzene, 1-methyl-4-propyl-	0.32	1.32	–	0.53
		Benzene, 1-ethenyl-4-methoxy-	–	–	–	0.32
		Benzene, (2-methyl-1-propenyl)-	0.62	–	–	–
		Benzene, 2-ethenyl-1,4-dimethyl-	0.28	–	–	–
		Benzene, 1-methyl-4-(1-methyl-2-propenyl)-	1.35	–	–	–
		Benzene, (2-ethenyl-1,4,4-trimethylpentyl)-	–	0.54	–	–
		Benzene, 1,1'-(1-methyl-1,2-ethanediyl) bis-	–	1	–	0.25
		Benzene, 1,3-dimethyl-	–	10.56	–	–
		Benzene, pentamethyl-	0.4	–	1	
		Benzene, (2-methyl-1-butenyl)-	–	–	–	0.46
		Benzene, (1-methyl-1-butenyl)-	–	–	–	0.78
		Benzene, (3-methyl-2-butenyl)-	–	–	–	0.27
		Benzene, 1-methoxy-4-(1-methylethyl)-	–	–	–	0.63
		Benzene, 1-methyl-4-(1-methylethenyl)	–	–	–	0.31
		Benzene, 2,4-diethyl-1-methyl-	–	–	–	0.36
		o-Isopropenyltoluene	–	–	–	0.42
		1,1'-Biphenyl, 2-methyl-	–	–	1.02	–

Continuation of Table 4

1	2	3	4	5	6	7
		Ethylbenzene	0.96	2,24	–	–
		o-Xylene	4.47	–	–	–
		Toluene	1.65	4.36	–	–
3	Phenols	Phenol	4.03	8.98	3.81	4.26
		Phenol, 2-methyl-	2.27	10.89	2.93	–
		Phenol, 3-methyl-	4.69	–		–
		Phenol, 4-methyl-	–	–	7.03	6.99
		Phenol, 2,3-dimethyl-	0.41	–	–	4.96
		Phenol, 4-ethyl-	0.60	–	–	–
		Phenol, 3,5-dimethyl-	5.41	–	–	–
		Phenol, 3,4-dimethyl-	–	–	–	0.9
		Phenol, 2,5-dimethyl-	0.44	–	–	4.18
		Phenol, 2,6-dimethyl-	–	–	–	1.05
		Phenol, 2-ethyl-	0.64	2.11	0.38	0.85
		Phenol, 3-ethyl-	–	–	4.81	–
		Phenol, 2-ethyl-5-methyl-	0.55	–	–	1.5
		Phenol, 2-ethyl-4-methyl-	–	–	–	2,54
		Phenol, 2,4,6-trimethyl-	1.59	–	–	–
		Phenol, 2,3,5-trimethyl-	–	–	0.17	–
		Phenol, 2,3,6-trimethyl-	–	–	–	0.92
		Phenol, 2-propyl-	–	–	1.42	–
		Phenol, 2-methyl-6-(2-propenyl)-	–	–	–	0.31
		Thymol	0.35	–	0.29	–
4	Polycyclic hydrocarbons	Naphthalene	0.87	–	–	1.69
		Naphthalene, 1-methyl-	2.25	3.06	–	4.41
		Naphthalene, 2-methyl-	–	–	2.95	–
		Naphthalene, 1-ethyl-	–	–	–	0.91
		Naphthalene, 2-ethyl-	0.25	0.28	0.96	–
		Naphthalene, 1,4-dimethyl-	2.11	–	1.6	1.21
		Naphthalene, 1,2-dimethyl-	–	0.51	–	–
		Naphthalene, 2,3-dimethyl-	–	0.41	1.92	3.02
		Naphthalene, 2,7-dimethyl-	–	–	1.47	–
		Naphthalene, 1,4,6-trimethyl-	0.27	0.33	–	3.24
		Naphthalene, 1,6,7-trimethyl-	1.09	–	–	–
		Naphthalene, 2,3,6-trimethyl-	–	–	4.23	–
		Naphthalene, 1,2,3,4-tetrahydro-5, 7-dimethyl-	–	0.32	–	–
		Naphthalene, 1,2,3,4-tetrahydro-1-methyl-	–	–	–	0.22
		Naphthalene, 1,2,3,4-tetrahydro-1,6,8-trimethyl-	–	–	–	0.25
		Naphthalene, 1-propyl-	–	–	0.37	0.25
		Naphthalene, 1,6-dimethyl-4-(1-methylethyl)-	–	–	–	0.55
		Fluorene	0.29	0.24	0.8	–
		Anthracene	0.32	0.38	–	–
		Anthracene, 2-methyl-	–	–	0.3	–
		Phenanthrene	–	–	2.12	1.03
		Phenanthrene, 2-methyl-	–	0.25	0.27	–
		Phenanthrene, 1-methyl-	–	–	–	0.47
		Phenanthrene, 1,7-dimethyl-	–	–	–	0.6
		Phenanthrene, 3,6-dimethyl-	–	–	0.21	–
		Phenanthrene, 2,3,5-trimethyl-	–	–	0.28	–
		Phenanthrene, 1-methyl-7-(1-methyl ethyl)-	–	0.21	–	0.3
		Azulene	–	1.08		
		1H-Indene, 2,3-dihydro-4,7-dimethyl-	–	–	–	0.58
		1H-Indene, 2,3-dihydro-1,1,5-trimethyl-	–	–	–	0.59
		1H-Indene, 2,3-dihydro-1,4,7-trimethyl-	–	–	–	0.92
		Fluorene	–	–	–	0.65
		9H-Fluorene, 2-methyl-	–	–	–	1.21
		2-Hydroxyfluorene	–	–	–	0.96

Continuation of Table 4

1	2	3	4	5	6	7
5	Heterocyclic hydrocarbons	Furan, 3-phenyl-	–	–	1.46	0.95
		Benzofuran, 2,3-dihydro-2-methyl-	0.51	–	–	–
		Benzofuran, 2-ethenyl-	0.47	–	–	–
		Dibenzofuran	–	–	0.45	0.42
		Dibenzofuran, 4-methyl-	0.43	–	0.38	0.34
		Benzenethanamine, N-(3-chloropropyl)-alpha-methyl-	–	2.04	–	–
		Benzenamine, 3-methyl-	–	1.57	–	–
		o-Toluidine	–	0.57	–	–
		5-aminoindole	–	0.43	–	–
		Pyridine, 3-ethyl-	–	0.49	–	–
		Pyridine, 3,4-dimethyl-	–	0.25	–	–
		Pyridine, 2,3-dimethyl-	–	–	–	0.3
		Quinoline, 2,6-dimethyl-	–	–	–	0.21

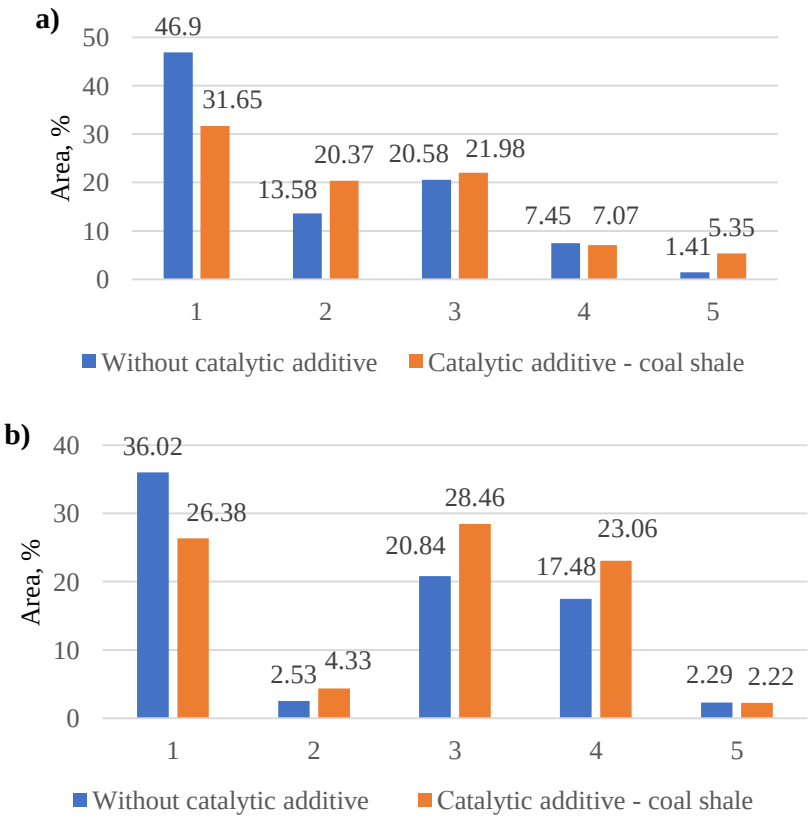

1 — Paraffin hydrocarbons; *2* — Aromatic hydrocarbons; *3* — Phenols;
4 — Polycyclic hydrocarbons; *5* — Heterocyclic hydrocarbons

Figure 1. Component composition of the 100–200 °C light fraction (*a*) and 200–300 °C middle fraction (*b*) of hydrogenate (420 °C, 60 min, 4 MPa, ratio 0.13)

The 100–200 °C light fraction, isolated from the products obtained by demetallization of the heavy fraction of coal tar on the "Coal Shale" catalytic additive, is characterized by a significantly lower content of marginal hydrocarbons compared to the light fraction isolated from the liquid product obtained by demetallization of the heavy fraction of coal tar "Without catalytic additive".

Paraffin hydrocarbons of light fraction obtained in experiments "Without catalytic additive" and with the "Coal shale" catalytic additive are represented by homologues of heptane, octane, decane, undecane, dodecane, heptadecane and eicosane, but the content of higher paraffins decreases at demetallization on the "Coal shale" catalytic additive (Table 4).

o-Xylene (4.47 %) and toluene (1.65 %) are present in the 100–200 °C fraction separated from the hydrogenate during demetallization "Without catalytic additive". In the same fraction, but obtained in the experiment with the "Coal shale" catalytic additive, o-xylene is absent, the toluene content increases to 4.36 % and Benzene, 1,3-dimethyl (10.56 %) is present in a significant amount.

The content of phenols slightly increases on the "Coal shale" catalytic additive, and the fraction consists of phenol (8.98 %), phenol, 2-methyl- (10.89 %) and phenol, 2-ethyl- (2.11 %).

The 100–200 °C fraction recovered in the "Without catalytic additive" demetallization process contains naphthalene, its derivatives, fluorene and anthracene, while in the 100–200 °C fraction obtained in the "Coal shale" catalytic additive demetallization process, polycyclic hydrocarbons are composed of naphthalenes, fluorene and anthracene, and azulene, and phenanthrenes are also present.

As illustrated in Table 4, the heterocyclic hydrocarbons in the first fraction, using the "Coal shale" catalytic additive, consist of amines and pyridines; during demetallization of heavy fraction of coal tar "Without catalytic additive" they are represented by oxygen-containing hydrocarbons.

Thus, the content of aromatic, heterocyclic compounds in the light fraction obtained on the "Coal shale" catalytic additive is higher than in the light fraction "Without catalytic additive", which is associated with the conversion of saturated hydrocarbons and phenols into the corresponding aromatic and heterocyclic hydrocarbons (Figure 1).

The 200–300 °C middle fraction, separated at fractionation of the hydrogenate of demetallization process of the heavy fraction of coal tar demetallization "Without catalytic additive" has significantly lower content of aromatic, polycyclic hydrocarbons and phenols in comparison with the second fraction obtained from the liquid product of demetallization with the use of the "Coal shale" catalytic additive.

The content of saturated hydrocarbons in the middle fraction of 200–300 °C in the presence of the "Coal Shale" catalytic additive is found to be lower than that of the middle fraction "Without catalytic additive", with a decrease from 36.02 % to 26.38 %.

The content of aromatic hydrocarbons in the middle fraction extracted during demetallization of the heavy fraction of coal tar of Shubarkol Komir JSC in the experiment with the "Coal shale" catalytic additive is twice that of the experiment "Without catalytic additive".

The "Coal shale" catalytic additive increases the yield of polycyclic hydrocarbons to 23 %, and phenols to 28.46 %; the content of heterocyclic compounds on the catalytic additive "Coal shale" practically does not change compared to the yield of heterocyclic hydrocarbons in the experiment "Without catalytic additive".

Thus, the "Coal shale" catalytic additive promotes aromatization and the formation of polycyclic compounds from saturated hydrocarbons in both hydrogenate fractions.

The concentration of rare and dispersed trace elements in the ash of the heavy fraction of coal tar, in solid products and residues of demetallization of the heavy fraction of coal tar, taking into account ash content, is presented in Table 5.

Table 5

Concentration of rare and dispersed trace elements in the demetallization products of the heavy fraction of coal tar of Shubarkol Komir JSC

№	Composition of the mixture	Demetallization conditions	Trace element content, g/t					
			Ga	Ge	Yb	Y	Zr	Nb
1	Heavy fraction of coal tar	Initial mixture	0.5	0.4	0.1	1.2	1.2	0.7
2	Heavy fraction of coal tar	Initial mixture with the "Coal Shale" catalytic additive, ratio 0.13	1.8	<0.3	0.3	4.3	8.9	1.2
3	Solid phase of hydrogenate obtained by demetallization of heavy fraction of coal tar with the "Coal shale" catalytic additive	420 °C, 4 MPa, 60 minutes, ratio 0.13	1.6	<0.2	0.2	0.2	26.0	1.3
4	Solid residue obtained after fractionation of the heavy fraction of coal tar hydrogenate with the "Coal shale" catalytic additive	420 °C, 4 MPa, 60 minutes, ratio 0.13	≤0.1	<0.1	<0.04	<0.4	0.9	<0.3

According to the results obtained, the heavy fraction of coal tar is characterized by an insignificant content of rare and dispersed trace elements. When adding the "Coal shale" catalytic additive, the content of

trace elements Ga, Yb, Y increases 3-3.8 times, and the content of Zr increases 7.5 times compared to the content of said trace elements in the initial fraction of coal tar without the “Coal shale” catalytic additive.

The content of trace elements in the solid residue obtained after fractionation of the heavy fraction of coal tar hydrogenate with the “Coal shale” catalytic additive is significantly lower than in the solid phase of the hydrogenate obtained by demetallization of the heavy fraction of coal tar with the “Coal shale” catalytic additive, which indicates the adsorption abilities of the “Coal shale” catalytic additive and the ability to obtain solid products with the high content of rare and dispersed trace elements.

Conclusions

Mathematical model of catalytic demetallization of the mixture of the heavy fraction of coal tar and shale is obtained. It has been found that coal shale effectively demetallizes the heavy fraction of coal tar and catalyzes the hydrogenation reactions of coal tar and affects the quantitative and qualitative change in the individual and group composition of the light and middle fractions of the hydrogenate. A high degree of demetallization of the heavy fraction of coal tar of Shubarkol Komir JSC is achieved while observing the temperature regime and the duration of the demetallization process. It should be noted that the ratio of the “Coal shale” catalytic additive to the heavy fraction of coal tar has a slight effect the degree of demetallization of the mixture of the heavy fraction of coal tar and coal shale.

It was found that the “Coal shale” catalytic additive increases the yield of liquid products of demetallization of the heavy fraction of coal tar four times compared to the demetallization of the heavy fraction of coal tar “Without catalytic additive”. Apparently, the “Coal shale” catalytic additive exhibits donor abilities and is a source of active hydrogen, activates molecular hydrogen to an atomic state, thereby explaining the high yield of the hydrogenate and the high degree of demetallization of trace elements.

The content of trace elements in the solid phase of the hydrogenate and in the solid residue obtained during fractionation of the hydrogenate, which increases in the presence of the "Coal shale" catalytic additive both in the initial heavy fraction of coal tar and the solid residue of demetallization of the heavy fraction of coal tar, has been established. It is shown that the total content of trace elements Ga, Ge, Y, Yb, Zr, Nb in the solid phase of demetallization of the heavy fraction of coal tar is 1.8 times higher than in the initial mixture of the heavy fraction of coal tar and the “Coal shale” catalytic additive.

The obtained results can be used when selecting alternative methods for processing heavy and solid hydrocarbon materials with the objective of concentrating valuable trace elements and predicting the composition of the resulting liquid products.

Funding

This research and APC was funded by the Ministry of Science and Higher Education of the Republic of Kazakhstan (registration No. 0123PK00217), state grant No. AP19679059.

*Author Information**

**The authors' names are presented in the following order: First Name, Middle Name and Last Name*

Murzabek Ispolovich Baikenov — Doctor of Chemical Sciences, Professor, Karaganda Buketov University, Universitetskaya street, 28, 100024, Karaganda, Kazakhstan; e-mail: murzabek_b@mail.ru; https://orcid.org/0000-0002-8703-0397

Dariya Serikovna Izbastenova (*corresponding author*) — PhD Doctoral Student, Karaganda Buketov University, Universitetskaya street, 28, 100024, Karaganda, Kazakhstan; e-mail: dom_dariya@mail.ru; https://orcid.org/0000-0002-1874-8477

Xintai Su — Professor, School of Environment and Energy, Guangdong Provincial Key Laboratory of Solid Wastes Pollution Control and Recycling, South China University of Technology, 510006, Guangzhou, Guangdong, PR China; e-mail: suxintai@scut.edu.cn; https://orcid.org/0000-0001-6615-5273

Almas Tusipkhan — PhD, Karaganda Buketov University, Universitetskaya street, 28, 100024, Karaganda, Kazakhstan; e-mail: almas_kz_22@mail.ru; https://orcid.org/0000-0002-6452-4925

Zeinep Baurzhanovna Akanova — Master Student, Karaganda Buketov University, Universitetskaya street, 28, 100024, Karaganda, Kazakhstan; e-mail: akanova01@mail.ru

Nazerke Zhumagalievna Balpanova —PhD, Karaganda Buketov University, Universitetskaya street, 28, 100024, Karaganda, Kazakhstan; e-mail: nazerke_90@mail.ru; https://orcid.org/0000-0003-3089-1871

Gulzhan Gausilevna Baikenova — Doctor of Chemical Sciences, Professor, Karaganda University of Kazpotrebsoyuz, Karaganda, Kazakhstan; e-mail: g.baikenova@keu.kz; https://orcid.org/0000-0002-2816-3341

Zhen Zhao — Professor, State Key Lab of Heavy Oil Processing, College of Science, China University of Petroleum, Beijing, 18# Fuxue Road, Chang Ping Distract, Beijing, 102249, China; Director of Institute of Catalysis for Energy and Environment, Dean of College of Chemistry & Chemical Engineering Shenyang Normal University, Shenyang, Liaoning 110034, China; e-mail: zhenzhao@cup.edu.cn; zhaozhen1586@163.com; https://orcid.org/0000-0003-0044-5512

Wencui Li — Associate Professor, Chemistry & Chemical Engineering Shenyang Normal University, Shenyang, Liaoning 110034, China; e-mail: wencuili1993@163.com; https://orcid.org/0000-0003-4344-7438

Author Contributions

The manuscript was written through contributions of all authors. All authors have given approval to the final version of the manuscript. CRediT: **Murzabek Ispolovich Baikenov** conceptualization, data curation, investigation, methodology, validation, visualization, writing-review & editing; **Dariya Serikovna Izbastenova** conceptualization, data curation, investigation, methodology, validation, visualization, writing-review & editing; **Xintai Su** conceptualization, supervision, writing-review&editing; **Almas Tusipkhan** conceptualization, data curation, supervision, validation, writing-review & editing, **Zeinep Baurzhanovna Akanova** demetallization**,** writing-review & editing; **Nazerke Zhumagalievna Balpanova** writing-review&editing; **Gulzhan Gausilevna Baikenova** writing-review&editing; **Zhen Zhao** BET analysis, supervision, writing-review & editing; **Wencui Li** BET analysis, supervision, writing-review & editing.

Conflicts of Interest

The authors declare no conflicts of interest.

References

1 Seredin, V. V. & Dai, S. (2012). Coal deposits as potential alternative sources for lanthanides and yttrium. *International Journal of Coal Geology*, *94*, 67–93. https://doi.org/10.1016/j.coal.2011.11.001

2 Lapidus, A. L., Khudyakov, D. S., Beilina, N. Yu., Trukhina, M. A., Kozlov, A. M. & Zhagfarov, F. G. (2022). Solid fossil fuels as a source of trace elements. *Solid Fuel Chemistry*, *56*(1), 1–14. https://doi.org/10.3103/S0361521922010037

3 Dai, S. & Finkelman, R. B. (2017). Coal as a promising source of critical elements: Progress and future prospects. *International Journal of Coal Geology*. https://doi.org/10.1016/j.coal.2017.06.005

4 Sorokin, A. P., Ageev, O. A., Dugin, S. V., & Popov, A. A. (2023). Metal Content of Brown Coals from the Raichikhinskoe Deposit (Priamurie, Far East): Conditions of Accumulation and Distribution and Prospects for Development. *Himiâ Tverdogo Topliva*, (1), 13–31. doi:10.31857/S0023117723010097

5 Park, S., Kim, M., Lim, Y., Yu, J., Chen, S., Woo, S. W., Yoon, S., Bae, S. & Kim, H. S. (2021). Characterization of rare earth elements present in coal ash by sequential extraction. *Journal of Hazardous Materials*, *402*, 123760. https://doi.org/10.1016/j.jhazmat.2020.123760

6 Silyutin, S. A., Shpirt, M. Ya. & Lavrinenko, A. A. (2016). Classification of solid fossil fuels and their processing products depending on trace elements contained in them. *Solid Fuel Chemistry*, *50*(3), 141–148. https://doi.org/10.3103/S0361521916030113

7 Al-Ayed, O. S., Qawaqneh, M. K., & Abu-Nameh, E. S. (2024). Tracing rare earth elements in oil shale ash. *Oil Shale*, *41*(2), 132–143 https://doi.org/10.3176/oil.2024.2.04

8 Vol-Epshtein, A. B., Shpil'berg, M. B., Platonov, V. V., & Rudenskii, A. V. (1987). Combustible shales as hydrogen donors in the thermal dissolution of the brown coal of the Kansk-Achinsk basin. *Solid Fuel Chemistry*, *21*(2), 70–72.

9 Magomedov, R.N., Popova, A.Z., Maryutina, T.A. et al. Current status and prospects of demetallization of heavy petroleum feedstock (Review). *Pet. Chem.*, *55*, 423–443 (2015). https://doi.org/10.1134/S0965544115060092

10 *Khadzhiev, S.N.*, & *Shpirt*, M.Y. (2012) Microelementy v neftyah I productah ih pererrabotki. [Trace Elements in Oils and Products of Their Processing]. M.: Nauka [in Russian]

11 Baikenov, M., Izbastenova, D., Sarsenbekova, A., Balpanova, N., Tusipkhan, A., Khalikova, Z., Rakhimzhanova, N., Kochegina, E., Tulebaeva, B., & Taurbaeva, G. (2024). Determination of the Kinetic Parameters of Thermal Degradation and

Hydrodemetallization of a Mixture of the Heavy Fraction of Low-Temperature Coal Tar and Coal Shale. *Energies*, *17*(7). https://doi.org/10.3390/en17071766

12 Baikenov, M. I., Ivannikova, A. V., Baikenova, G. G., Khalikova, Z. S., Kochegina, E. V., Rakhimzhanova, N. Z., Karimova, A. B., & Kezdikbaeva, A. T. (2016). Effect of iron additives on the thermal degradation of coal from the Shubarkol deposit. *Solid Fuel Chemistry*, *50*(5), 300–305. https://doi.org/10.3103/S0361521916050037

13 Musina, G. N., Ibatov, M. K., Baikenov, M. E., Zhaksybayeva, G. Sh., & Zhaslan, R. K. (2017). Catalytic hydrogenation of a mixture of coal and heavy oil residue fractions. *Bioscience Research*, *14*(4), 1110–1119. https://doi.org/10.24200/sci.2018.50555.1757

14 Tyanakh, S., Baikenov, M. I., Ma, F.-Y., Fomin, V. N., Baikenova, G. G., Ashimhanov, A. S., & Seitzhan, R. S. (2023). Determination of Optimal Conditions for Catalytic Hydrogenation of Oil Sludge (Atasu-Alashankou). *Eurasian Journal of Chemistry*, *2023*(2), 139–146. https://doi.org/10.31489/2959-0663/2-23-15

15 Akhmetkarimova, Z. S., Baikenov, M. I., & Ma, F.-Y. (2016). Calculation of the thermodynamic parameters of a fraction of primary coal tar. *Solid Fuel Chemistry*, *50*(5), 277–281. https://doi.org/10.3103/S0361521916050025

16 Oleinikova, G. A., Kudryashov, V. L., Vyalov, V. I., & Fadin, Y. Y. (2015). Determination of trace elements in brown coals by inductively coupled plasma mass spectrometry. *Solid Fuel Chemistry*, *49*(2), 109–116. https://doi.org/10.3103/S0361521915020093

17 Akhnazarova, S.L., & Kafarov V.V. (1985). Metody optimizacii eksperimenta v himicheskoi tehnologii [Experiment Optimization in Chemistry and Chemical Engineering]. M.: Vysshaya Shkola [in Russian].

How to Cite: Kudaibergenov**,** S.E. (2024) Catalytic Properties of Polyampholytes, Polyampholyte-Metal Complexes, Polyampholyte-metal Nanoparticles and Polyampholyte-Enzyme Conjugates: A Mini-Review. *Eurasian Journal of Chemistry, 29, 3(115), 42-54.* https://doi.org/10.31489/2959-0663/3-24-8

Review

Received: 9 June 2024 | Revised: 13 August 2024 |
Accepted: 16 August 2024 | Published online: 13 September 2024

UDC 541.64+544.47

https://doi.org/10.31489/2959-0663/3-24-8

Sarkyt E. Kudaibergenov

Institute of Polymer Materials and Technology, Almaty, Kazakhstan
(Author's e-mail: skudai@mail.ru)

Catalytic Properties of Polyampholytes, Polyampholyte-Metal Complexes, Polyampholyte-Metal Nanoparticles and Polyampholyte-Enzyme Conjugates: a Mini-Review

This mini-review briefly discusses the catalytic properties of polyampholytes, polyampholyte-metal complexes, polyampholyte-metal nanoparticles and polyampholyte-catalase conjugates. Polyampholyte-based catalysts can mimic enzyme functions, facilitating reactions like hydrolysis, decomposition, hydrogenation, and oxidation of various substrates. Special focus is given to amphoteric hydrogels and cryogels that encapsulate metal nanoparticles or enzymes. These materials have demonstrated effectiveness in the hydrogenation of nitroaromatic compounds, oxidation of disulfide and aliphatic (or aromatic) alcohols under mild conditions, both in batch and flow-through reactors. Kinetic parameters, turnover numbers (TON), turnover frequencies (TOF), and activation energies are presented for a series of specific catalytic processes. Notably, flow-through reactors exhibit significantly higher catalytic efficiency compared to batch reactors and can be used continuously for extended periods. Additionally, the review explores the potential of light-driven hydrogen and oxygen evolution reactions from water, facilitated by metal nanoparticles within amphoteric hydrogels in the presence of photosensitizers.

Keywords: Polyampholyte-metal complexes, polyampholyte-metal nanoparticles, polyampholyte-enzyme conjugates, catalysis, decomposition, hydrogenation, oxidation, water splitting.

Professor **Sarkyt E. Kudaibergenov** is a prominent Kazakh polymer scientist, known for his research into water-soluble and water-swelling polyampholytes, macromolecular complexes, polymer-stabilized nanoparticles, polymeric catalysis, and stimuli-responsive materials for various applications. Currently he is director of private institution "Institute of Polymer Materials and Technologies" established by him in 1999. He has co-authored 20 monographs and textbooks, published in Kazakh, Russian, Polish and English, as well as over 400 research articles and reviews, more than 150 of which have appeared in international peer-reviewed journals. He has received awards and recognition for his research, including the State Prize of the Republic of Kazakhstan in the field of Science and Technology (1986), the "Parasat" award for being the most published and internationally cited Kazakhstani author (2010), a medal "For merits in the development of science in the Republic of Kazakhstan" from the Ministry of Science and Education of the Republic of Kazakhstan (2012), the K.I. Satpayev Prize for the development of specialty polymers for application in petrochemistry and nanotechnology (2019), and the State Scientific Scholarship for scientists and specialists who have made an outstanding contribution to the development of science and technology (2020). For outstanding achievements in basic science in 2022 he has been recognized as "Best Researcher" by the Ministry of Science and Education of the Republic of Kazakhstan. Despite achieving numerous successes and making significant contributions to the field of physical chemistry of polymers, Professor S.E. Kudaibergenov's enduring interest lies in polyampholytes — a subject he has explored since 1979. He has published several reviews and fundamental monographs on this topic, including "Polyampholytes: Synthesis, Characterization, and Application" (Kluwer Academic/Plenum Publishers, 2002, USA), "Polyampholytes: Past, Present, Perspectives" (2021, Center for Operational Printing, 2021, Kazakhstan), "Polyampholytes in Advanced Polymer Science and Emerging Technologies" (CRS Press, 2024, Boca Raton and London).

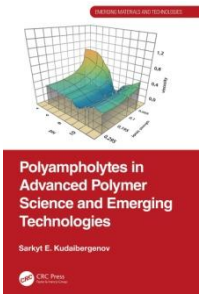

Dear Colleagues,

We are pleased to share great news! In September 2024, Professor Kudaibergenov's new book «**Polyampholytes in Advanced Polymer Science and Emerging Technologies**» was just published by CRC Press. This monograph reviews the innovative studies in this field over the past two decades, with the aim to analyze and systematize the literature in the context of emerging technologies.

Table of Contents

1. Introduction. 2. Water-Soluble Polyampholytes. 3. Hydrophobically-Modified Polyampholytes (HMPA). 4. Nanogels, Microgels and Macroporous Gels of Polyampholytes. 5. Macromolecular Complexes of Polyampholytes. 6. Polyampholytes in Biotechnology and Medicine. 7. Polyampholytes in Catalysis. 8. Application of Polyampholytes in Emerging Technologies. 9. Conclusions.

Brief Description of the Book

Polyampholytes are unique polymers containing acid/base and/or anionic/cationic groups in the main or side chains. Water-soluble and water-swelling polyampholytes exhibit properties that provide broad potential as structural biomaterials, drug delivery and chemo-mechanical systems, biosensors, energy storage devices, supercapacitors, and actuators, among others.

This book will appeal to readers who conduct materials research for biomedical, water treatment, and environmental remediation applications.

Contents

Introduction

Synthetic water-soluble polymers, with their abundance of functional groups and conformational flexibility, are prime candidates for designing active and selective catalysts that emulate enzyme functions [1]. The electrostatic interactions, hydrogen bonds, coordination bonds, and hydrophobic entrapment in polyampholytes, polyampholyte-metal complexes, and polyampholyte-metal nanoparticles serve as active and selective centers, catalyzing hydrolysis, decomposition, hydrogenation, and oxidation of various substrates [2]. Polymer-protected nanoparticles [3, 4], porous polymeric gels, surfaces of polymeric thin films/membranes [5–11], and stimuli-responsive polymers [12] are widely used as catalysts. Macroporous amphoteric cryogels, containing metal nanoparticles or enzymes in their pores, can be employed for catalytic reactions in both batch-type and continuous-flow-type reactors [5, 6]. There is significant interest in heterogeneous catalytic hydrogenation of various substrates in continuous-flow reactors [13–16] and the immobilization of enzymes within three-dimensional polymers for use as "green" catalysts [17–20]. These flow-through reactors are catalytically several orders of magnitude more efficient and can be used continuously over long periods. A precise combination of enzymes, mono- and bimetallic nanoparticles within nano-, micro-, and macro-sized polymeric gels, cryogels, and membranes can create synergistic effects in flow-through catalytic reactions.

Catalysis by Polyampholytes

The hydrolysis of the positively charged ester 3-acetoxy-N-trimethylaniline iodide (ATMAI), the negatively charged ester 3-nitro-4-acetoxybenzoic acid (NABA), and the neutral ester *p*-nitrophenylacetate (PNPA) was catalyzed by 4(5)-vinylimidazole-co-acrylic acid (VI-*co*-AA) and 4(5)-vinylimidazole-*co*-maleic acid (VI-*co*-MA) copolymers in a 28.5 vol.% ethanol–water mixture [21]. The results were compared with those obtained using monomeric analogs, specifically imidazole and γ-4(5)-imidazolebutyric acid. For the solvolysis of ATMAI, the catalytic activities of the monomeric and polymeric catalysts increased in the following order: VI-co-MA > VI-co-AA > γ-4(5)-imidazolebutyric acid > imidazole. The strongest catalytic effect was observed with a copolymer containing 42–50 mol.% of imidazole units, attributed to the optimal isolation of acid–base sequences. (Figure 1).

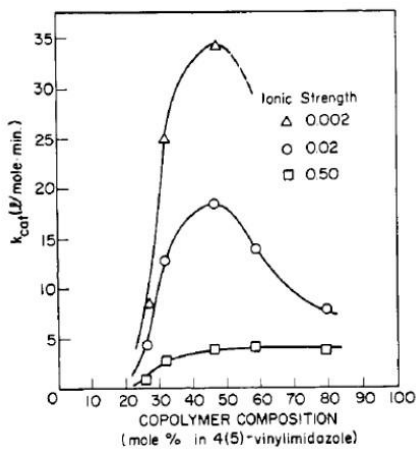

Figure 1. Effects of VI-*co*-AA composition and ionic strength on k_{cat}-catalyzed solvolysis of ATMAI. Solvent, 28.5 % ethanol–water; pH, 9.0; T, 25 °C.
Reprinted with permission from Ref. [21] (Overberger C. G., Maki H. Esterolytic catalysis by copolymers containing imidazole and carboxyl functions. *Macromolecules* 1970, 3, 214–220. Copyright 1970, American Chemical Society)

However, substituting acrylic acid with vinylsulfonic acid significantly reduces the hydrolytic activity of polyampholytes. This decrease is likely due to the high ionization degree of sulfonic acid, which leads to the formation of strong ion pairs between imidazole and sulfonic groups, compared to the weaker interactions with carboxylic groups. The proposed mechanism for ATMAI hydrolysis involves electrostatic interactions between carboxylate anions and the positively charged parts of the substrate, while imidazole molecules attack the ester groups. The catalytic activity of alternating VI-*co*-MA and statistical VI-*co*-AA equimolar polyampholytes was studied in the hydrolysis of *p*-NPA, ATMAI, and NABA. For the alternating copolymer at pH > 9.0, the hydrolysis reaction rate decreases in the following order: NABA > *p*-NPA > ATMAI. In contrast, for the statistical polyampholyte, this order is reversed. The difference in catalytic activity between these copolymers is attributed to the varying pKa values of the carboxylic groups.

The authors of [22–27] used phenylimidazole–acrylic acid (PI-AA), phenylimidazole–methacrylic acid (PI-MAA), and phenylimidazole–N-vinylpyrrolidone (PI-NVP) as polymer catalysts with ATMAI as the substrate. Kinetic analysis indicates that the substrate-binding affinity of the copolymers increases in the order PI-NVP > PI-MAA > PI-AA, which correlates with the hydrophobicity of the comonomers in the order NVP > MAA > AA. ATMAI molecules are bound to PI-NVP primarily through hydrophobic interactions. The PI-AA catalyst interacts with the substrate via both hydrophobic interactions (through PI units) and electrostatic forces (through carboxylate anions). The complex formation between PI-MAA and ATMAI involves contributions from both hydrophobic groups (PI and α-methyl groups of MAA) and electrostatic interactions. The rate of hydrolysis of cationic esters with the general formula S_n^+ in the presence of 5(6)-vinylimidazole and acrylic acid in 40:60 vol.% propanol–water mixtures decreases in the order $S_2^+ > S_7^+ > S_{12}^+ > S_{18}^+$. Once again, copolymers containing 45–55 mol.% of imidazole units exhibit the highest catalytic activity. Substrate molecules with long acyl groups are less efficiently catalyzed due to steric hindrance. However, when the reaction is conducted in a methanol–water (40:60 vol.%) mixture, the opposite effect is observed. Thus, with the catalytic activity of the copolymers increasing as the length of the substrate molecules grows.

Modified polyacrylamide-based amphoteric cryogels were tested as catalytically active substances in transesterification of glyceryl oleate [28]. The highest conversion of glyceride was equal to 88.4 %, and the yield of methyl oleate is about 64 %.

Thus, synthetic polyampholytes actively participate in the hydrolysis of negatively charged, positively charged, and neutral esters, similar to histidine-containing proteins in living organisms. However, when metal ions are coordinated with acid-base groups, the catalytic properties of polyampholyte-metal complexes are significantly enhanced, enabling hydrogen decomposition (catalase-like activity), hydrogenation, oxidation, and isomerization of various substrates. The following subchapter describes the catalysis by polyampholyte-metal complexes.

Catalysis by Polyampholyte-Metal Complexes

Catalysis by polyampholyte-metal complexes typically occurs through the formation of coordination bonds between metal ions and substrate molecules, followed by the creation of intermediate mixed complexes [29]. Polyampholyte-metal (Cu^{2+}, Co^{2+}, Mn^{2+}, Ag^+) complexes were used as catalysts for decomposition of hydrogen peroxide (H_2O_2) [30, 31]. Neither polyampholytes alone nor metal ions exhibit catalytic activity on their own. However, polyampholyte-metal complexes significantly accelerate hydrogen peroxide decomposition, following the Michaelis-Menten kinetic model. Activation of H_2O_2 by polyampholyte-metal complexes was successfully used for the degradation of azo dyes [32].

A palladium complex of poly(4-vinylpyridine-*co*-acrylic acid) (4VP-*co*-AA) was prepared and used for hydrogenation of aromatic nitro compounds, in particular, nitrobenzene, 2-, 3-, and 4-nitroanailines; 2-, 3- and 4-nitrophenols; 2-, 3- and 4-nitroanisols; and 4-nitrobenzaldehyde to corresponding aniline compounds (Figure 2) [33].

The initial hydrogenation rate for all *p*-substituted nitrobenzenes increases in the order *p*-OH > *p*-OCH_3 > > H > *p*-NH_2 > *p*-CHO demonstrating especially good catalytic activity for the hydrogenation of nitrophenols and nitroanisoles. The comparison of hydrogenation rate of different isomers of nitroaniline gives an order of *p*- > *o*- > *m*-substituted nitrobenzenes. The 4VP-co-AA/Pd complex exhibits high stability, sustaining 4-5 cycles of hydrogenation for *p*-nitrobenzene and 4-nitroanisole, with yields 100 % of aniline and 98.8 % of 4-methoxyaniline respectively.

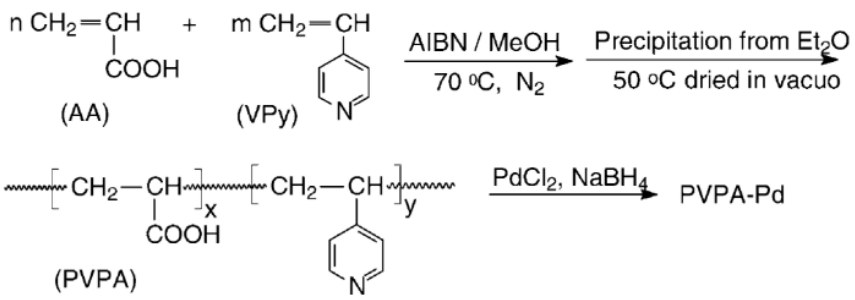

Figure 2. Preparation of poly(4-vinylpyridine-*co*-acrylic acid) copolymer (PVPA) and its palladium complex. Reproduced with permission from Ref. [33]

Raj et al. [34] developed a tunable organic−inorganic hybrid catalyst consisting of a (poly-N,N-diallyl-N-hexylamine-*alt*-maleic acid) and phosphotungstic acid ($H_3PW_{12}O_{40}$) forming polyoxometalate (POM) supramolecular structures (Figure 3).

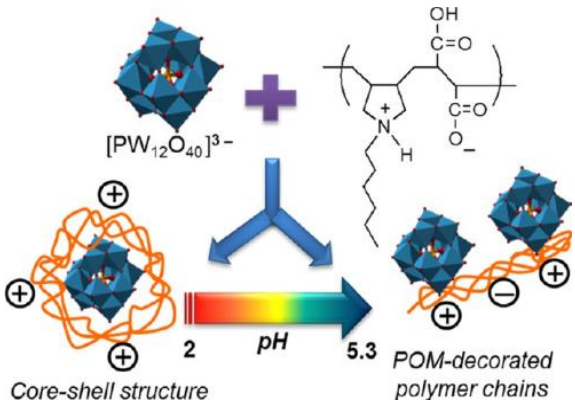

Figure 3. Stabilization of $[PW_{12}O_{40}]^{3-}$ by (poly-N,N-diallyl-N-hexylamine-*alt*-maleic acid) and formation of pH dependent core-shell structure and POM-decorated polymer chains. Reproduced with permission from Ref. [34] (Raj G., Swalus C., Guillet R.A., Devillers M., Nysten B., Gaigneaux E.M. Supramolecular organization in organic–inorganic heterogeneous hybrid catalysts formed from polyoxometalate and poly(ampholyte) polymer. *Langmuir* 2013, 29, 4388−4395. Copyright 2023, American Chemical Society)

The supramolecular organization is driven by electrostatic interactions between the positively charged polyampholyte and anionic POM. Given POM's large size and charge, POM entities are encapsulated by the polymer chains. By tuning the supramolecular assembly of these organic-inorganic hybrids, one can control the catalytic properties of POM heterogeneous catalysts in various chemical transformations. Patent literature [35] also details the use of palladium and platinum nanoparticles stabilized by polymeric carbo-, sulfo-, and phosphobetaines as fuel cell catalysts.

Transforming of metal ions coordinated with the functional groups of polyampholytes into metal nanoparticles is effective tool for creating active, selective, and stable catalysts, particularly because most catalytic reactions occur under mild conditions. In this process, the role of functional polymers is to stabilize the nanoparticles and protect them from aggregation.

Polyampholyte-Protected Metal Nanoparticles in Catalysis

Incorporating noble and transition metal ions into amphoteric nano-, microgels, and macroporous gels as templates during reduction opens new avenues for developing effective catalytic systems [36, 27]. From the relevant literature, it is well known that both hydrogels and cryogels of amphoteric nature can be used for the immobilization of metal nanoparticles [5, 6, 37]. Different shaped gold nanoparticles, i.e., triangular, hexagonal, spherical and rod-like particles in the range of 3–10 μm, can be immobilized within the amphoteric hydrogels and cryogels and distributed at the surface and inner parts of micro- and macropores (40–100 μm). For example, the microgels of poly2-(methacryloyloxy) ethyl] dimethyl (3-sulfopropyl) ammonium hydroxide p(SBMA) containing Ni nanoparticles catalyze the hydrogenation 4-nitrophenol (4-NP),

2-nitrophenol (2-NP), and 4-nitroaniline (4-NA) to corresponding aminophenols [38]. Hereby, the reduction process was monitored by measuring the decrease of the absorption peaks at 414 nm, 400 nm, and 380 nm for 2-NP, 4-NP, and 4-NA, respectively. The activation energy of the hydrogenation of 4-NP and thermodynamic parameters, i.e., enthalpy, entropy, and Gibbs energy were calculated. The cyclic tests for the prepared p(SBMA)-Ni composites were carried out for the reduction of 4-NP. The catalytic activity of p(SBMA)-Ni was decreased to 37 % after the first cycle, and to 10 % after the third cycle. This decrease can be related to structural composite breakdown under release of Ni nanoparticles.

Gold nanoparticles (AuNPs) protected by sulfonated cardo poly(arylene ether sulfone) SPES (abbreviated as Au@SPES) were obtained in the presence of $NaBH_4$ as a reducing agent [39]. The SPES-modified gold nanoparticles were stable at pH between 2 and 14. The TEM micrographs show well-dispersed AuNPs smaller than 4 nm with a relatively narrow size distribution. It is in good agreement with the average AuNPs particles (4.2 nm) determined from the Scherrer equation. The Au@SPES was used as recyclable catalyst in the aerobic oxidation of 1-phenylethan-1-ol (Table 1).

Table 1

Oxidation of 1-phenylethan-1-ol to acetophenone by Au@SPES

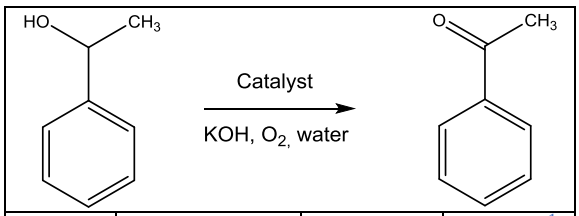

Entry	Catalyst	Yield, %[a]	TOF, h^{-1}
1	SPES	0	0
2	AuNPs	25	5
3[b]	Au@SPES	84	16.8
4[c]	Au@SPES	83	16.6
5[d]	Au@SPES	84	16.8

The oxidation reaction takes places in an aqueous solution in mild conditions in the presence of 1 mol.% of Au@SPES and KOH. However, it does not occur with the SPES and only 25 % conversion is observed in the presence of AuNPs (Table 1, entries 1,2). The oxidation of 1-phenylethan-1-ol to acetophenone occurs quantitatively (99 %) maintaining six runs. The Au@SPES precipitates near the isoelectric point (IEP) of the SPES that is convenient to separate and reuse the catalyst.

Macroporous amphoteric cryogels containing metal nanoparticles in pores can be used for catalytic reactions as batch-type and continuous-flow-type reactors [40–45] (Figure 4).

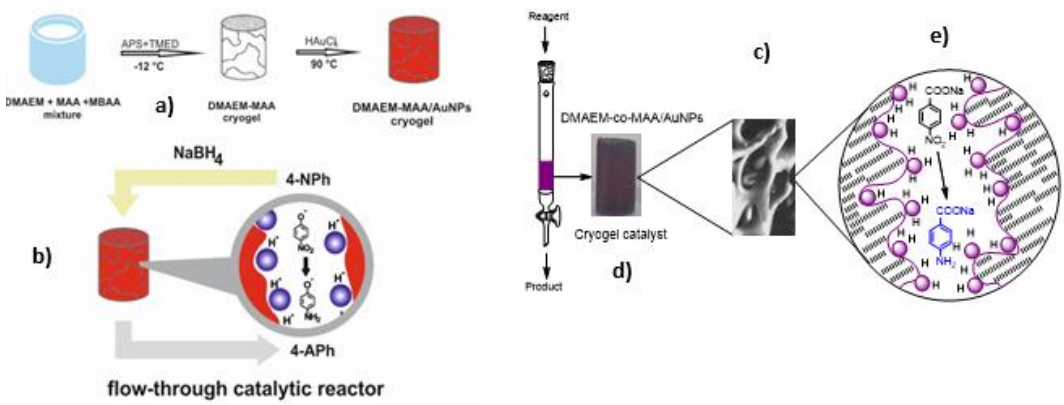

Figure 4. Fabrication of macroporous amphoteric cryogel based on N,N-dimethylaminoethylmetacrylate and methacrylic acid (DMAEM-*co*-MAA) with immobilized AuNPs (*a*) and schematic representation of monolith flow-through catalytic reactor used for hydrogenation of 4-NP (*b*) and *p*-NBA (*c*) over DMAEM-*co*-MAA/AuNPs catalysts. The violet colored sample corresponds to macroporous cryogel DMAEM-*co*-MAA containing AuNPs (*d*) while the violet dots are schematic image of AuNPs (*e*) in cryogel pores. Reproduced with permission from Refs. [42, 44]

Amphoteric cryogel DMAEM-*co*-MAA under heating conditions effectively reduces rhodium, palladium, gold and silver ions and forms fine well-dispersed metal nanoparticles [46]. The DMAEM-*co*-MAA cryogel containing the AuNPs was used as a flow-through catalytic reactor in hydrogenation of 4-nitrophenol (4-NP) and oxidation of D,L-dithiotreitol (DTT) [43]. The DTT forms a stable six-membered ring with an internal disulfide bond once oxidized. The hydrogenation and oxidation products of 4-NP and DTT are 4-aminophenol (4-AP) and disulfide (DS) respectively. The activation energy (E_a), turnover number (TON), turnover frequency (TOF) of hydrogenation and oxidation reactions are presented in Table 2.

Table 2

The activation energy (E_a), TON and TOF at hydrogenation of 4-NP and oxidation of DTT over macroporous DMAEM-*co*-MAA/AuNPs flow-through catalytic reactor

Macroporous flow-through catalyst	Substrate	E_a, kJ·mol^{-1}	TON	TOF, h^{-1}	Run	Ref.
DMAEM-*co*-MAA/AuNPs	4-NP	7.52	38.17	21.56	50	[42]
	DTT	–	985.2	412.2	10	[43]

The catalytic reduction of *p*-nitrobenzoic acid (*p*-NBA) by palladium (PdNPs) and gold nanoparticles (AuNPs) immobilized within DMAEM-*co*-MAA cryogel matrix was also carried out [47]. It should be noted that the DMAEM-*co*-MAA cryogel itself does not produce *p*-aminobenzoic acid (*p*-ABA). The products of hydrogenation of *p*-NBA over DMAEM-co-MAA/AuNPs catalyst are: 1) *p*-ABA, 2) *p,p'*-azodibenzoate and 3) sodium 4-(4-aminobenzamido)benzoate (Figure 5).

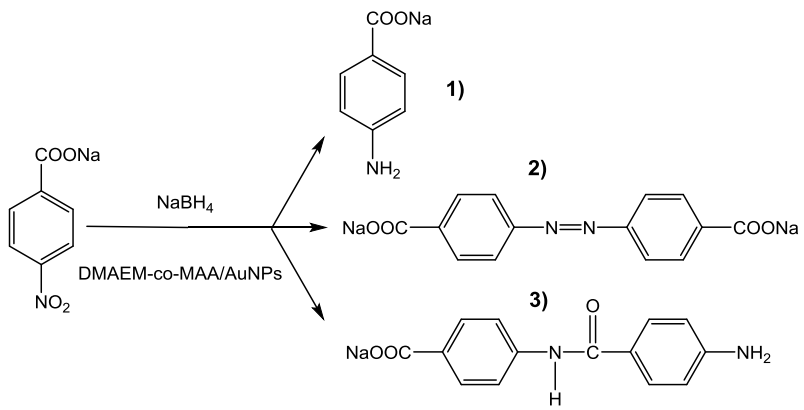

Figure 5. Hydrogenation products of *p*-nitrobenzoic acid sodium salt over DMAEM-co-MAA/AuNPs catalyst. 1) *p*-aminobenzoic acid sodium salt; 2) *p,p*'-azodibenzoate; 3) sodium 4-(4-aminobenzamido)benzoate. Reproduced with permission from Ref. [46]

In case of P(DMAEM-*co*-MAA)/PdNPs the formation of only *p*-ABA with conversion degree 40 % at [*p*-NBA]:[$NaBH_4$] = 1:50 mol/mol and 100 % at [*p*-NBA]:[$NaBH_4$] = 1:200 mol/mol is observed.

Catalytic Properties of Catalase Immobilized within Polyampholyte Cryogels

Special interest may represent physical (adsorption, encapsulation, entrapment) and chemical (covalent attachment, crosslinking) immobilization of enzymes within macroporous gel matrix for obtaining a new generation of flow-through biocatalysts that may have significant potential in biotechnology, fine chemical, food and pharmaceutical industries [47, 48]. The advantages and drawbacks of cryogel-based flow-through catalytic reactor were outlined in [6].

The efficiency of amphoteric catalase encapsulated within amphoteric cryogel matrix in oxidation of ethanol, *iso*-propanol and *n*-butanol by hydrogen peroxide, oxygen and air in batch and flow-through reactor was compared (Figure 6) [49, 50].

The micron-sized cryogel samples (from 10 to 50 μm) provided a free flow of aliphatic alcohol-hydrogen peroxide mixture under the gravity and hydrostatic pressure. The oxidized products of ethanol, isopropanol and *n*-butanol are acetaldehyde, acetone and butyraldehyde with the yields of 97, 87.6 and 80 %, respectively. The optimal conditions for oxidation of aliphatic alcohols are: pH ~ 6.4, temperature range 5–20 °C and volume ratio of substrate to reducing agent 1:1.

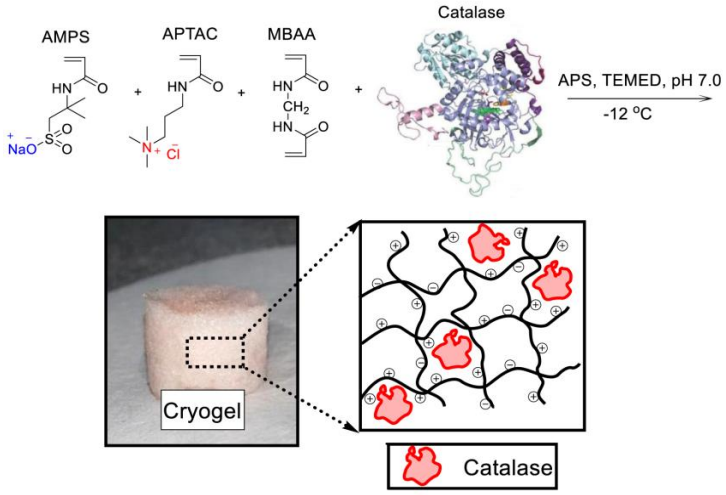

Figure 6. Synthetic protocol of encapsulation of catalase within APTAC-AMPS amphoteric cryogel matrix. Reproduced with permission from Refs. [49, 50]

The batch type reactor was also applied for the oxidation of ethanol by catalase embedded into a polyampholytic cryogel matrix using the hydrogen peroxide, molecular oxygen and air as oxidants [50]. The conversion degree of ethanol to acetaldehyde was equal to ~ 97–98 %.

The reusability of cryogel-entrapped catalase in batch reactor was evaluated. It was found that the conversion degree of ethanol to acetaldehyde insignificantly decreases over successive five runs, and after the fifth runs becomes 57.3 %. The calculated TON and TOF values for oxidation of ethanol by hydrogen peroxide, oxygen and air in the presence of monolith and powder cryogels are represented in Table 3.

Table 3

The values of TON and TOF calculated for oxidation of ethanol [50]

Oxidant	H_2O_2		O_2		Air	
	monolith	powder	monolith	powder	monolith	powder
$TON \cdot 10^{-7}$ [a)]	18.3	17.9	18.4	18.2	11.3	11.4
$TOF \cdot 10^{-7}$ [b)]	0.6	0.6	0.6	0.6	0.4	0.4
Notes: [a)] TON is in mol of product/(mol Cat); [b)] TOF is in mol of product/(mol Cat·min).						

The TOF value for the flow-through catalytic reactor was six times greater than that of the batch laboratory reactor. The successive oxidation of the isopropanol-hydrogen peroxide mixture resulted in a reduced yield of acetone, likely caused by the collapse of the cryogel matrix. The results of SEM confirmed that the shrinking of cryogel pores in water-organic solvent mixtures reduced the volume of cryogel samples, leading to a decreased flow rate and contact time. UV-Vis spectroscopy revealed that catalase remained within the cryogel matrix without any signs of leaching. After ten cycles of alcohol oxidation, the initial morphology of the cryogel-encapsulated catalase was completely altered. This change is probably due to the oxidative degradation of the cryogel matrix's internal structure by oxygen atoms and/or hydroxyl radicals produced during the hydrogen peroxide decomposition by catalase.

Thus, both monolith and powder cryogels containing the catalase are suitable for the oxidation of aliphatic alcohols into their corresponding carbonyl compounds. The advantages of enzyme-entrapped cryogel samples include the minimal volume of catalyst needed, a high surface-to-volume ratio, high selectivity, increased productivity, energy savings, and adherence to “green chemistry” principles. However, the primary drawback of cryogel microreactors is their weak mechanical properties. A significant issue is the chemical degradation of the cryogel matrix and the leaching of the enzyme from the 3D network, which can lead to contamination of the final products. This problem can be mitigated through the covalent immobilization of enzymes within the cryogel matrix.

Polyampholyte-Based Photocatalytic Systems

Recently new-generation catalysts for water splitting are being developed in combination with light harvesters or photosensitizers [51–53]. One example is entrapping of supramolecular light harvesting assemblies (perylene monoimide (PMI)-based-chromophore) for photocatalytic production of hydrogen within polyampholyte hydrogels [54] (Figure 7).

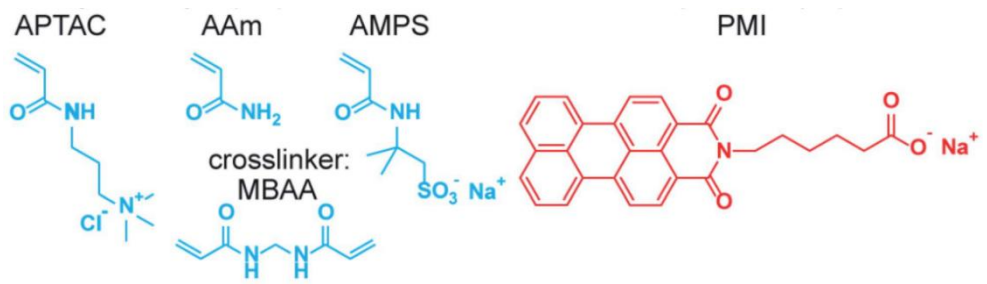

Figure 7. Anionic (AMPS), cationic (APTAC), neutral (AAm) monomers, crosslinker (MBAA) and perylene monoimide (PMI)-based-chromophore used for synthesis of polyampholyte hydrogel. Reproduced with permission from Ref. [54]

Hybrid hydrogels made from PMI and polyampholyte were assessed for their ability to perform photocatalytic proton reduction. When exposed to light, these hydrogels, containing the thiomolybdate catalyst $Na_2[Mo_3S_{13}]$ in an ascorbic acid solution at pH 4, successfully produced hydrogen. Initial experiments indicated that these systems could be reused for multiple photocatalysis cycles after refreshing the small molecule components. Another example is poly(dehydroalanine)-based (PDha) amphoteric hydrogels containing Pt nanoparticles (PtNPs), a thiomolybdate catalyst ($[Mo_3S_{13}]^{2-}$), or a cobalt polyoxometalate catalyst ($Co_4POM = [Co_4(H_2O)_2(PW_9O_{34})_2]^{10-}$) and $[Ru(bpy)_3]^{2+}$ which were applied as reusable heterogeneous catalysts for hydrogen evolution (HER) and oxygen evolution reactions (OER) when irradiated under visible light [55, 56]. Formation of hybrid [Ru]@PtNPs@PDha hydrogel and photocatalytic hydrogen evolution reaction carried out in a polymer network is schematically shown in Figure 8.

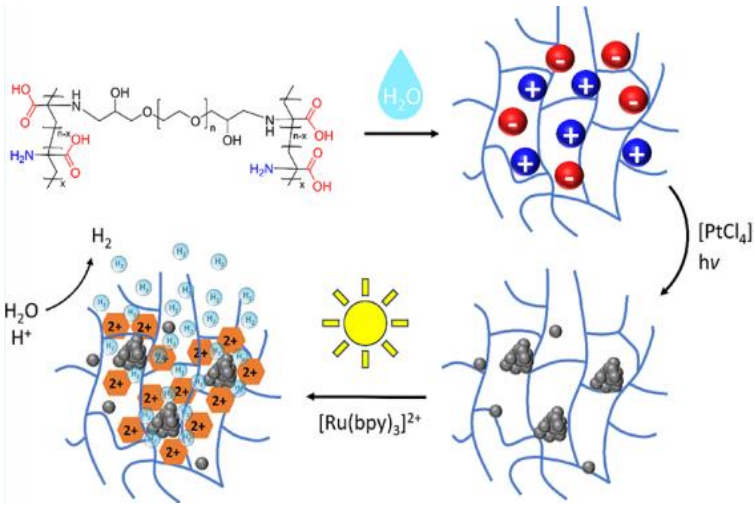

Figure 8. Electrostatic attachment of $[Ru(bpy)_3]_{2+}$ within the PDha-based amphoteric hydrogel, in situ formation of PtNPs and the photocatalytic hydrogen evolution reaction carried out in a polymer network. Reproduced with permision from Ref. [55]

PtNPs can reduce protons and produce hydrogen under visible light if combined with a suitable photosensitizer $[Ru(bpy)_3]_{2+}$. The catalytic activity of [Ru]@PtNPs@PDha for H_2 evolution by visible light irradiation resulted in a H_2 production rate of 28.5 μmol· g^{-1}·h^{-1}. For $[Ru(bpy)_3]_{2+}$/PtNPs molar ratios of 80, 8, and 0.8 the measured TON was equal to 350, 80, and 52, respectively. This work shows a straightforward approach to hybrid hydrogels for light-driven catalysis, although the presented approach is still prone to photodegradation and leaching depending on the choice of catalyst or photosensitizer.

The creation of core-shell hybrid materials with a TiO_2 core and a shell of polyampholytic poly(dehydroalanine)-*g*-(*n*-propylphosphonic acid acrylamide) (PDha-*g*-PAA@TiO_2) enabled effective immobilization of the photosensitizer Eosin Y (EY) and facilitated electronic interactions between EY and the TiO_2 core [57]. This configuration resulted in significant H_2 generation under visible light. The improved light-driven catalytic activity is credited to the unique core-shell design, where the graft copolymer serves as a bridge, facilitating electron and proton transfer while also preventing EY degradation. Further catalytic enhancement of PDha-*g*-PAA@TiO_2 was achieved by introducing $[Mo_3S_{13}]^{2-}$ cluster anions as a hydrogen-evolution cocatalyst (Figure 9).

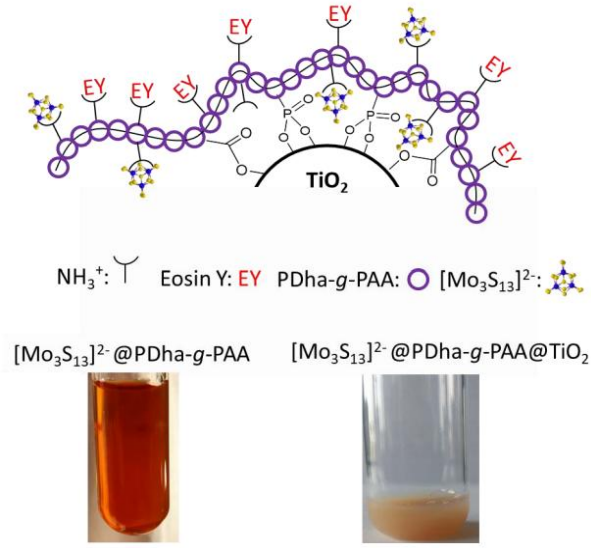

Figure 9. Schematic illustration of proposed interactions between PDha-*g*-PAA and TiO_2, Eosin Y, and $[Mo_3S_{13}]^{2-}$. Reproduced with permision from Ref. [57]

Zwitterionic conjugated polymer is emerging class of organic photocatalyst for light-driven hydrogen production from water due to their photoactive conjugated backbones and hydrophilic ionic side chains [58]. The photocatalytic efficiency of anionic, cationic and amphoteric polyelectrolytes with the thiophene (T)-dibenzo[b,d]thiophene sulfone donor–acceptor backbone was compared. Poly(zwitterionic) photocatalyst behaves the best activity with a hydrogen evolution rate of 55.2 $mmol \cdot g^{-1} \cdot h^{-1}$ under full-arc Xe light irradiation, which is 1.4-, 1.7-, and 10-fold as compared to those of anionic and cationic precursors, respectively.

Table 4 summarizes the activation energy (E_a), turnover number (TON), and turnover frequency (TOF) values of various polyampholyte-based catalysts as reported in the literature. Notably, pure catalase [59] and catalase immobilized within the APTAC-AMPS cryogel matrix exhibit exceptionally high TON in the decomposition of hydrogen peroxide [60] and the oxidation of ethanol [50], both with negative activation energies. Thermodynamically, the negative activation energies can be attributed to the exothermic nature of these catalytic reactions [59].

The main difference between polyampholyte-metal and polyampholyte-metal nanoparticle catalysis lies in the mechanism of the catalytic reaction. In the former case, the reaction proceeds through the formation of coordination bonds between metal ions and substrate molecules, leading to the creation of intermediate mixed complexes [29]. In the latter case, catalytic reactions occur on metal nanoparticles that are immobilized within the polymer matrix. Polyampholyte-metal complexes typically involve transition metal ions such as copper, nickel, and cobalt, which have the ability to form chelate complexes. Conversely, in polyampholyte-metal nanoparticle systems, noble metal ions like silver, gold, palladium, rhodium, and platinum (in cationic or anionic complex forms) are commonly used. It should be noted, however, that polyampholyte-metal complexes can sometimes be reduced to metal nanoparticles during the hydrogenation of substrates. For example, in Ref. 29, a palladium complex of poly(4-vinylpyridine-*co*-acrylic acid) (4VP-*co*-AA) used for the hydrogenation of aromatic nitro compounds can contain both palladium ions and palladium nanoparticles.

It is evident that immobilizing enzymes within hydrogel or cryogel matrices is a promising approach for applications in both batch and flow-through catalytic reactors. Cryogels, in particular, with their tunable po-

rosity, offer an effective and versatile tool for the development of novel biotechnological and industrial applications [50]. The TON and TOF values for hydrogen generation from water using linear and crosslinked polyampholytes containing photocatalysts in the form of metal nanoparticles and photosensitizers [54–57] are lower than those observed for polyampholyte-metal complexes but higher than those for polyampholyte-metal nanoparticles. This discrepancy is likely due to the multicomponent nature of the catalytic system, the complex, multistage processes of electron and proton transfer, as well as issues related to photodegradation and catalyst leaching. In our previous study [42], we detected gradual leaching of palladium and gold nanoparticles from the surface of amphoteric cryogels during sequential hydrogenation of *p*-nitrobenzoic acid (*p*-NBA).

Table 4

The activation energy (E_a), TON, and TOF values for different types of catalysts and catalytic reactions

Catalyst	Substrate	E_a, kJ·mol^{-1}	TON, h^{-1}	TOF, h^{-1}	Ref.
4VP-*co*-AA/Pd^{2+}	*p*-nitrobenzene	–	2000	–	[33]
DMAEM-MAA/PdNPs	*p*-nitrophenol	13.8	–	–	[42]
DMAEM-MAA/AuNPs	*p*-nitrophenol	7.5	38	21.5	[42]
Catalase	H_2O_2	–14.0	$(10–15)\cdot10^{10}$	–	[60]
APTAC-AMPS/Catalase	ethanol	–7.31	$(11.4–18.4)\cdot10^{7}$	$(4–6)\cdot10^{7}$	[50]
AAm-APTAC-AMPS/PMI	H_2O	–	–	107.4	[54]
[Ru]@PtNPs@PDha	H_2O	–	50–350	–	[55, 56]
PDha-*g*-PAA@TiO_2	H_2O	–	> 500	–	[57]

Conclusions

Polyampholytes and their derivatives, including polyampholyte-metal complexes, polyampholyte-metal nanoparticles, and polyampholyte-enzyme conjugates, exhibit remarkable catalytic activity, stability, and selectivity in various chemical reactions, such as the hydrolysis of esters, hydrogenation of nitrocompounds, and oxidation of both aliphatic and aromatic alcohols. Macroporous amphoteric cryogels embedded with metal nanoparticles and enzymes have proven to be effective catalysts in both batch and continuous-flow reactor systems. Comparative analysis of activation energy, turnover number (TON), and turnover frequency (TOF) values indicates that macroporous flow-through reactors demonstrate superior efficiency over their batch-type counterparts. In the realm of photocatalysis, particularly in the context of water splitting — a crucial process for sustainable solar energy conversion — polyampholyte/polyzwitterionic hydrogels represent an advanced scaffold. These hydrogels are capable of immobilizing photosensitizer dyes and catalysts in close proximity, thereby enhancing electron transfer efficiency. Their porous structure allows for the free movement of reactants and products, which is essential for efficient hydrogen and oxygen evolution reactions. Inspired by natural photosynthesis, these innovative hydrogels are poised to play a pivotal role in advancing affordable and efficient solar energy technologies. In the near future, polyampholyte-based nanogels, microgels, and membranes containing metal ions, metal nanoparticles, enzymes, and photosensitive substances could become promising soft materials for applications in the field of catalysis.

Funding

This research was funded by the Science Committee of the Ministry of Science and Higher Education of the Republic of Kazakhstan (Grant No. AP14869287).

*Author Information**

**The authors' names are presented in the following order: First Name, Middle Name and Last Name*

Sarkyt Elekenovich Kudaibergenov — Doctor of Chemical Sciences, Director of the Institute of Polymer Materials and Technology, Microregion "Atyrau 1", Building 3/1, 050019, Almaty, Kazakhstan; *e-mail:* skudai@mai.ru; https://orcid.org/0000-0002-1166-7826

References

1 Bekturov, E.A., Kudaibergenov, S.E. (1996). Catalysis by Polymers. Heidelberg: Huthig and Wepf Verlag. https://doi.org/10.1002/9783527614677.ch1

2 Kudaibergenov, S.E. (2024). Polyampholytes in Advanced Polymer Science and Emerging Technologies. Boca Raton and London: CRS Press. https://doi.org/10.1201/9781003431404

3 Bekturov E.A., Kudaibergenov, S.E., Ibraeva, Zh.E. (2019). Polimery v nanotechnologii [Polymers in Nanotechnology]. Almaty: Center for Operational Printing.

4 Ibraeva, Zh.E., Kudaibergenov, S.E., Bekturov E.A. (2013). Stabilizatziya nanochastitz metallov gidrofilnymi polimerami [Stabilization of Metal Nanoparticles by Hydrophilic Polymers]. Saarbrücken: Lap Lambert.

5 Kudaibergenov, S.E. (2019). Physicochemical, Complexation and Catalytic Properties of Polyampholyte Cryogels. *Gels*, *5*, 8. https://doi.org/10.3390/gels5010008

6 Kudaibergenov, S.E., Dzhardimalieva, G.I. (2020). Flow-through Catalytic Reactors based on Metal Nanoparticles Immobilized within Porous Polymeric Gels and Surfaces/Hollows of Polymeric Membranes. *Polymers*, *13*, 572. https://doi.org/10.3390/polym12030572

7 Kudaibergenov, S.E., Tatykhanova, G.S., Selenova, B.S. (2016). Polymer Protected and Gel Immobilized Gold and Silver Nanoparticles in Catalysis. *J. Inorg. Organomet. Polym. Mater*. *26*, 1198–1211. https://doi.org/10.1007/s10904-016-0373-z

8 Dzhardimalieva, G.I., Zharmagambetova, A.K., Kudaibergenov, S.E., Uflyand, I.E. (2020). Polymer-Immobilized Clusters and Metal Nanoparticles in Catalysis. *Kinetics and Catalysis*, *61*, 198–223. https://dx.doi.org/10.1134/S0023158420020044

9 Kudaibergenov S.E., Tatykhanova G.S. (2013). Physico-Chemical and Catalytic Properties of Polymer-Protected and Hydrogel-Immobilized Gold, Silver and Palladium Nanoparticles. *International Journal of Biology and Chemistry*, *6*(2), 40–49. https://ijbch.kaznu.kz/index.php/kaznu/article/view/98

10 Baygazieva, E.K., Yesmurzayeva, N.N., Tatykhanova, G.S., Mun, G.A., Khutoryanskiy, V.V., Kudaibergenov, S.E. (2014). Polymer Protected Gold Nanoparticles: Synthesis, Characterization and Application in Catalysis. *International Journal of Biology and Chemistry*, *7*(1), 14–23. https://doi.org/10.26577/2218-7979-2014-7-1-14-23

11 Kudaibergenov, S., Tatykhanova, G., Bakranov, N., Tursunova, R. (2017). Layer-by-Layer Thin Films and Coatings Containing Metal Nanoparticles in Catalysis. In J. Thirumalai (Ed.). *Thin Film Processes — Artifacts on Surface Phenomena and Technological* Facets (pp. 147–164). https://doi.org/10.5772/67215

12 Dolya, N.A., Kudaibergenov, S.E. (2018). Catalysis by Thermoresponsive Polymers. In V.V. Khutroyanskiy and T.K. Georgiu (Eds.). *Temperature‐Responsive Polymers: Chemistry, Properties and Applications* (pp. 357-377). John Wiley & Sons Ltd: Hoboken, NJ, USA. https://doi.org/10.1002/9781119157830.ch15

13 Irfan, M., Glasnov, T.N, Kappe, C.O. (2011). Heterogeneous Catalytic Hydrogenation Reactions in Continuous-Flow Reactors. *ChemSusChem*, *4*, 300–316. https://doi.org/10.1002/cssc.201000354

14 Moreno-Marrodan, C., Liguori, F., Barbaro, P. (2017). Continuous-Flow Processes for the Catalytic Partial Hydrogenation Reaction of Alkynes. *Beilstein J. Org. Chem*. *13*, 734–754. https://doi.org/10.3762/bjoc.13.73

15 Masuda, K., Ichitsuka, T., Koumura, N., Sato, K., Kobayashi, S. (2018). Flow Fine Synthesis with Heterogeneous Catalysts. *Tetrahedron*, *74*(15), 1705–1730. https://doi.org/10.1016/j.tet.2018.02.006

16 Altshuler, G.N., Shkurenko, G.Yu., Gorlov, A.A. (2013). Hydrogenation of p-Nitrobenzoic Acid Esters in Nanoreactors based on Sulfonated Polymer Networks. *Butlerov Communications*, *36*(12), 105–109.

17 Demirci, S., Sahiner, N. (2021). Superporous Neutral, Anionic, and Cationic Cryogel Reactors to Improved Enzymatic Activity and Stability of α-Glucosidase Enzyme via Entrapment Method. *Chem. Eng. J. 409*, 128233. https://doi.org/10.1016/j.cej.2020.128233

18 Guajardo, N. Immobilization of Lipases using Poly(vinyl) Alcohol. *Polymers*, *15*, 2021. https://doi.org/10.3390/polym15092021

19 Stanescu, M.D., Fogorasi, M., Boris, L.B.L., Gavrilas, S., I. Lozinsky, V.I. (2010). New Potential Biocatalysts by Laccase Immobilization in PVA Cryogel Type Carrier. *Appl. Biochem. Biotechnol*. 160, 1947–1954. https://doi.org/10.1007/s12010-009-8755-0

20 Atiroglu, V., Atiroglu, At., Atiroglu, Ah., Al-Hajri, A.S., Ozacar, M. (2024). Green Immobilization: Enhancing Enzyme Stability and Reusability on Eco-friendly Support. *Food Chem*. 448, 138978. https://doi.org/10.1016/j.foodchem.2024.138978

21 Overberger, C.G., Maki, H. (1970). Esterolytic Catalysis by Copolymers Containing Imidazole and Carboxyl Functions. *Macromolecules*, *3*, 214–220. https://doi.org/10.1021/ma60014a018

22 Takeishi, M., Hara, O., Nino, S., Hayama, S. (1979). Sequence Distribution and Solvolytic Activity of Copolymers Containing Imidazole Groups. *Macromolecules*, *12*, 531–532. https://doi.org/10.1021/ma60069a038

23 Tanaka, J., Yamada, A. (1983). Hydrolysis of Phenyl Esters Catalyzed by Alternating Copolymers Containing Imidazolyl and Carboxyl Groups. *Makromol. Chem. 184*, 2041–2047. https://doi.org/10.1002/macp.1983.021841009

24 Shimidzu, T., Furuta, A., Nakamoto, Y. (1974). Catalytic Activity of Poly(4(5)-vinylimidazole-*co*-acrylic acid) in the Hydrolyses of 3-Acetoxy-N-trimethylanilinium Iodide and *p*-Nitrophenyl Acetate in Aqueous Solution. *Macromolecules*, *7*, 160–166. https://doi.org/10.1021/ma60038a003

25 Kunitake, T., Shinkai, S. (1972). Imidazole Catalysis in Aqueous Systems. VII. Enzymelike Catalytic Hydrolyses of Phenyl Esters by Copolymers Containing Imidazole and Carboxylate Functions. *Makromol. Chem. 151*, 127–138. https://doi.org/10.1002/macp.1972.021510110

26 Overberger, G.C., Podsiadli, C.J. (1974). Conformational Effects and Cooperative Interactions in Poly[5(6)-vinylbenzimidazole]-Catalyzed Solvolysis of Anionic, Long-chain Substrates. *Bioorg. Chem. 3*, 16–34. https://doi.org/10.1016/0045-2068(74)90027-3

27 Overberger, G.C., Podsiadli, C.J. (1974). Cooperative Effects Involved in Esterolytic Reactions of Cationic Chain Esters Catalyzed by Benzimidazole-containing Polymers. *Bioorg. Chem. 3*, 35–54. https://doi.org/10.1016/0045-2068(74)90028-5

28 Yang, C., Liu, G.F., Zhou, X.L., Liu, Y.R., Wang, J., Tian, L.L., Hu, X.Y., Wang, Y.Y. (2015). Polyacrylamide based Cryogels as Catalysts for Biodiesel. *Catal. Lett. 145*, 1778–1783. https://doi.org/10.1021/ie5010866

29 Tsuchida, E., Nishide, H. (1977). Polymer-Metal Complexes and Their Catalytic Activity. *Adv. Polym. Sci. 24*, 1–87. https://doi.org/10.1007/3-540-08124-0_1

30 Bekturov, E.A., Kudaibergenov, S.E., Sigitov, V.B. (1986). Complexation of Amphoteric Copolymer of 2-Methyl-5-Vinylpyridine-Acrylic Acid with Copper(II) ions and Catalase-like Activity of Polyampholyte-Metal Complexes. *Polymer 27*, 1269–1272. https://doi.org/10.1016/0032-3861(86)90017-0

31 Sigitov, V.B., Kudaibergenov, S.E., Bekturov, E.A. (1987). Complexation of Copper(II) with Polyampholyte 2-Methyl-5-Vinylpyridine-Acrylic Acid. *Koord. Khim. 13*, 600–604.

32 Lombardo Lupano, L.V., Lázaro Martínez, J.M., Piehl, L.L., de Celis, E.R., Dall' Orto, V.C. (2013). Activation of H_2O_2 and Superoxide Production using a Novel Cobalt Complex based on a Polyampholyte. *Applied Catalysis A: General, 467*, 342–354. https://doi.org/10.1016/j.apcata.2013.08.002

33 Xi, X., Liu, Y., Shi, J., Cao, S. (2003). Palladium Complex of Poly(4-Vinylpyridine-*co*-Acrylic Acid) for Homogeneous Hydrogenation of Aromatic Nitro Compounds. *Journal of Molecular Catalysis A: Chemical*, *192*, 1–7. https://doi.org/10.1016/S131-1169(02)00327-8

34 Raj, G., Swalus, C., Guillet, R.A., Devillers, M., Nysten, B., Gaigneaux, E. M. (2013). Supramolecular Organization in Organic–Inorganic Heterogeneous Hybrid Catalysts formed from Polyoxometalate and Poly(ampholyte) Polymer. *Langmuir*, *29*, 4388−4395. https://doi.org/10.1021/la400055t

35 Bonsel H., Deckers G., Frank G., Millauer H., Soczka-Gut T. (2002). Polybetaine-stabilized Platinum Nanoparticles, Method of their Production for Fuel Cell Catalysts. *US Patent* No. 6,391,818. 2002.

36 Campo Dall' Orto, V., Lazaro-Martinez, J.M. (2016). Design, Characterization and Environmental Applications of Hydrogels with Metal Ion Coordination Polymers. *Emerging Concepts in Analysis and Applications of Hydrogels* (S.B. Majee, ed.), 101–130. INTECH. Rijeka, Croatia. https://doi.org/10.5772/62902

37 Kudaibergenov, S.E., Nuraje, N., Khutoryanskiy, V.V. (2012). Amphoteric Nano-, Micro-, and Macrogels, Membranes, and Thin Films. *Soft Matter*, *8*, 9302–9321. https://doi.org/10.1039/C2SM25766A

38 Ajmal, M., Demirci, S., Siddiq, M., Aktas, N., Sahiner, N. (2015). Betaine Microgel Preparation from 2-(Methacryloyloxy)ethyl]dimethyl (3-sulfopropyl) Ammonium Hydroxide and Its Use as a Catalyst System. *Colloids and Surfaces A: Physicochem. Eng. Aspects*, *486*, 29–37. https://doi.org/10.1016/j.colsurfa.2015.09.028

39 Li, S., Wu, Y., Wang, J., Zhang, Q., Kou, Y., Zhang, S. (2010). Double-Responsive Polyampholyte as a Nanoparticle Stabilizer: Application to Reversible Dispersion of Gold Nanoparticles. *J. Mater. Chem. 20*, 4379–4384. https://doi.org/10.1039/C0JM00255K

40 Kudaibergenov, S., Adilov, Zh., Berillo, D., Tatykhanova, G., Sadakbaeva, Zh., Abdullin, Kh., Galaev, I. (2012). Novel Macroporous Amphoteric Gels: Preparation and Characterization. *eXPRESS Polymer Letters. 6*(5) 346–353. https://doi.org/10.3144/expresspolymlett.2012.38

41 Tatykhanova, G., Sadakbayeva, Zh., Berillo, D., Galaev, I., Abdullin, Kh., Adilov, Zh., Kudaibergenov, S. (2012). Metal Complexes of Amphoteric Cryogels based on Allylamine and Methacrylic Acid. *Macromol. Symp. 317-318*, 7–17. https://doi.org/10.1002/masy.201100075

42 Klivenko, A.N., Tatykhanova, G.S., Nuraje, N., Kudaibergenov, S. (2015). Hydrogenation of *p*-Nitrophenol by Gold Nanoparticles Immobilized within Macroporous Amphoteric Cryogel based on N,N-Dimethylaminoethylmethacrylate and Methacrylic acid. *Bulletin of Karaganda University, Ser. Chem*. *4*(80), 10-15.

43 Klivenko, A.N., Yergazieva, E., Kudaibergenov, S.E. (2016). Gold Nanoparticles Stabilized by Amphoteric Cryogel — Perspective Flow-through Catalytic Reactor for Oxidation and Reduction Processes. *International Conference on Nanomaterials: Application & Properties (NAP)*, 02NSA03-1-02NSA03-5, https://doi.org/10.1109/NAP.2016.7757304

44 Tatykhanova, G.S., Klivenko, A.N., Kudaibergenova, G.M., Kudaibergenov, S.E. (2016). Flow-through Catalytic Reactor based on Amphoteric Cryogels and Gold Nanoparticles. *Macromol. Symp. 363*, 49–56. https://doi.org/10.1002/masy.201500137

45 Aldabergenov, M., Dauletbekova, M., Shakhvorostov, A., Toleutay, G., Klivenko, A., Kudaibergenov, S. (2018). Hydrogenation of Nitroaromatic Compounds by Gold Nanoparticles Immobilized within Macroporous Amphoteric Cryogels in Aqueous Solutions. *J. Chem. Technol. Metal*. *53*, 17–26.

46 Kudaibergenov, S., Dauletbekova, M., Toleutay, G., Kabdrakhmanova, S., Seilkhanov, T., Abdullin, Kh. (2018). Hydrogenation of *p*-Nitrobenzoic Acid by Gold and Palladium Nanoparticles Immobilized within Macroporous Amphoteric Cryogels in Aqueous Solution. *J. Inorg. Organomet. Polym. 28*, 2427–2438, https://doi.org/10.1007/s10904-018-0930-8.ee

47 Imam, H.T, Marr, P.C., Marr, A.C. (2021). Enzyme Entrapment, Biocatalyst Immobilization without Covalent Attachment. *Green Chem. 23*, 4980. https://doi.org/10.1039/d1gc01852c

48 Altunbas, C., Aslan, A., Kusat, K., Sahiner, M., Akgöl, S., Sahiner, N. (2022). Synthesis and Characterization of a New Cryogel Matrix for Covalent Immobilization of Catalase. *Gels 8*, 501. https://doi.org/10.3390/gels8080501

49 Smagulova, I., Tatykhanova, G., Shakhvorostov, A., Akbayeva, D., Kudaibergenov, S. (2021). Oxidation of iso-ropanol and n-Butanol by Catalase encapsulated within Macroporous Polyampholyte Cryogel Matrix. *Polym. Adv. Technol*. *32*, 3817–3826. https://doi.org/10.1002/pat.5396

50 Akbayeva, D.N., Smagulova, I.A., Maksotova, K.S., Bakirova, B.S., Tatykhanova, G.S., Kudaibergenov, S.E. (2023). In situ Entrapment of Catalase within Macroporous Cryogel Matrix for Ethanol Oxidation: Flow-through Mode versus Batch Reactor. *Catalysts 13*, 1075. https://doi.org/10.3390/catal13071075

51 Nuraje, N., Asmatulu, R., Kudaibergenov, S. (2012). Metal Oxide-based Nanomaterials for Solar Energy Conversion: A Review. *Current Inorganic Chemistry 2*, 124–146.

52 Afroz, K., Moniruddin, M., Bakranov, N., Kudaibergenov, S., Nuraje, N. (2018). A Heterojunction Strategy to Improve the Visible Light Sensitive Water Splitting Performance of Photocatalytic Materials. *Journal of Materials Chemistry A. 6*(44), 21696–21718. https://doi.org/10.1039/C8TA04165B

53 Weingarten, A.S., Kazantsev, R.V., Palmer, L.C., McClendon, M., Koltonow, A.R., Samuel, A.P.S., Kiebala, D.J., Wasielewski, M.R., Stupp, S. I. (2014). Self-assembling Hydrogel Scaffolds for Photocatalytic Hydrogen Production. *Nature Chemistry 6*, 964–970. https://doi.org/10.1038/nchem.2075

54 Sai, H., Erbas, A., Dannenhoff er, A., Huang, D., Weingarten, A., Siismets, E., Jang, K., Qu, K., Palmer, L.C., de la Cruz, M.O., Stupp, S.I. (2020). Chromophore Amphiphile — Polyelectrolyte Hybrid Hydrogels for Photocatalytic Hydrogen Production. *J. Mater. Chem. A 8*, 158–168. https://doi.org/10.1039/c9ta08974h

55 Çeper, T., Nabiyan, A., Neumann, C., Turchanin, A., Schacher, F.H. (2023). Visible-Light-Driven Hydrogen Evolution of PtNP/$[Ru(bpy)_3]^{2+}$/Polyampholyte Hybrid Hydrogels. *ACS Appl. Polym. Mater*. https://doi.org/10.1021/acsapm.3c01051

56 Çeper, T., Langer, M., Vashistha, N., Dietzek-Ivansic, B., Streb, C., Rau, S., Schacher, F.H. (2024). Poly(dehydroalanine)-based Hydrogels as Efficient Soft Matter Matrices for Light-driven Catalysis. *Macromol. Rapid Commun*. https://doi.org/10.1002/marc.202300448

57 Nabiyan, A., Neumann, C., Heiland, M., Turchanin, A., Streb, C., Schacher, F.H. (2021). Polyampholytic Graft Copolymers as Matrix for TiO_2/Eosin Y/$[Mo_3S_{13}]^{2-}$ Hybrid Materials and Light-driven Catalysis. *Chem. Eur. J. 27*, 16924–16929. https://doi.org/10.1002/chem.202100091

58 Li, Q., Li, K-H., Liu, L-N., Xue, Z-X., Xu, Z-W., Li, W-S. (2023). Conjugated Polyelectrolyte Photocatalysts: The Use of Zwitterionic Side Groups for High Performance. *ACS Appl. Polym. Mater*. *5*(10), 8570–8578. https://doi.org/10.1021/acsapm.3c01665

59 Trawczynska, I. (2020). New Method of Determining Kinetic Parameters for Decomposition of Hydrogen Peroxide by Catalase. Catalysts, *10*, 323. https://doi.org/10.3390/catal10030323

60 Smejkal, G., Kakumani S. (2019). Enzymes and Their Turnover Numbers. *Expert Review on Proteomics*, *16*, 543–544. https://doi.org/10.1080/14789450.2019.1630275

How to Cite: Bayeshov, A., Bayeshova, A.K. & Turlybekova, M.N. (2024) Catalytic Effect of Titanium Ions on the Cathodic Reduction of Selenium (VI), Copper (II), Uranium (VI) Ions and Other Metals in an Aqueous Solutions. *Eurasian Journal of Chemistry, 29, 3(115), 55-64.* https://doi.org/10.31489/2959-0663/3-24-13

Article

Received: 28 June 2024 | Revised: 22 August 2024 |
Accepted: 9 September 2024 | Published online: 23 September 2024

UDC 544.6.476

https://doi.org/10.31489/2959-0663/3-24-13

Abduali Bayeshov, Azhar K. Bayeshova*, Makpal N. Turlybekova

Center of Physico-Chemical Methods of Research and Analysis, Al-Farabi Kazakh National University, Almaty, Kazakhstan
*(*Corresponding author's e-mail: azhar_b@bk.ru)*

Catalytic Effect of Titanium Ions on the Cathodic Reduction of Selenium (VI), Copper (II), Uranium (VI) Ions and Other Metals in an Aqueous Solutions

It is known that catalytic processes are widely applied in the field of organic chemistry; however they also play a significant role in inorganic chemistry. Nonetheless, numerous unresolved issues persist in the technology of inorganic substances and the extraction of metals and nonmetals in their elemental states. This publication aims to consolidate the results of our pioneering research utilizing the redox Ti (IV)–Ti (III) system, which demonstrates a catalytic action on the cathodic reduction of selenium (VI), copper (II), platinum (IV), palladium (IV), bismuth, arsenic (V) ions, uranium (VI), as well as manganese dioxide suspension. It has been demonstrated that in the presence of the redox Ti (IV)–Ti (III) system, hard-to-reduce selenate ions can be reduced at room temperature. The catalytic action of the redox Ti (IV)–Ti (III) system has been reliably demonstrated, and the reaction mechanism has been established. In the electrochemical production of metal powders (Cu, Pt, Pd, Bi) at cathode current densities exceeding the limiting value, a portion of the current is irreversibly lost to the discharge of hydrogen ions. Consequently, the current efficiency (CE) for powder production does not exceed 80 %. We have established that in the presence of titanium (IV) ions, due to their catalytic action, the CE increases by more than 15 %. It has also been shown that during the cathodic polarization of hexavalent uranium its reduction to uranium (IV) in the presence of the catalyst increases by more than 50 %. The reduction of hard-to-reduce arsenate ions in the presence of titanium (IV) ions proceeds with high CE to the active trivalent state, and further reduction can proceed electrochemically. The cathodic reduction of a manganese dioxide suspension was investigated. In the presence of a catalyst — titanium (IV) ions, manganese in this dioxide is reduced to the divalent state with a current efficiency exceeding 90 %.

Keywords: catalytic action, titanium (IV) ions, copper ions, uranyl ions, arsenate ions, selenate ions, manganese dioxide, metal powders.

Introduction

It is well known catalytic reactions are widely used in almost all cases of synthesis of both organic and inorganic substances. Catalysis is divided into homogeneous and heterogeneous, and catalyst can be various substances, including metals, their oxides, alloys, and other types of simple and complex substances.

A catalyst is a chemical substance that accelerates a reaction without being consumed in the process. The action of catalysts is most often explained by their ability to lower the activation energy of reactions. In the presence of a catalyst, the reaction proceeds through intermediate stages that differ from those occurring without the catalyst, and these stages are energetically more accessible [1]. Reactions involving catalysts are aimed at solving many pressing contemporary issues, including environmental problems (wastewater treatment), alternative energy, and more [2].

In the chemical industry, more than 50 % of all productions are based on the use of catalysts. The role of catalysis in organic chemistry is of great significance, particularly in the practice of typical high-volume processes for organic substances and oil refining [3], as well as in the fine organic synthesis of vitamins and pharmaceuticals [4]. Particular attention is paid to the state of catalyst particles [5]. In addition, it is well known that catalysts play an enormous role in biological systems. The majority of chemical reactions occurring in the digestive system, blood and cells of animals and humans are catalytic. Catalysts, known in this context as enzymes, are simple or complex proteins. It should be noted that the human body contains approximately 30,000 different enzymes, each of which serves as an effective catalyst for its specific reaction. Thus, catalytic processes play a huge role in many biochemical reactions, particularly in the vital functions of organisms [6–8].

We are interested in the reactions occurring in hydro electrometallurgical processes, which are of great significance in the mining, processing of mineral resources and the extraction of valuable elements from

them. In this regard, the purpose of this review is to describe the existing methods of reducing hard-to-reduce ions of certain elements and present new methods proposed by the authors using catalytic systems.

The electrochemical refining of copper-containing ores results in the production of the crude copper which contains a range of impurities, including harmful substances and valuable rare metals such as selenium and tellurium. During the dissolution of copper anodes, valuable components migrate into copper-electrolyte sludge, which serves as the primary source for extracting gold, silver, selenium and tellurium [9, 10]. During practically all methods of processing copper-electrolyte sludge, the production of hexavalent selenium and tellurium is observed, and reducing them to their elemental state presents a significant challenge.

This paper will focus on the most well-known methods for reducing hard-to-reduce chalcogen-containing anions. The reduction of selenium (VI) in alkaline solutions is only possible at temperatures above 200 °C in an autoclave and requires the use of strong reducing agents such as hydrogen, sulfides and elemental sulfur or organic reagents [11]. The reduction of selenate and tellurate ions in concentrated hydrochloric acid solutions at boiling, [12, 13] point results in the formation of only the tetravalent state:

$$H_2XO_4 + 2HCl \xrightarrow{t\ boil} H_2XO_3 + Cl_2 + H_2O \quad (1)$$

Subsequently the compounds are reduced to their elemental state by the action of sulfur dioxide:

$$H_2XO_3 + 2SO_2 + 2H_2O \rightarrow X^0 + 2H_2SO_4 \quad (2)$$

It should be noted that the process is complex and two-stage. During the course of the specified reactions, working conditions deteriorate to the maximum extent. In addition, chemical methods for both alkaline and acidic medium are technologically inefficient, which is why electrochemical methods are often employed. However, the complexity of the electrochemical reduction of hexavalent selenium and tellurium is associated with the electrostatic repulsion of negatively charged particles from the cathode surface. Selenate and tellurate ions, moreover, have tetrahedral and octahedral forms, respectively, in which the reducible elements are uniformly shielded by oxygen atoms, which obviously creates additional kinetic difficulties. Therefore, the reduction reactions of these anions in aqueous solutions on the cathode are practically impossible. Monographs and articles [12, 13] devoted to the chemistry and metallurgy of chalcogens unequivocally indicate that selenate ions do not exhibit electrochemical activity, and data on the cathodic reduction of these ions are practically absent. Consequently they can be classified as hard-to-reduce and even non-reducible anions. Only limited data [10] indicate that the selenate ion is not reduced in the pH range of 0.28–13.5. Based on the values of standard reaction potentials involving selenium (VI):

$$SeO_4^{2-} + 8H^- + 6e \rightarrow Se + 4H_2O \quad E^0 = +0{,}877\ B \quad (3)$$

It can be argued that the progression of these electrode processes is thermodynamically quite probable. We are closely following scientific research in the field of selenium, tellurium and arsenic technologies. However, we have not come across any work specifically focused on the reduction of selenate, tellurate, and arsenate ions at room temperature using catalytic systems.

In this regard, we believe that research dedicated to developing methods for the reduction of difficult-to-reduce ions with the extraction of elemental selenium is highly relevant. The objective of this publication is to consolidate the results of studies first conducted by us, using the redox Ti (IV)–Ti (III) system, which exerts a catalytic effect on the reduction processes of selenate and arsenate ions, as well as on the electrochemical reduction reactions of copper, platinum, palladium, bismuth, and uranium ions.

In our opinion, the potential of this reduction method for hard-to-reduce compounds can be expanded. This may be achieved by implementing catalytic processes under macroelectrolysis conditions involving various inorganic anions, particularly tellurium (VI), selenium (VI), and others.

In this case, results are both interesting and useful, and contribute to the solution of significant technological issues, particularly related to the extraction of selenium and tellurium from selenate and tellurate acid solutions.

Experimental

In the case of the reduction of selenate ions, the experiments were carried out in a thermostated electrolyzer with separated electrode spaces at 25 °C. Stainless steel (1X18H10T) was used as the cathode material, while graphite was used as the anode. The quantity of electricity was measured using a copper coulometer. The amount of selenium released was determined by the decrease in the concentration of seleni-

um (VI) in the solution and the mass of the elemental selenium precipitate. During electrolysis, selenium was deposited in the cathode space as a fine red amorphous precipitate and settled to the bottom of the electrolyzer [14]. All other experiments were conducted under similar conditions, modifying the electrode material and the electrolyte composition. Preliminary experiments have shown that in the presence of variable-valent titanium cations, selenium (VI) and tellurium (VI) cations are cathodically reduced to the elemental state even at room temperature with a high current efficiency.

Results and Discussion

The electrochemical reduction of hard-to-reduce anions in the presence of redox systems (variable-valent cations) proceeds in several stages. For example, the reduction of selenate ions in the presence of Ti (IV)–Ti (III) ions proceeds schematically as illustrated in the scheme shown in Scheme 1 (the individual reactions were previously detailed in [13], however, the overall scheme is presented here for the first time).

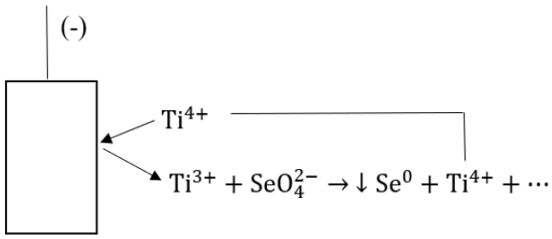

Scheme 1. Scheme for the reduction of hard-to-reduce selenium (VI) anions at the cathode in the presence of variable-valent cations

The following section will provide a detailed account of the sequential processes depicted in Scheme 1:

1) Diffusion of titanium (IV) ions to the cathode surface;
2) Discharge of titanium (IV) ions, i.e. reduction to the trivalent state;
3) Diffusion of titanium (III) ions away from the cathode surface;
4) Diffusion of selenate ions to the cathode surface;
5) Redox reaction, i.e. the interaction of the charge carrier produced on the cathode surface — titanium (III) ions with a hard-to-reduce selenate ion.

We note that any of the mentioned stages can be limiting, depending on the experimental conditions, the characteristics of the anion, and variable-valent cations. Titanium (IV) ions undergo a reversible change in valence acting as a charge shuttle. Their function is to facilitate the ransfer of electrons from the cathode to the anion that is difficult to reduce and to act as a catalyst for the process.

The experimental results showed that titanium (III) reduces selenium (VI) to its elemental state almost instantly at room temperature.

The impact of varying concentrations of titanium (IV) and sulfuric acid concentrations, current density and electrolysis duration on the current efficiency of selenium (VI) reduction has been investigated.

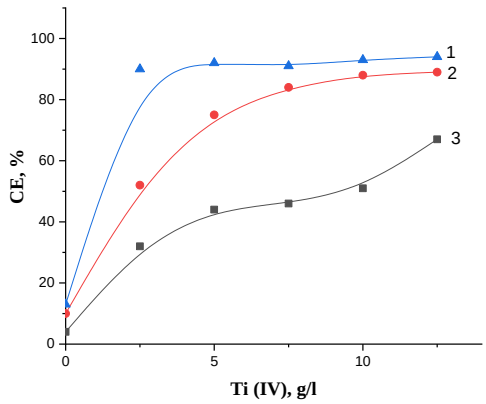

Figure 1. Dependence of the current efficiency of selenium production on titanium (IV) ion concentration (H_2SO_4 — 100 g/L, i_k — 100 A/m^2, τ — 2 h) at initial selenium (VI) ion concentrations, g/L: *1* — 30.4; *2* — 14.4; *3* — 5.1

The concentration of titanium (IV) ions significantly affects the current efficiency of selenate ion reduction. Under certain conditions, the CE reduction of selenate ions exceeds 90 % (Figure 1). We attribute the influence of titanium (IV) ions on the selenium (VI) reduction process to the catalytic action of the redox Ti (IV)–Ti (III) system.

According to the scheme presented in Scheme 1, the processes occurring at the cathode and in the near-cathode space can be represented by reaction (4).

$$TiO^{2+} + e + 2H^{+} \rightarrow Ti^{3+} + H_2O \quad (4)$$

We demonstrated for the first time that titanium (III) ions in the cathode space reduce selenate ions, indicating the progression of the redox reaction occurs (5). As a result of reaction (5), titanium (IV) ions are regenerated and then discharged again at the cathode.

$$6Ti^{3+} + SeO_4^{2-} + 2H_2O \rightarrow Se + 6TiO^{2+} + 4H^{+} \quad (5)$$

Thus, the process can be considered as catalytic, as the nature of the occurring reactions and their sequence fit into Scheme 1. From a thermodynamic perspective, the plausibility of this process is supported by the standard potentials (E^0) of $SeO_4^{2-} - Se$ and Ti (IV) – Ti (III) systems, which are +0.877 V and +0.099 V respectively.

The reduction of hard-to-reduce ions in the presence of titanium (IV) ions, i.e., a catalyst, has another significant advantage. Selenium is known to have semiconductor properties and, therefore, high resistance. If selenium were to deposit directly on the cathode, the cathode would eventually become passivated. However, when using a catalyst (titanium ions), the production of selenium occurs not on the electrode surface, but in the near-cathode layer.

Thus, through comprehensive research, we have shown for the first time that selenate ion, known as a "hard-to-reduce" anion, can be reduced in the presence of variable-valent titanium cations, which act as charge carriers [14].

We consider it appropriate to demonstrate the possibility of using the Ti (IV)–Ti (III) system in processes related to the cathodic reduction of copper (II). It is known that during the electrolytic production of cathode copper at current densities exceeding the limiting value, a powdery metal is produced. During this process, the discharge of hydrogen ions is an unavoidable side reaction. As a result, the current efficiency of the target product is significantly reduced. Our research aimed to increase the current efficiency of copper powder [15]. It has been shown for the first time that the current efficiency can be increased by introducing tetravalent titanium ions into the electrolyte as a catalyst. In the presence of titanium (IV) ions, their reduction occurs at the cathode in accordance with the reaction (4).

The trivalent titanium produced in the near-cathode space interacts with copper (II) ions according to reaction (6).

$$Cu^{2+} + 2Ti^{3+} + 2H_2O \rightarrow Cu^{0} + 2TiO^{2+} + 4H^{+} \quad (6)$$

It is observed that as a consequence of reaction (6), an additional amount of copper powder is produced, and the current efficiency is accordingly enhanced, while titanium (IV) ions are simultaneously regenerated. It has been established that the addition of titanium (IV) ions increases the current efficiency by more than 15 %. This evidence substantiates the occurrence of an electro catalytic cycle in this process. In the existing known method, part of the current is consumed for hydrogen evolution, resulting in low current efficiency. The introduction titanium (IV) ions into the solution results in the utilization of a portion of the current for the reduction of copper (II) ions, thereby generating an additional amount of copper powder. Thanks to this approach (the introduction of titanium ions), the current efficiency of copper powder significantly increases (Fig. 2). As can be seen from Figure 2, at cathode current densities of 1000 A/m^2 and 5000 A/m^2, the current efficiency of copper powder production in the presence of titanium (IV) ions is 82.2 % and 98.1 %, respectively. In the absence of titanium (IV) ions, the current efficiency is 55.2 % and 82.9 %.

It should be noted that copper powder obtained in our laboratory in the presence of titanium (IV) is fine-grained. The high dispersity (0.1–0.3 μm) is explained by the fact that metal powder is produced as a result of chemical reaction (6). Figure 3 shows micrographs of copper powders obtained with the catalytic action of titanium (IV) ions. The micrographs of the copper powders were obtained using scanning electron microscopy (SEM) with a JEOL JSM-6610LV scanning electron microscope (Japan).

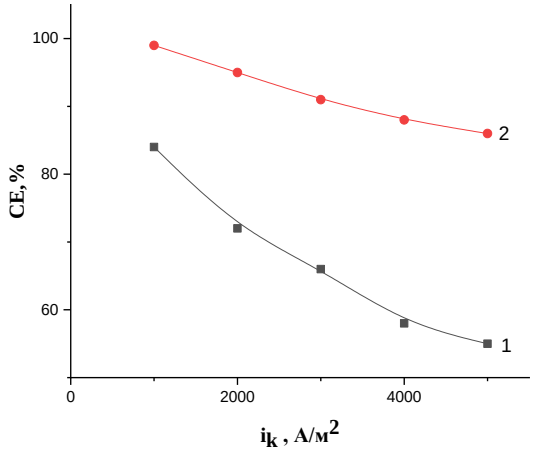

Figure 2. The effect of current density on the current efficiency of copper powder;
electrolyte composition of the electrolyte: 100 g/L H_2SO_4, 8 g/L Cu (II);
Curve 1: in the absence of Ti (IV) ions; Curve 2: in the presence of 4.0 g/L Ti (IV) ions

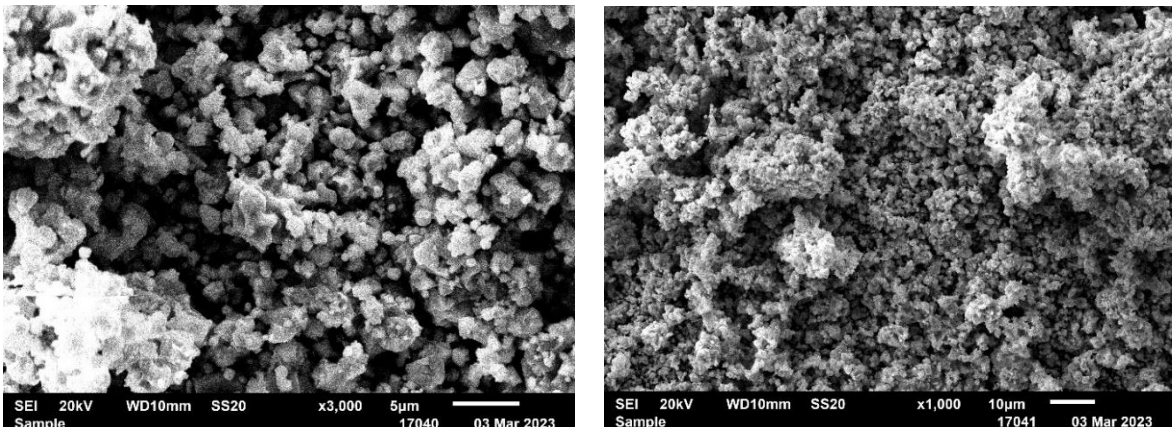

Figure 3. Micrographs of copper powders

The catalytic effect of titanium (IV) ions is also observed in other cases. For instance, during the cementation of copper (II) ions from slightly acidic solutions using metallic zinc, the production of fine copper powders is observed. The ability to produce fine copper powders also has significant practical implications. Fine and ultrafine copper powders are widely used in various chemical processes. For example, ultrafine powder can be used to almost completely recover silver from spent fixer solutions. Additionally, test results have shown that fine copper powder is one of the best additives for metallized lubricants, providing enhanced wear resistance [15].

The production fine powders of other metals, such as including bismuth, platinum, palladium, also has significant practical applications. The feasibility of synthesizing these powders using a catalytic system consisting of titanium ions has been demonstrated [16–18].

One of the promising and efficient methods for removing harmful impurities from various electrolytes, particularly arsenic, is the electrochemical method. However, challenges arise due to the low electrochemical activity of pentavalent arsenic. In this regard, we have studied the cathodic behavior of pentavalent arsenic in sulfuric acid solutions on solid electrodes. No reduction current is observed in the voltammogram of arsenic (V) recorded on a copper electrode. The reduction of arsenic compounds, in particular titanium arsenate, on a copper electrode is characterized by the appearance of a cathode current wave [19]. Apparently, the reduction of this arsenate occurs as a result of direct contact of solid particles with the cathode surface. In this case, titanium (IV) ions are first reduced to the trivalent state according to reaction (7).

$$(TiO)_3(AsO_4)_2 + 6H^+ + 3e \rightarrow 3Ti^{3+} + 2AsO_4^{3-} + 3H_2O \quad (7)$$

Then, a redox reaction (8) occurs in the near-cathode space, thanks to the values of the standard potentials of the Ti (IV)–Ti (III) and $AsO_4^{2-} - AsO_2^-$ systems, the values of which, respectively, are +0.099 V and + 0.977 V.

$$2Ti^{3+} + AsO_4^{3-} \rightarrow 2TiO^{2+} + AsO_2^- \quad (8)$$

It has been experimentally shown that reaction (8) can indeed occur. The trivalent arsenic produced as a result of reaction (8) is easily reduced at the cathode. The electrochemical behavior of arsenic (V) in the presence of titanium (IV) ions has been studied. The experiments were carried out using the method of rational experimental design. The influence of temperature (X_1), sulfuric acid concentration (X_2) and introduced titanium ions (X_3), current density (X_4), and experiment duration (X_5) on the degree of arsenic extraction from solution was studied. In the presence of titanium (IV) ions, the degree of arsenic extraction increases sharply. The mechanism of the arsenic (V) reduction process can be represented as follows: titanium (IV) is reduced to titanium (III) at the cathode, the latter in the near-cathode space reduces arsenic (V) to the trivalent electrochemically active state according to reaction (8). At the same time, titanium (IV) ions are regenerated and again participate in the cathodic process.

Thus, it has been established that in the presence of titanium (IV) ions, the degree of arsenic extraction under optimal conditions reaches 90 % as compared 12–13 % without titanium (IV). This fact has practical significance, particularly for purifying copper refining electrolyte from arsenic at the deep cleaning stage.

It is known that pure and ultrapure metals, widely used in semiconductor technology, are usually obtained from their hydrides. In this regard, numerous research papers are devoted to the development of methods for obtaining hydrides. For example, in works [20–24], methods for producing arsin (arsenic hydride) are described. The most common method is the decomposition of metal arsenides by acids:

$$Zn_3As_2 + 6HCl \rightarrow 2AsH_3 + 3ZnCl_2 \quad (9)$$

or the reduction of oxygen-containing compounds with metallic zinc in an acidic medium:

$$2NaAsO_2 + 6Zn + 7H_2SO_4 \rightarrow 2AsH_3 + Na_2SO_4 + 6ZnSO_4 + 4H_2O \quad (10)$$

The arsin content in the gas phase reaches 50 %.

These reactions have several disadvantages: for example, preliminary synthesis of arsenides is required, thus, needing additional reagents. Moreover, these reactions produce by-products are produced that require processing, introducing new challenges.

Traditionally, arsin is obtained by electrochemical methods, which have advantages over chemical methods [23, 24]. However, they also have their downsides. Arsin is typically derived from a solution of trivalent arsenic — As_2O_3, which is very poorly soluble in water (4.44 g in 100 ml of water at 60°). This low solubility of arsenic trioxide limits the use of more concentrated solutions and reduces the productivity of the process. Given these limitations, it is preferable to use solutions of pentavalent arsenic. However, challenges arise since arsenic (V) is electrochemically inactive. To address this, we propose integrating the redox Cr (III)–Cr (II) system.

It is worth noting that there are no literature reports on using catalytic systems for obtaining arsenic or its hydride.

Since the solubility of pentoxide is more than 15 times higher than that of trioxide, using arsenic (V) solutions is of great practical interest. In this regard, we have studied the influence of the redox Cr (III)–Cr (II) system on the production of arsine during the reduction of arsenic (V). The electrocatalytic reduction of arsenic (V) in the presence of chromium (III) proceeds according to reaction (11).

$$Cr^{3+} + e \rightarrow Cr^{2+} \quad (11)$$

Chromium (II) ions produced in the cathode space as a result of the reaction (11) interact with arsenic (V) to produce arsin, since the redox Cr (III)–Cr (II) system has a more negative potential than the As (V)–As (III) system.

$$2\,AsO_4^{3-} + 5Cr^{2+} + 2H^+ \rightarrow 2AsH_3 + 5Cr^{3+} + 8H_2O \quad (12)$$

Further, chromium (III) ions are regenerated and thus a catalytic cycle is realized. The standard potentials of the Cr (III)–Cr (II) and As (V)–As (III) systems are –0.408 V and +0.1 V, respectively.

Under optimal conditions, the efficiency is 52–61 %.

The present research is focused on developing methods for uranium extraction.

One of the stages of uranium production technology is the reduction of the hexavalent state to the tetravalent state. Cathodic reduction seems promising. The study [26] presents the results of the study of the process of cathodic reduction of uranium (VI) to uranium (IV) in a solution of nitric acid containing hydrazine. The disadvantage of this method is the high corrosive activity of nitric acid and the complexity of the electrolyte composition, etc.

The authors of study [27] investigated the process of cathodic reduction of uranium (VI) to uranium (IV) in sulfuric acid solutions using an ionite membrane. The main disadvantage of this method is that the current efficiency of uranium (VI) reduction does not exceed 75–80 %, due to the high overvoltage reduction of the ion under study. We have shown that in the presence of the redox Ti (III)–Ti (IV) system, the current output increases to 99 %.

We have established for the first time that using the Ti (IV)–Ti (III) catalytic system facilitates the reduction of hexavalent uranium to the tetravalent state, achieving high current efficiency. Table 1 shows the results of studies investigating the effect of titanium (IV) ion concentration on the current efficiency of uranium (VI) reduction to uranium (IV).

Table 1

Influence of titanium (IV) ion concentration on current efficiency of hexavalent uranium reduction: [U^{6+}] — 10 g/L, H_2SO_4 — g/L, i_k — 100 A/m^2, τ — 1 h, t= 25 °C

C(Ti^{4+}), g/L	0	0.5	1.0	2.0	3.0	4.0
CE, %	53.3	54	79.95	86.7	94.6	99.1

The data presented in Table 1 show that with an increase in the concentration of titanium (IV) ions, the current efficiency of uranyl reduction increases by more than 35 %. This can be explained by the catalytic action of titanium (IV) ions (Scheme 2), similar to the cases of selenium (VI) and copper (II) ion reduction.

$$2Ti^{4+} + 2e \rightarrow 2Ti^{3+}$$

$$U^{6+} + 2Ti^{3+} \rightarrow U^{4+} + Ti^{4+}$$

Scheme 2. Schematic diagram of the catalytic reduction of uranium (VI)

The results of these studies enable an overall increase in uranium production efficiency. The potential involvement of the Ti (IV)–Ti (III) catalytic system has also been demonstrated by us in the case of manganese-containing ores [28]. It is worth noting that manganese in the ore present as the mineral pyrolusite, which is practically insoluble in acidic and alkaline solutions. Therefore, to extract manganese from the ore, it needs to be reduced to the divalent state, in which manganese compounds become well soluble. To achieve this, manganese-containing ore is heated in a hydrogen atmosphere up to 100 °C to convert it into a soluble form. This process is complex and energetically inefficient. Through our research aimed at finding the most feasible methods for processing manganese ores, we proposed a method for the cathodic reduction of manganese dioxide. The essence of the method is to cathodically treat a suspension of manganese-containing ore in a sulfuric acid solution in the presence of titanium (IV) ions. This increases the manganese ion transition to the solution, as shown Table 2, reaching up to 94.9 % $MnO_2 \cdot xH_2O$.

Table 2

Dependency of manganese extraction degree during cathodic polarization of manganese dioxide a suspension (L:S = 4:1, 150 g/L of H_2SO_4, i_k=300 A/m^2, τ=1 hour) [28]

C(Ti^{4+}), g/L	0	0.5	1.0	2.0	4.0	8.0
α, %	40.1	55.0	78.4	86.6	90.1	94.9

The mechanism of titanium (IV) ions action is similar to the cases we have presented for selenium, copper, uranium ions, etc.

Thus, based on numerous fundamental and applied studies, the catalytic action of a redox system based on multivalent titanium ions (in some cases chromium ions) on the progress of a number of reactions occurring in hydrometallurgy has been demonstrated.

For the first time, it has been shown that number of cathodic reactions in the presence of titanium ions proceed at a higher rate, resulting in an increase in the efficiency of technological processes.

It has been established that the mechanism of the catalytic action of titanium ions may vary depending on the experimental conditions and the object of the study.

Conclusions

Based on the above, the following conclusions can be formulated:

– The catalytic action of titanium (IV) ions on the cathodic reduction of selenium (VI), copper (II), uranium (VI) ions, and other metals in aqueous solutions has been demonstrated. It has been established that the mechanism of the catalytic action of titanium (IV) ions can vary depending on the conditions. For example, during the reduction of hard-to-reduce selenate ion, which does not exhibit electrochemical activity, titanium (IV) ions are initially reduced to titanium (III) ions at the cathode. These ions then react with selenate ions in the cathodic layer to produce elemental selenium. During this process, titanium (IV) ions are regenerate and are again reduced at the cathode to the trivalent state. These reactions occur cyclically, indicating the catalytic action of titanium ions.

In the case of reducing copper (II), platinum (IV), palladium (IV), bismuth (II) ions in the presence of titanium (IV) ions, the current efficiency for the production of metal powders increases by more than 15 %. Here as well, the catalytic action of titanium (IV) ions and cyclic repetition of the processes are also observed.

For the cathodic reduction of uranium (VI) and hard-to-reduce arsenic anions, the reaction mechanism appears different. Titanium (III) ions produced at the cathode reduce uranium (VI) ions to the tetravalent state. In the case of arsenate ions, reduction proceeds to trivalent ions, and manganese dioxide is reduced to soluble divalent state. Our research results demonstrate the potential for:

– the reduction of selenate ions in the presence of the redox Ti (IV)-Ti (III) system at room temperature, resulting in the production of elemental selenium;

– the application of the Ti (IV)-Ti (III) system in processes involving the cathodic reduction of copper (II) and other metals, leading to the production of ultrafine powders;

– the reduction of arsenate ions with the production of trivalent arsenic ions, which can subsequently be converted to elemental arsenic;

– the use of the redox Ti (IV)-Ti (III) system for the reduction of hexavalent uranium to the tetravalent state with high current efficiency;

– the involvement of the redox Ti (IV)-Ti (III) system in the processing of manganese-containing ores.

Funding

This research is carried out within the framework of a state order for the implementation of a targeted financing program: BR18574219 «Development of environmentally safe technologies for obtaining innovative products from natural and man-made raw materials of Kazakhstan».

*Author Information**

**The authors' names are presented in the following order: First Name, Middle Name and Last Name*

Abduali Bayeshov — Doctor of Chemical Science, Professor, Academician of the National Academy of Sciences of the Republic Kazakhstan, Leading Researcher, Center of Physico-Chemical Methods of Research and Analysis, Al-Farabi Kazakh National University, al-Farabi Ave., 71, 050040, Almaty, Kazakhstan; e-mail: bayeshov@mail.ru; https://orcid.org/0000-0003-0745-039X

Azhar Kospanovna Bayeshova (*corresponding author*) — Doctor of Technical Sciences, Professor, Leading Researcher, Center of Physico-Chemical Methods of Research and Analysis, Al-Farabi Kazakh National University, al-Farabi Ave., 71, 050040, Almaty, Kazakhstan; e-mail: azhar_b@bk.ru; https://orcid.org/0000-0002-9076-8130

Makpal Nyshangalievna Turlybekova —Research Associate, Center of Physico-Chemical Methods of Research and Analysis, Al-Farabi Kazakh National University, al-Farabi Ave., 71, 050040, Almaty, Kazakhstan; e-mail: m.t.89@mail.ru; https://orcid.org/0000-0002-9030-159X

Author Contributions

The manuscript was written through contributions of all authors. All authors have given approval to the final version of the manuscript. CRediT: **Abduali Bayeshov** conceptualization, methodology, validation, visualization, writing-original draft, writing-review & editing; **Azhar Kospanovna Bayeshova** conceptualization, resources, supervision, validation, writing-review & editing; **Makpal Nyshangalievna Turlybekova** data curation, investigation, formal analysis, visualization.

Conflicts of Interest

The authors declare no conflict of interest.

References

1 Weller, M., Weller, M. T., Overton, T., Rourke, J., & Armstrong, F. (2014). *Inorganic chemistry*. Oxford: Oxford University Press.

2 Saha, B., Fan, M., & Wang, J. (Eds.). (2015). *Sustainable catalytic processes*. Newnes.

3 Potekhin, V.M., Potekhin, V.V. (2017). *Osnovy teorii himicheskih processov tehnologii organicheskih veshestv I neftepererabotki [Fundamentals of the theory of chemical processes, technology of organic substances and oil refining]*. Saint-Petersburg: Himizdat [in Russian].

4 Sulman, E. M., Matveeva, V.G. (2013). Kataliz v tonkom organicheskom sinteze vitaminov i lekarstvennyx preparatov [Catalysis in fine organic synthesis of vitamins and drugs]. Resource and energy saving technologies in the chemical and petrochemical industry: *V Mezhdunarodnaya konferenciya Rossiyskogo himicheskogo obshchestva imeni D.I Mendeleeva (29-30 oktyabrya 2013 goda) — V International Conference of the Russian Chemical Society named after D.I. Mendeleev"* (pp. 34–35). Russia: All-Russian public organization "Russian Chemical Society named after D.I. Mendeleev" [in Russian].

5 Mokhov, V. M., Popov, Y. V., & Sccherbakova K.V. (2019). Kolloidnye i nanorazmernye katalizatory v organicheskom sinteze. XIV. Vosstanovitelnoe aminirovanie i amidirovanie karbonitrilov pri katalize nanochasticami nikelya [Colloidal and nanosized catalysts in organic synthesis. XIV. Reductive amination of carbonyl compounds catalyzed by nickel nanoparticles]. *Zhurnal obshey himii — Journal of General Chemistry*, *86*(4), 609–616 [in Russian]. https://doi.org/10.1134/S1070363219120016

6 Varfolomeev, S. D. (2007). Fizicheskaya i strukturnaya himiya fermentativnogo kataliza. Sistemniy podhod: ot pervichnoy struktury do elementarnogo akta [Physical and structural chemistry of enzymatic catalysis. A Systematic approach: From primary structure to the elementary act]. *Kinetika i kataliz — Kinetics and Catalysis*, *48*(4), 499-509 [in Russian]. https://doi.org/10.1134/s0023158407040039

7 Schramm, V. L. (2006). Introduction: principles of enzymatic catalysis. *Chemical Reviews*, *106*(8), 3029–3030. https://doi.org/10.1021/cr050246s

8 Savinova, A. A., Pantyukh, V. V. (2023). Rol fermentov v metabolizme [The role of enzymes in metabolism]. Challenges of modernity and strategies for the development of society in a new reality: *XVI Mezhdunarodnaya nauchno-prakticheskaya konferenciya (25 aprelya 2023 goda) — XVI International Scientific and Practical Conference.* (pp. 85–88). Makhachkala: LLC "ALEF Publishing house" [in Russian].

9 Lyapishchev, Yu. B. (2006). Sovremennoe sostoyanie pererabotki elektrolitnyh shlamov mednogo proizvodstva [Current state of processing of electrolyte sludge from copper production]. *Zapiski gornogo instituta — Notes of the Mining Institute*, *167*(2), 245–247 [in Russian].

10 Graver, T. N., Zaitseva, I. G., & Kosover, V. M. (1977). *Selen i tellur: novaya tehnologiya polucheniya i rafinirovaniya [Selenium and tellurium: a new technology for obtaining and refining]*. Moscow: Metallurgy [in Russian].

11 Buketov, E. A., & Ugorets, M. Z. (1975). *Gidrohimicheskoe okislenie halkogenov i halkoenidov [Hydrochemical oxidation of chalcogens and chalcogenides]*. Alma-Ata: Nauka [in Russian].

12 Kudryavtsev, A.A. (1968). *Himiya i tehnologiya selena I tellura [Chemistry and technology of selenium and tellurium]*. Moscow: Metallurgy [in Russian].

13 Bayeshov, A., & Bayeshova, A. (2020). A reduction phenomenon on the anode surface: Selenate and copper (II) ions reduction to their elemental state on the anode surface. *Journal of Chemical Technology and Metallurgy*, *55*, 1105–1110.

14 Bayeshov, A., Bayeshova, A., Zhanbekov, K., Zhubanys, M., & Naguman, P. (2022). Recovery of "Hard-to-Recover" Selenate Ions in Sulfuric Acid Solutions during Polarization of Titanium Electrodes by Industrial Alternating Current. *Inorganics*, *10*(6), 72. https://doi.org/10.3390/inorganics10060072

15 Bayeshov, A., Bayeshova, A., Abduvaliyeva, U., & Buketova, A. (2022). Mechanisms for Ultrafine Copper Powders Electrolytes Production in the Presence of Titanium Ions. *Portugaliae Electrochimica Acta*, *40*(5), 373–381. http://dx.doi.org/10.4152/pea.2022400505

16 Bayeshov, A., Bazarkyzy, B., & Abzhalov, B.S. (2021). Method for producing bismuth powder. RK Patent 6667.

17 Bayeshov, A., Myrzabekov, B., & Ivanov, N.S. (2012). Method for producing platinum powder. RK Patent 27338.

18 Bayeshov, A., Ivanov, N.S., & Zhurinov, M.Zh. (2008). Method for producing palladium powder. RK Patent 19925.

19 Bayeshov, A., Kozhakov, B.E., Ugorets, M.Z., & Buketov, E.A. (1983). Elekrohimicheskoe vosstanovlenie pyativalentnogo myshyaka [Electrochemical reduction of pentavalent arsenic]. *Complex use of mineral raw materials*, *6*(44) [in Russian].

20 Fedorov, V. A., Potolokov, N. A., Menshchikova, T. K., & Brekhovskikh, M. N. (2018). Hydride method for obtaining high-purity arsenic. *Inorganic Materials*, *54*(10), 1092–1098. https://doi.org/10.1134/S0002337X18100068

21 Fedorov, V. A., Menshchikova, T. K., Vargunin, A. I., Nikonov, K. S., Brekhovskikh, M. N., & Myslitsky, O. E. (2021). Methods for obtaining high-purity arsenic and its compounds. *Inorganic Materials*, *57*(11), 1161–1173. https://doi.org/10.31857/S0002337X2111004X

22 Baranov Yu.I., Smetanin A.V., Turygin V.V., Tomilov A.P., Khudenko A.V., & Chernykh I.N. SU Patent 2203983.

23 Tomilov, A. P., Smetanin, A. V., Chernykh, I. N., & Smirnov, M. K. (2001). Electrode reactions involving arsenic and its inorganic compounds. *Russian Journal of Electrochemistry*, *37*(10), 997-1011. https://doi.org/10.1023/A:1012396309686

24 Kvaratskheli, Y. K., Shatalov, V. V., Demin, Y. V., Kondratiev, A. G., & Khorozova, O. D. RU Patent 2369666 C1.

25 Bayeshov, A., Kozhakov, B.E. SU Patent 1300884. (not subject to publication in the open press).

26 Wei, Y. Z., Fang, B., Arai, T., & Kumagai, M. (2004). Electrochemical reduction of uranium (VI) in nitric acid-hydrazine solution on glassy carbon electrode. *Journal of radioanalytical and nuclear chemistry*, *262*, 409–415. doi:10.1023/b:jrnc.0000046770.86000.d6

27 Smirnova, N. M., Glukhova, L. P., Glazkova, I. N., Abakumov, B. N., & Shibarov, V. N. (1999). Opyt promyshlennoy ekspluatacii elektrolizerov s kationitovymi membranami dlya vosstanovleniya urana (VI) do urana (IV) [Experience of industrial operation of electrolyzers with cationite membranes for the reduction of uranium (VI) to uranium (IV)]. *Atomnaya Energia — Atomic Energy*, *86*(5), 339-342 [in Russian]. https://doi.org/10.1007/bf02673564

28 Bayeshova A.K., Bayeshov A., Bayeshova S.A., & Makhanbetov A.B. (2008). Method for dissolving manganese dioxide in sulfuric acid solution. RK Patent 5436.

How to Cite: Sushko, E.S., Zenkov, A.V., & Kudryasheva, N.S. (2024) Effects of Selenite-Ions on a Luminescence Enzymatic System. *Eurasian Journal of Chemistry, 29, 3(115), 65-71*. https://doi.org/10.31489/2959-0663/3-24-6

Article

Received: 9 June 2024 | Revised: 8 August 2024 |
Accepted: 13 August 2024 | Published online: 13 September 2024

UDC 543.94-026.616

https://doi.org/10.31489/2959-0663/3-24-6

Ekaterina S. Sushko[1,2*], Andrei V. Zenkov[2], Nadezhda S. Kudryasheva[1,2]

[1]*Institute of Biophysics SB RAS, Federal Research Center 'Krasnoyarsk Science Center SB RAS', Krasnoyarsk, Russia;*
[2]*School of Fundamental Biology and Biotechnology, Siberian Federal University, Krasnoyarsk, Russia*
*(*Corresponding author's e-mail: kkovel@yandex.ru)*

Effects of Selenite Ions on a Luminescence Enzymatic System

This paper elucidates biochemical and physicochemical aspects of toxicity of a redox-active compound in organisms. Sodium selenite (Na_2SeO_3) was chosen as a model redox-active compound; a coupled enzymatic system from luminous marine bacteria was applied to imitate a biochemical process. We demonstrated that Na_2SeO_3 suppressed bioluminescence of the enzyme system; the effective inhibition concentration was 10^{-2} M. Besides that, Na_2SeO_3 decreased the content of reactive oxygen species (ROS) in aqueous solutions (enzyme-free media) at $>10^{-3}$ M. Addition of enzymes and their substrates to these solutions enhanced this decrease. Correlations between dependencies of the ROS content and bioluminescence intensity on the concentration of Na_2SeO_3 were positive and high, confirming the ROS involvement in the bioluminescence suppression in Na_2SeO_3 solutions. Hence, we observed the disturbance of the native biochemical oxidative functions of dissolved oxygen derivatives under exposure to redox-active toxicants. The effects of Na_2SeO_3 on the bacterial enzyme system should be further compared with those on bacterial cells, which are traditionally used as a toxicity bioassay. Additionally, the use of natural microorganisms is perspective due to their ability of redox transformation of toxic selenium oxoanions to elemental selenium. This ability is important as it provides: (1) natural detoxification of water ecosystems, and (2) biosynthesis of selenium nanoparticles.

Keywords: selenite ions, ecological monitoring, toxicity mechanism, bacterial enzymatic assay, reactive oxygen species, redox processes, luminescence, enzymatic system, sodium selenite.

Introduction

Luminous marine bacteria are a basis of a well-known bioassay which is widely applied in ecological investigations. This method implies that the bacterial luminescence is a physiological function inherent in this microorganism; and, hence, the bioluminescence intensity can be used as a quantitative characteristic of environmental toxicity. Due to a high sensitivity, simplicity, and high rates of analyses, the bacterial bioassay has been used for more than 60 years for toxicity monitoring [1–4]. One more important advantage of the bioluminescence assay is concerned with detailed investigation of effects of various compounds on the bacteria and related systems, e.g., enzymatic reactions, cellular membranes, etc. [5–7].

Study of effects of toxic compounds on enzymatic reactions elucidates the mechanisms of toxic impacts on living organisms.

Application of enzymatic bioluminescent reactions is a fairly new direction in toxicology. In 1990, an enzyme system of bacterial reactions was proposed as a bioluminescence toxicity assay [8]. This bioassay is based on the system of coupled enzymatic reactions catalyzed by enzymes — bacterial luciferase and NAD(P)H:FMN-oxidoreductase:

$$\mathrm{NADH + FMN \xrightarrow{NAD(P)H:FMN\text{-}oxidoreductase} NAD^+ + FMNH^-}\,, \quad (1)$$

$$\mathrm{FMNH^- + RCHO + O_2 \xrightarrow{luciferase} FMN + RCOO^- + H_2O} + h\nu\ (490\ \mathrm{nm})\,. \quad (2)$$

The enzyme system is sensitive to redox-active compounds and depends on their concentration and redox parameters [5, 6, 9]. Both of the bioluminescence assays, enzymatic and bacterial, were previously applied to characterize antioxidant [10–14] and prooxidant [15–16] effects of bioactive compounds, as well as to reveal the activity of reactive oxygen species (ROS) in these effects.

ROS are a group of compounds that contain oxygen with unpaired electrons. The group of ROS includes, but is not limited to, the following compounds: superoxide anion radicals ($O_2{\cdot}-$), hydrogen peroxide (H_2O_2), hydroxyl radical (·OH), singlet oxygen ($^1O_2$), hypochlorite (HOCl), hydroperoxyl radical (HOO·), and others. ROS are involved into physiological reactions in organisms, and thereby they are always present in physiological concentrations in organisms [17, 18]. ROS serve as multifunctional compounds in organisms: they can act as pleiotropic signaling agents [19], apoptosis factors [20–23], amplifiers of the cytotoxic

effect of drugs in tumor cells [24, 25]. The formation of ROS occurs both in pathological and physiological conditions. Processes of oxidation of biological molecules are usually accompanied by the ROS generation [26, 27]. At concentrations above the physiological levels, ROS are highly toxic for biological systems, as they initiate degradation of nucleic acids, structural proteins, and lipids of cell membranes [28]. Hence, the physiological role of ROS in cellular processes is essential; ROS are involved in natural functions of biological systems, being produced or utilized in metabolic processes. Maintaining the ROS balance is a vital function of organisms. However, ROS can suppress physiological functions under the conditions of their excessive production. In solutions of redox-active exogenous compounds, ROS initiate primary physicochemical processes followed by changes of rates of various intracellular processes, including bioluminescence reactions. Therefore, a role of ROS in bioluminescence enzymatic systems (reactions 1 and 2) exposed to redox-active compounds is of interest.

Bioluminescence assay systems, both enzymatic and cellular, have not been applied yet to study bioeffects of selenium compounds. Complex functions of selenium in natural environments are well-known: selenium is a vital microelement at low concentrations and a highly toxic element at higher concentrations. On the one hand, selenium is a component of enzymatic processes, it protects cells from oxidative stress. On the other hand, an acute toxicity is inherent in selenium oxoanions — selenite (SeO_3^{2-}) and selenate (SeO_4^{2-}). An excessive selenium content in aquatic environments leads to various defects, disorders of the immune system, in the development of embryos in juvenile and adult fish, as well as to a decrease in fertility. Excessive selenium disrupts the stability of aquatic ecosystems and has a counterproductive effect on fish farming [29–31]. The consequences of excessive selenium for humans are heart disease, dermatitis, joint pain, and brittle nails [32].

Natural selenium pollution occurs due to weathering of selenium-rich soils, rocks, and volcanic eruptions. Additionally, selenium is released during industrial activities — oil production, metal smelting [33], burning of fossil fuels, mining, and the use of nuclear fuel. Selenium enters the environment in the form of oxides, then they are hydrolyzed and dissolved in water bodies in the form of oxoanions.

There exists a biogeochemical cycle of selenium compounds in nature, and microorganisms play a key role in this cycle. Bacteria can reduce selenium oxoanions to elemental selenium and form selenium nanoparticles. Bacterially synthesized selenium nanoparticles can be used as food additives, drug delivery agents, as well as adsorbents in the human body. Selenium nanoparticles have an advantage over metal-containing nanoparticles, due to potential inactivation of metal ions [34]. Properties of bacterially synthesized selenium nanoparticles have intensively been studied [34–41].

The current work aimed to study the effects of sodium selenite (Na_2SeO_3) on the bioluminescence system of enzymatic reactions that is responsible for glowing of luminous marine bacteria. We analyzed changes in the ROS content and bioluminescence intensity under exposure to Na_2SeO_3; the exposure time and selenite concentration were varied. Priority attention was paid to redox processes in the bioeffects of Na_2SeO_3.

Experimental

Bioluminescence enzymatic assay

Bioluminescence enzymatic assay was applied to evaluate the inhibition ability of Na_2SeO_3 in biochemical processes. The composition and construction of this system are presented in section “Bioluminescence Enzymatic Assay” in [16].

Luminol chemiluminescence assay

To determine the role of ROS in the inhibition ability of Na_2SeO_3, the ROS content was studied in the absence and presence of Na_2SeO_3; distilled water and bioluminescence enzyme system solutions were used as media for the measurements. The chemiluminescence intensity was registered just after the bioluminescence signal detection. The ROS concentration in the experimental samples was evaluated using a calibration curve [16].

Reagents for this assay are presented in section “*Luminol Chemiluminescence Assay*” in [16].

A 3×10^{-5} M alkaline luminol solution was applied. The chemiluminescence reaction was initiated by 1.2×10^{-4} M $K_3[Fe(CN)_6]$.

Measurements of bioluminescence/chemiluminescence intensities and statistical processing

A biochemiluminometer Luminoskan Ascent (Thermo Electron Corporation, USA) was applied to carry out all luminescence measurements at 25 °C [16]. Maximal values of chemi- and bioluminescence intensities

were registered and analyzed. All solutions of Na_2SeO_3 were 'non-colored' and do not have an effect of 'optic filter' [16]. All measurements were carried out in 5–10 replicates with an injector system. I^{rel} and ROS^{rel} were calculated as described in [16]. The SD values for I^{rel} and ROS^{rel} did not exceed 0.2 (GraphPad Prism 8, GraphPad Software, Inc., USA).

Correlation coefficients r between I^{rel} and ROS^{rel} were calculated [16, 43].

Results and Discussion

Bioluminescence kinetics was registered in solutions of sodium selenite, Na_2SeO_3. Figure 1 presents the time courses of bioluminescence intensity at different concentrations of Na_2SeO_3, during 120 min of observation. It can be seen that lower concentrations of selenite ($<5\times10^{-3}$ M) do not significantly change the bioluminescence intensity, while higher concentrations inhibit it. The results of the same experiment are presented in Figure 2A as the bioluminescence intensity, I^{rel}, vs. the concentration of Na_2SeO_3. The absence of the effect (I^{rel} is close to 1) and higher-concentration inhibition ($I^{rel}<1$) are evident from this Figure as well. The concentration at which bioluminescence was inhibited by 50 % appeared to be ca. 10^{-2} M for all times of exposure to Na_2SeO_3.

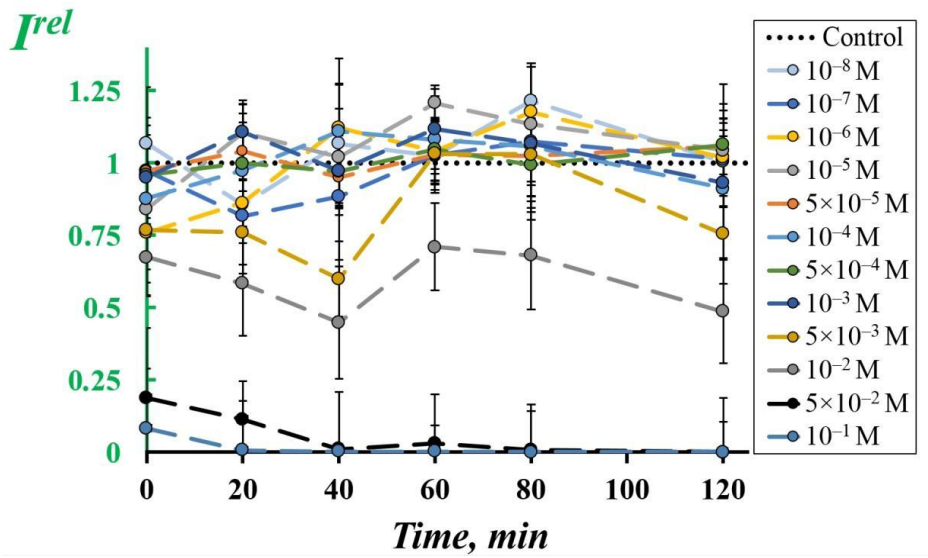

Figure 1. Relative intensity of bioluminescence of the enzyme system, I^{rel}, at various concentrations of Na_2SeO_3. "Control" — in the absence of Na_2SeO_3

The reason why the low-concentration interval of Na_2SeO_3 was analyzed is related to our intention to compare effects of Na_2SeO_3 on the enzymatic system and bacterial cells (the latter result has not been published yet) at similar conditions, as well as to conclude on the involvement of enzymatic processes in bioeffects of Na_2SeO_3 in cellular systems. It is known [5–8] that bacterial cells are often more sensitive to toxic compounds than enzyme reactions due to the involvement of additional processes and structures (cell membranes and others).

We analyzed the content of ROS, ROS^{rel}, in the solutions of the enzyme preparation and compared it to the bioluminescence intensity in those solutions, I^{rel} (Figure 2B and Figure 2A, respectively).

Figure 2B presents the ROS content in the absence and presence of the enzyme preparation. The dependence of the ROS content on the concentration of Na_2SeO_3 in enzyme-free solutions is presented with a dark-red curve. It can be seen that Na_2SeO_3 does not significantly affect the ROS content at $<10^{-3}$ M and suppresses it ($ROS^{rel}<1$) at higher concentrations. The suppression can be explained by oxidation of selenite to selenate (i.e., SeO_3^{2-} to SeO_4^{2-}); ROS can serve as oxidizing agents in this process.

It is evident from Figure 2B that the addition of the enzyme system to Na_2SeO_3 (enzyme-free) solutions decreases, as a rule, the ROS level at all Na_2SeO_3 concentrations. This effect could be explained by ROS consumption in the oxidative reaction catalyzed by bacterial luciferase (reaction 2) [44, 45].

To confirm the involvement of ROS in bioluminescence inhibition, we calculated correlation coefficients r between the dependencies of ROS^{rel} and I^{rel} on the concentration of Na_2SeO_3 (Figure 2A and Figure 2B). The r-values appeared to be positive and of high value: 0.88, 0.72, 0.89, 0.81, 0.82, and 0.87 at times of

exposure: 0, 20, 40, 60, 80, and 120 min, respectively. This result indicates that a lack of ROS in the solutions of Na_2SeO_3 initiates bioluminescence inhibition; the result confirms that ROS participate directly in the bioluminescence enzymatic reactions. Similar conclusions were made earlier using other bioactive compounds [12, 13, 16, 46].

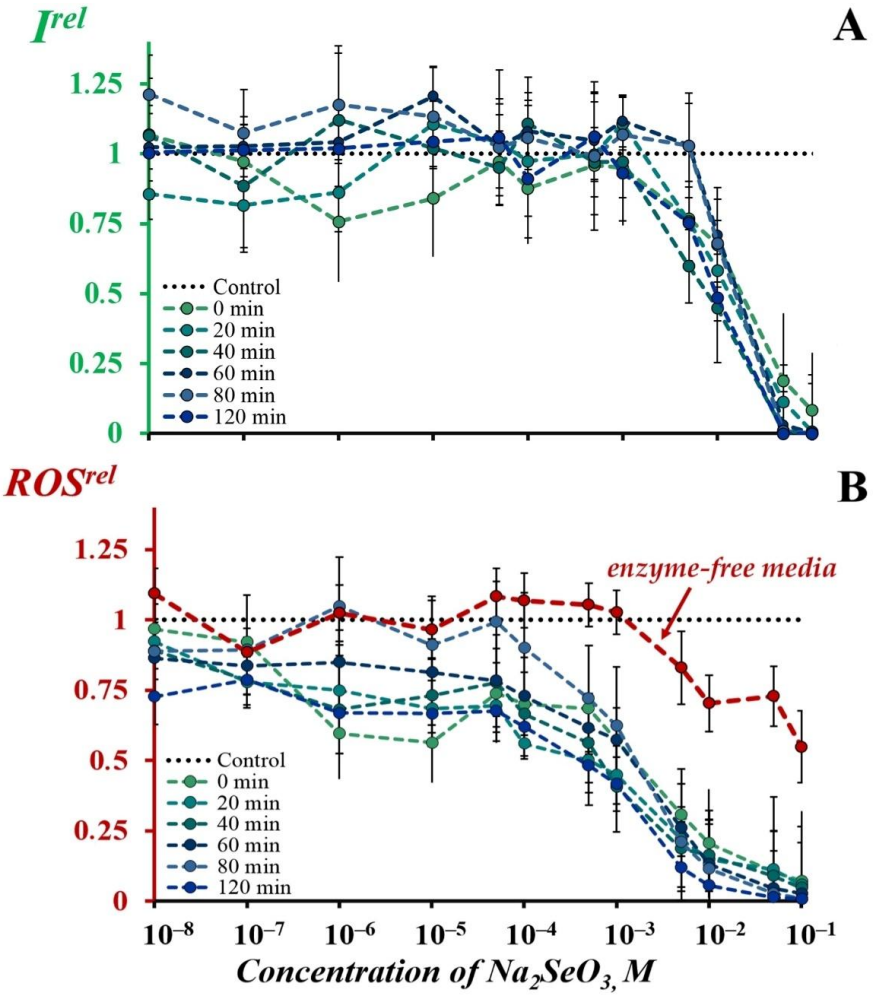

Figure 2. The dependence of relative bioluminescence intensity, I^{rel} (A,) and relative ROS content, ROS^{rel} (B), on Na_2SeO_3 concentration in enzymatic solutions. "Control" was measured in the absence of Na_2SeO_3. The content of ROS in the control enzyme solution was 4.6×10^{-6} M, in enzyme-free solution — 4.7×10^{-7} M

Therefore, bioluminescence of the enzymatic system from a luminous marine bacterium is sensitive to Na_2SeO_3. The inhibition activity of Na_2SeO_3 is characterized by the effective concentration $EC_{50} = 10^{-2}$ M. Na_2SeO_3 decreases the ROS content in aqueous solutions (enzyme-free media) at $>10^{-3}$ M. Addition of enzymes and their substrates to these solutions enhanced this decrease. Correlations between the dependencies of ROS^{rel} and I^{rel} on the Na_2SeO_3 concentration were found, confirming the ROS involvement in the bioeffects of Na_2SeO_3 on the bacterial enzymatic system.

Conclusions

The purpose of this article is related to the biochemical aspect of the toxicity of redox-active compounds. Sodium selenite (Na_2SeO_3) was chosen as a model of an inorganic redox-active compound due to its toxicity in the environment and the ability of microorganisms to biotransform it into neutral selenium. The enzymes from luminous marine bacteria were applied to imitate a biochemical process. Inhibition of the enzymatic activity by Na_2SeO_3 was evaluated and related to the activity of reactive oxygen species (ROS) in aqueous media, thus demonstrating the disturbance of vital oxidative functions of dissolved oxygen derivatives under exposure to redox-active toxicants. Hence, a physicochemical approach to the study of the toxic effects of redox compounds in organisms was presented.

Our further research will be aimed at studying the effect of Na_2SeO_3 on the bacterial cells and comparing its effect on bacterial enzymes. In general, the importance of bacterial biotransformation of toxic selenium oxoanions into elemental selenium is due to the fact that it provides detoxification of natural aquatic ecosystems contaminated with selenium compounds. Additionally, bacterial biosynthesis of selenium nanoparticles is very promising for biotechnology, biomedicine, pharmacology, dietetics and electronics.

Funding

This research was funded by the Russian Science Foundation and Krasnoyarsk Territory and Krasnoyarsk Regional Fund of Science (Grant No. 24–24–20001). Enzyme purification was supported by the State Assignment of the Ministry of Science and Higher Education of the Russian Federation, project FWES-2024-0018.

*Author Information**

**The authors' names are presented in the following order: First Name, Middle Name and Last Name*

Ekaterina Sergeevna Sushko (*corresponding author*) — Junior Researcher, Laboratory of Photobiology, Institute of Biophysics SB RAS, Federal Research Center 'Krasnoyarsk Science Center SB RAS', Akademgorodok Street, 50/50, 660036, Krasnoyarsk, Russia; Assistant of Department of Biophysics, School of Fundamental Biology and Biotechnology, Siberian Federal University, Svobodny Avenue, 79, 660041, Krasnoyarsk, Russia; e-mail: kkovel@yandex.ru; https://orcid.org/0000-0002-4524-6413

Andrei Valerievich Zenkov — Student of Department of Biophysics, School of Fundamental Biology and Biotechnology, Siberian Federal University, Svobodny Avenue, 79, 660041, Krasnoyarsk, Russia; e-mail: andrei.zenkow222@yandex.ru

Nadezhda Stepanovna Kudryasheva — Doctor of Physics and Mathematical Sciences, Leading Researcher of Laboratory of Photobiology, Institute of Biophysics SB RAS, Federal Research Center 'Krasnoyarsk Science Center SB RAS', Akademgorodok Street, 50/50, 660036, Krasnoyarsk, Russia; Professor of Department of Biophysics, School of Fundamental Biology and Biotechnology, Siberian Federal University, Svobodny Avenue, 79, 660041, Krasnoyarsk, Russia; e-mail: n-qdr@yandex.ru; https://orcid.org/0000-0001-5315-8002

Author Contributions

The manuscript was written through contributions of all authors. All authors have given approval to the final version of the manuscript. CRediT: **Ekaterina Sergeevna Sushko** methodology, investigation, formal analysis, visualization, writing-review & editing; **Andrei Valerievich Zenkov** investigation, formal analysis, visualization, writing-review & editing; **Nadezhda Stepanovna Kudryasheva** conceptualization, formal analysis, funding acquisition, project administration, supervision, validation, writing-original draft, writing-review & editing.

Conflicts of Interest

The authors declare no conflict of interest.

References

1 Bulich, A.A., & Isenberg, D.L. (1981). Use of the luminescent bacterial system for the rapid assessment of aquatic toxicity. *ISA transactions*, *20*(1), 29–33.

2 Girotti, S., Ferri, E.N., Fumo, M.G., & Maiolini, E. (2008). Monitoring of environmental pollutants by bioluminescent bacteria. *Analytica Chimica Acta*, *608*(1), 2–29. https://doi.org//10.1016/j.aca.2007.12.008.

3 Roda, A., Pasini, P., Mirasoli, M., Michelini, E., & Guardigli, M. (2004). Biotechnological application of bioluminescence and chemiluminescence. *Trends in Biotechnology*, *22*(6), 295–303. https://doi.org//10.1016/j.tibtech.2004.03.011.

4 Abbas, M., Adil, M., Ehtisham-ul-Haque, S., Munir, B., Yameen, M., Ghaffar, A., Shar, G.A., Tahir, M.A., & Iqbal, M. (2018). *Vibrio fischeri* bioluminescence inhibition assay for ecotoxicity assessment: A review. *Science of the Total Environment*, *626*, 1295–1309. https://doi.org//10.1016/j.scitotenv.2018.01.066.

5 Kudryasheva, N.S. (2006). Bioluminescence and exogenous compounds: Physico-chemical basis for bioluminescent assay. *Journal of Photochemistry and Photobiology B: Biology*, *83*(1), 77–86, https://doi.org/10.1016/j.jphotobiol.2005.10.003.

6 Kudryasheva, N., Vetrova, E., Kuznetsov, A., Kratasyuk, V., & Stom, D. (2002). Bioluminescence assays: Effects of quinones and phenols. *Ecotoxicology and Environmental Safety*, *53*(2), 221–225. https://doi.org/10.1006/eesa.2002.2214.

7 Kudryasheva, N., Kratasyuk, V., Esimbekova, E., Vetrova, E., Nemtseva, E., & Kudinova, I. (1998). Development of bioluminescent bioindicators for analysis of environmental pollution. *Field Analytical Chemistry & Technology*, *2*(5), 277–280. https://doi.org/10.1002/(SICI)1520-6521(1998)2:5 %3C277::AID-FACT4 %3E3.0.CO;2-P.

8 Kratasyuk, V.A. (1990). Principles of luciferase biotesting. In B. Jezowska-Trzebiatowska, B. Kochel, J. Stawinski, & I. Strek (Eds.), *Biological Luminescence* (pp. 550–558). World Scientific, Singapore.

9 Vetrova, E.V., Kudryasheva, N.S., & Kratasyuk, V.A. (2007). Redox compounds influence on the NAD(P)H:FMN–oxidoreductase–luciferase bioluminescent system. *Photochemical & Photobiological Sciences*, *6*(1), 35–40. https://doi.org/10.1039/b608152e.

10 Kudryasheva, N.S., Kovel, E.S., Sachkova, A.S., Vorobeva, A.A., Isakova, V.G., & Churilov, G.N. (2017). Bioluminescent enzymatic assay as a tool for studying antioxidant activity and toxicity of bioactive compounds. *Photochemistry and Photobiology*, *93*(2), 536–540. https://doi.org/10.1111/php.12639.

11 Sachkova, A.S., Kovel, E.S., Churilov, G.N., Stom, D.I., & Kudryasheva, N.S. (2019). Biological activity of carbonic nanostructures–Comparison via enzymatic bioassay. *Journal of Soils and Sediments*, *19*, 2689–2696. https://doi.org/10.1007/s11368-018-2134-9.

12 Kovel, E.S., Kicheeva, A.G., Vnukova, N.G., Churilov, G.N., Stepin, E.A., & Kudryasheva, N.S. (2021). Toxicity and antioxidant activity of fullerenol $C_{60,70}$ with low number of oxygen substituents. *International Journal of Molecular Sciences*, *22*(12), 6382. https://doi.org/10.3390/ijms22126382.

13 Sushko, E.S., Vnukova, N.G., Churilov, G.N., & Kudryasheva, N.S. (2022). Endohedral Gd-containing fullerenol: Toxicity, antioxidant activity, and regulation of reactive oxygen species in cellular and enzymatic systems. *International Journal of Molecular Sciences*, *23*(9), 5152. https://doi.org/10.3390/ijms23095152.

14 Stepin, E.A., Sushko, E.S., Vnukova, N.G., Churilov, G.N., Rogova, A.V., Tomilin, F.N., & Kudryasheva, N.S. (2024). Effects of Endohedral Gd-containing fullerenols with a different number of oxygen substituents on bacterial bioluminescence. *International Journal of Molecular Sciences*, *25*(2), 708. https://doi.org/10.3390/ijms25020708.

15 Bondarenko, L.S., Kovel, E.S., Kydralieva, K.A., Dzhardimalieva, G.I., Illés, E., Tombácz, E., Kicheeva, A.G., & Kudryasheva, N.S. (2020). Effects of modified magnetite nanoparticles on bacterial cells and enzyme reactions. *Nanomaterials*, *10*(8), 1499. https://doi.org/10.3390/nano10081499.

16 Kicheeva, A.G., Sushko, E.S., Bondarenko, L.S., Kydralieva, K.A., Pankratov, D.A., Tropskaya, N.S., Dzeranov, A.A., Dzhardimalieva, G.I., Zarrelli, M., & Kudryasheva, N.S. (2023). Functionalized magnetite nanoparticles: Characterization, bioeffects, and role of reactive oxygen species in unicellular and enzymatic systems. *International Journal of Molecular Sciences*, *24*(2), 1133. https://doi.org/10.3390/ijms24021133.

17 Yang, S., & Lian, G. (2020). ROS and diseases: Role in metabolism and energy supply. *Molecular and Cellular Biochemistry*, *467*, 1–12. https://doi.org/10.1007/s11010-019-03667-9.

18 Yang, B., Chen, Y., & Shi, J. (2019). Reactive oxygen species (ROS)-based nanomedicine. *Chemical Reviews*, *119*(8), 4881–4985. https://doi.org/10.1021/acs.chemrev.8b00626.

19 Sies, H., & Jones, D.P. (2020). Reactive oxygen species (ROS) as pleiotropic physiological signalling agents. *Nature Reviews Molecular Cell Biology*, *21*(7), 363–383. https://doi.org/10.1038/s41580-020-0230-3.

20 Fan, J., Ren, D., Wang, J., Liu, X., Zhang, H., Wu, M., & Yang, G. (2020). Bruceine D induces lung cancer cell apoptosis and autophagy via the ROS/MAPK signaling pathway in vitro and in vivo. *Cell Death & Disease*, *11*(2), 126. https://doi.org/10.1038/s41419-020-2317-3.

21 Su, L.-J., Zhang, J.-H., Gomez, H., Murugan, R., Hong, X., Xu, D., Jiang, F., & Peng, Z.-Y. (2019). Reactive oxygen species-induced lipid peroxidation in apoptosis, autophagy, and ferroptosis. *Oxidative Medicine and Cellular Longevity*, *2019*, 5080843. https://doi.org/10.1155/2019/5080843.

22 Tavsan, Z., & Kayali, H.A. (2019). Flavonoids showed anticancer effects on the ovarian cancer cells: Involvement of reactive oxygen species, apoptosis, cell cycle and invasion. *Biomedicine & Pharmacotherapy*, *116*, 109004. https://doi.org/10.1016/j.biopha.2019.109004.

23 Fleury, C., Mignotte, B., & Vayssière, J.-L. (2002). Mitochondrial reactive oxygen species in cell death signaling. *Biochimie*, *84*, 131–141. https://doi.org/10.1016/S0300-9084(02)01369-X.

24 Fernandez-Gil, B.I., Guerra-librero, A., Shen, Y.-Q., Florido, J., Martínez-Ruiz, L., García-López, S., Adan, C., Rodríguez-Santana, C., Acuña-Castroviejo, D., Quiñones-Hinojosa, A., Fernández-Martínez, J., Moneim, A.E.A., López, L.C., Ferrer, J.M.R. & Escames, G. (2019). Melatonin enhances cisplatin and radiation cytotoxicity in head and neck squamous cell carcinoma by stimulating mitochondrial ROS generation, apoptosis, and autophagy. *Oxidative Medicine and Cellular Longevity*, *2019*, 7187128. https://doi.org/10.1155/2019/7187128.

25 Gheena, S., & Ezhilarasan, D. (2019). Syringic acid triggers reactive oxygen species–mediated cytotoxicity in $HepG_2$ cells. *Human and Experimental Toxicology*, *38*(6), 694–702. https://doi.org/10.1177/0960327119839173.

26 Sies, H., Belousov, V.V., Chandel, N.S., Davies, M.J., Jones, D.P., Mann, G.E., Murphy, M.P., Yamamoto, M., & Winterbourn, C. (2022). Defining roles of specific reactive oxygen species (ROS) in cell biology and physiology. *Nature Reviews Molecular Cell Biology*, *23*(7), 499–515. https://doi.org/10.1038/s41580-022-00456-z.

27 Jakubczyk, K., Dec, K., Kałduńska, J., Kawczuga, D., Kochman, J., & Janda, K. (2020). Reactive oxygen species — sources, functions, oxidative damage. *Polski Merkuriusz Lekarski*, *48*(284), 124–127.

28 Hasanuzzaman, M., Bhuyan, M.H.M.B., Parvin, K., Bhuiyan, T.F., Anee, T.I., Nahar, K., Hossen, M.S., Zulfiqar, F., Alam, M.M., & Fujita, M. (2020). Regulation of ROS metabolism in plants under environmental stress: A review of recent experimental evidence. *International Journal of Molecular Sciences*, *21(22)*, 8695. https://doi.org/10.3390/ijms21228695.

29 Lemly, A.D., & Smith, G.J. (1987). Aquatic Cycling of Selenium: Implications for Fish and Wildlife. *Fish and Wildlife Leaflet 12*. Fish and Wildlife Service: Washington, DC, USA.

30 Lin, W., Zhang, J., Xu, J. -F., & Pi, J. (2021).The advancing of selenium nanoparticles against infectious diseases. *Frontiers in Pharmacology*, *12*, 682284. https://doi.org/10.3389/fphar.2021.682284.

31 Sumana, S.L., Chen, H., Shui, Y., Zhang, C., Yu, F., Zhu, J., & Su, S. (2023). Effect of dietary selenium on the growth and immune systems of fish. *Animals*, *13*(18), 2978. https://doi.org/10.3390/ani13182978.

32 Werkneh, A.A., Gebretsadik, G.G. & Gebru, S.B. (2023). Review on environmental selenium: Occurrence, public health implications and biological treatment strategies. *Environmental Challenges*, *11*, 100698. https://doi.org/10.1016/j.envc.2023.100698.

33 Lemly, A.D. (2004). Aquatic selenium pollution is a global environmental safety issue. *Ecotoxicology and Environmental Safety*, *59*(1), 44–56. https://doi.org/10.1016/S0147-6513(03)00095-2.

34 Serov, D.A., Khabatova, V.V., Vodeneev, V., Li, R., & Gudkov, S.V. (2023). A Review of the antibacterial, fungicidal and antiviral properties of selenium nanoparticles. *Materials*, *16*(15), 5363. https://doi.org/10.3390/ma16155363.

35 Ojeda, J.J., Merroun, M.L., Tugarova, A.V., Lampis, S., Kamnev, A.A., & Gardiner, P.H.E. (2020*)*. Developments in the study and applications of bacterial transformations of selenium species. *Critical Reviews in Biotechnology*, *40*(8), 1250–1264. https://doi.org/10.1080/07388551.2020.1811199.

36 Sonkusre, P., Nanduri, R. Gupta, P. & Cameotra, S.S. (2014). Improved extraction of intracellular biogenic selenium nanoparticles and their specificity for cancer chemoprevention. *Journal of Nanomedicine & Nanotechnology*, *5*(2), 1000194. http://dx.doi.org/10.4172/2157-7439.1000194.

37 Yazdi, M.H. Mahdavi, M. Setayesh, N. Esfandyar, M., & Shahverdi, A.R. (2013). Selenium nanoparticle-enriched *Lactobacillus brevis* causes more efficient immune responses in vivo and reduces the liver metastasis in metastatic form of mouse breast cancer. *DARU Journal of Pharmaceutical Sciences*, *21*, 33. https://doi.org/10.1186/2008-2231-21-33.

38 Eszenyi, P., Sztrik, A., Babka, B., & Prokisch, J. (2011). Elemental, nano-sized (100-500 nm) selenium production by probiotic lactic acid bacteria. *International Journal of Bioscience Biochemistry and Bioinformatics*, *1*(2), 148–152. https://doi.org/10.7763/IJBBB.2011.V1.27.

39 Tugarova, A.V., Mamchenkova, P.V., Khanadeev, V.A., & Kamnev, A.A. (2020). Selenite reduction by the rhizobacterium *Azospirillum brasilense*, synthesis of extracellular selenium nanoparticles and their characterization. *New Biotechnology*, *58*, 17–24. https://doi.org/10.1016/j.nbt.2020.02.003.

40 Kamnev, A.A., Mamchenkova, P.V., Dyatlova, Y.A., & Tugarova, A.V. (2017). FTIR spectroscopic studies of selenite reduction by cells of the rhizobacterium *Azospirillum brasilense* Sp7 and the formation of selenium nanoparticles. *Journal of Molecular Structure*, *1140*, 106–112. https://doi.org/10.1016/j.molstruc.2016.12.003.

41 Tugarova, A.V., Mamchenkova, P.V., Dyatlova, Y.A., & Kamnev, A.A. (2018). FTIR and Raman spectroscopic studies of selenium nanoparticles synthesised by the bacterium *Azospirillum thiophilum*. *Spectrochimica Acta, Part A: Molecular and Biomolecular Spectroscopy*, *192*, 458–463. https://doi.org/10.1016/j.saa.2017.11.050.

42 Kuznetsov, A.M., Rodicheva, E.K., & Shilova, E.V. (1996). Bioassay based on lyophilized bacteria. *Biotekhnologiya*, *9*, 57–61 (in Russian).

43 Gmurman, V.E. (1968). *Fundamentals of probability theory and mathematical statistics.* English translation edited by Berenblut, I.I. Iliffe Book Ltd.: London, Great Britain.

44 Nemtseva, E.V., & Kudryasheva, N.S. (2007). The mechanism of electronic excitation in bacterial bioluminescent reaction. *Russian Chemical Reviews*, *76*(1), 101–112. https://doi.org/10.1070/RC2007v076n01ABEH003648.

45 Hastings, J.W., & Gibson, Q.H. (1963). Intermediates in the bioluminescent oxidation of reduced flavin mononucleotide. *Journal of Biological Chemistry*, *238*(7), 2537–2554. https://doi.org/10.1016/S0021-9258(19)68004-X.

46 Kolesnik, O.V., Rozhko, T.V., Lapina, M.A., Solovyev, V.S., Sachkova, A.S., & Kudryasheva, N.S. (2021). Development of cellular and enzymatic bioluminescent assay systems to study low-dose effects of thorium. *Bioengineering*, *8*(12), 194. https://doi.org/10.3390/bioengineering8120194.

How to Cite: Kolesnik, O.V., Grabovoy, A.S., Badun, G.A., Churilov, G.N., & Kudryasheva, N.S. (2024) Radioprotective Properties of Fullerenol: Cellular, Biochemical and Physicochemical Approaches. *Eurasian Journal of Chemistry, 29, 3(115), 72-81.* https://doi.org/10.31489/2959-0663/3-24-9

Article

Received: 9 June 2024 | Revised: 5 August 2024 |
Accepted: 13 August 2024 | Published online: 13 September 2024

UDC 544.344.015.4-17

https://doi.org/10.31489/2959-0663/3-24-9

Olga V. Kolesnik[1,2*], Aleksey S. Grabovoy[2], Gennadii A. Badun[3], Grigoriy N. Churilov[4], Nadezhda S. Kudryasheva[1,2]

[1]*Federal Research Center "Krasnoyarsk Science Center" of the Siberian Branch of the Russian Academy of Sciences, "Institute of Biophysics of the Siberian Branch of the Russian Academy of Sciences", Krasnoyarsk, Russia;*
[2]*Siberian Federal University, Krasnoyarsk, Russia;*
[3]*Lomonosov Moscow State University, Moscow, Russia;*
[4]*Federal Research Center "Krasnoyarsk Science Center" of the Siberian Branch of the Russian Academy of Sciences, "Institute of Physics of the Siberian Branch of the Russian Academy of Sciences", Krasnoyarsk, Russia*
*(*Corresponding author's e-mail: olga.kolesnik.krsk@gmail.com)*

Radioprotective Properties of Fullerenol: Cellular, Biochemical and Physicochemical Approaches

The search for optimal radioprotective methods and tools under low-dose radiation exposures represents a pressing issue in the field of modern radioecology. The objective of the study was to investigate the radioprotective properties of fullerenol $C_{60,70}O_y(OH)_x$, ($x+y$ = 24–28), a water-soluble polyhydroxylated fullerene derivative with an electron-deficient aromatic carbon structure. Tritium, a radionuclide of low decay energy, was selected to simulate an exposure to low-dose irradiation (< 0.05 Gy). We applied luminous marine bacteria *Photobacterium phosporeum* as a model cellular object to monitor radiation bioeffects; the bioluminescence intensity of the bacteria was used as a tested biological parameter. Tritium activated the bacterial luminescence; the addition of fullerenol (< $3\cdot10^{-3}$ g/L) "mitigated" the activation, thus revealing the radioprotective capacity of fullerenol for the marine microorganism. To evaluate the mechanisms of radioprotection of fullerenol in tritiated water, we investigated the effects of fullerenol on: (1) the content of reactive oxygen species and (2) the intensity of bioluminescence in the bacterial enzymatic reaction. Tritiated water produced moderate deviations from the control values, whereas the addition of fullerene brought these values closer to the 'control' ones. All observed effects were attributed to variations in the ionic balance of the aqueous medium, which resulted in the activation of bacterial functions through cell membranes.

Keywords: tritium, fullerenol, radioprotection, luminescence, bacteria, bioassay, enzymes, reactive oxygen species.

Introduction

Low-intensity radioactive contamination is causing increasingly serious environmental problems. These problems usually results from the intensive exploitation of natural resources and nuclear power plants operation. The sensitivity of organisms to low doses (<0.1Gy) is a subject of interest for scientists. Variations in sensitivity in different molecular environments are of particular interest; molecules of natural and artificial origin can serve as radiomodifying agents of varying efficacy.

We consider tritium (^{3}H) as a suitable object to examine low-dose bioeffects in water ecosystems. Tritium is a widespread radioisotope with a half-life of 12.4 years and a low energy of radioactive decay (5.7 keV) [1, 2]. Tritium occurs in nature mainly in the form of tritiated water (HTO) [3]. There are now three main sources of tritium: (1) natural formation in the upper layers of the atmosphere as a result of the splitting of nuclides by cosmic rays and reactions involving the capture of nitrogen and oxygen particles [4]; (2) residual activity from nuclear weapons tests [5]; and (3) decay products of the nuclear fuel cycle [3]. The monitoring of tritium concentrations in the vicinity of power plants is currently a subject of heightened interest. As tritium levels decline, there is a need to monitor lower levels of tritium activity in the environment [6–8].

The unique ability of ^{3}H to substitute protium (^{1}H) in biological macromolecules is a reason of tritium' chronic toxicity. Tritium decays to form primary products, namely ionized isotope of helium-3 ($^3He^+$), an electron, and antineutrino:

$$^3_1\mathrm{H} \xrightarrow{\beta^-} {}^3_2\mathrm{He}^+ + e^- + \tilde{\nu} \qquad (1)$$

The bioeffects of tritium are caused by charged products of its radioactive decay (i.e. cation of helium ${}^{3}_{2}He^{+}$ and electron). The decay products initiate a charge transfer chain in external solutions and within the organisms themselves. It is important to note the extreme activity of the helium ion ${}^{3}_{2}He^{+}$, which rigidly accepts an electron from the aqueous environment or organic molecules, completing its outer shell to form a stable noble gas shell. The introduction of tritium into organisms results in the disruption of hydrogen bonds within living cells, thereby preventing the synthesis of organic structures [9, 10]. Furthermore, the electron-acceptor activity of ${}^{3}_{2}He^{+}$ leads to the disruption of the structure of crucial macromolecules responsible for the vital activity of living organisms, namely DNA, proteins, enzymes [11, 12].

Therefore, ionization of an aqueous medium is usually the main external factor under low-dose tritium exposures. Ionization affects the outer cell walls, resulting in membrane activation and related intracellular processes. This effect is known to promote the activation of bioluminescence of marine bacteria in tritiated water [12–17] and can be considered as a biophysical mechanism underlying the “hormesis” phenomenon [18–23].

The primary application of luminous bacteria is in environmental toxicity monitoring, as evidenced by numerous studies [12, 24–27]. Rapidness, accuracy, sensitivity and simplicity are the advantages of bacteria-based bioluminescent assays. The method is based on the changes in luminescence intensity under exposure to an analyzed sample. The bioassay detects ecosystem conditions upon exposure to toxic substances, in both acute and chronic forms of toxicity. Interference with bacterial metabolism at any level is indicated by a change in light emission. The effects of toxicants on the enzymatic chemiluminescent processes responsible for the luminescence of bacteria are of a particular interest. The system of two enzymatic reactions (2, 3) is commonly used as a model for such processes. This system is based on two bacterial enzymes, namely luciferase and NADH:FMN-oxidoreductase.

$$\mathrm{FMN + NADH \xrightarrow{NADH:FMN\text{-}oxidoreductase} FMN \cdot H^{-} + NAD^{+}} \quad (2)$$

$$\mathrm{FMN \cdot H_2 + RCHO + O_2 \xrightarrow{luciferase} FMN + RCOOH + H_2O + h\upsilon} \quad (3)$$

This coupled enzyme system has been employed as a luminescent enzymatic bioassay since 1990 [28]. A detailed description of this system has been presented in [29, 30]. The effects of various toxicant groups on the enzyme system have been reviewed in [31].

Bioluminescence systems of varying complexities (cell-based and enzyme-based) permit the elucidation of patterns of toxicant exposure at two distinct levels: cellular and biochemical.

Biological responses to low-dose radiation are usually explained by the involvement of reactive oxygen species (ROS) in metabolic processes [32, 33]. ROS comprise a group of mutually transforming and chemically active forms of oxygen-containing compounds [34] with lifetimes ranging from nanoseconds to hours [35]. ROS can occur in biochemical reactions as free radicals, ion-radicals (positively or negatively charged), and molecules. The group of ROS includes, but is not limited to, the following compounds: superoxide anion radicals ($O_2{\cdot}-$), hydrogen peroxide (H_2O_2), hydroxyl radical ($\cdot OH$), singlet oxygen (${}^{1}O_2$), hypochlorite (HOCl), hydroperoxyl radical ($HOO\cdot$), and others.

Traditionally, ROS are thought to cause oxidative stress and cell damage [33]. ROS are constantly produced by living organisms during respiration, as well as modified and consumed during metabolic activity. Currently, the beneficial functions of low and moderate doses of ROS are known and discussed; ROS are responsible for many vital physiological functions, namely proliferation, migration, differentiation and others [36–38]. Their roles vary considerably depending on the ROS types, the reactions in which they are involved and the target molecules with which they react. ROS are natural by-products of metabolic oxidative processes and are involved to cell signal transmission and homeostasis. The involvement of ROS in the bioeffects of nanostructures is currently under active investigation [39–41].

It is known that radioactive decay of radioisotopes in aerated aqueous solutions leads to the ROS formation [14, 42, 43], which can affect inhabitants of aquatic environments. The ROS involvement in the bioeffects of radionuclides and gamma-radiation has been studied in [12, 15, 42, 43]; luminescent bacteria and their enzymatic reactions have been used as model biological objects in these studies. Biological responses to radiation can vary depending on the molecular composition of aqueous solutions. The presence of organic molecules in water solutions can alter the ionic and radical states of radionuclides, affecting, thereby, the environment of aquatic inhabitants. For example, humic substances, products of natural oxidative decomposition of organic matter in sediments, are known to be native attenuators of radiotoxicity in aqueous

solutions. Direct and indirect mechanisms of radioprotective activity of humic substances have been reviewed [15, 44].

Fullerenols are water-soluble derivatives of fullerenes with considerable potential as artificial radioprotectors. They represent a promising class of compounds with applications in physics, chemistry, nanobiotechnology, pharmacology, and biomedicine. The hypothetical structure of the fullerenol is illustrated in Figure 1B.

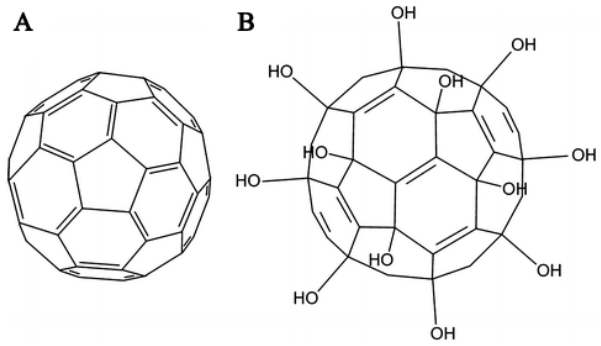

Figure 1. Hypothetical structure of fullerene C_{60} (*A*); fullerenol $C_{60}(OH)_{24}$ (*B*) [45]

Considerable attention has been devoted to the physicochemical properties of fullerenes and fullerenols, with a particular focus on their capacity to generate and capture ROS and reactive nitrogen forms [46, 47]. Additionally, fullerenol has been demonstrated to influence the formation of water radiolysis products, including H_2O_2 and hydroxyl radicals. Furthermore, it has been shown to prevent DNA and protein damage.

The idea of using fullerene derivatives to protect cells is related to their chemical and biological properties [49, 50]. Fullerenes and their derivatives are known to be effective radical traps and antiradical agents due to their highly conjugated π-system and low-energy vacant molecular orbitals [51]. The radioprotective activity of fullerenols has been reported earlier in [52, 53]. However, these studies focused on higher organisms; marine microorganisms and their enzymes have not yet been used.

The objective of the study was to investigate the radioprotective activity of fullerenol $C_{60,70}O_y(OH)_x$, (x = 22–24, y = 2–4) in tritiated water (HTO) under exposure to low-dose radiation (< 0.05 Gy). Marine luminescent bacteria were selected as the model biological object for this study. The impact of fullerenol on the luminescence intensity of the bacteria, the rate of their enzymatic reactions, and the ROS content in the bacterial suspensions were investigated.

Experimental

Preparations and Reagents

The bacterial samples were prepared from lyophilized bacteria *Photobaterium phosphoreum* according to the standard technique [15, 54].

The enzymatic kit was previously described in reference [55]; it was produced at the Institute of Biophysics, SB RAS, Krasnoyarsk, Russia. The chemicals required for the enzymatic assay and assay procedure were provided as follows [55].

Tritiated water, HTO, JSC Isotope, Russia, was used as a source of tritium. The preparation of HTO was described in [15]. The final specific radioactivities in the aqueous media were 0.03 and 500 MBq/L.

Fullerenol $C_{60,70}O_y(OH)_x$, where (x+y = 24–28), was synthesized and characterized as described in [55]. The preparation was produced by fullerene hydroxylation in nitric acid followed by the hydrolysis of the polynitrofullerenes [56]. The fullerenol preparation was characterized by infrared spectroscopy in the KBr matrix using a Fourier spectrometer VERTEX 70 (Bruker Optik GmbH, Ettlingen, Germany). The number of -OH groups was estimated by X-ray photoelectron spectroscopy using a UNI-SPECS spectrometer (SPECS Gmbh, Berlin, Germany) [57, 58] Chromatographic analysis showed that the fullerenol preparation involved 60 % of $C_{60}O_y(OH)_x$ and 40 % of $C_{70}O_y(OH)_x$.

Fullerenol solutions were prepared in distilled water. The bioluminescence intensity was preliminary measured in a wide range of fullerenol concentrations (10^{-16}–10^{-1} g/L) in order to select concentrations, which did not change the bioluminescence intensity. The following fullerenol concentrations were selected

for further experiments: 10^{-15}–$3 \cdot 10^{-3}$ g/L. The results obtained were in agreement with the data presented in [55, 59, 60].

The chemiluminescence reagents were described in [60].

Luminescent Assay System Composition

Bacterial Assay

Bacterial bioluminescence kinetics was studied in non-radioactive samples (controls), as well as in radioactive samples in the absence and presence of fullerenol.

Enzymatic Assay

The solutions of chemicals were prepared as described in [60].

The enzyme solutions were non-radioactive (control) samples, radioactive samples and radioactive samples with fullerenol.

Bioluminescence Registration

A standard procedure for the bioluminescence measurements was described in detail in [12, 54]. Bioluminescence intensities of the control and radioactive samples were measured and compared in the presence and absence of fullerenol similar to [15].

The bioluminescence intensity was registered as described in [61, 62].

Chemiluminescence Measurements

The luminol chemiluminescent method [63–65] was used.

Statistical processing

All measurements were carried out in 4-6 replicates. Statistical evaluations were carried out employing the Student's t-test. The experimental error of the measurements did not exceed 12 %.

Results and Discussion

We studied the effects of HTO on bacterial luminescence in the absence and presence of fullerenol. The results are shown in Figure 2.

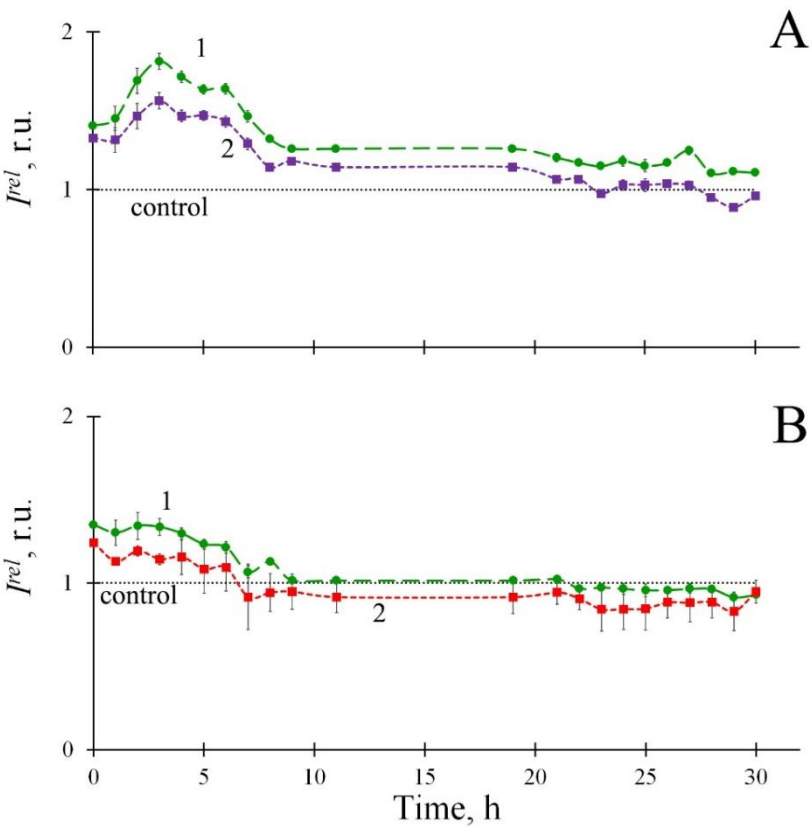

Figure 2. Kinetics of bacterial bioluminescence, I^{rel}, in HTO in the absence (1) and presence (2) of fullerenol. Specific activity of HTO: (A) 500 MBq/L; (B) 0.03 MBq/L. Fullerenol concentration: (A) 10^{-11} g/L; (B) 10^{-9} g/L

Two concentrations of HTO were chosen as examples, namely 500 and 0.03 MBq/L. The independence of bacterial luminescence response on concentration/radioactivity of HTO was found and discussed previously [13, 26] in a wide range of HTO concentrations (10^{-3} – $2{\cdot}10^{2}$ MBq/L).

Activation of bioluminescence ($I^{rel} > 1$) can be seen in the absence of fullerenol (Fig. 2A, B, curves 1) from the start of the chronic exposure. Over time, activation decreased to the control values.

Tritium activation was observed in previous works [12, 16, 26]; it was associated with the "hormesis" model [18–23], which always includes an activation stage. The activation was explained by the ionization of the aqueous medium with subsequent stimulation of cellular processes, membrane and enzymatic, as well as accumulation of ROS.

In the presence of fullerenol (Fig. 2A, B, curves 2) a shift of the kinetic curves closer to the control was observed, revealing a 'mitigation' of the tritium effects. This mitigation can be explained by the ability of fullerenol to reversibly accept/donate electron density, thereby changing a radical state of aqueous media [41]. Therefore, Figures 2A, B demonstrate the radioprotective ability of fullerenol in HTO. The ability is quantitatively comparable to that of humic substances — natural detoxifying and radioprotective agents [15].

To elucidate the mechanism of radioprotection, the effect of fullerenol (at 10^{-11} and 10^{-9} g/L) on the (i) content of ROS (ROS^{rel}) in bacterial suspension and (ii) the intensity of bioluminescence of the enzymatic system (I^{rel}) — were studied in HTO (500 and 0.03 MBq/L).

As an example, Figure 3 combines three types of the experimental measurements in HTO in the absence and presence of fullerenol: (A) bacterial luminescence intensity, I^{rel}, (B) ROS content in the bacterial suspension, ROS^{rel}, and (C) luminescence intensity of the enzyme system, I^{rel}. The exposure time of 4 h was chosen for the presentation. Bacterial luminescence intensity, I^{rel}, is presented in Figure 3A (green and red columns) according to the data in Figure 2A.

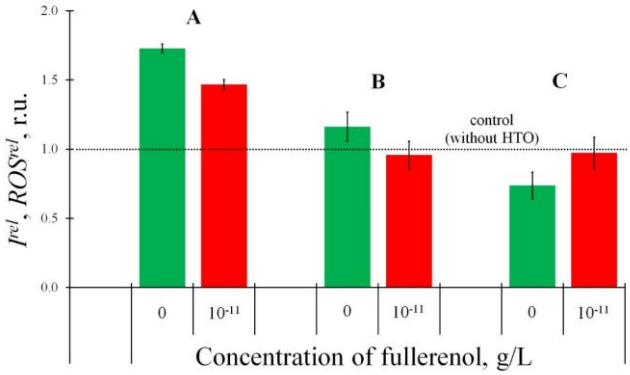

Figure 3. Relative luminescence intensity, I^{rel}, and ROS content, ROS^{rel}, in the absence and presence of fullerenol, 10^{-11} g/L. Time of exposure was 4 h; HTO specific radioactivity was 500 MBq/L. (*A*) — bacterial luminescence, (*B*) — ROS content, (*C*) — luminescence of the enzyme system

We registered an insignificant but reliable increase of ROS content in the bacterial suspension, ROS^{rel}, exposed to HTO — up to *ca.* 1.2 (Fig. 3B, green column). A similar increase in ROS content under similar conditions was previously observed in [12, 15]; it was attributed to the intensification of bacterial metabolic processes, resulting in additional ROS production. It is noteworthy that the luminol chemiluminescence method did not register an increase in the content of ROS in HTO media without bacteria [12–14], but the addition of bacteria resulted in a significant increase in the content of ROS [12]. It was concluded that the higher level of ROS in bacterial suspensions exposed to HTO is the result of a multi-step process involving: ionization of the aqueous media due to radioactive decay of tritium, stimulation of bacterial membrane receptors, intensification of intracellular processes including oxidative ones, and extra ROS production into the external media.

The addition of fullerenol (10^{-11} g/L) brought ROS^{rel} closer to the control (red column, Fig. 3B), probably, due to reversible electron-donor activity of fullerenol and related decrease of ion-radical oxygen particles (components of ROS group).

Suppression of the bioluminescence intensity of the enzyme system, I^{rel}, down to *ca.* 0.75 (green column, Fig. 3C) could be explained in a similar way: it is probably caused by additional ionization of the media in the presence of HTO. Obviously, the suppression of the intensity of the bioluminescent enzyme system

can not be responsible for the activation of bacterial bioluminescence by HTO (Fig. 2A, B). This result corresponds to the conclusion [12–17] on the determining role of the bacterial cell membrane in the activation of bacterial bioluminescence under the exposure to tritium. An approach of I^{rel} to the control (Fig. 3C, red column) could be similarly explained by deionization of water media induced by fullerenol.

Therefore, we can explain the radioprotective ability of fullerenols in bacteria media by (1) the tendency to reversible electron donation/reception and (2) the predominant role of the cell membrane of bacteria exposed to tritium. The same ability of fullerenol in HTO is probably responsible for moderate effects on ROS levels and luminescence of the enzymatic system. However, the latter two factors are not decisive for the radioprotective ability of fullerenol towards bacterial cells.

Conclusions

The aim of this work was to evaluate the radioprotective potential of fullerenol, a water-soluble polyhydroxylated fullerene derivative with an electron-deficient aromatic carbon structure, and an effective catalyst due to its ability to reversible electron acceptance. A radionuclide with a low decay energy, tritium, was chosen to simulate an exposure to low-dose irradiation (< 0.05 Gy). The luminous marine bacterium was used as a model cellular object to monitor the effect of radiation on its luminescence as a physiological function of the organism. Tritium activated the bacterial luminescence; the addition of fullerenol ($< 3\cdot10^{-3}$ g/L) "mitigated" the activation effect, bringing the kinetic curve closer to the "control" (bacteria without tritium). Thus, the radioprotective ability of fullerenol for a marine microorganism was demonstrated.

Biochemical and physicochemical mechanisms of radioprotection were of particular interest. We studied the ROS content in bacterial suspensions and the luminescence intensity of the bacterial enzymatic reaction; two concentrations of tritiated water were used (0.03 and 500 MBq/L), concentrations of fullerenol varied at $< 3\cdot10^{-3}$ g/L. Tritium produced moderate deviations from control values (positive ones for ROS content and negative ones for luminescence of the enzyme system). The addition of fullerene brought these values closer to the 'control' ones. All effects of tritium and fullerenol were attributed to changes in the ionic balance in aqueous media, resulting in activation of bacterial functions via the cell membrane. A direct influence of tritium and fullerenol on intracellular enzyme processes was not confirmed. The variation of ROS content in bacteria suspensions is probably a secondary result related to bacterial metabolism and its adaptation to external media.

Further studies should be aimed to explore bacterial membrane functions under various conditions of low-dose radioactive exposures. Additionally, variations of potential radioprotectors of different chemical structure are of practical interest.

Funding

This research was funded by the Russian Science Foundation No. 23-26-10018, Krasnoyarsk Regional Science Foundation. The purification of enzymes was supported by the State Assignment of the Ministry of Science and Higher Education of the Russian Federation, project No. FWES-2024-0018.

*Author Information**

**The authors' names are presented in the following order: First Name, Middle Name and Last Name*

Olga Vladislavovna Kolesnik (*corresponding author*) — Junior Researcher, Federal Research Center "Krasnoyarsk Science Center" of the Siberian Branch of the Russian Academy of Sciences, "Institute of Biophysics of the Siberian Branch of the Russian Academy of Sciences", Akademgorodok, 50/50, 660036, Krasnoyarsk, Russia; Administrative Coordinator, Department of Biomedical Systems and Complexes, Siberian Federal University, Svobodny ave., 79, 660041, Krasnoyarsk, Russia; e-mail: olga.kolesnik.krsk@gmail.com; https://orcid.org/0000-0002-4637-875X

Aleksey Sergeevich Grabovoy — Student, Department of Biophysics, Siberian Federal University, Svobodny ave., 79, 660041, Krasnoyarsk, Russia; e-mail: lexxx1595@gmail.com

Gennadii Alexandrovich Badun — Candidate of Chemical Sciences, Associate Professor, Department of Chemistry, Lomonosov Moscow State University, Leninskie Gory 1 build. 3, 119991, Moscow, Russia; e-mail: badunga@yandex.ru; https://orcid.org/0000-0002-9792-8432

Grigory Nikolaevich Churilov — Doctor of Technical Sciences, Professor, Head of Laboratory of the Analytical Methods for Substance Research, Federal Research Center "Krasnoyarsk Science Center" of the

Siberian Branch of the Russian Academy of Sciences, "Institute of Physics of the Siberian Branch of the Russian Academy of Sciences", Akademgorodok 50/38, 660036, Krasnoyarsk, Russia; e-mail: churilov@iph.krasn.ru; https://orcid.org/0000-0003-2889-490X

Nadezhda Stepanovna Kudryasheva — Doctor of Sciences in Physics and Mathematics, Leading Researcher, Federal Research Center "Krasnoyarsk Science Center" of the Siberian Branch of the Russian Academy of Sciences, "Institute of Biophysics of the Siberian Branch of the Russian Academy of Sciences", Akademgorodok, 50/50, 660036, Krasnoyarsk, Russia; Professor — Department of Biophysics, Siberian Federal University, Svobodny ave., 79, 660041, Krasnoyarsk, Russia; e-mail: n-qdr@yandex.ru; https://orcid.org/0000-0001-5315-8002

Author Contributions

The manuscript was written through contributions of all authors. All authors have given approval to the final version of the manuscript. CRediT: **Olga Vladislavovna Kolesnik** data curation, formal analysis, investigation, methodology, visualization, writing — original draft, writing — review & editing; **Aleksey Sergeevich Grabovoy** formal analysis, investigation, visualization, writing — original draft; **Gennadii Alexandrovich Badun** — conceptualization, methodology, resources; **Grigory Nikolaevich Churilov** – methodology, resources; **Nadezhda Stepanovna Kudryasheva** conceptualization, data curation, methodology, project administration, validation, supervision, validation, visualization, writing — original draft, writing — review & editing.

Conflicts of Interest

The authors declare no conflict of interest.

References

1 Eyrolle, F., Ducros, L., le Dizès, S., Beaugelin-Seiller, K., Charmasson, S., Boyer, P., & Cossonnet, C. (2018). An updated review on tritium in the environment. *Journal of Environmental Radioactivity*, *181*, 128–137. https://doi.org/10.1016/j.jenvrad.2017.11.001

2 Feng, B., & Zhuo, W. H. (2022). Levels and behavior of environmental tritium in East Asia. *Nuclear Science and Techniques*, *33*(7), 1–19. https://doi.org/10.1007/s41365-022-01073-3

3 Ojovan, M. I., Lee, W. E., & Kalmykov, S. N. (2019). Short-Lived Waste Radionuclides. In *An Introduction to Nuclear Waste Immobilisation* (pp. 145–154). Elsevier. https://doi.org/10.1016/B978-0-08-102702-8.00011-X

4 Geyh, M. A., & Schleicher, H. (1990). Radiometric Dating Methods. In *Absolute Age Determination* (pp. 51–134). Springer Berlin. https://doi.org/10.1007/978-3-642-74826-4

5 Libby, W. F. (1963). Moratorium tritium geophysics. *Journal of Geophysical Research*, *68*(15), 4485–4494. https://doi.org/10.1029/JZ068i015p04485

6 Larsen, G., & Babineau, D. (2020). An Evaluation of the Global Effects of Tritium Emissions from Nuclear Fusion Power. *Fusion Engineering and Design*, *158*(3), 111690. https://doi.org/10.1016/j.fusengdes.2020.111690

7 Cook, G. T., Passo, C. J., & Carter, B. (2003). Environmental liquid scintillation analysis. In *Handbook of Radioactivity Analysis* (pp. 537–607). Elsevier. https://doi.org/10.1016/B978-012436603-9/50011-9

8 Kendall, C., & Doctor, D. H. (2003). Stable Isotope Applications in Hydrologic Studies. In H.D. Holland & K.K. Turekian (Eds.) *Treatise on Geochemistry* (pp. 319–364). Elsevier. https://doi.org/10.1016/B0-08-043751-6/05081-7

9 Jaeschke, B. C., & Bradshaw, C. (2013). Bioaccumulation of tritiated water in phytoplankton and trophic transfer of organically bound tritium to the blue mussel, *Mytilus edulis*. *Journal of Environmental Radioactivity*, *115*, 28–33. https://doi.org/10.1016/j.jenvrad.2012.07.008

10 Zapponi, G. A., & Marcello, I. (2006). Low-Dose Risk, Hormesis, Analogical and Logical Thinking. *Annals of the New York Academy of Sciences*, *1076*(1), 839–857. https://doi.org/10.1196/annals.1371.076

11 Nakamura, H., Miyanishi, H., Yasunaga, T., Fujiwara, S., Mizuguchi, T., Nakata, A., Miyazaki, T., Otsuka, T., Kenmotsu, T., Hatano, Y., & Saito, S. (2020). Molecular dynamics study on DNA damage by tritium disintegration. *Japanese Journal of Applied Physics*, *59*, SAAE01. https://doi.org/10.7567/1347-4065/ab460d

12 Rozhko, T. V., Nogovitsyna, E. I., Badun, G. A., Lukyanchuk, A. N., & Kudryasheva, N. S. (2019). Reactive Oxygen Species and low-dose effects of tritium on bacterial cells. *Journal of Environmental Radioactivity*, *208–209*, 106035. https://doi.org/10.1016/j.jenvrad.2019.106035

13 Selivanova, M. A., Mogilnaya, O. A., Badun, G. A., Vydryakova, G. A., Kuznetsov, A. M., & Kudryasheva, N. S. (2013). Effect of tritium on luminous marine bacteria and enzyme reactions. *Journal of Environmental Radioactivity*, *120*, 19–25. https://doi.org/10.1016/j.jenvrad.2013.01.003

14 Selivanova, M., Rozhko, T., Devyatlovskaya, A., & Kudryasheva, N. (2014). Comparison of chronic low-dose effects of alpha- and beta-emitting radionuclides on marine bacteria. *Central European Journal of Biology*, *9*(10), 951–959. https://doi.org/10.2478/s11535-014-0331-0

15 Rozhko, T. V., Kolesnik, O. V., Badun, G. A., Stom, D. I., & Kudryasheva, N. S. (2020). Humic Substances Mitigate the Impact of Tritium on Luminous Marine Bacteria. Involvement of Reactive Oxygen Species. *International Journal of Molecular Sciences*, *21*(18), 6783. https://doi.org/10.3390/ijms21186783

16 Rozhko, T. V., Badun, G. A., Razzhivina, I. A., Guseynov, O. A., Guseynova, V. E., & Kudryasheva, N. S. (2016). On the mechanism of biological activation by tritium. *Journal of Environmental Radioactivity*, *157*, 131–135. https://doi.org/10.1016/j.jenvrad.2016.03.017

17 Bondareva, L., Kudryasheva, N., & Tananaev, I. (2022). Tritium: Doses and Responses of Aquatic Living Organisms (Model Experiments). *Environments*, *9*(4), 51. https://doi.org/10.3390/environments9040051

18 Calabrese, E. (2018). Hormesis: Path and Progression to Significance. *International Journal of Molecular Sciences*, *19*(10), 1–15. https://doi.org/10.3390/ijms19102871

19 Jargin, S. (2018). Hormesis and radiation safety norms: Comments for an update. *Human & Experimental Toxicology*, *37*(11), 1233–1243. https://doi.org/10.1177/0960327118765332

20 Shibamoto, Y., & Nakamura, H. (2018). Overview of Biological, Epidemiological, and Clinical Evidence of Radiation Hormesis. *International Journal of Molecular Sciences*, *19*(8), 1–16. https://doi.org/10.3390/ijms19082387

21 Ge, H., Zhou, M., Lv, D., Wang, M., Xie, D., Yang, X., Dong, C., Li, S., & Lin, P. (2020). Novel Segmented Concentration Addition Method to Predict Mixture Hormesis of Chlortetracycline Hydrochloride and Oxytetracycline Hydrochloride to Aliivibrio fischeri. *International Journal of Molecular Sciences*, *21*(2), 481. https://doi.org/10.3390/ijms21020481

22 Kaiser, J. (2003). Sipping From a Poisoned Chalice. *Science*, *302*(5644), 376–379. https://doi.org/10.1126/science.302.5644.376

23 Calabrese, E. J. (2013). Hormetic mechanisms. *Critical Reviews in Toxicology*, *43*(7), 580–606. https://doi.org/10.3109/10408444.2013.808172

24 Kolesnik, O. V., Rozhko, T. V., & Kudryasheva, N. S. (2023). Marine Bacteria under Low-Intensity Radioactive Exposure: Model Experiments. *International Journal of Molecular Sciences*, *24*(1). https://doi.org/10.3390/ijms24010410

25 Girotti, S., Ferri, E. N., Fumo, M. G., & Maiolini, E. (2008). Monitoring of environmental pollutants by bioluminescent bacteria. *Analytica Chimica Acta*, *608*(1), 2–29. https://doi.org/10.1016/j.aca.2007.12.008

26 Kudryasheva, N. S., & Rozhko, T. V. (2015). Effect of low-dose ionizing radiation on luminous marine bacteria: radiation hormesis and toxicity. *Journal of Environmental Radioactivity*, *142*, 68–77. https://doi.org/10.1016/j.jenvrad.2015.01.012

27 Roda, A., Guardigli, M., Michelini, E., & Mirasoli, M. (2009). Bioluminescence in analytical chemistry and in vivo imaging. *Trends in Analytical Chemistry*, *28*(3), 307–322. https://doi.org/10.1016/j.trac.2008.11.015

28 Kratasyuk, V. A. (1990). Principle of luciferase biotesting. In B. Jeżowska-Trzebiatowska, B. Kochel, J. Sławiński & W. Stręk (Eds.), *Biological Luminescence* (p. 550). WSPC. https://doi.org/10.1142/9789814539807

29 Esimbekova, E. N., Torgashina, I. G., Kalyabina, V. P., & Kratasyuk, V. A. (2021). Enzymatic Biotesting: Scientific Basis and Application. *Contemporary Problems of Ecology*, *14*(3), 290–304. https://doi.org/10.1134/S1995425521030069

30 Esimbekova, E. N., Kalyabina, V. P., & Kratasyuk, V. A. (2018). Application of bioluminescent enzymatic tests in ecotoxicology. *Journal of International Scientific Publications*, *12*, 135–146.

31 Kudryasheva, N. S. (2006). Bioluminescence and exogenous compounds: Physico-chemical basis for bioluminescent assay. *Journal of Photochemistry and Photobiology B: Biology*, *83*(1), 77–86. https://doi.org/10.1016/j.jphotobiol.2005.10.003

32 Matsumoto, H., Hamada, N., Takahashi, A., Kobayashi, Y., & Ohinishi, T. (2007). Vanguards of Paradigm Shift in Radiation Biology: Radiation-Induced Adaptive and Bystander Responses. *Journal of Radiation Research*, *48*(2), 97–106. https://doi.org/10.1269/jrr.06090

33 Smith, R. W., Wang, J., Schültke, E., Seymour, C. B., Bräuer-Krisch, E., Laissue, J. A., Blattmann, H., & Mothersill, C. E. (2013). Proteomic changes in the rat brain induced by homogenous irradiation and by the bystander effect resulting from high energy synchrotron X-ray microbeams. *International Journal of Radiation Biology*, *89*(2), 118–127. https://doi.org/10.3109/09553002.2013.732252

34 Sharma, P., Jha, A. B., Dubey, R. S., & Pessarakli, M. (2012). Reactive Oxygen Species, Oxidative Damage, and Antioxidative Defense Mechanism in Plants under Stressful Conditions. *Journal of Botany*, *2012*, 1–26. https://doi.org/10.1155/2012/217037

35 Su, Y., Song, H., & Lv, Y. (2019). Recent advances in chemiluminescence for reactive oxygen species sensing and imaging analysis. *Microchemical Journal*, *146*(July 2018), 83–97. https://doi.org/10.1016/j.microc.2018.12.056

36 Phaniendra, A., Jestadi, D. B., & Periyasamy, L. (2015). Free Radicals: Properties, Sources, Targets, and Their Implication in Various Diseases. *Indian Journal of Clinical Biochemistry*, *30*(1), 11–26. https://doi.org/10.1007/s12291-014-0446-0

37 Griendling, K. K., Touyz, R. M., Zweier, J. L., Dikalov, S., Chilian, W., Chen, Y. -R., Harrison, D. G., & Bhatnagar, A. (2016). Measurement of Reactive Oxygen Species, Reactive Nitrogen Species, and Redox-Dependent Signaling in the Cardiovascular System. *Circulation Research*, *119*(5), 39–75. https://doi.org/10.1161/RES.0000000000000110

38 Suzen, S., Gurer-Orhan, H., & Saso, L. (2017). Detection of Reactive Oxygen and Nitrogen Species by Electron Paramagnetic Resonance (EPR) Technique. *Molecules*, *22*(1), 181. https://doi.org/10.3390/molecules22010181

39 Sushko, E. S., Vnukova, N. G., Churilov, G. N., & Kudryasheva, N. S. (2022). Endohedral Gd-Containing Fullerenol: Toxicity, Antioxidant Activity, and Regulation of Reactive Oxygen Species in Cellular and Enzymatic Systems. *International Journal of Molecular Sciences*, *23*(9), 5152. https://doi.org/10.3390/ijms23095152

40 Kicheeva, A. G., Sushko, E. S., Bondarenko, L. S., Kydralieva, K. A., Pankratov, D. A., Tropskaya, N. S., Dzeranov, A. A., Dzhardimalieva, G. I., Zarrelli, M., & Kudryasheva, N. S. (2023). Functionalized Magnetite Nanoparticles: Characterization, Bioeffects, and Role of Reactive Oxygen Species in Unicellular and Enzymatic Systems. *International Journal of Molecular Sciences*, *24*(2), 1–23. https://doi.org/10.3390/ijms24021133

41 Stepin, E. A., Sushko, E. S., Vnukova, N. G., Churilov, G. N., Rogova, A. V., Tomilin, F. N., & Kudryasheva, N. S. (2024). Effects of Endohedral Gd-Containing Fullerenols with a Different Number of Oxygen Substituents on Bacterial Bioluminescence. *International Journal of Molecular Sciences*, *25*(2), 4–7. https://doi.org/10.3390/ijms25020708

42 Alexandrova, M., Rozhko, T., Vydryakova, G., & Kudryasheva, N. (2011). Effect of americium-241 on luminous bacteria. Role of peroxides. *Journal of Environmental Radioactivity*, *102*(4), 407–411. https://doi.org/10.1016/j.jenvrad.2011.02.011

43 Azzam, E. I., Jay-Gerin, J. -P., & Pain, D. (2012). Ionizing radiation-induced metabolic oxidative stress and prolonged cell injury. *Cancer Letters*, *327*(1–2), 48–60. https://doi.org/10.1016/j.canlet.2011.12.012

44 Bondareva, L., & Kudryasheva, N. (2021). Direct and Indirect Detoxification Effects of Humic Substances. *Agronomy*, *11*(2), 198. https://doi.org/10.3390/agronomy11020198

45 Injac, R., Prijatelj, M., & Strukelj, B. (2013). Fullerenol Nanoparticles: Toxicity and Antioxidant Activity. In D. Armstrong & D.J. Bharali (Eds.), *Oxidative Stress and Nanotechnology* (pp. 75–100). Humana Press. https://doi.org/10.1007/978-1-62703-475-3_5

46 Vileno, B., Jeney, S., Sienkiewicz, A., Marcoux, P. R., Miller, L. M., & Forró, L. (2010). Evidence of lipid peroxidation and protein phosphorylation in cells upon oxidative stress photo-generated by fullerols. *Biophysical Chemistry*, *152*(1–3), 164–169. https://doi.org/10.1016/j.bpc.2010.09.004

47 Lao, F., Li, W., Han, D., Qu, Y., Liu, Y., Zhao, Y., & Chen, C. (2009). Fullerene derivatives protect endothelial cells against NO-induced damage. *Nanotechnology*, *20*(22), 225103. https://doi.org/10.1088/0957-4484/20/22/225103

48 Gudkov, S. V, Guryev, E. L., Gapeyev, A. B., Sharapov, M. G., Bunkin, N. F., Shkirin, A. V, Zabelina, T. S., Glinushkin, A. P., Sevost'yanov, M. A., Belosludtsev, K. N., Chernikov, A. V., Bruskov, V. I., & Zvyagin, A. V. (2019). Unmodified hydrated C60 fullerene molecules exhibit antioxidant properties, prevent damage to DNA and proteins induced by reactive oxygen species and protect mice against injuries caused by radiation-induced oxidative stress. *Nanomedicine: Nanotechnology, Biology and Medicine*, *15*(1), 37–46. https://doi.org/10.1016/j.nano.2018.09.001

49 Grebowski, J., Kazmierska, P., & Krokosz, A. (2013). Fullerenols as a New Therapeutic Approach in Nanomedicine. *BioMed Research International*, *2013*, 1–9. https://doi.org/10.1155/2013/751913

50 Grebowski, J., & Krokosz, A. (2010). Fullerenes in radiobiology. *Postepy biochemii*, *56*(4), 456–462.

51 Grebowski, J., Krokosz, A., Konarska, A., Wolszczak, M., & Puchala, M. (2014). Rate constants of highly hydroxylated fullerene C60 interacting with hydroxyl radicals and hydrated electrons: Pulse radiolysis study. *Radiation Physics and Chemistry*, *103*, 146–152. https://doi.org/10.1016/j.radphyschem.2014.05.057

52 Trajković, S., Dobrić, S., Jaćević, V., Dragojević-Simić, V., Milovanović, Z., & Dordević, A. (2007). Tissue-protective effects of fullerenol $C_{60}(OH)_{24}$ and amifostine in irradiated rats. *Colloids and Surfaces B: Biointerfaces*, *58*(1), 39–43. https://doi.org/10.1016/j.colsurfb.2007.01.005

53 Vesna, J., Danica, J., Kamil, K., Viktorija, D. S., Silva, D., Sanja, T., Ivana, B., Zoran, S., Zoran, M., Dubravko, B., & Aleksandar, D. (2016). Effects of fullerenol nanoparticles and amifostine on radiation-induced tissue damages: Histopathological analysis. *Journal of Applied Biomedicine*, *14*(4), 285–297. https://doi.org/10.1016/j.jab.2016.05.004

54 Kuznetsov, A. M., Rodicheva, E. K., & Shilova, E. V. (1996). Bioassay based on lyophilized bacteria. *Biotekhnologiya*, *9*, 57–61.

55 Kovel, E., Sachkova, A., Vnukova, N., Churilov, G., Knyazeva, E., & Kudryasheva, N. (2019). Antioxidant Activity and Toxicity of Fullerenols via Bioluminescence Signaling: Role of Oxygen Substituents. *International Journal of Molecular Sciences*, *20*(9), 2324. https://doi.org/10.3390/ijms20092324

56 Churilov, G. N., Krätschmer, W., Osipova, I. V., Glushenko, G. A., Vnukova, N. G., Kolonenko, A. L., & Dudnik, A. I. (2013). Synthesis of fullerenes in a high-frequency arc plasma under elevated helium pressure. *Carbon*, *62*, 389–392. https://doi.org/10.1016/j.carbon.2013.06.022

57 Li, J., Zhang, M., Sun, B., Xing, G., Song, Y., Guo, H., Chang, Y., Ge, Y., & Zhao, Y. (2012). Separation and purification of fullerenols for improved biocompatibility. *Carbon*, *50*(2), 460–469. https://doi.org/10.1016/j.carbon.2011.08.073

58 Li, J., Wang, T., Feng, Y., Zhang, Y., Zhen, M., Shu, C., Jiang, L., Wang, Y., & Wang, C. (2016). A water-soluble gadolinium metallofullerenol: Facile preparation, magnetic properties and magnetic resonance imaging application. *Dalton Transactions*, *45*(21), 8696–8699. https://doi.org/10.1039/c6dt00223d

59 Sachkova, A. S., Kovel, E. S., Churilov, G. N., Guseynov, O. A., Bondar, A. A., Dubinina, I. A., & Kudryasheva, N. S. (2017). On mechanism of antioxidant effect of fullerenols. *Biochemistry and Biophysics Reports*, *9*, 1–8. https://doi.org/10.1016/j.bbrep.2016.10.011

60 Kovel, E. S., Kicheeva, A. G., Vnukova, N. G., Churilov, G. N., Stepin, E. A., & Kudryasheva, N. S. (2021). Toxicity and antioxidant activity of fullerenol c60, 70 with low number of oxygen substituents. *International Journal of Molecular Sciences*, *22*(12). https://doi.org/10.3390/ijms22126382

61 Abbas, M., Adil, M., Ehtisham-ul-Haque, S., Munir, B., Yameen, M., Ghaffar, A., Shar, G. A., Asif Tahir, M., & Iqbal, M. (2018). Vibrio fischeri bioluminescence inhibition assay for ecotoxicity assessment: A review. *Science of The Total Environment*, *626*, 1295–1309. https://doi.org/10.1016/j.scitotenv.2018.01.066

62 Bulich, A. A., & Isenberg, D. L. (1981). Use of the luminescent bacterial system for the rapid assessment of aquatic toxicity. *ISA Transactions*, *20*(1), 29–33.

63 Luzina, E. L., & Popov, A. V. (2009). Synthesis and anticancer activity of N-bis(trifluoromethyl)alkyl-N′-thiazolyl and N-bis(trifluoromethyl)alkyl-N′-benzothiazolyl ureas. *European Journal of Medicinal Chemistry*, *44*(12), 4944–4953. https://doi.org/10.1016/j.ejmech.2009.08.007

64 Tarasova, A. S., Kislan, S. L., Fedorova, E. S., Kuznetsov, A. M., Mogilnaya, O. A., Stom, D. I., & Kudryasheva, N. S. (2012). Bioluminescence as a tool for studying detoxification processes in metal salt solutions involving humic substances. *Journal of Photochemistry and Photobiology B: Biology*, *117*, 164–170. https://doi.org/10.1016/j.jphotobiol.2012.09.020

65 Kolesnik, O. V., Rozhko, T. V., Lapina, M. A., Solovyev, V. S., Sachkova, A. S., & Kudryasheva, N. S. (2021). Development of Cellular and Enzymatic Bioluminescent Assay Systems to Study Low-Dose Effects of Thorium. *Bioengineering*, *8*(12), 194. https://doi.org/10.3390/bioengineering8120194

How to Cite: Hasanguliyeva, N.M., Shakunova, N.V., & Litvishkov, Y.N. (2024) Microwave Solid-Phase Synthesis of Ni-Co Ferrites and their Activities in Liquid-Phase Oxidation of *m*-Xylene. *Eurasian Journal of Chemistry, 29, 3(115), 82-91.* https://doi.org/10.31489/2959-0663/3-24-1

Article

Received: 19 February 2024 | Revised: 30 June 2024 | Accepted: 11 July 2024 | Published online: 02 August 2024

UDC 544.47:544.344:544.54

https://doi.org/10.31489/2959-0663/3-24-1

Nargalam M. Hasanguliyeva, Ninel V. Shakunova*, Yuriy N. Litvishkov

Institute of Catalysis and Inorganic Chemistry named after acad. M. Nagiyev of Ministry of Science and Education of Republic of Azerbaijan, Baku, Azerbaijan

*(*Corresponding author's e-mail: nqasanquliyeva@mail.ru)*

Microwave Solid-Phase Synthesis of Ni-Co Ferrites and their Activities in Liquid-Phase Oxidation of *m*-Xylene

In this paper, the activity of mono- and di-substituted cobalt and nickel ferrites prepared by microwave solid-phase synthesis was studied in the reaction of liquid-phase oxidation of *m*-xylene to *m*-toluic acid. It was established that among the tested samples, the di-substituted ferrites of spinel structure with the composition of $Ni_{0,6}Co_{0,4}Fe_2O_4$ have the shortest induction period and the highest initial rate of oxygen absorption. In order to clarify the role of the active surface of the $Ni_{0.6}Co_{0.4}Fe_2O_4$ catalyst and the volumetric conversions of *m*-xylene in the nucleation stage of primary xylyl radicals, the dependence of the induction period. Furthermore the rate of oxygen absorption was investigated as a function of the time of introduction of the inhibitor into the oxidized *m*-xylene at different ratios of the total size of the heterogeneous surface to the volume of *m*-xylene loaded into the reactor (S/V). The dependence of the selectivity of the process to the targeted product, *m*-toluic acid, on the specific surface area of the catalyst samples was established and it was shown that selectivity to the by-product, *m*-methylbenzyl alcohol, increased and selectivity to *m*-toluic acid decreased in the case of cobalt ferrite with a relatively low specific surface area. It was shown that at the first stage reaction (5–10 min.), i.e., in conditions of an as yet undeveloped radical chain reaction, in the presence of disubstituted ferrites of the composition ($Ni_{1-x}Co_xFe_2O_4$), in comparison with monosubstituted ferrites, a higher initial rate of formation of the primary oxidation product of *m*-xylene — *m*-methylbenzylhydroperoxide (main intermediate product obtained during formation of *m*-toluic acid) is observed. The correlation of the activity of mono- and disubstituted Ni-Co ferrites, in the conditions of developed heterogeneous catalytic conversion of *m*-xylene, disubstituted Ni-Co ferrites are also characterized by higher rate of heterogeneous nucleation of free radicals and heterogeneous catalytic conversion of the intermediate product — *m*-toluic aldehyde to *m*-toluic acid. This, in turn, provides a high degree of selectivity for the targeted product with the yield of 79.8 %.

Keywords: nanodispersed catalysts, monoferrits, diferrits, solid-phase synthesis, natural magnetite, microwave radiation, liguid-phase oxidation, heterogeneous-catalytic conversion.

Introduction

The study of the heterogeneous catalytic liquid-phase oxidation patterns of alkyl aromatic compounds in the presence of metal compounds of variable valency is of great importance in the streamlined synthesis of the products of this reaction, which are mainly mono- and poly-carboxylic acids [1–8].

These compounds are of significant practical value for organic synthesis due to their functionality, for example, in the preparation of widely-used physiologically active substances and pharmaceuticals [9–11].

One of the effective methods for directing the above-mentioned liquid-phase process in the direction of high rate, conversion and selectivity to targeted products is the use of highly-dispersed (nano-sized) heterogeneous catalysts — complex metal oxides of variable valency [12–19].

In particular, due to such universal properties as high thermodynamic stability and corrosion resistance, mechanical hardness and high adsorption capacity, spinel-type ferrites with single and double displacement of Fe^{2+} and Fe^{3+} atoms with variable valence metals are of interest as potential heterogeneous catalysts of this type [20, 21].

The preceding studies [22, 23] present the results of microwave solid-phase synthesis of mono-substituted and double Ni–Co ferrites completed on the basis of $Ni^{(II)}$, $Co^{(II)}$ oxides and natural magnetite concentrate taken from the Dashkesan magnetite deposit (Gazakh economical region, Dashkesan city, Azerbaijan) and their initiating activity estimation in the reaction of liquid-phase oxidation of alkyl aromatic hydrocarbons.

It was found that a high initial formation rate of the primary product of *m*-xylene oxidation, *m*-methylbenzylhydroperoxide, a crucial product that determines the efficiency of further development of the reaction in the direction of the formation of *m*-toluic acid, is observed in the presence of samples with a spinel structure ($Ni_{1-x}Co_xFe_2O_4$) formed under the thermal influence of microwave radiation, under conditions of an undeveloped radical-chain reaction.

A series of experiments were conducted to determine the activity of the synthesized catalysts. This article presents the results of the study of the heterocatalytic nucleation and continuation of chains in the initial period and during the period of the developed reaction of liquid-phase oxidation of *m*-xylene to *m*-toluic acid, in the presence of both monosubstituted Ni- and Co-ferrites, and ferrites of the composition $Ni_{0.6}Co_{0.4}Fe_2O_4$

Experimental

As precursors for the solid-phase synthesis of nickel-cobalt mono- and di-substituted ferrites, divalent metal oxides MO: CoO (purity 99.9) and NiO (purity 99.9), *m*-xylene, as well as magnetite concentrate (Fe_3O_4) with an iron content of 70.4 % were used.

Prior to their heat treatment by microwave radiation the aforementioned oxides and magnetite were subjected to solid-phase interaction through simultaneous mechanical mixing in an electric agate mortar and pestle for 1 hour.

Thermal treatment of ferrite samples was carried out in an installation designed on the basis of a microwave oven EM-G5593V (Panasonic) with a resonator volume of 25 liters in the varying the magnetron power between 200–800 W with an operating frequency of 2450 MHz. The charge temperature was controlled with a CEM DT-8858 infrared pyrometer with a temperature measurement range of 50–1300 °C.

The conditions required for the formation of phase composition of the samples and their morphology are described in detail in [22, 23]. The samples used in this study were finely dispersed crystallites with linear dimensions in the range of 80–170 nm and a specific surface area of 11–63 m^2/g which varied depending on the chemical composition.

Characteristics of metal oxides used in our work CoO (Purity 99.9, GOST 4467-79 Russia) and NiO (purity 99.9, GOST 4331-78 Russia), *m*-hylene (GOST 9410-78), magnetit concentrate Fe_2O_3 with 70 % (GOST 16589-86) are presented in [24–27].

The conversion of *m*-xylene was carried out in an installation combining a reaction unit — a bubble column with d_{out} = 25 mm, h = 100 mm with an external circulation circuit of gas flow (N_2+O_2). The device design enabled carrying out the reaction both in the mode of stationary values of partial pressures of oxygen in the circulation circuit (flow-circulation mode) and in a continuously changing partial pressure of oxygen due to flow (or circulation) rate (circulation mode).

m-Xylene was converted in a solution of *o*-dichlorobenzene (T_b = 179 °C), which was inert to oxidative transformation under the experimental conditions. The inert diluent of the contacting air flow was nitrogen previously purified from oxygen impurities over a Cu/SiO_2 catalyst.

The partial pressure of oxygen in the circulating gas flow was also varied by introducing reduced O_2 from a gas-cylinder. The concentration of oxygen dissolved in the liquid phase was calculated using chromatographic technique for determination of the gas content in hydrocarbons [28] which is dependent on the partial pressure of oxygen in the bubbling gas flow.

The main part of the component composition of the liquid phase of the catalysts was identified by gas chromatographic analysis comparing the values of the retention volumes of the reaction products with those found for individual reactive products.

Quantitative analysis of gas-liquid chromatography was performed by the internal standard method (octanol-1 label) on an LKhM-80 MD device (3rd model) using a flame ionization detector with controlled heating of the column heating oven. Silicone SE-30, 10 % on a solid support of hezosorbe AWHMD was used as a stationary phase.

The concentration of carbon dioxide in the gaseous mixture at the outlet of the reactor was determined using a gas chromatograph (LKhM-80 MD device, detector — katharometer column, l = 3.6 m, d_{out} = 3 mm, filled with the “Porapak QS” phase) with controlled heating thermostat in the temperature range 30÷65 with the rate of temperature elevation of 3/min. A mixture of oxygen and nitrogen was separated into individual components in the parallel column, l = 1.2 m, d_{out} = 3 mm, filled with NaX zeolite.

The carrier gas (He) rate in the columns was maintained within the range of 50–65 mL/min.

The content of *m*-methylbenzylhydroperoxide in the catalyzate was determined by iodometric titration of samples according to the technique described in [29] in the presence of starch as an indicator and was calculated using the formula:

$$\%\ \text{hydroperoxide} = \frac{V \cdot M}{Q \cdot 200}, \quad (1)$$

where V — volume of 0.1N $Na_2S_2O_3$ solution used for titration of released iodine; M — molecule weight of hydroperoxide (137 atomic mass unit), Q — weighed sample of catalysate.

In order to identify the dependence of the absorption rate of oxygen by the reaction medium on its concentration in the liquid phase, by special experiments, it was established that the dissolution isotherms of the oxygen in the reaction mixture in the region of observed linearity:

$$C_{O_2} = K_{O_2} \div P_{O_2}, \quad (2)$$

where $C_{O_2} \cdot 10^{-3}$, mol/L concentration of dissolved oxygen; K_{O_2} — solubility coefficient of O_2 in *m*-xylene at fixed temperature; P_{O_2} — partial pressure of oxygen in the gas flow, it was established that the temperature dependence of K_{O_2} coefficient is described by the following equation:

$$\lg K_{O_2} = -\frac{6500}{R \cdot T}, \quad (3)$$

here, 6500 is activation energy of dissolution of oxygen in *m*-xylene; R — universal gas constant $R =$ 8,314 462 618 153 24 J/(mol·K); T — temperature, K.

The rate of nucleation of free radicals was measured according to the following procedure. The rate of oxygen absorption (W_0) in the presence of the free radical inhibitor N,N´-di-β-naphthyl-*p*-phenylenediamine (5.5÷6.0·10-4 mol/L) introduced into the system during the reaction was calculated using the formula:

$$W_{\text{inh}} = \frac{2\Delta[\text{InH}]}{S \cdot \tau_{\text{inh}}}, \quad (4)$$

where W_{inh} — the inhibitor consumption rate (mol/m^2 min), Δ[InH] — the amount of consumed inhibitor (mol); S — the surface area of the catalyst sample (m^2), 2 — the stoichiometric inhibition coefficient, τ_{inh} — the time period on the abscissa axis at extrapolation in coordinates $1/W_0 - \tau$ (Fig. 1). The moment of introduction of the inhibitor was taken as the beginning of the time coordinate. The consumption of the inhibitor was monitored by the accumulation of a colored product of its oxidation — di-β-naphthyl-p-quinonediimine, the concentration of which in selected catalytic samples was determined on an SF-4A spectrophotometer in regard to light wave absorption at λ_{max} = 480 μm and molar extinction coefficient $\varepsilon = 1.1 \cdot 10^4$ L/mol·cm.

Selectivity to targeted products was evaluated as ratio of yield of corresponding product to conversion of *m*-xylene to the total reaction products:

$$S_i(\text{wt.}\%) = \frac{Q_i}{\sum Q_i} \cdot 100, \quad (5)$$

where S_i — selectivity to targeted product of reaction; Q_i — weight of target products (g), Q_i — total amount of obtained products (g).

The statistical manipulation of the experimental results was ultimately aimed at determining the confidence interval boundary [29]:

$$\left[M - t_{n,p} \frac{S}{\sqrt{n}}; \quad M + t_{n,p} \frac{S}{\sqrt{n}} \right], \quad (6)$$

where M — average value of the data extraction; S — standard deviation; $t_{n,\,p}$ — table value of Student's distribution with a number of degrees of freedom (n) and confidence factor (P); n — number of elements in taken extraction of corresponding experiments.

Calculation was carried out using MS Excel (Windows 10) computational hardware and software in confidence level P = 95 % and preliminary computation of the standard deviation (S), in n = 3–4 sample size.

Results and Discussion

The objective of the experiments was to ascertain whether the inhibitor could potentially impede the formation of free radicals. To this end, the initial rates of oxygen absorption were measured under conditions

where identical quantities of freshly prepared catalysts and catalysts filtered from a solution (5.5×10^{-4} mol/l) of the inhibitor, N,N´-di-β-naphthyl-p-phenylenediamine, were employed.

The experiments mentioned above, demonstrated that the amount of a chemisorbed inhibitor present was insufficient to impede the nucleation centers of free radicals on the surface of catalysts. Consequently the observed difference in oxygen absorption rates in the absence and presence of the inhibitor can be attributed to the interaction of the inhibitor and free radicals in the bulk liquid phases (Fig. 1).

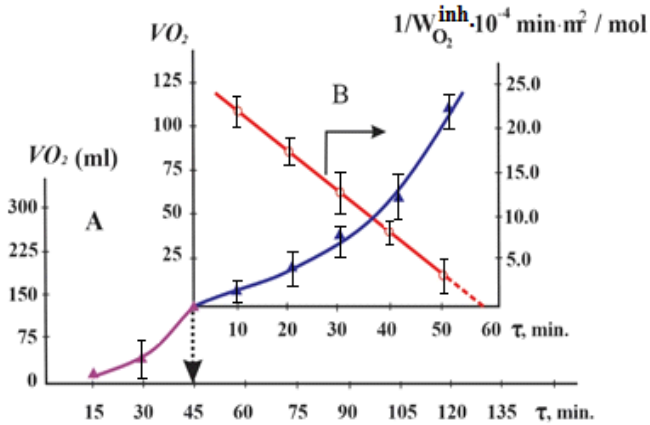

Figure 1. The kinetics of oxygen adsorbtion in the absence of an inhibitor (*A*), with the introduction of (5.5×10^{-4} mol/L) N,N´-di-β-naphthyl-p-phenylenediamine (*B*) (marked with an arrow) and the reciprocal value of the absorption rate of oxygen in the presence of a catalyst with the composition $Ni_{0.6}Co_{0.4}Fe_2O_4$. Temp. 413 K, the ratio of the catalyst surface area to the volume of the hydrocarbon phase (S/V) = $2\cdot10^5$ m^{-1}. Confidence level P = 95 % and sample size n = 3

Experiments in which the initial rates of oxygen absorption were measured in the presence of identical loads of samples of freshly prepared catalysts and catalysts filtered from a N,N´-di-β-naphthyl-p-phenylenediamine solution (5.5×10^{-4} mol/L) showed the absence in noticeable quantities of the chemisorbed inhibitor capable of blocking the nucleation centers of the free radicals.

Figure 2 shows a histogram representing the dependence of the initial rate of heterogeneous catalytic chain initiation during the oxidation of *m*-xylene in the presence of synthesized Ni–Co ferrites and the conversion rate which does not exceed 3–5 %. At this conversion rate the formation of free radicals by hydroperoxide branching of chains and, consequently, the effect of the radicals on the kinetics of the radical chain process can be disregarded.

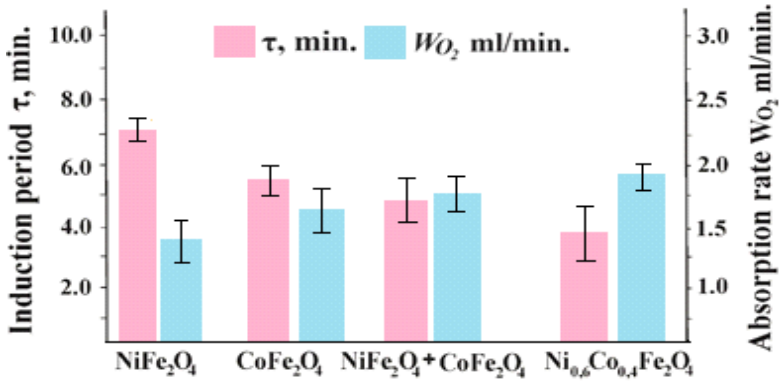

Figure 2. Dependence of the induction period (τ) and the initial absorption rate of oxygen (Wo_2) in the presence of synthesized catalysts in the liquid-phase oxidation of *m*-xylene. Conditions: Temperature 403 K; the weight concentration of catalysts is 2.5 %. Confidence level P = 95 % and sample size n = 3, 4.

The initiating activity data of the synthesized double Ni–Co ferrites were compared with the activities of mono-substituted samples, as well as a mechanical mixture of ferrites ($NiFe_2O_4$ + $CoFe_2O_4$) taken in a mass ratio of 1:1.

It has been established that the introduction of the inhibitor at the starting moment of the reaction does not result in complete inhibition of oxygen absorption, and this fact is not due to the insufficient efficiency of the used inhibitor, but is associated with the presence of uninhibited heterogeneous catalytic conversion pattern of xylene. Among the tested samples, spinel samples with the composition $Ni_{0.6}Co_{0.4}Fe_2O_4$ are characterized by the shortest induction period and the highest initial rate of oxygen absorption.

The dependence of the induction period and the rate of oxygen absorption on the time of introduction of the inhibitor into the oxidized *m*-xylene at different ratios of the total value of the heterogeneous surface to the volume of *m*-xylene charged into the reactor (S/V) was studied in order to clarify the role of the active surface of the $Ni_{0,6}Co_{0,4}Fe_2O_4$ catalyst and the volumetric transformations of *m*-xylene in the stage of nucleation of primary xylyl radicals.

It can be seen in Figure 3 that with an increase in the S/V ratio the amount of the introduced catalyst increases, a more intense decay of the induction period is observed starting from the time of introduction of the inhibitor.

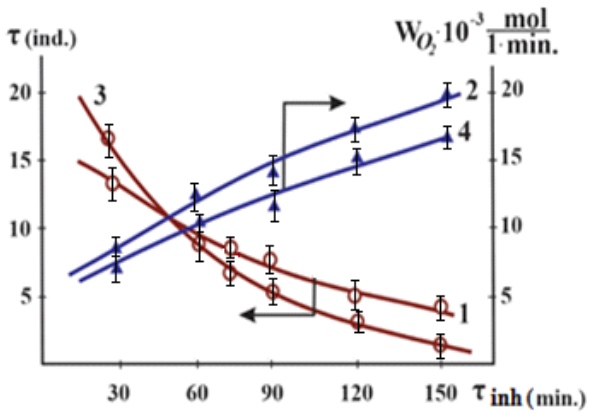

Figure 3. Dependence of the induction period and the rate of oxygen absorption on the time of introduction of the inhibitor during the conversion of *m*-xylene in the presence of the catalyst $Ni_{0.6}Co_{0.4}Fe_2O_4$; and the value of the rate of oxygen absorption at the time of introduction of the inhibitor. (1 and 2) — S/V = $31.4 \cdot 10^5$ m^{-1}; (3, 4) — $15,7 \cdot 10^5$ m^{-1}. (Conditions: temp. 403K, p = 0,25 at.; $V_{m\text{-xyl.}}$= 40 mL, V_{gas} = 35 L/h). Confidence level P = 95 % and sample size n = 3–4

In this case, there is also a more intense increase in the absorption rate of oxygen measured at the time of introduction of the inhibitor.

This phenomenon can be attributed to the heterogeneous catalytic nucleation of free xylyl radicals during the interaction of the converted *m*-xylene with the active surface of the $Ni_{0.6}Co_{0.4}Fe_2O_4$ catalyst.

At the same time, a more intense decay of the induction period is observed starting from the time of introduction of the inhibitor during the period of the developed reaction.

This indicates an increase in the proportion of the branched chain mechanism in the formation process of free radicals, which occurs in the bulk of the liquid phase of oxidized *m*-xylene in the presence of a less catalyst sample by mass (Fig. 3).

As is known, the composition of hydrocarbon oxidation products, including alkyl aromatic compounds, is determined by various directions of conversions of the primarily formed peroxide radicals ROO. During conversion in the bulk of the liquid phase, the main direction of the homogeneous chain continuation reaction is the interaction of the initial hydrocarbon with the formation of hydroperoxides [30–35]:

$$ROO^{\cdot} + RH \rightarrow ROOH + R^{\cdot} \quad (7)$$

The decomposition of hydroperoxides catalyzed by the heterogeneous surface usually leads to the formation of the corresponding alcohols as molecular products:

$$\begin{gathered} S^* + ROOH \rightarrow [ROOH^{\delta-}\ldots.S^{\delta+}] \\ [ROOH^{\delta-}\ldots.S^{\delta+}] \rightarrow RO^{\cdot} + [S^{\delta+}\ldots.OH^{\delta-}] \\ RO^{\cdot} + RH \rightarrow ROH + R^{\cdot} \end{gathered} \quad (8)$$

As an alternative reaction of chain continuation may involve the interaction of peroxide radicals with active centers located on the surface of the catalysts resulting in the formation of aldehydes:

$$RH_2OO^{\cdot} + S^* \rightarrow [RH_2OO^{\cdot}\ldots.\ S^*]$$
$$[RH_2OO^{\cdot}\ldots.\ S^*] \rightarrow RHO + [S^{\delta+}\ldots.\ OH^{\delta-}] \rightarrow S^* + RO^{\cdot} + H_2O \quad (9)$$
$$[S^{\delta+}\ldots.O\text{-}O..^{\delta-}] + RHO \rightarrow [S^{\delta+}\ldots.O\text{-}OH^{\delta-}] + RO^{\cdot}$$

Analysis of the composition of the catalyzate in the initial and subsequent periods of the reaction proceeding in the presence of mono- and di-substituted ferrites showed that the selectivity to *m*-methylbenzyl alcohol increases (Tables 1, 2) in cobalt ferrite with a relatively low specific surface area.

Table 1

Conversion of *m*-xylene in the presence of mono- and di-substituted ferrites of Co and Ni (Conditions: Temp. 403 K; $V_{m\text{-xylene}}$ = 40 ml; υ air flow 35 L/h)

S/V $м^{-1}$ $\times 10^5$	τ, reaction time, min	Conversion of *m*-xylene, %	Selectivity to reaction products % (wt.) (± Confidence interval with Student's distribution in α = 0.05)				
			Hydroperoxide of *m*-methyl benzele	*m*-methyl-benzyl alcohol	*m*-toluic aldehyde	*m*-toluic acid	*i*-phthalic acid
$NiFe_2O_4$ ($S_{sp.\ sur.}$ = 23 m^2/g)							
5.75	20	4.2 ±0.7	3.7±0.7	31.5±0.8	46.5±0.7	18.3±0.5	–
5.75	60	15.8±0.6	2.3±0.8	13.2±0.3	44.8±0.6	39.7±0.5	–
5.75	120	51.6±0.8	1.8±06	8.8±0.9	27.2±0.8	60.6±0.4	1.6±0.8
$CoFe_2O_4$ ($S_{sp.\ sur.}$ = 11 m^2/g)							
2.75	20	3.4±0.5	4.2±0.5	32.8±0.6	47.3±0.2	15.7±0.4	–
2.75	60	14.4±0.3	2.8±0.6	14.6±0.4	42.3±0.5	38.9±0.3	1.4±0.9
2.75	120	47.7±0.2	2.2±0.8	10.6±0.6	23.8±0.6	59.7±0.2	3.7±0.5
$Ni_{0.6}Co_{0.4}Fe_2O_4$ ($S_{sp.\ sur.}$= 63 m^2/g)							
15.70	20	6.3±0.8	2.8±0.7	15.6±0.5	48.4±0.2	33.2±0.3	–
15.70	60	27.2±0.5	1.6±0.8	10.8±0.7	32.8±0.5	53.1±0.2	1.7±0.8
15.70	120	68.6±0.2	0.8±0.9	5.4±0.8	19.4±0.6	70.2±0.2	4.2±0.6

*$S_{sp.\ sur.}$ — Specific surface area of the catalyst.

Table 2

Conversion of *m*-xylene in the presence of mono- and di-substituted ferrites of Co and Ni (Conditions: Temp. 413 K; $V_{m\text{-xylene}}$ = 40 ml; υ air flow 35 L/h)

S/V $м^{-1}$ $\times 10^5$	τ, reaction time, min	Conversion of *m*-xylene, %	Selectivity to reaction products % (wt.) (± Confidence interval with Student's distribution in α = 0.05)				
			Hydroperoxide of *m*-methyl benzele	*m*-methyl benzyl alcohol	*m*-toluic aldehyde	*m*-toluic acid	*i*-phthalic acid
$NiFe_2O_4$ ($S_{sp.\ sur.}$ = 23 m^2/g)							
5.75	20	6.8±0.6	3.2±0.7	28.7±0.5	37.5±0.3	30.6±0.3	–
5.75	60	25.3±0.5	1.8±0.8	10.2±0.5	35.6±0.4	52.4±0.3	–
5.75	120	54.2±0.5	1.3±0.8	6.4±0.3	22.3±0.4	67.2±0.2	2.8±0.8
$CoFe_2O_4$ ($S_{sp.\ sur.}$ = 11 m^2/g)							
2.75	20	6.2±0.5	3.4±0.5	30.4±0.2	42.5±04	23.7±0.5	–
2.75	60	34.4±0.3	2.4±0.6	12.3±0.5	37.4±0.5	45.4±03	2.5±0.7
2.75	120	49.6±0.3	1.7±0.5	8.8±0.5	21.4±0.5	63.8±0.2	4.3±0.6
$Ni_{0.6}Co_{0.4}Fe_2O_4$ ($S_{sp.\ sur.}$= 63 m^2/g)							
15.70	20	10.3±0.4	1.7±0.6	10.2±0.3	37.8±0.2	50.3±0.3	–
15.70	60	37.4±0.3	1.2±0.7	7.6±0.5	22.6±0.5	64.9±0.2	3.7±0.6
15.70	120	75.3±0.2	0.5±0.9	3.8±0.6	9.7±0.6	79.8±0.3	6.2±0.5

This fact can be interpreted as evidence for the predominance of the hydroperoxide mechanism of chain continuation in the presence of cobalt monoferrite. In this case, as illustrated in Figure 2, the rate of chain continuation in the bulk liquid phase with the participation of *m*-methylbenzylhydroperoxide (Scheme 8) is greater than the rate of chain continuation with the participation of *m*-toluylaldehyde (Scheme 9) during the period of the developed reaction.

Assuming that the formation process of the free radicals is determined by the stage of heterogeneous catalytic initiation of chains under conditions of an undeveloped chain reaction. Consequently it may be possible to estimate the rate of this process in the form of the difference between the rate of oxygen absorption in the presence of the inhibitor and the rate of chain inhibition:

$$W_R = -W_{\text{inh}} \tag{10}$$

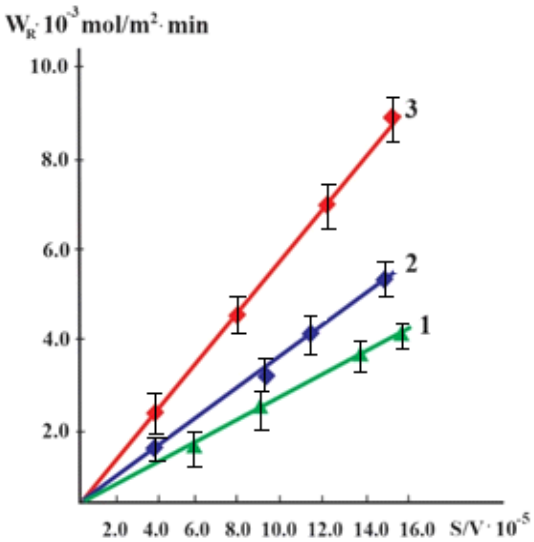

Figure 4. Dependence of the initial rate of heterogeneous catalytic initiation of chains on the surface of $NiFe_2O_4$ (1); $CoFe_2O_4$ (2) and $Ni_{0,6}Co_{0,4}Fe_2O_4$ (3) samples on the ratio of their total surface area to the initial volume of *m*-xylene (S/V), which is variable by changing the catalyst loading; Conditions: reaction temperature 413K, volume of loaded *m*-xylene; 40 mL, υ air flow 35 L/h. Confidence level P = 95 % and sample size n = 3

The observed proportionality of W_R to the amount can be explained by the following scheme of free radical formation during the interaction of *m*-xylene with active centers on the heterogeneous surface of the catalyst (it is assumed that step 2 is slow):

$$\begin{aligned} &1.\quad \mathrm{RH} + \mathrm{Z}_{(\text{oxid.})} \xrightarrow{k_i} \mathrm{R} \cdot \mathrm{Z}_{(\text{reduc.})} \\ &2.\quad \mathrm{Z}_{(\text{reduc.})} \xrightarrow{k_2\ \text{slow}} \mathrm{Z}_{(\text{oxid.})} + \mathrm{H}_2, \end{aligned} \tag{11}$$

where $Z_{(oxid.)}$ — oxidized center, $Z_{(reduc.)}$ — reduced center located on the surface of the catalyst.

The results presented in Tables 1 and 2, demonstrate that the catalysts are involved in the initiation and continuation of reaction chains, as well as in the formation of oxygen-containing molecular reaction products in the heterocatalytic liquid-phase oxidation process of *m*-xylene in the presence of both mono- and di-substituted ferrites.

It was established that, based on a set of parameters including the selectivity towards the targeted product — *m*-toluic acid, di-substituted Ni–Co ferrites exhibited an advantage under comparable reaction conditions by a relatively high rate of heterogeneous nucleation of free radicals and further heterogeneous catalytic conversion of the intermediate product — *m*-tolualdehyde into *m*-toluic acid.

Conclusions

Summarizing the results of the research, we can state that mono- and di-substituted nickel and cobalt ferrites synthesized by microwave solid-phase synthesis, particularly samples of the $Ni_{0.6}Co_{0.4}Fe_2O_4$ composition with a spinel structure, are characterized by higher rate of oxygen adsorbed by the reaction system in the initial period and in the period of the developed reaction of liquid-phase oxidation of *m*-xylene to *m*-toluic acid.

The high rate of heterogeneous catalytic conversion of the intermediate reaction product — *m*-toluic aldehyde into *m*-toluic acid provides the high selectivity to the targeted product of the process.

*Author Information**

**The authors' names are presented in the following order: First Name, Middle Name and Last Name*

Nargalam Muzaffar gizi Hasanguliyeva — PhD in Chemistry, Leading Researcher, Institute of Catalysis and Inorganic Chemistry named after acad. M. Nagiyev of Ministry of Science and Education of the Republic of Azerbaijan, Ave. H. Javid 113, Az 1143, Baku, Azerbaijan; e-mail: nqasanquliyeva@mail.ru; https://orcid.org/0000-0003-4709-238x

Ninel Vladislavovna Shakunova (*corresponding author*) — PhD in Chemistry, Senior Researcher, Institute of Catalysis and Inorganic Chemistry named after acad. M. Nagiyev of Ministry of Science and Education of the Republic of Azerbaijan, Ave. H. Javid 113, Az 1143, Baku, Azerbaijan; e-mail: shakunova_ninel@mail.ru; https://orcid.org/0000-0002-9218-6839

Yuriy Nikolaevich Litvishkov — Doctor of Chemistry, Professor, Corresponding Member of ANAS, Institute of Catalysis and Inorganic Chemistry named after acad. M. Nagiyev of Ministry of Science and Education of the Republic of Azerbaijan, Ave. H. Javid 113, Az 1143, Baku, Azerbaijan; e-mail: yuriylit@rambler.ru; https://orcid.org/0000-0003-0662-1257

Author Contributions

All authors contributed to the preparation of the manuscript. All authors approved the final version of the manuscript. CRediT: **Nargalam Muzaffar gizi Hasanguliyeva** — conducting research, obtaining data, analyzing results, data manipulation, writing an article; **Ninel Vladislavovna Shakunova** — experimentation, data manipulation, text processing; **Yuri Nikolayevich Litvishkov** — conceptual development, research methodology, editing, approval of the final version of the article.

Conflicts of Interest

The authors declare no conflict of interest.

Acknowledgments

Authors express their gratitude to the management of the institute and all organizational structures — the library, the analytical department for providing assistance for the compilation of the article.

References

1 Sokolova, V.V., Naymushina, I.V., Sadikova, A.N., Mantabayeva, A.A., Tashmukhambetova, J.Kh., & Kairbekov, J.K. (2012). Polimerno-immobilizovanniye kompleksi kobalta (II), nanesennye na steklo, kak katalizatory protsessa oksigenatsii toluola. [Polymer-immobilized cobalt (II) complexes deposited on glass as catalysts for the process of oxygenation of toluene]. *Aktualnye problemy gumanitarnykh i estestvennykh nauk — Current problems of humanities and natural sciences, 7* (42), 18–23 [in Russian].

2 Buxarkina, T.V., Verjithinskaya, S.V., Fedyushkina, A.Q., Belousov, Yu.A., & Borisov, Yu.A. (2020). Poluchenie aromaticheskikh kislot zhidkofaznym okisleniem uglevodorodov. [Preparation of aromatic acids by liquid-phase oxidation of hydrocarbons]. *Nauchnyi zhurnal Rossiiskogo gazovogo obshchestva — Scientific Journal of the Russian Gas Society, 1*(24), 28–37 [in Russian].

3 Tsang, S.C., Zhu, J., & Yu, K.M.K. (2006). Selective catalytic oxidation of alkylaromatic molecules by nanosize water droplets containing Co^{2+} species in supercritical carbon dioxide fluid. *Journal of Experimental Nanoscience, 1*(4), 435–456. https://doi.org/10.1080/17458080601067682

4 Shangareev, D.R., Antonova, T.N., Abramov, I.G., Sivova, T.S., & Danilova, A.S. (2021). Catalytic Liquid-Phase Oxidation of Cyclooctene to 1,2-Epoxycyclooctane Using Molecular Oxygen. *Kinetics and Catalysis, 62*(1), 98–102. https://doi.org/10.1134/s0023158421010080

5 Digurov, N.G., Bukharkina, T.V., Verzhichinskaya, S.V., & Makarov, M.Y. (2010). Liquid-phase oxidation of ethylbenzene with air oxygen in the presence of a mixed cobalt-manganese catalyst. *Oil and Gas Technologies (scientific and technological journal*), 3, 31–36.

6 Lebedeva, N.V., Koshel, G.N., & Koshel, S.G. (2020). Liquid Phase Catalytic Oxidation 3,5-Xylenol. *Izvestiia Vysshikh Uchebnykh Zavedenii Khimiia Khimicheskaia Tekhnologiia — News of Higher Educational Institutions Chemistry Chemical Technology, 63*(3), 4–9. https://doi.org/10.6060/ivkkt.20206303.6095

7 Shakunova, N.V., Zulfuqarova, S.M., Aleskerova, Z.F., Faradjev, Q.M., & Litvishkov, Yu.N. (2005). Nekotorye zakonomernosti zhidkofaznogo okisleniia *m*-ksilola v prisuststvii katalizatorov Co-Mn/Al_2O_3/Al-karkas. [Some regularities of liquid-phase oxidation of *m*-xylene in the presence of Co-Mn/Al_2O_3/Al-framework catalysts]. *J. Neftepererabotka i neftekhimiia — J. Oil Refining and Petrochemistry*, 12, 21–23 [in Russian].

8 Lyu, Q., Dong, J., He, R., Sun, W., & Zhao, L. (2021). Modeling of the Co-Mn-Br catalyzed liquid phase oxidation of *p*-xylene to terephthalic acid and *m*-xylene to isophthalic acid. *Chemical Engineering Science, 232*, 116340. https://doi.org/10.1016/j.ces.2020.116340

9 Brel, A.K., Lisina, S.V., Budayeva, Yu.N., & Rodina, N.V. (2013). Sintez i psikhotropnye svoistva solei N-(4-gidroksibenzoil)glitsina i N-(4-atsetoksibenzoil)glitsina. [Synthesis and psychotropic activity of N-(4-hydroxybenzoyl)glycine and N-(4-acetoxybenzoyl)glycine salts]. *Fund. Issled*. — *Fundamental research*, 10, Pt9, 1963–1967 [in Russian].

10 Gritsenko, I.S., Taran, S.Q., & Isaev, S.Q., et al. (2014). Lekarstvennye sredstva alifaticheskoi i aromaticheskoi struktury: lektsii po farmatsevticheskoi khimii dlia studentov farmatsevticheskikh fakultetov vysshikh uchebnykh zavedenii III–IV urovnei akkreditatsii [Medicines of aliphatic and aromatic structure: lectures on pharmaceutical chemistry for students of pharmaceutical faculties of higher educational institutions of III-IV levels of accreditation]. *Khim. Izdatelstvo NUF*. — *Chemical Publishing house NUPh*, 147 [in Russian].

11 Aristanova, T.A. (2022). Farmatsevticheskaia khimiia [Pharmaceutical chemistry]. Almaty: Medet Group. — Almaty: «Medet Group», T.2. 524 [in Russian].

12 Knobl, S. (2003). The synthesis and structure of a single-phase, nanocrystalline MoVW mixed-oxide catalyst of the Mo_5O_{14} type. *Journal of Catalysis, 215*(2), 177–187. https://doi.org/10.1016/s0021-9517(03)00006-x

13 Litvishkov Yu.N., Zulfuqarova S.M., Shakunova N.M., & Aleskerova Z.F. (2004). Zhidkofaznoe okislenie *m*-ksilola v prisutstvii karkasnogo katalizatora Co-Mn/Al_2O_3/Al. [Liquid-phase oxidation of *m*-xylene in presence of Co-Mn/Al_2O_3/Al framework catalyst]. *Azerbaidzhanskii khimicheskii zhurnal — Azerbaijan Chemistry Journal*, 4, 22–26 [in Russian].

14 Litvishkov, Yu.N., Tretyakov, V.F., Talishinskaya, P.M., Shakunova, N.M., Zulfugarova, S.M., Aleskerova, Z.F., Mardanova, N.M., & Kashkay, A.M. (2013). Mikrovolnovaia intensifikatsiia geterogenno-kataliticheskoi zhidkofaznoi reaktsii okisleniia *m*-ksilola v prisutstvii nanostrukturirovannogo katalizatora Co-Mn/Al_2O_3/Al. [Microwave intensification of heterogeneous catalytic liquid-phase oxidation reaction of *m*-xylene in the presence of nanostructured-Co-Mn/Al_2O_3/Al catalyst]. *Nanotekhnologii: nauka i proizvodstvo*. — *Nanotechnology: science and production, 1*(22), 15–22 [in Russian].

15 Masood, Z., Ikhlaq, A., Akram, A., Qazi, U. Y., Rizvi, O. S., Javaid, R., Alazmi, A., Madkour, M., & Qi, F. (2022). Application of Nanocatalysts in Advanced Oxidation Processes for Wastewater Purification: Challenges and Future Prospects. *Catalysts, 12*(7), 741. https://doi.org/10.3390/catal12070741

16 Majeed Ahmed, L. (2021). Bulk and Nanocatalysts Applications in Advanced Oxidation Processes. *Oxidoreductase, 7*, 107–111. https://doi.org/10.5772/intechopen.94234

17 Avramenko, V.A., Bratskaya, S. Yu., Karpov, P.A., Mayorov, V. Yu., Mironenko, A.Yu., Palamarchuk, M.S., & Sergienko, V.I. (2010). Macroporous catalysts for liquid-phase oxidation on the basis of manganese oxides containing gold nanoparticles. *Doklady Physical Chemistry, 435*(2), 193–197. https://doi.org/10.1134/s0012501610120018

18 Ahmed, L.M., Ivanova, I., Hussein, F.H., & Bahnemann, D.W. (2014). Role of Platinum Deposited on TiO_2 in Photocatalytic Methanol Oxidation and Dehydrogenation Reactions. *International Journal of Photoenergy*, 1–9. https://doi.org/10.1155/2014/503516

19 Krumova, K., & Cosa, G. (2016). Chapter 1. Overview of Reactive Oxygen Species. Comprehensive Series in Photochemical & *Photobiological Sciences*, 1–21. https://doi.org/10.1039/9781782622208-00001

20 Kharisov, B.I., Dias, H.V.R., & Kharissova, O.V. (2019). Mini-review: Ferrite nanoparticles in the catalysis. *Arabian Journal of Chemistry, 12*(7), 1234–1246. https://doi.org/10.1016/j.arabjc.2014.10.049

21 Kaur, M., & Kaur, N. (2016). Ferrites: Synthesis and Applications for Environmental Remediation. Ferrites and Ferrates: Chemistry and Applications in Sustainable Energy and Environmental Remediation, 113–136. https://doi.org/10.1021/bk-2016-1238.ch004

22 Litvishkov, Yu.N., Zul'fugarova, S.M., Aleskerova, Z.F., Gasangulieva, N.M., Shakunova, N.V., & Aleskerov, A.G. (2018). Microwave Synthesis of Co, Ni, Cu, Zn Ferrites. *Russian Journal of Applied Chemistry, 91*(5), 793–801. https://doi.org/10.1134/s1070427218050105

23 Hasanguliyeva, N.M., Shakunova, N.M., Litvishkov, Yu.N., Samedova, R.A. (2023). Mikrovolnovoi sintez ferritov Ni-Co i ikh initsiiruyushchaya aktivnost v zhidkofaznom okislenii alkilaromaticheskikh uglevodorodov. [Microwave synthesis of Ni-Co ferrites and their initiating activities in liquid-phase oxidation of alkyl aromatic hydrocarbons]. *Neftepererabotka i neftekhimiia — Oil Refining and Petrochemistry.* 9, 38–44 [in Russian].

24 GOST 4467–79. (1979). Reaktivy. Kobalt (II, III) oksid. Tekhnicheskie usloviia [Reagents. Cobalt (II, III) oxide. Specifications]. *Gosudarstvennyi standart SSSR — State standard of the USSR* [in Russian].

25 GOST 4331-78. (1980). Reaktivy. Nikelia okis chernaia. Tekhnicheskie usloviia [Reagents. Nickelic black oxide. Specifications]. *Gosudarstvennyi standart SSSR — State standard of the USSR* [in Russian].

26 GOST 9410-78. (1980). Ksilol neftianoi. Tekhnicheskie usloviia [Petroleum xylol. Specifications]. *Gosudarstvennyi standart SSSR — State standard of the USSR.* [in Russian]

27 GOST 16589–86. (1988). Rudy zheleznye tipa zhelezistykh kvartsitov. Metod opredeleniia zheleza magnetita [Iron ores of iron quartzite type. Method for determination of magnetite iron]. *Gosudarstvennyi standart SSSR — State standard of the USSR* [in Russian].

28 Budanov, V.V., & Lefedova, O.V. (2011). Kineticheskie modeli zhidkofaznykh reaktsii [Kinetic models of liquid-phase reactions]. Uchebnoe posobie, Ivanovo — Study guide, Ivanovo. 177 [in Russian].

29 Antanovskiy, V.L., & Khursan, S.L. (2003). Fizicheskaia khimiia organicheskikh peroksidov [Physical chemistry of organic peroxides]. Moscow: Akademkniga — Moscow: Academic book, 391 [in Russian].

30 Guo, B., & Yuan, Y. (2015). A comparative review of methods for comparing means using partially paired data. *Statistical Methods in Medical Research, 26*(3), 1323–1340. https://doi.org/10.1177/0962280215577111

31 Bach, R.D., Ayala, P.Y., & Schlegel, H.B. (1996). A Reassessment of the Bond Dissociation Energies of Peroxides. An ab initio Study. *Journal of the American Chemical Society, 118*(50), 12758–12765. https://doi.org/10.1021/ja961838i

32 Exner, O. (1983). Stereochemical and conformational aspects of peroxy compounds. *Peroxides*, 85–96. Portico. https://doi.org/10.1002/9780470771730.ch2

33 Rossiter, B.E., & Frederick, M.O. (2013). Triphenylmethyl Hydroperoxide. *Encyclopedia of Reagents for Organic Synthesis*. https://doi.org/10.1002/047084289x.rt363m.pub2

34 Matsui, K. (2006). Green leaf volatiles: hydroperoxide lyase pathway of oxylipin metabolism. *Current Opinion in Plant Biology, 9*(3), 274–280. https://doi.org/10.1016/j.pbi.2006.03.002

35 Noyori, R., Aoki, M., & Sato, K. (2003). Green oxidation with aqueous hydrogen peroxide. *Chemical Communications, 16*, 1977. https://doi.org/10.1039/b303160h

How to Cite: Andreeva, A.V., Baimuratova, R.K., Dorokhov, V.G., Akkuratov, A.V., Shilov, G.V., Kugabaeva, G.D., Golubeva, N.D., & Dzhardimalieva, G.I. (2024) Rational Synthesis of UiO-66 and its Application in the Hydrogenation Reaction of p-Chloronitrobenzene. *Eurasian Journal of Chemistry, 29, 3(115), 92-108.* https://doi.org/10.31489/2959-0663/3-24-10

Article

Received: 9 June 2024 | Revised: 29 July 2024 |
Accepted: 31 July 2024 | Published online: 19 August 2024

UDC 542.973+547.92

https://doi.org/10.31489/2959-0663/3-24-10

Anastasia V. Andreeva[1,2], Rose K. Baimuratova[1*], Victor G. Dorokhov[1], Alexander V. Akkuratov[1], Gennadii V. Shilov[1], Gulsara D. Kugabaeva[1,3], Nina D. Golubeva[1], Gulzhian I. Dzhardimalieva[1,3]

[1]Federal Research Center of Problems of Chemical Physics and Medicinal Chemistry, Russian Academy of Sciences, Chernogolovka, Russia;
[2]Lomonosov Moscow State University, Moscow, Russia;
[3]Moscow Aviation Institute (National Research University), Moscow, Russia
*(*Corresponding author's e-mail: Roz_Baz@mail.ru)*

Rational Synthesis of UiO-66 and its Application in the Hydrogenation Reaction of p-Chloronitrobenzene

Hydrogenation is a widely used reaction in the oil processing and industrial organic synthesis. UiO-66 is a promising porous organic-inorganic material that can be used as a support for catalytically active particles. The key part in the application of highly porous UiO-66 is the search of a simple synthesis method that meets international environmental standards. In this study, a "rational" method for the synthesis of MOFs was used to produce UiO-66. The use of pre-synthesized multinuclear zirconia clusters facilitates the synthesis of the desired network topology, enabling the process to be conducted in an environmentally friendly aqueous solution. The effects of reaction temperature, linker volume concentration and solvent type on the specific surface area and thermal properties were also evaluated in this work. We studied the composition, structure and physicochemical properties of the obtained compounds by IR spectroscopy, TGA and XRD analysis. The proposed procedure has been shown to yield UiO-66 with high specific surface area (S_{BET} = 885 m^2/g) and to extend the thermal stability range up to 490 °C. The post-synthetic modification of the obtained UiO-66 with the introduction of catalytically active Pd (Pd/UiO-66) was carried out, and high selectivity (83,0 %) of the obtained Pd/UiO-66 exhibited high selectivity in the hydrogenation reaction of p-chloronitrobenzene into p-chloroaniline in comparison with the traditional Pd/Al_2O_3.

Keywords: metal-organic frameworks, UiO-66, heterogeneous catalysts, Pd/UiO-66, hydrogenation, p-Chloronitrobenzene, zirconium complexes, terephthalic acid, hydrogenation of nitroderivatives.

1. Introduction

Metal-organic frameworks (MOFs) represent a novel class of porous materials that offer the potential for targeted structural design through the modification of either the coordinating metal or organic linkers. The extended surface area and porosity of MOFs render them suitable for a multitude of applications for gas storage [1] and separation [2], as photosensitive elements [3], electrolytes [4], adsorbents [5], drug delivery agents [6], sensor materials [7] and supports in catalytic systems [8]. Such variety of applications is related to the structure features (various shape and size of pores [9], surface area [10], high crystallinity, etc.) and limitless functional properties (magnetic [11], electrically conductive [12], etc.).

The use of MOFs [13] as supports for catalytically active agents [14] is one of the promising routes, because such structures have a homogeneous porous surface. Heterogeneous catalysis and the creation of novel types of heterogeneous catalysts [15] are actual directions for research; their development makes the important industrial processes easier and less expensive by avoiding the final product extraction from solutions [16]. Heterogeneous catalysts based on MOFs can be industrially utilized with concurrent execution of the following conditions: the obtained catalysts should demonstrate stable operation at low temperatures of hydrogenation process and be insensitive to various impurities contained in the feedstock, while retaining high catalytic activity or selectivity; maintain long lifetime and be suitable for regeneration with its production being inexpensive and compliant with enforceable environmental standards [17]. Therefore, this study employs a "rational" method for the synthesis of MOFs, entailing the use of polynuclear molecular complexes as a source of secondary building units (SBUs) [18–20]. Pre-synthesized multinuclear clusters directed the synthesis to the desired network topology; it makes it possible to eliminate toxic coordinating solvents

(DMF, DEF etc.) and to perform the synthesis in a green aqueous solution [21]. In addition, a rational approach to the preparation of MOFs avoids the drawbacks of standard solvothermal methods, leading to the formation of mixed phases and the production of polycrystalline or amorphous structures [22].

Zirconium (IV) [23] is the optimal candidate for use as a framework-forming metal in the creation of metal-organic coordination polymers (CPs) suitable for heterogeneous catalysis, due to the high chemical, mechanical and thermal stability of zirconium-based compounds. The hexanuclear Zr_6 nodes can be treated as a universal node for coordination of many organic linkers with various topologies. Such nodes have Lewis acid properties due to the presence of Zr^{4+} [24], and metal-organic frameworks based on them can directly act as catalysts [25]. Nevertheless, in this work the use of zirconium MOFs as a support for catalytically active particles is of interest.

In 2008, Cavka et al. [26] synthesized MOFs with $Zr_6(\mu^3\text{-}O)_4(\mu^3\text{-}OH)_4$ nodes and various ligands for the first time: terephthalic acid (UiO-66), 4,4'-biphenyl-dicarboxylic acid (UiO-67) and 4,4'-[p-terphenyl]-dicarboxylic acid (UiO-68). Due to the high coordination number of the zirconium cluster, these structures have a large specific surface area, high thermal, chemical and mechanical stability in comparison with other MOFs. However, UiO-66 is the most stable one, due to its smaller pore size. It is known that for porous materials there is a risk of collapse of the structure during solvent removal, and this effect intensifies with the increase of the pore size with longer linkers in UiO-67 and UiO-68 [27]. While embracing attractive and exceptional characteristics, these Zirconium-based metal-organic frameworks (Zr-MOFs) still require further exploration of their sensitivity towards synthesis conditions [28] and research for an optimal method for their preparation [29].

The outstanding physicochemical characteristics of UiO-66 became the basis for the application of these structures in fuel cells [30], catalysis [31, 22], and greenhouse gas adsorption [32]. Zr-MOFs are promising supports for catalytically active particles which are vastly utilized in hydrogenation reactions [33–35]. We have previously shown that catalytic systems based on Zr-MOFs of UiO-66 series with different linkers (1,4-benzene dicarboxylic, 2-amino-1,4-benzene dicarboxylic and 2,6-naphthalene dicarboxylic acids) demonstrate high selectivity in industrially significant reactions such as hydrogenation of phenylacetylene and allyl alcohol [36].

The reaction for generation of such important organic intermediates as halogenanilines which are widely used in industrial production of medicines, pesticides and pigments, remains highly relevant when catalytic properties of hydrogenation catalysts are studied [37]. The most common way to obtain such compounds is the reduction of the corresponding aromatic nitro derivatives by selective hydrogenation on transition metal catalysts [38]. However, high operating costs due to contamination of catalysts during the reaction and low selectivity hinder the widespread use of such approaches for the production of halogen-containing amines. In addition, the generation of hydrochloric acid due to dechlorination has an effect on the catalytic activity and often leads to reactor corrosion [39]. Deep hydrogenation and chlorine removal can be minimized by addition of inhibitors to the mixture; however this approach is based on a complicated mechanism with an increased number of variables that require careful consideration. Therefore, the development of a new type of catalysts that can selectively work under soft conditions represents a significant challenge.

Although, the concept of immobilization of nanoparticles onto MOFs matrices has recently been successfully demonstrated, attempt at synthesis of chemically stable MOFs based on $Zr_6(\mu^3\text{-}O)_4(\mu^3\text{-}OH)_4$ with high specific surface area in non-toxic solvents is a challenging task. Therefore, the aim of this research is to address the challenges associated with the development of catalytic hydrogenation systems based on a novel class of porous materials that can operate effectively under mild conditions, while also being cost-effective and in compliance with international environmental standards. The proposed approach involves a method for the synthesis of highly porous MOFs.

This work presents the optimization of the synthesis methodology of coordination polymer $[Zr_6O_4(OH)_4(C_8H_4O_4)_6]_n$ for the creation of UiO-66-based nanostructured Pd-containing heterogeneous catalyst with improved specific surface area and thermal properties. Furthermore the catalytic properties of the obtained Pd/UiO-66 in the hydrogenation reaction of p-chloronitrobenzene have been studied.

2. Experimental

2.1. Reactants and reagents

Potassium chloride (KCl, ch.pr.), palladium (II) chloride ($PdCl_2$, ch.pr.), zirconyl chloride octahydrate ($ZrOCl_2{\cdot}8H2O$, p.a.), terephthalic acid ($C_8H_6O_4$, TPA, p.a.), 1-chloro-4-nitrobenzene ($C_6H_4ClNO_2$, **ch.pr.**), acetic acid (CH_3COOH, p.a), sodium borohydride ($NaBH_4$, p.a), sodium hydroxide (NaOH, p.a.), anhydrous

γ-aluminum oxide powder (γ-Al_2O_3, SBET = 40–50 m^2/g, tech.), hydrochloric acid (HCl) were purchased from Ruskhim chemical company (Moscow, Russia) and were used without further purification). Polyethylene Glycol 1500 (PEG-1500, $H(OCH_2CH_2)_nOH$, for synthesis) was supplied by Aldrich company. Ethanol, acetonitrile, isopropyl alcohol and cyclohexene of REAKHIM grades were supplied by Chimmed Group and purified according to standard methods. The purity was confirmed by High-Performance Liquid Chromatography (HPLC).

2.2. Synthesis methods

2.2.1. Synthesis methodology of coordination polymer based on pre-synthesized cluster $[Zr_6O_4(OH)_4(CH_3COO)_{12}]$

1) In the initial stage of the procedure, 5 mL of 2M CH_3COOH was added dropwise to 5 mL of 1M $ZrOCl_2 \cdot 8H_2O$ to obtain a hexanuclear zirconium cluster according to the procedure from the literature [40]. The mixture was cured at 55 °C for 120 min.

2) At the next step, 0.814 g (4.9 mmol) of terephthalic acid dissolved in aqueous KOH or DMF solution according to Table 1 was added to the mixture to obtain UiO-66. For some experiments CH3COOH was also added to the TPA solution to increase the crystallinity of the obtained polymers. The mixture was left at the fixed temperature for 120 minutes upon the addition of the organic ligand solution. The obtained coordination polymers were extracted by centrifugation at 4500 rev/min and flushed with solvent several times. The samples were treated with methanol in a Soxhlet extractor (16 h, 70 °C) and subsequently dried in vacuum (10^{-3} Torr, 55 °C, 10 h) in order to remove the solvent that had been physically adsorbed in the pores.

Table 1

Conditions for the synthesis of samples representing MOFs of UiO-66 type

Sample	Solvent	Solvent volume, mL	Reaction temperature, °C	m(CH_3COOH), g	Mixing speed, rev/min
Sample 1	H_2O	25	25	–	200
Sample 2	H_2O	100	25	–	1000
Sample 3	H_2O	25	50	–	200
Sample 4	H_2O	25	75	–	200
Sample 5	DMF	15	25	–	200
Sample 6	H_2O	25	25	5.4	200
Sample 7	DMF	15	25	5.4	200

2.2.2. Methodology for encapsulation of Pd nanoparticles into the pores of metal-organic frameworks [36]

Using the selected sample, a heterogeneous catalyst was prepared at a rate of 0.5 % Pd per 1 g of support. To this end, 0.017 g (0.095 mmol) of $PdCl_2$ was dissolved in 100 mL of methanol in the presence of 0.019 g (0.254 mmol) of KCl to obtain the soluble salt K_2PdCl_4. Then 0.2 g of PEG-1500 and 1 g of coordination polymer were added to the solution. The mixture was kept for 150 minutes at 68 °C until the precipitate acquired a distinctive dark brown color. The product was extracted by centrifugation and subjected to vacuum drying (10^{-3} Torr, 55 °C, 10 h). The ratio of the reactants was increased up to 4 times to obtain a heterogeneous catalyst containing 2 % Pd.

2.2.3. Synthesis of a compare catalyst Pd/Al_2O_3

A solution of palladium chloride was added in portions of 2–3 mL to 100 mL of aqueous suspension of γ-Al_2O_3 with a concentration of 50 g/L heated to 50 °C. The reaction mixture was kept under stirring at magnetic stirrer (200 rev/min) and temperature 50 °C for one hour.

$PdCl_2$ (0.250 g, 1.41 mmol) was dissolved in 25 mL of water by adding 1.4 mL of 18.5 % HCl solution (7 mmol). Once the palladium chloride had been fully dissolved, the pH was increased to neutral (pH ≈ 6–7) by the addition of 1 M NaOH.

An alkaline aqueous solution of $NaBH_4$ (1.41 mmol, $m(NaBH_4)/m(NaOH)$ = 0,1) was added dropwise to the obtained suspension to recover Pd. The mixture was stepwise cured out at 50 °C for 30 minutes and at 90 °C for 30 minutes under stirring conditions on a magnetic stirrer (200 rev/min). The obtained catalyst was separated by filtration and dried in an oven (60 °C, 10 h).

2.3. Research techniques

2.3.1. X-ray diffraction

X-ray diffraction analysis of the samples was conducted on a powder diffractometer Aeris Benchtop (Malvern PANalytical, the Netherlands) in the range of scattering angles from 5 to 50 °C (scanning step 2θ — 0.002°C, emission — CuK_{α}, λ = 1,5406 Å).

2.3.2. Fourier transform infrared spectroscopy (FT-IR).

The identification of functional groups of the obtained compounds was carried out on a Perkin-Elmer Spectrum 100 infrared Fourier spectrometer (USA, 2006) equipped with an attachment for frustrated total internal reflection (FTIR) with a diamond prism for single reflection. The penetration depth for the material with deep refractive index (2.43) at 1000 cm^{-1} is 1.66 microns. FT-IR-FTIR spectra were recorded in the range of 360–4000 cm^{-1} at room temperature using 24 scans and the definition of 2 cm^{-1}. The baseline of the obtained spectra was corrected in the OPUS program.

2.3.3. Identification of specific surface area and porosity

The specific surface area of samples, average radius and pore size distribution were determined by low-temperature nitrogen adsorption (at 77 K) on the sorption analyzer "AUTOSORB-1" ("Quantachrome", USA) by static volumetric method. The interaction between adsorbent and adsorbate in porous solids occurs by physisorption process, which makes the specific surface area an important property. The Brunauer-Emmett-Teller (BET) model was used to determine the surface area of porous materials from the isotherms of N_2 gas adsorption. The BET method is based on the hypothesis of multilayer adsorption proceeding through the formation of a monolayer of adsorbent molecules on the adsorbate surface.

The shape of six types of adsorption-desorption isotherms gives information about the presence of micro- and mesopores, as well as the shape of pores if the isotherm has a hysteresis loop. The volume and surface of micropores were determined by the t-method, and the distribution of pore volume was plotted using the BJH theory [41].

2.3.4. Thermogravimetric analysis

The thermal stability of composites was evaluated by the temperature of the start of decarboxylation by thermogravimetric analysis using a TGA/SDTA851e METTLER TOLEDO thermal analyzer (Mettler Toledo, Switzerland). The samples were heated in a nitrogen atmosphere at a heating rate of 10 °C/min at a temperature range extending from 25 to 550 °C.

2.3.5. Elemental analysis

Elemental analysis was performed to determine the concentration of nanoparticles on the surface of catalytic systems. The Pd concentration was determined using the atomic absorption spectro-meter "AAS-3" (Zeiss, Germany).

2.3.6. Methodology for determination of catalytic activity

The process of hydrogenation of p-chloronitrobenzene (1.0 ± 0.001 g) was carried out in a duck-type non-flow glass reactor in isopropyl alcohol at fixed atmospheric hydrogen pressure (0.1 MPa) and temperature 48.5 °C under intensive stirring conditions (180–240 shakes per minute). The amounts of catalysts were 0.3 ± 0.005 g. Hydrogen was supplied to the reactor from a calibrated receiver with a water gate. The partial pressure of water vapor was subtracted from the total atmospheric pressure to determine the own gas pressure, then the gas volume was normalized. The catalyst was treated with hydrogen for 15 minutes in the reactor under stirring before the addition of p-chloronitrobenzene. The reaction rate was calculated graphically from the slope of the starting parts of the kinetic curves of hydrogen flow rate.

2.3.7. Methodology for the study of mixture composition

Progress of the hydrogenation of p-chloronitrobenzene was investigated by HPLC method on Helicon EX-1800 machine (Wufeng, China). Chromatograms were recorded on Orbit C18 column (150×4.6 mm, 5 mm) using acetonitrile/water mixture (6/4) at 40 °C and flow rate of 1 mL/min. The detector wavelengths were 254 and 290 nm.

3. Results and Discussion

3.1. Composition and structure of synthesized MOFs

The most common method for the obtaining of zirconium-based metal-organic coordination polymers is the direct mixing of the metal salt and the selected linker in DMF solution, as the majority of dicarboxylic aromatic acids are insoluble [42–46]. However, such process may lead to generation of different phases, which does not yield the desired structural topology [22, 47]. Accordingly, a "rational" method for the synthesis of MOFs, using polynuclear molecular complexes as sources of secondary building units, was em-

ployed in this work. Previously, we demonstrated the versatility of this approach to obtain a series of UiO-66 isostructural MOFs with different organic ligands (1,4-benzene dicarboxylic, 2-amino-1,4-benzene dicarboxylic, and 2,6-naphthalenedicarboxylic acids) [36]. However, the resulting MOFs exhibited reduced surface areas; therefore, the proposed methodology for the synthesis of UiO-66 coordination polymer was improved in this work.

A series of UiO-66-type MOFs was obtained through the initial formation of a hexanuclear zirconium acetate complex with further replacement of the acetic acid residues with terephthalic acid residues (Table 1).

The system of chemical equations describing the proposed low-temperature process of obtaining the UiO series coordination polymers with the terephthalic organic ligand is presented below:

Step 1. Formation of inorganic building block:

$$ZrCl_4 + H_2O \rightarrow ZrOCl_2 + 2HCl$$

$$6ZrOCl_2 + 12CH_3COOH \rightarrow Zr_6O_4(OH)_4(CH_3COO)_{12} + 12HCl \quad pH \approx 1{,}5;\ 55\ °C$$

Step 2. Synthesis of UiO-66

$$C_8H_6O_4 + 2KOH \rightarrow K_2C_8H_4O_4 + 2H_2O$$

$$Zr_6O_4(OH)_4(CH_3COO)_{12} + 6K_2C_8H_4O_4 \rightarrow [Zr_6O_4(OH)_4(C_8H_4O_4)_6]_n + 12CH_3COOK$$

The impact of reaction temperature, linker volume concentration and solvent polarity on the specific surface area and thermal properties was also evaluated in this work (Table 1). It was shown that the increase of the reaction temperature up to 75 °C leads to the formation of mixed crystalline and amorphous products (Fig. 1, **Sample 4**). The use of DMF as a solvent resulted in the formation of a gel phase, which presented challenges in terms of solvent removal and the extraction of the pure product (Table 3).

3.1.1. Phase composition

The structures of the coordination polymers were confirmed by X-ray diffraction analysis. Most of the obtained samples had X-ray diffractograms with narrow diffraction maximums, it indicates the mainly crystalline-lytic phase state (Fig. 1). The observed peaks position agrees with the calculated spectrum taken from the literature [26] and confirms the structure of the samples. The formation of mixed phases with increasing synthesis temperature is confirmed by detecting multiple secondary reflections on the X-ray diffraction pattern of **Sample 4** (reaction temperature — 75 °C). Additionally the formation of by-products is observed with increasing temperature (2 Θ° ≈ 28,43). The formation of an arm below 7° for **Sample 5** obtained in DMF may be associated with the reflection plane 110 and reo phase defects [48–50]. The broadening of the main peak, can also be attributed to the presence of defects in the structure, which may be explained by the competition between acetic and terephthalic acids for carboxylate sites on $Zr_6O_4(OH)_4(COO)_{12}$ clusters [49]. It is known that defects in the structure of MOFs increase the catalytic activity indicating that inorganic nodes can be conceptualized as Lewis/Brønsted centers [51, 52].

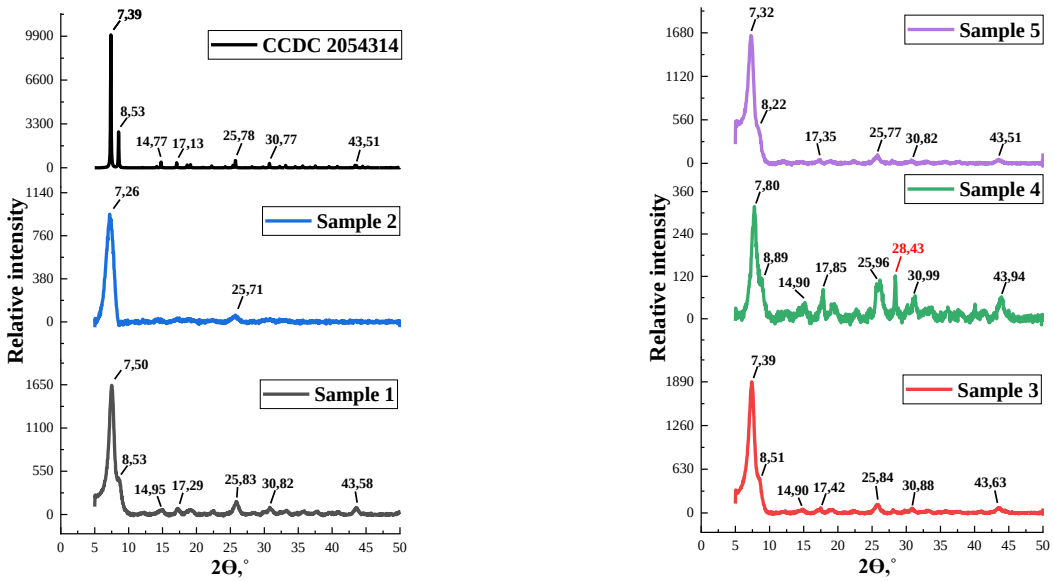

Figure 1. X-ray diffraction patterns of synthesized MOFs

3.1.2. Identification of functional groups by FTIR-ATR spectroscopy

The primary obtaining of the hexanuclear zirconium acetate complex $Zr_6O_4(OH)_4(COO)_{12}$ with the formation of coordination polymers by replacement of the acetic acid residues with terephthalic acid residues occurs during the synthesis. However, the exchange reaction may not occur completely in the case of high temperature synthesis, as evidenced by the detection of absorption bands characteristic of terephthalic acid (Fig. 2). For instance, bands of asymmetric vibrations of the –CO (in COO^-) appear in the region of 1676 $см^{-1}$ for **Samples 3** and **4**. Probably, the formation of the target product occurs worse at high temperatures of UiO-66 coordination polymer synthesis. This may be due to unfavorable reactions, which suggests that a temperature range limitation is necessary for the target exchange reaction. For **Sample 5**, the intensity of the –CO bond bands was lower, but the presence of the non-reacted acid band was also observed. The specific for the Zr–O bond absorption bands at 470 cm^{-1} were observed for each of the samples.

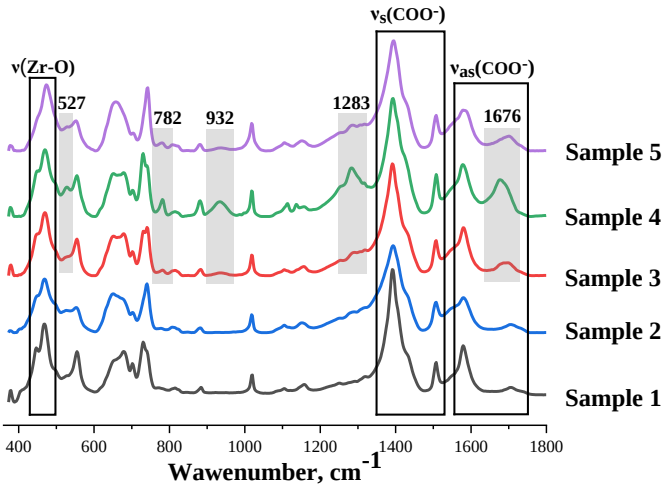

Figure 2. FTIR-ATR spectra of synthesized MOFs

The addition of modulator can reduce the rate of nucleation and delay crystal growth. Consequently, it leads to the formation of highly crystalline coordination polymers (examples of this approach are known from the literature [53]). Therefore, we attempted to improve the crystallinity of the samples by adding excess of acetic acid. The samples were obtained in aqueous solution (**Sample 6**) and in DMF (**Sample 7**) and their structures were studied by IR spectroscopy (Figure 3). IR spectra of the obtained samples are totally identical to the spectrum of the initial ligand. That demonstrated the impossibility of formation of the coordination polymer structure under these conditions. Therefore, we demonstrated the impracticality of increasing the amount of acetic acid to achieve higher crystallinity in the case of the used methodology.

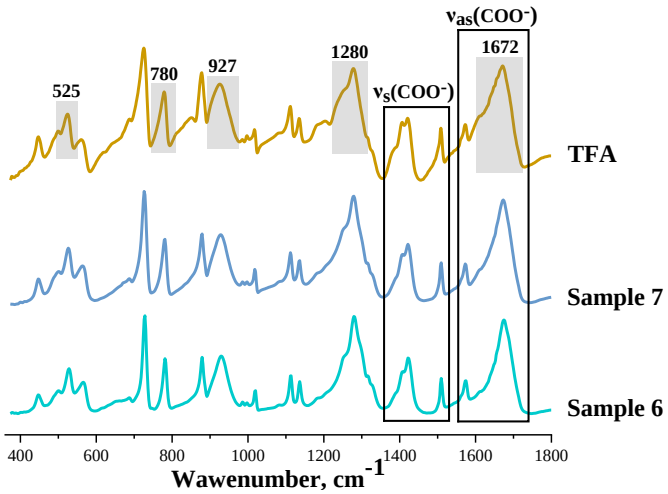

Figure 3. FTIR-ATR spectra of samples synthesized with addition of excessive acetic acid during the synthesis compared to the original ligand (TPA)

3.1.3 Results of the study of specific surface area

The major property of supports of catalytically active particles is the developed specific surface area; therefore, it was important to evaluate this property of the obtained coordination polymers. According to the nitrogen adsorption-desorption isotherms (Fig. 4), all the obtained MOFs have developed specific surface area. The isotherms are classified as type IV according to the IUPAC classification, with a hysteresis loop indicating the mesoporous structure of the samples. The hysteresis shape of the isotherm of **Sample 1** indicates nearly cylindrical pores (type H1). The other samples have an irregular, more chaotic pore structure with hysteresis type H2.

In order to characterize the porosity of the obtained catalysts in details, the external surface area was estimated. It is known that nanoparticles of catalytically active metal can potentially be localized directly in external pores ($S_{external}$ / S_{BET}). It is shown that the use of terephthalic acid solution at low volume concentration during synthesis (**Sample 2**) leads to a considerable proportion of the external surface area of the obtained coordination polymer accounting for approximately 60 %. **Sample 2** has the highest share of external surface area, so it was selected for further use as a support for catalytically active particles (Table 2).

The share of micropores unsuitable for encapsulation of Pd nanoparticles grows with increasing reaction temperature (**Samples 3**, **4**); therefore, it was optimal to carry out the synthesis at room-temperature. It should be noted that the determined values of specific surface area for UiO-66 are comparable to the values obtained in DMF, but they remain below the theoretical maximum (Table 4).

Table 2

Specific surface area, volume of pores and average pore diameter of the synthesized MOFs

Sample	S_{BET}, m^2/g	V_p, cm^3/g	Average pore diameter, nm	t-method		
				S_{micro}, m^2/g	$S_{external}$, m^2/g	$S_{external}$/ S_{BET}, %
Sample 1	885 ± 71	0.80 ± 0.06	8.9 ± 0.7	362 ± 72	523 ± 42	59.1
Sample 2	707 ± 57	0.29 ± 0.02	3.6 ± 0.3	193 ± 39	514 ± 41	72.7
Sample 3	726 ± 58	0.23 ± 0.02	3.6 ± 0.3	389 ± 78	338 ± 27	46.5
Sample 4	760 ± 61	0.28 ± 0.02	3.6 ± 0.3	402 ± 80	359 ± 29	47.1
Sample 5	801 ± 64	0.53 ± 0.04	6.0 ± 0.5	383 ± 78	418 ± 33	52.2

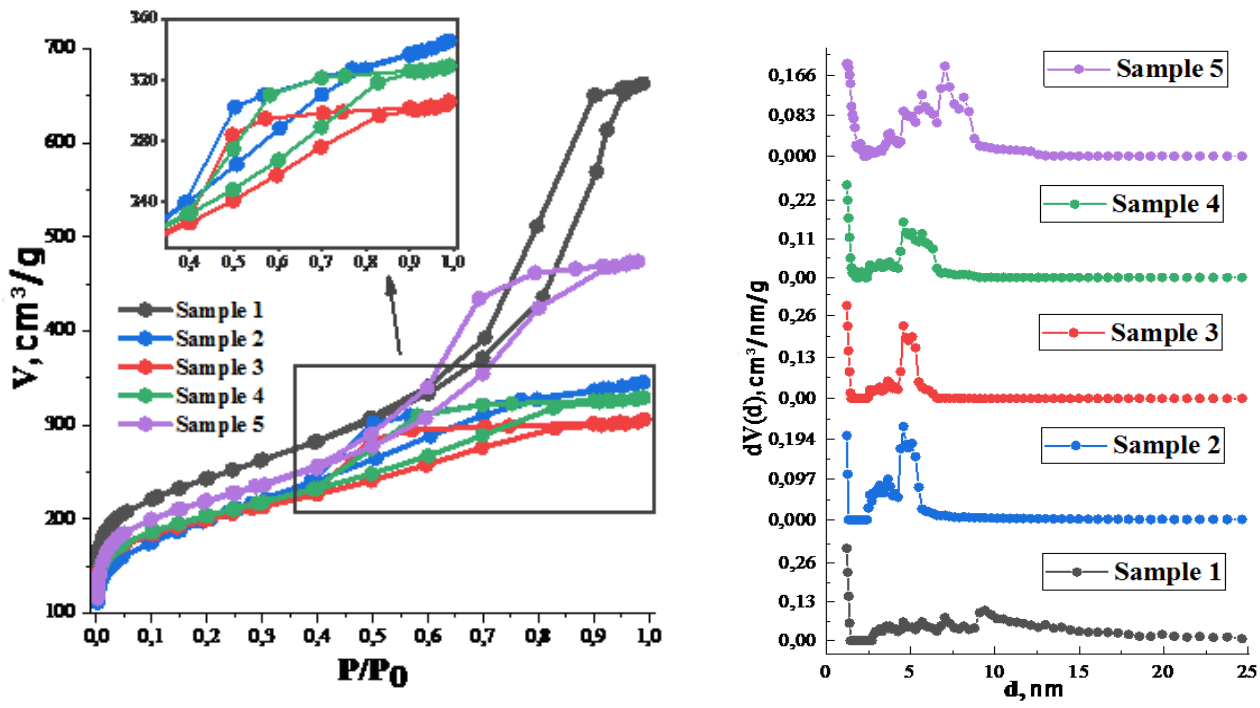

a *b*

Figure 4. Nitrogen adsorption-desorption isotherms (a) and pore size distribution (b) of the synthesized MOFs

3.1.4. The results of the thermal stability

All samples have three stages of mass loss according to the TGA curves (Fig. 5). The first stage, at temperatures up to 200 °C, involved the elimination of the residual solvent physically adsorbed in the pores of the coordination polymers. This high temperature of mass loss is caused by strong coordinating interactions. The following step included decarboxylation. A deeper decomposition of the coordination polymer framework with the formation of zirconium oxide occurred at temperatures above 450 °C.

Sample 5, synthesized using DMF solvent, contained more sorbed solvent molecules and had the lowest temperature of 10 % mass loss at the first stage of decomposition (207 °C) (Table 3). This may be caused by the formation of a gel phase during synthesis, making it difficult to remove the solvent when drying the sample, as well as the stronger interactions between DMF molecules and zirconium metal centers [54].

Table 3

Results of thermogravimetric analysis of UiO-66 samples obtained under different conditions

Sample	$T_{5\,\%}$, °C	$T_{10\,\%}$, °C	$T_{20\,\%}$, °C	$T_{30\,\%}$, °C	T_{max}, °C	$\Delta m_{25\text{-}450}$, mass %	Residual mass at 600 °C, mass %
Sample 1	345	490	539	554	552	7,6	43,7
Sample 2	161	333	527	553	557	12,9	46,7
Sample 3	165	337	532	557	554	12,6	41,6
Sample 4	180	341	529	555	557	13,1	42,9
Sample 5	111	206	512	546	553	15,6	47,3

Note – *$T_{5\,\%}$, $T_{10\,\%}$, $T_{20\,\%}$, $T_{30\,\%}$ — temperatures of 5 %, 10 %, 20 %, 30 % mass loss; T_{max} — temperature of maximum decomposition rate according to DTG curve*

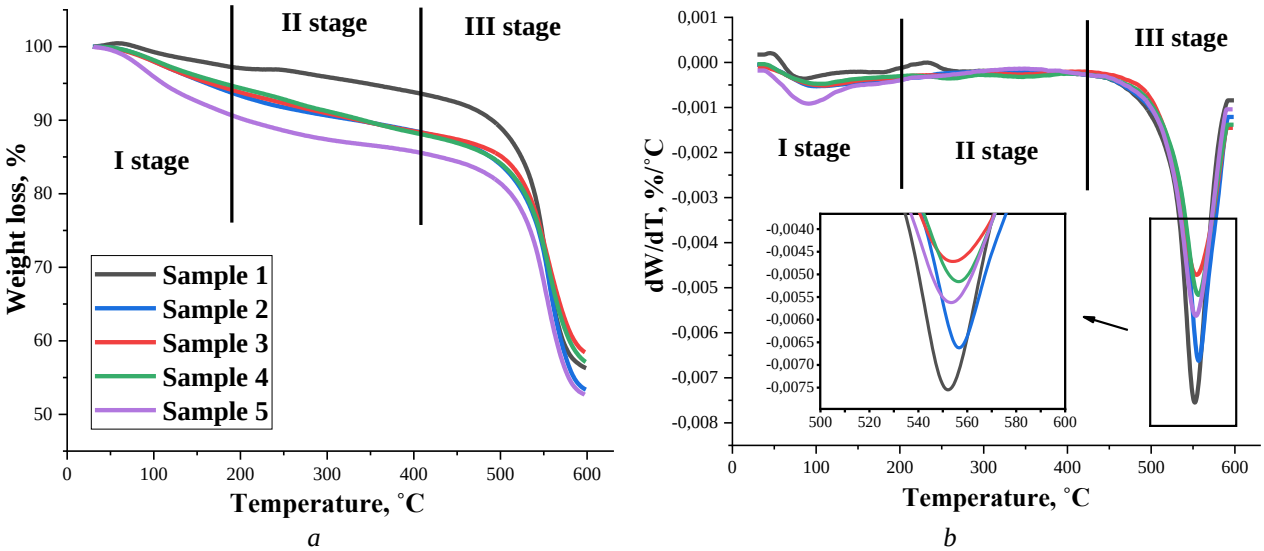

Figure 5. TGA curves (*a*) and their differential form (*b*) of UiO-66 samples obtained under different conditions

The results of thermogravimetric analysis demonstrated high thermal stability of the samples and the potential for practical application at temperatures up to 450 °C. Moreover, for **Sample 1**, the mass loss at this temperature was about 7.6 %, indicating the absence of decarboxylation with preservation of structure at high temperatures.

As a result of this research, a sample indicated as **Sample 1** was selected as a support, having an optimal surface area with a high share of external pores (which can potentially be filled with catalytically active metal nanoparticles), high thermal stability and chemical purity.

The physicochemical properties of the investigated coordination polymer were compared with the previously obtained sample [36] ($[Zr_6O_4(OH)_4(\text{terephthalic acid})_{12}]_n$, S_{BET} = 360 ± 29 m^2/g, $T_{10\,\%}$ = 146.62 ± 0.01 °C). As a result, the present method provides a 2,5-fold increase of the specific surface area from 360 to 885 m^2/g and extends the range of thermal stability up to 490 °C (Table 4). Solvothermal, microwave, electrochemical or mechanical methods are most commonly used to produce UiO-66. It is noted that the use of

microwave oven can increase the nucleation rate of synthesis and electrochemical methods can provide more accurate control of process parameters [43, 45, 55, 56]. Most of the methods use DMF as solvent, and modulation approaches restricting crystal growth are used to obtain more crystalline products. The major significance for the formation of the target structure in such reactions is the molar ratio of modulator and Zr [50]. In this work, the increase of modulator amount above equimolar values prevented the formation of the desired structure in aqueous solution synthesis. Obviously, the concentration of the modulator plays a crucial role in the formation of UiO-66, as it is necessary to select the concentration of the competing ligand to achieve a process that limits crystal growth.

Table 4

Comparison table of physicochemical properties of UiO-66 obtained under different reaction conditions

Sample	Synthesis conditions	$T_{10\,\%}$, °C	S_{BET}, m^2/g	Ref.
$[Zr_6O_4(OH)_4(TFA)_{12}]_n$(UiO-66)	$ZrCl_4$, CH_3COOH, H_2O, 55 °C	146,62 ± 0,01	360 ± 29	[36]
$[Zr_6O_4(OH)_4(TFA)_{12}]_n$(UiO-66)	$ZrOCl_2$, CH_3COOH, H_2O, 25 °C	490,54 ± 0,01	885 ± 71	This work
UiO-66	$ZrCl_4$, DMF, 120 °C	-	410	[50]
UiO-66	$ZrCl_4$, HCl, DMF, 120 °C	-	212-1647	[50]
UiO-66	$ZrCl_4$, DMF/H_2O = 100, 120°C.	-	940	[54]
UiO-66	$Zr(OnPr)_4$, DMF/1-propanol, CH_3COOH, 25°	-	960-1290	[57]
UiO-66	$ZrOCl_2$, DMF, 60 °C	-	634	[58]

3.2. Catalytic properties of the synthesized Pd-doped catalysts

3.2.1. Hydrogenation of cyclohexene

Catalytic system was synthesized based on the obtained coordination polymer by applying of 0,5 wt% palladium nanoparticles on 1 gram of support and three cycles of cyclohexene hydrogenation reaction were carried out to compare and evaluate the catalytic activity.

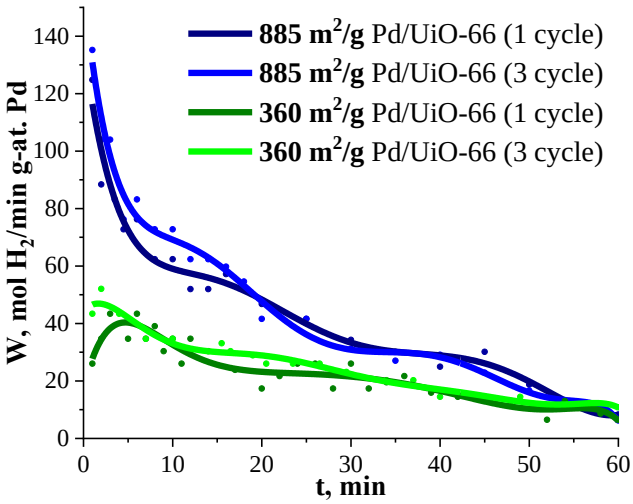

Figure 6. Dependence of cyclohexene hydrogenation rate on the reaction time in repeated cycles

Figure 6 shows that the use of the obtained coordination polymer with improved characteristics increased the initial hydrogenation rate by 3 times and reduced the total process time from ~90 to ~60 minutes.

3.2.2. Hydrogenation reaction of p-chloronitrobenzene

The catalytic properties were investigated in the industrially important hydrogenation reaction of p-chloronitrobenzene. Selective hydrogenation of nitro derivatives of benzene to obtain halogen substituted products is an important problem, since such compounds are widely used in the production of drugs, pesticides and pigments [37]. In addition, the dechlorination of benzene amino derivatives is often accompanied by the release of active chlorine and hydrochloric acid (Scheme 1), leading to corrosion and environmental pollution [39], so minimizing of this process is an important issue.

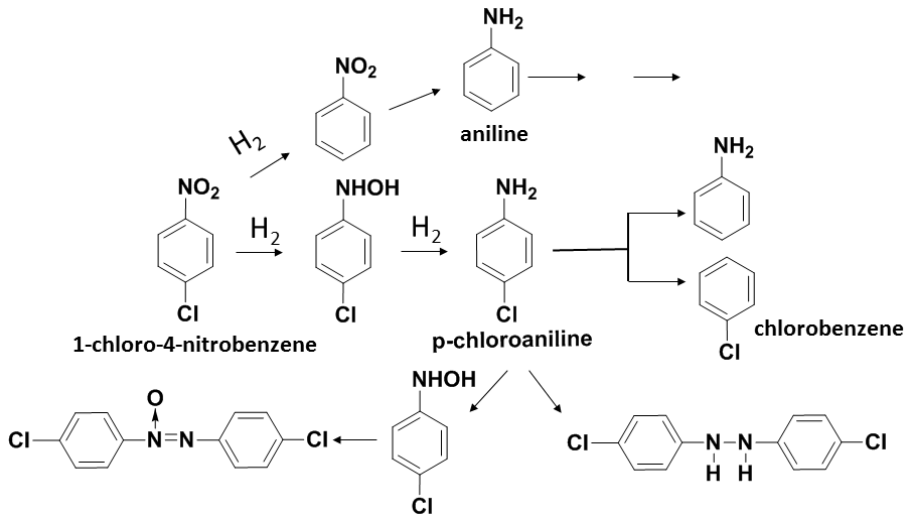

Scheme 1. Main paths of nitrochlorobenzene hydrogenation reaction

The catalytic system comprising Pd 1.7 ± 0.1 wt.%/g of support was obtained based on the synthesized **Sample 1**. Its characteristics were compared with the commercial Pd/Al_2O_3 catalyst (palladium content — 1.8 ± 0.1 wt.%).

The X-ray diffractogram profile of the Pd/UiO-66 catalyst is identical to the X-ray diffractogram of the initial MOFs, it indicates the preservation of the structure after the Pd nanoparticles deposition. Reflexes at 2 Θ° ≈ 40.12; 46.66; 68.12 corresponding to the metal Pd can be found on the X-ray diffractogram (Pd (46-1043), Fig. 7). The identification of Pd on Al_2O_3 is difficult due to the overlap of the support peaks.

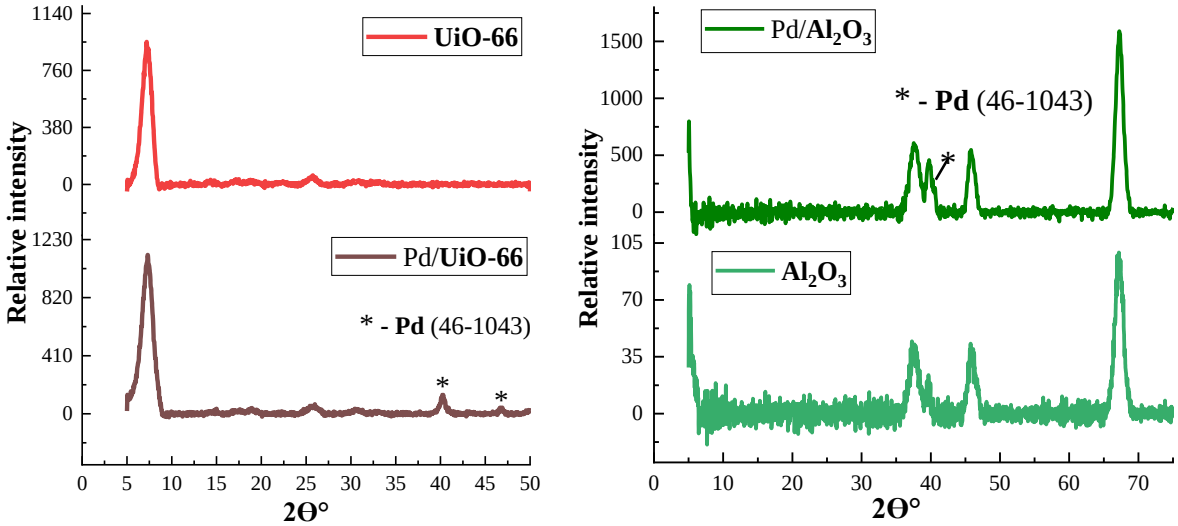

Figure 7. X-ray diffraction patterns of the obtained catalysts before and after palladium deposition

The morphology and distribution of palladium were analyzed by TEM microscopy. The homogeneous distribution of palladium nanoparticles on the surface of the coordination polymer UiO-66 can be seen in the presented TEM photographs (Fig. 8). Other situation is observed for the industrial support of catalytically active particles (Al_2O_3). The nanoparticles are aggregated on the surface of aluminum oxide. Particles with sharp edges of the inhomogeneous shape of the initial Al_2O_3 can be seen in TEM images with a resolution of 0.5 μ. The average size of particles on the surface of the analyzed catalytic systems ranged from 5 to 20 nm (Fig. 9).

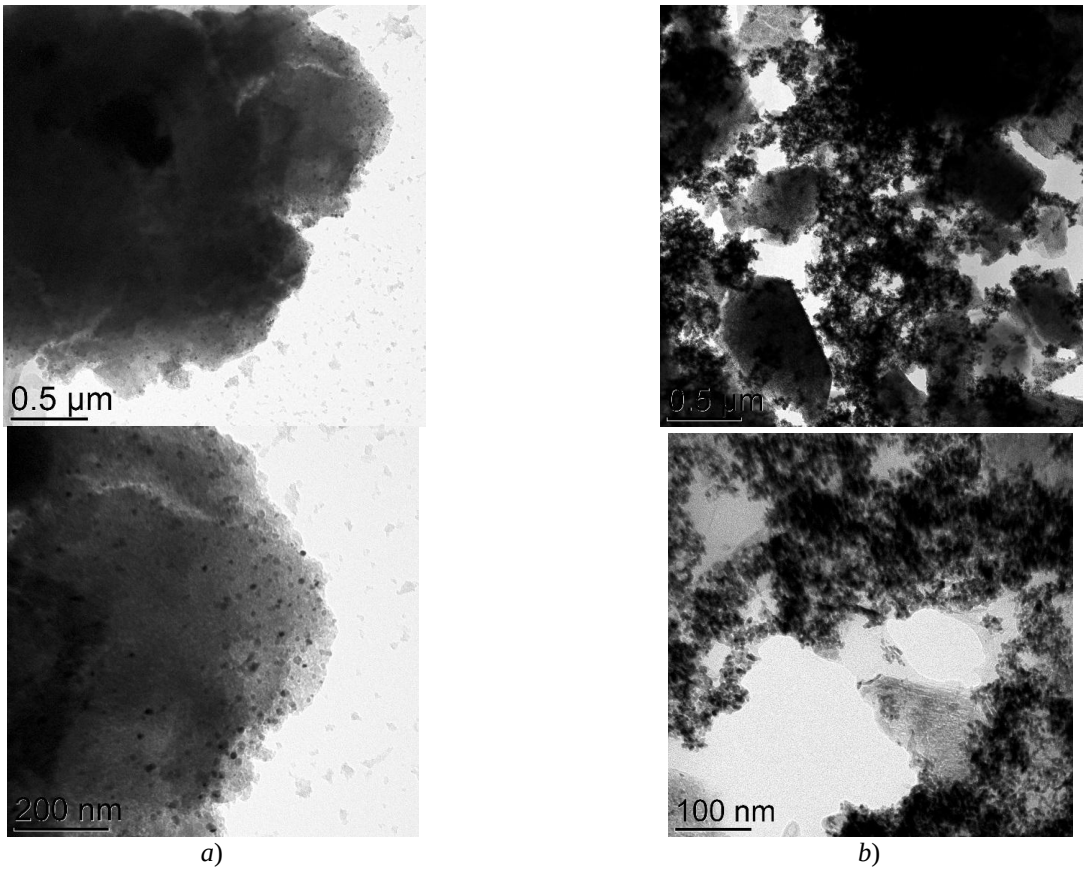

Figure 8. TEM images of the Pd/UiO-66 (a) and Pd/Al_2O_3 (b) surface

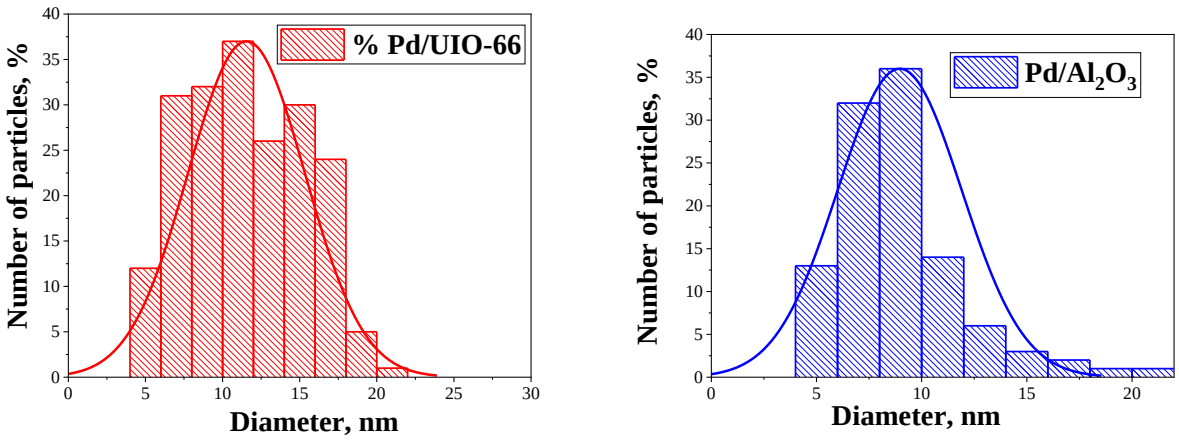

Figure 9. Histograms of Pd nanoparticle size distribution derived from TEM images

High-Performance Liquid Chromatography (HPLC) was used to analyze the time-dependent change of the mixture composition during the hydrogenation reaction. During the hydrogenation of p-chloronitrobenzene in the presence of Pd/Al_2O_3, the aniline content in the mixture was about ~20 % four minutes after the start of the process (Fig. 10). The complete conversion of the substrate was achieved after ten minutes, but the hydrogenation rates remained sufficiently high to ultimately result in a dechlorination process and the formation of unidentified reaction by-products.

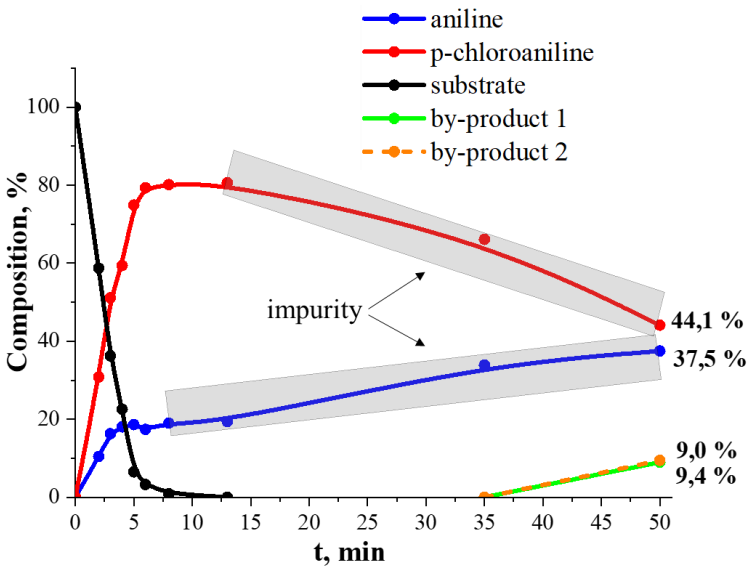

Figure 10. Dependence of reaction mixture composition on time during hydrogenation of p-chloronitrobenzene on the Pd/Al_2O_3 catalyst

The hydrogenation of p-chloronitrobenzene on the proposed Pd/UiO-66 catalytic system proceeded significantly longer. It may be explained by successive processes of adsorption and desorption of substrate in MOF pores before interaction with Pd active centers. Nevertheless, the observed reaction occurred with high selectivity of ~83 % up to the formation of p-chloroaniline (Fig. 11).

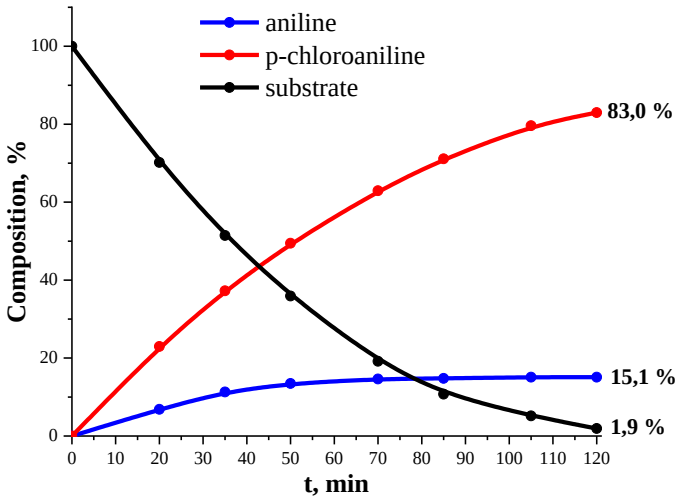

Figure 11. Dependence of reaction mixture composition on time during hydrogenation of p-chloronitrobenzene on the Pd/UiO-66 catalyst

Figure 12 shows the chromatograms of hydrogenation reaction products obtained by the process on two catalysts. In the case of Pd/Al_2O_3, the formation of many unidentified by-products (red circles on the chromatogram) leads to impurity of the target product (p-chloroaniline) and a decrease of selectivity below 44 %.

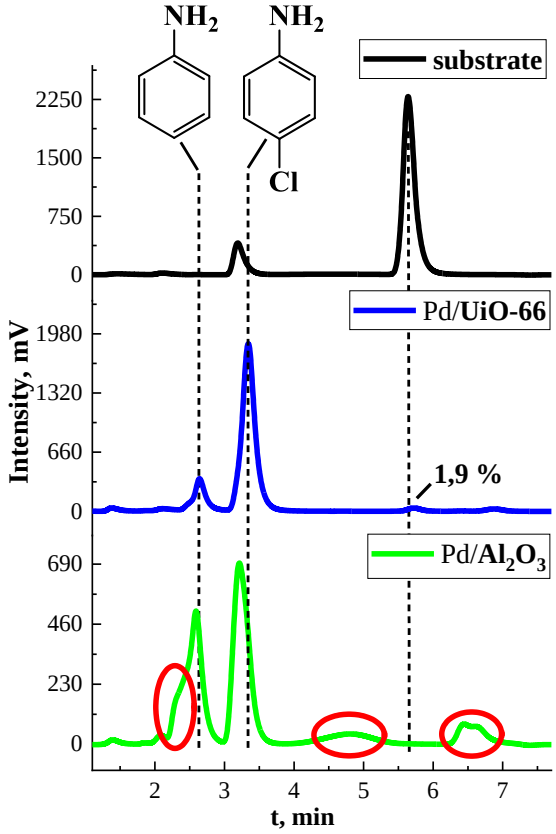

Figure 12. HPLC of the hydrogenation reaction mixture on different catalysts at a hydrogen consumption rate $w(H_2) < 0.6$ mL/min

In turn, using of the suggested catalytic system Pd/UiO-66 enables to obtain pure p-chloroaniline with high selectivity (83.0 %) at 98.1 % conversion (Table 5).

Table 5

Results of hydrogenation reaction of p-chloronitrobenzene using synthesized catalysts

Catalysts	P-chloraniline selectivity, %	Conversion, %
Pd/UiO-66	83,0	98,1
Pd/Al_2O_3	<44	100

Note – The conditions of the experiment: m_{cat} = 0,300 g; m_{sub} = 1,000 g; solvent — isopropanol (40 mL); T = 48,5 °C; p = 1 atm.

4. Conclusions

In this study, UiO-66 was obtained using a "rational" method for the synthesis of MOFs in aqueous solution. We demonstrated that increasing synthesis temperature from 25 °C to 75 °C lead to the increase of the share of micropores in the structure, as well as to the formation of amorphous MOFs and other by-products. The use of DMF as a solvent in this approach led to the formation of gel phase, complicating the removal of solvent and extraction of pure product. The addition of a modulator (acetic acid) in excess of equimolar quantities prevented the formation of the desired structure.

The composition, structure and physicochemical properties of the obtained compounds were studied by IR spectroscopy, TGA and XRD analysis. The results demonstrate that the proposed methodology effectively enhances the specific surface area by 2.5 times from 360 to 885 m^2/g and extends the range of thermal stability up to 490 °C.

The catalytic system Pd/UiO-66 was prepared through the post-synthetic modification of the obtained UiO-66 by encapsulation of catalytically active Pd. The ability of the obtained catalyst to carry out the reaction with high selectivity (83.0 %), in comparison with traditional Pd/Al_2O_3, was shown in the hydrogenation reaction of p-chloronitrobenzene to p-chloroaniline.

The use of pre-synthesized inorganic building blocks $Zr_6(\mu^3\text{-}O)_4(\mu^3\text{-}OH)_4$ demonstrates the potential of a rational stepwise approach for the synthesis of UiO-66, and could be a low-temperature scalable eco-friendly way to produce such highly porous materials.

Funding

This work has been carried out in accordance with the state tasks, state registration 124013000757-0, 12211170004-8, and 124013000722-8 using the equipment of the Multi-User Analytical Center of FRC PCP and MC RAS.

*Author Information**

**The authors' names are presented in the following order: First Name, Middle Name and Last Name*

Anastasia Vyacheslavovna Andreeva — Graduate Student, Department of Fundamental Physical and Chemical Engineering, Lomonosov Moscow State University, 119991, Moscow, Russia; Laboratory Assistant, Federal Research Center of Problems of Chemical Physics and Medicinal Chemistry, Russian Academy of Sciences, 142432, Chernogolovka, Moscow region, Russia; e-mail: andreevaav13@yandex.ru

Rose Kurmangalievna Baimuratova *(corresponding author)* — Candidate of Chemical Sciences, Junior Researcher, Federal Research Center of Problems of Chemical Physics and Medicinal Chemistry, Russian Academy of Sciences, 142432, Chernogolovka, Moscow region, Russia; e-mail: roz_baz@mail.ru; https://orcid.org/0000-0002-8389-6871

Victor Grigorievich Dorokhov — Candidate of Chemical Sciences, Head of Laboratory of Catalytic Synthesis of Organic Compounds, Federal Research Center of Problems of Chemical Physics and Medicinal Chemistry, Russian Academy of Sciences, 142432, Chernogolovka, Moscow region, Russia; e-mail: vicd@icp.ac.ru

Alexander Vitalievich Akkuratov — Candidate of Chemical Sciences, Head of Laboratory of Photosensitive and Electroactive Materials Department of Polymers and Composite Materials, Federal Research Center of Problems of Chemical Physics and Medicinal Chemistry, Russian Academy of Sciences, 142432, Chernogolovka, Moscow region, Russia; e-mail: akkuratow@yandex.ru; https://orcid.org/0000-0001-8750-0048

Gennadii Viktorovich Shilov — Candidate of Physical and Mathematical Sciences, Senior Researcher, Federal Research Center of Problems of Chemical Physics and Medicinal Chemistry, Russian Academy of Sciences, 142432, Chernogolovka, Moscow region, Russia; e-mail: genshil@icp.ac.ru

Gulsara Damirovna Kugabaeva — PhD Student, Moscow Aviation Institute (National Research University), 125993, Moscow, Russia; Junior Researcher, Federal Research Center of Problems of Chemical Physics and Medicinal Chemistry, Russian Academy of Sciences, 142432, Chernogolovka, Moscow region, Russia; e-mail: gulsara_kugabaev@mail.ru

Nina Danilovna Golubeva — Senior Researcher, Federal Research Center of Problems of Chemical Physics and Medicinal Chemistry, Russian Academy of Sciences, 142432, Chernogolovka, Moscow region, Russia; e-mail: nd_golubeva@mail.ru

Gulzhian Iskakovna Dzhardimalieva — Doctor of Chemical Sciences, Head of Laboratory of Metallopolymers, Federal Research Center of Problems of Chemical Physics and Medicinal Chemistry, Russian Academy of Sciences, 142432, Chernogolovka, Moscow region, Russia; e-mail: dzhardim@icp.ac.ru; https://orcid.org/0000-0002-4727-8910

Author Contributions

The manuscript was written through contributions of all authors. All authors have given approval to the final version of the manuscript. CRediT: **Anastasia Vyacheslavovna Andreeva** investigation, visualization, writing-original draft; **Rose Kurmangalievna Baimuratova** conceptualization, methodology, data curation, writing-review & editing; **Victor Grigorievich Dorokhov** investigation, methodology, data curation, supervision; **Alexander Vitalievich Akkuratov** investigation, methodology, data curation; **Shilov Gennadii Viktorovich** investigation, formal analysis; **Gulsara Damirovna Kugabaeva** validation, data curation, for-

mal analysis; **Golubeva Nina Danilovna** data curation, formal analysis, validation; **Gulzhian Iskakovna Dzhardimalieva** conceptualization, data curation, resources, supervision, writing-review & editing.

Conflicts of Interest

The authors declare no conflict of interest.

References

1 Li, B., Wen, H.-M., Zhou, W., & Chen, B. (2014). Porous Metal–Organic Frameworks for Gas Storage and Separation: What, How, and Why? *The Journal of Physical Chemistry Letters, 5*(20), 3468–3479. https://doi.org/10.1021/jz501586e

2 Semerci, F., Yeşilel, O. Z., Soylu, M. S., Keskin, S., & Büyükgüngör, O. (2013). A two-dimensional photoluminescent cadmium(II) coordination polymer containing a new coordination mode of pyridine-2,3-dicarboxylate: Synthesis, structure and molecular simulations for gas storage and separation applications. *Polyhedron, 50*(1), 314–320. https://doi.org/10.1016/j.poly.2012.10.009

3 Wang, H., Liu, Z., Liu, Z., Jiang, J., & Li, G. (2021). Photo-Dissociable Fe $^{3+}$ -Carboxylate Coordination: A General Approach toward Hydrogels with Shape Programming and Active Morphing Functionalities. *ACS Applied Materials & Interfaces, 13*(49), 59310–59319. https://doi.org/10.1021/acsami.1c19458

4 Liu, J., Zheng, M., Wu, S., & Zhang, L. (2023). Design strategies for coordination polymers as electrodes and electrolytes in rechargeable lithium batteries. *Coordination Chemistry Reviews, 483*, 215084. https://doi.org/10.1016/j.ccr.2023.215084

5 Xiao, L., Xiong, Y., Tian, S., He, C., Su, Q., & Wen, Z. (2015). One-dimensional coordination supramolecular polymer [Cu(bipy)(SO4)]n as an adsorbent for adsorption and kinetic separation of anionic dyes. *Chemical Engineering Journal, 265*, 157–163. https://doi.org/10.1016/j.cej.2014.11.134

6 Xiang, S., Liu, J., Han, G., Zhang, W., Long, Y., Deng, Y., Wang, B., & Weng, Q. (2023). Design of red-emitting 1D zinc coordination polymer for targeted drug delivery to nucleus. *Chemical Engineering Journal, 470*, 144177. https://doi.org/10.1016/j.cej.2023.144177

7 Shukla, A. K., Verma, V., Goriyan, P., Rani, A., Verma, A., Singh, A., Yadav, B. C., Baimuratova, R. K., Andreeva, A. V., & Dzhardimalieva, G. I. (2024). Zr6O4(OH)4 Based Metal-Organic Frameworks for the Enhanced Chemiresistive Sensing of Ethanol. *Journal of Inorganic and Organometallic Polymers and Materials*, 1–16. https://doi.org/10.1007/s10904-023-02986-1

8 Bavykina, A., Kolobov, N., Khan, I. S., Bau, J. A., Ramirez, A., & Gascon, J. (2020). Metal–Organic Frameworks in Heterogeneous Catalysis: Recent Progress, New Trends, and Future Perspectives. *Chemical Reviews, 120*(16), 8468–8535. https://doi.org/10.1021/acs.chemrev.9b00685

9 De Almeida, F. B., Da Silva Cunha, M., Barros, W. P., De Abreu, H. A., & Diniz, R. (2020). Structure, Electronic, Magnetic, and Gas Adsorption Properties of Zinc(II) and Cobalt(II) Coordination Polymers Assembled from Isonicotinylhydrazine and Trimesic Acid. *The Journal of Physical Chemistry C, 124*(38), 21103–21112. https://doi.org/10.1021/acs.jpcc.0c06479

10 Wang, J., Fan, Y., Tan, Y., Zhao, X., Zhang, Y., Cheng, C., & Yang, M. (2018). Porphyrinic Metal–Organic Framework PCN-224 Nanoparticles for Near-Infrared-Induced Attenuation of Aggregation and Neurotoxicity of Alzheimer's Amyloid-β Peptide. *ACS Applied Materials & Interfaces, 10*(43), 36615–36621. https://doi.org/10.1021/acsami.8b15452

11 Agarwal, R. A., Aijaz, A., Sañudo, C., Xu, Q., & Bharadwaj, P. K. (2013). Gas Adsorption and Magnetic Properties in Isostructural Ni(II), Mn(II), and Co(II) Coordination Polymers. *Crystal Growth & Design, 13*(3), 1238–1245. https://doi.org/10.1021/cg3016904

12 Zhang, C., Fan, K., Chen, Y., Wu, Y., & Wang, C. (2021). Conjugated Coordination Polymers as Electrodes for Rechargeable Batteries. *ACS Applied Electronic Materials, 3*(5), 1947–1958. https://doi.org/10.1021/acsaelm.1c00297

13 Sánchez-Serratos, M., Raziel Álvarez, J., González-Zamora, E., & Ibarra, I. A. (2017). Porous Coordination Polymers (PCPs): New Platforms for Gas Storage. *Journal of the Mexican Chemical Society, 60*(2). https://doi.org/10.29356/jmcs.v60i2.72

14 Wang, Q., & Astruc, D. (2020). State of the Art and Prospects in Metal–Organic Framework (MOF)-Based and MOF-Derived Nanocatalysis. *Chemical Reviews, 120*(2), 1438–1511. https://doi.org/10.1021/acs.chemrev.9b00223

15 Huang, Y. -B., Wang, Q., Liang, J., Wang, X., & Cao, R. (2016). Soluble Metal-Nanoparticle-Decorated Porous Coordination Polymers for the Homogenization of Heterogeneous Catalysis. *Journal of the American Chemical Society, 138*(32), 10104–10107. https://doi.org/10.1021/jacs.6b06185

16 Dhakshinamoorthy, A., Asiri, A. M., & Garcia, H. (2019). Formation of C–C and C–Heteroatom Bonds by C–H Activation by Metal Organic Frameworks as Catalysts or Supports. *ACS Catalysis, 9*(2), 1081–1102. https://doi.org/10.1021/acscatal.8b04506

17 Guo, M., Zhang, M., Liu, R., Zhang, X., & Li, G. (2022). State-of-the-Art Advancements in Photocatalytic Hydrogenation: Reaction Mechanism and Recent Progress in Metal-Organic Framework (MOF)-Based Catalysts. *Advanced Science, 9*(1), 2103361. https://doi.org/10.1002/advs.202103361

18 Ockwig, N. W., Delgado-Friedrichs, O., O'Keeffe, M., & Yaghi, O. M. (2005). Reticular Chemistry: Occurrence and Taxonomy of Nets and Grammar for the Design of Frameworks. *Accounts of Chemical Research, 38*(3), 176–182. https://doi.org/10.1021/ar020022l

19 Yaghi, O. M., O'Keeffe, M., Ockwig, N. W., Chae, H. K., Eddaoudi, M., & Kim, J. (2003). Reticular synthesis and the design of new materials. *Nature, 423*(6941), 705–714. https://doi.org/10.1038/nature01650

20 Baimuratova, R. K., Zhinzhilo, V. A., Uflyand, I. E., Dmitriev, A. I., Zhidkov, M. V., Ovanesyan, N. S., Kugabaeva, G. D., & Dzhardimalieva, G. I. (2023). Low-Temperature Synthesis of Metal–Organic Coordination Polymers Based on Oxo-centered Iron Complexes: Magnetic and Adsorption Properties. *Russian Journal of Physical Chemistry A, 97*(4), 735–748. https://doi.org/10.1134/S0036024423040064

21 Bondarenko, L., Baimuratova, R., Reindl, M., Zach, V., Dzeranov, A., Pankratov, D., Kydralieva, K., Dzhardimalieva, G., Kolb, D., Wagner, F. E., & Schwaminger, S. P. (2024). Dramatic change in the properties of magnetite-modified MOF particles depending on the synthesis approach. *Heliyon*, e27640. https://doi.org/10.1016/j.heliyon.2024.e27640

22 Bennett, T. D., & Cheetham, A. K. (2014). Amorphous Metal–Organic Frameworks. *Accounts of Chemical Research, 47*(5), 1555–1562. https://doi.org/10.1021/ar5000314

23 Zha, Q., Rui, X., Wei, T., & Xie, Y. (2014). Recent advances in the design strategies for porphyrin-based coordination polymers. *CrystEngComm, 16*(32), 7371–7384. https://doi.org/10.1039/C4CE00854E

24 Nikoofar, K., & Khademi, Z. (2016). A review on green Lewis acids: Zirconium(IV) oxydichloride octahydrate (ZrOCl2·8H2O) and zirconium(IV) tetrachloride (ZrCl4) in organic chemistry. *Research on Chemical Intermediates, 42*(5), 3929–3977. https://doi.org/10.1007/s11164-015-2260-6

25 Hou, P., Ma, M., Zhang, P., Cao, J., Liu, H., Xu, X., Yue, H., Tian, G., & Feng, S. (2021). Catalytic transfer hydrogenation of furfural to furfuryl alcohol using easy-to-separate core–shell magnetic zirconium hydroxide. *New Journal of Chemistry, 45*(5), 2715–2722. https://doi.org/10.1039/D0NJ05638C

26 Cavka, J. H., Jakobsen, S., Olsbye, U., Guillou, N., Lamberti, C., Bordiga, S., & Lillerud, K. P. (2008). A New Zirconium Inorganic Building Brick Forming Metal Organic Frameworks with Exceptional Stability. *Journal of the American Chemical Society, 130*(42), 13850–13851. https://doi.org/10.1021/ja8057953

27 Deria, P., Chung, Y. G., Snurr, R. Q., Hupp, J. T., & Farha, O. K. (2015). Water stabilization of Zr_6 -based metal–organic frameworks via solvent-assisted ligand incorporation. *Chemical Science, 6*(9), 5172–5176. https://doi.org/10.1039/C5SC01784J

28 Piscopo, C. G., Polyzoidis, A., Schwarzer, M., & Loebbecke, S. (2015). Stability of UiO-66 under acidic treatment: Opportunities and limitations for post-synthetic modifications. *Microporous and Mesoporous Materials, 208*, 30–35. https://doi.org/10.1016/j.micromeso.2015.01.032

29 Pakamorė, I., Rousseau, J., Rousseau, C., Monflier, E., & Szilágyi, P. Á. (2018). An ambient-temperature aqueous synthesis of zirconium-based metal–organic frameworks. *Green Chemistry, 20*(23), 5292–5298. https://doi.org/10.1039/C8GC02312C

30 Yang, F., Huang, H., Wang, X., Li, F., Gong, Y., Zhong, C., & Li, J. -R. (2015). Proton Conductivities in Functionalized UiO-66: Tuned Properties, Thermogravimetry Mass, and Molecular Simulation Analyses. *Crystal Growth & Design, 15*(12), 5827–5833. https://doi.org/10.1021/acs.cgd.5b01190

31 Dutta, S., & Lee, I. S. (2021). Metal–organic framework based catalytic nanoreactors: Synthetic challenges and applications. *Materials Chemistry Frontiers, 5*(11), 3986–4021. https://doi.org/10.1039/D1QM00242B

32 Rayder, T. M., Bensalah, A. T., Li, B., Byers, J. A., & Tsung, C. -K. (2021). Engineering Second Sphere Interactions in a Host–Guest Multicomponent Catalyst System for the Hydrogenation of Carbon Dioxide to Methanol. *Journal of the American Chemical Society, 143*(3), 1630–1640. https://doi.org/10.1021/jacs.0c08957

33 Gong, Y., Yuan, Y., Chen, C., Chaemchuen, S., & Verpoort, F. (2020). Palladium metallated shell layer of shell@core MOFs as an example of an efficient catalyst design strategy for effective olefin hydrogenation reaction. *Journal of Catalysis, 392*, 141–149. https://doi.org/10.1016/j.jcat.2020.09.037

34 Jiang, H., Zhang, W., Kang, X., Cao, Z., Chen, X., Liu, Y., & Cui, Y. (2020). Topology-Based Functionalization of Robust Chiral Zr-Based Metal–Organic Frameworks for Catalytic Enantioselective Hydrogenation. *Journal of the American Chemical Society, 142*(21), 9642–9652. https://doi.org/10.1021/jacs.0c00637

35 Kassie, A. A., & Wade, C. R. (2020). Catalytic Activity of a Zr MOF Containing POCOP-Pd Pincer Complexes. *Organometallics, 39*(12), 2214–2221. https://doi.org/10.1021/acs.organomet.0c00164

36 Baimuratova, R. K., Andreeva, A. V., Uflyand, I. E., Shilov, G. V., Bukharbayeva, F. U., Zharmagambetova, A. K., & Dzhardimalieva, G. I. (2022). Synthesis and Catalytic Activity in the Hydrogenation Reaction of Palladium-Doped Metal-Organic Frameworks Based on Oxo-Centered Zirconium Complexes. *Journal of Composites Science, 6*(10), 299. https://doi.org/10.3390/jcs6100299

37 Zhang, M., Liu, Y., Zhao, H., Tao, J., Geng, N., Li, W., & Zhai, Y. (2021). Pd Anchored on a Phytic Acid/Thiourea Polymer as a Highly Active and Stable Catalyst for the Reduction of Nitroarene. *ACS Applied Materials & Interfaces, 13*(17), 19904–19914. https://doi.org/10.1021/acsami.0c23007

38 Wang, X., Liang, M., Zhang, J., & Wang, Y. (2007). Selective Hydrogenation of Aromatic Chloronitro Compounds. *Current Organic Chemistry, 11*(3), 299–314. https://doi.org/10.2174/138527207779940856

39 Jaf, Z. N., Altarawneh, M., Miran, H. A., Almatarneh, M. H., Jiang, Z. -T., & Dlugogorski, Bogdan. Z. (2018). Catalytic Hydrogenation of p -Chloronitrobenzene to p -Chloroaniline Mediated by γ-Mo_2N. *ACS Omega, 3*(10), 14380–14391. https://doi.org/10.1021/acsomega.8b01936

40 Hennig, C., Weiss, S., Kraus, W., Kretzschmar, J., & Scheinost, A. C. (2017). Solution Species and Crystal Structure of Zr(IV) Acetate. *Inorganic Chemistry, 56*(5), 2473–2480. https://doi.org/10.1021/acs.inorgchem.6b01624

41 Lowell, S., Shields, J. E., Thomas, M. A., & Thommes, M. (2004). Characterization of Porous Solids and Powders: Surface Area, Pore Size and Density (Vol. 16). Springer Netherlands. https://doi.org/10.1007/978-1-4020-2303-3

42 Tanaka, S. (2020). Mechanochemical synthesis of MOFs. *Metal-Organic Frameworks for Biomedical Applications*, 197–222. Elsevier. https://doi.org/10.1016/B978-0-12-816984-1.00012-3

43 Ghoorchian, A., Afkhami, A., Madrakian, T., & Ahmadi, M. (2020). Electrochemical synthesis of MOFs. *Metal-Organic Frameworks for Biomedical Applications*, 177–195. Elsevier. https://doi.org/10.1016/B978-0-12-816984-1.00011-1

44 Zavyalova, A. G., Kladko, D. V., Chernyshov, I. Yu., & Vinogradov, V. V. (2021). Large MOFs: Synthesis strategies and applications where size matters. *Journal of Materials Chemistry A*, *9*(45), Article 45. https://doi.org/10.1039/D1TA05283G

45 Khan, N. A., & Jhung, S. H. (2015). Synthesis of metal-organic frameworks (MOFs) with microwave or ultrasound: Rapid reaction, phase-selectivity, and size reduction. *Coordination Chemistry Reviews*, *285*, 11–23. https://doi.org/10.1016/j.ccr.2014.10.008

46 Stock, N., & Biswas, S. (2012). Synthesis of Metal-Organic Frameworks (MOFs): Routes to Various MOF Topologies, Morphologies, and Composites. *Chemical Reviews*, *112*(2), 933–969. https://doi.org/10.1021/cr200304e

47 Huang, L. (2003). Synthesis, morphology control, and properties of porous metal–organic coordination polymers. *Microporous and Mesoporous Materials*, *58*(2), 105–114. https://doi.org/10.1016/s1387-1811(02)00609-1

48 Chammingkwan, P., Shangkum, G. Y., Mai, L. T. T., Mohan, P., Thakur, A., Wada, T., & Taniike, T. (2020). Modulator-free approach towards missing-cluster defect formation in Zr-based UiO-66. *RSC Advances*, *10*(47), 28180–28185. https://doi.org/10.1039/D0RA04812G

49 Shearer, G. C., Chavan, S., Bordiga, S., Svelle, S., Olsbye, U., & Lillerud, K. P. (2016). Defect Engineering: Tuning the Porosity and Composition of the Metal–Organic Framework UiO-66 via Modulated Synthesis. *Chemistry of Materials*, *28*(11), 3749–3761. https://doi.org/10.1021/acs.chemmater.6b00602

50 Chen, X., Li, Y., Fu, Q., Qin, H., Lv, J., Yang, K., Zhang, Q., Zhang, H., & Wang, M. (2022). An efficient modulated synthesis of zirconium metal–organic framework UiO-66. *RSC Advances*, *12*(10), 6083–6092. https://doi.org/10.1039/D1RA07848H

51 Feng, Y., Chen, Q., Jiang, M., & Yao, J. (2019). Tailoring the Properties of UiO-66 through Defect Engineering: A Review. *Industrial & Engineering Chemistry Research*, *58*(38), Article 38. https://doi.org/10.1021/acs.iecr.9b03188

52 Feng, X., Jena, H. S., Krishnaraj, C., Leus, K., Wang, G., Chen, H., Jia, C., & Van Der Voort, P. (2021). Generating Catalytic Sites in UiO-66 through Defect Engineering. *ACS Applied Materials & Interfaces*, *13*(51), 60715–60735. https://doi.org/10.1021/acsami.1c13525

53 Feng, D., Wang, K., Wei, Z., Chen, Y. -P., Simon, C. M., Arvapally, R. K., Martin, R. L., Bosch, M., Liu, T. -F., Fordham, S., Yuan, D., Omary, M. A., Haranczyk, M., Smit, B., & Zhou, H. -C. (2014). Kinetically tuned dimensional augmentation as a versatile synthetic route towards robust metal–organic frameworks. *Nature Communications*, *5*(1), 5723. https://doi.org/10.1038/ncomms6723

54 Vetlitsyna-Novikova, K. S., Butova, V. V., Pankin, I. A., Shapovalov, V. V., & Soldatov, A. V. (2019). Zirconium-Based Metal-Organic UiO-66, UiO-66-NDC and MOF-801 Frameworks. Influence of the Linker Effect on the Hydrogen Sorption Efficiency. *Journal of Surface Investigation: X-Ray, Synchrotron and Neutron Techniques*, *13*(5), 787–792. https://doi.org/10.1134/S1027451019050173

55 Zorainy, M. Y., Kaliaguine, S., Gobara, M., Elbasuney, S., & Boffito, D. C. (2022). Microwave-Assisted Synthesis of the Flexible Iron-based MIL-88B Metal–Organic Framework for Advanced Energetic Systems. *Journal of Inorganic and Organometallic Polymers and Materials*, *32*(7), 2538–2556. https://doi.org/10.1007/s10904-022-02353-6

56 Thomas-Hillman, I., Laybourn, A., Dodds, C., & Kingman, S. W. (2018). Realising the environmental benefits of metal–organic frameworks: Recent advances in microwave synthesis. *Journal of Materials Chemistry A*, *6*(25), Article 25. https://doi.org/10.1039/C8TA02919A

57 DeStefano, M. R., Islamoglu, T., Garibay, S. J., Hupp, J. T., & Farha, O. K. (2017). Room-Temperature Synthesis of UiO-66 and Thermal Modulation of Densities of Defect Sites. *Chemistry of Materials*, *29*(3), 1357–1361. https://doi.org/10.1021/acs.chemmater.6b05115

58 Taddei, M., Van Bokhoven, J. A., & Ranocchiari, M. (2020). Influence of Water in the Synthesis of the Zirconium-Based Metal–Organic Framework UiO-66: Isolation and Reactivity of $[ZrCl(OH)_2(DMF)_2]Cl$. *Inorganic Chemistry*, *59*(11), 7860–7868. https://doi.org/10.1021/acs.inorgchem.0c00991

How to Cite: Ivanova, N.M., Vissurkhanova, Ya.A., Soboleva, Ye.A., & Kenzhetaeva, S.O. (2024) Copper Nanoparticles Supported on Nickel Ferrite: Synthesis and Electrocatalytic Activity. *Eurasian Journal of Chemistry, 29, 3(115), 109-118.* https://doi.org/10.31489/2959-0663/3-24-2

Article

Received: 8 March 2024 | Revised: 30 June 2024 |
Accepted: 19 July 2024 | Published online: 02 August 2024

UDC 544.653.3+546.56-121+544.478 https://doi.org/10.31489/2959-0663/3-24-2

Nina M. Ivanova[1*], Yakha A. Vissurkhanova[1,2],
Yelena A. Soboleva[1], Saule O. Kenzhetaeva[2]

[1]*LLP "Institute of Organic Synthesis and Coal Chemistry of the Republic of Kazakhstan", Karaganda, Kazakhstan;*
[2]*Karaganda Buketov University, 28, Karaganda, Kazakhstan*
*(*Corresponding author's e-mail: nmiva@mail.ru)*

Copper Nanoparticles Supported on Nickel Ferrite: Synthesis and Electrocatalytic Activity

Cu(x)/$NiFe_2O_4$(y) magnetic composites with different component ratios were prepared by chemical reduction of copper cations in the presence of sonicated nickel ferrite. Separately synthesized Cu and $NiFe_2O_4$ nanoparticles, as well as composites of copper particles supported on nickel ferrite, were characterized by X-ray diffraction spectroscopy and scanning electron microscopy. Based on the determination of the specific surface area, the $NiFe_2O_4$ sample heat-treated at 500 °C was selected as the support for the catalytically active Cu particles. The electrocatalytic activity of Cu(x)/$NiFe_2O_4$(y) composites deposited on a cathode was investigated in the electrohydrogenation of acetophenone (APh). It was shown that the electrocatalytic activity of these composites appears starting from the percentage ratio of their components x:y = 40:60. This was expressed as an increase in the rate of electrocatalytic hydrogenation of APh and its conversion compared to the electrochemical reduction of APh under similar conditions. It was suggested that the slightly lower rate of APh hydrogenation on Cu/$NiFe_2O_4$ composites compared to Cu particles is due to the poor electrical conductivity of the nickel ferrite support.

Keywords: copper nanoparticles, chemical reduction, nickel ferrite carrier, co-precipitation method, catalysts, electrocatalytic hydrogenation, acetophenone, 1-phenylethanol.

Introduction

A significant advantage of magnetic catalysts over conventional "non-magnetic" catalysts is the ability to extract them from the reaction medium using a magnet with minimal loss of mass and activity. The use of magnetic catalysts ensures the high efficiency of catalytic reactions in general and contributes to their classification as processes that meet the basic postulates of "green chemistry" [1, 2].

Catalysts consisting of catalytically active mono- and bimetallic nanoparticles supported on magnetic carriers represent a distinct group among all magnetic catalysts that have attracted increased attention from researchers in the field of catalysis [1, 2]. Iron oxides are most commonly used as magnetic carriers, and the most studied is magnetite, Fe_3O_4. The demand for magnetite nanoparticles is determined by their magnetic properties, chemical stability, low toxicity, high specific surface area, cost-effectiveness, and relative ease of production [3, 4]. In this case, catalysts on Fe_3O_4 support are characterized by good reducibility and are widely used in various catalytic processes for environmental purification, as electrodes in electrocatalysis, in organic synthesis, drug delivery, cancer treatment, etc. [3–7].

Transition metal ferrites with magnetic properties are much less frequently used as supports for catalytically active particles than magnetite, and such studies have been described in the literature. For example, palladium nanoparticles supported on cobalt ferrite and zinc ferrite were shown to be effective in the ligand-free Suzuki coupling reaction [8, 9]. Catalysts consisting of Pd nanoparticles immobilized on nickel ferrite and magnetite modified with an amine were used for the hydrogenation of some of compounds with unsaturated C–C bonds, as well as nitro compounds and azides [10]. The catalytic activity of $NiFe_2O_4$@Cu nanoparticles was studied in the reduction reactions of nitroaromatic compounds using sodium borohydride, whose conversion to the corresponding amines was 30–100 %, depending on the structure of the starting nitroarenes [11]. Core-in-shell magnetic $NiFe_2O_4$@Au nanoparticles were prepared by gold reduction on the surface of nickel ferrite using the amino acid methionine as a reducing agent [12]. In [13], the structural and magnetic properties of composites of silver nanoparticles deposited on the surface of silica-coated nickel ferrite nanoparticles ($Ni_{1.43}Fe_{1.7}O_4$-SiO_2/Ag) were investigated.

The aim of this work is to prepare composites consisting of copper nanoparticles deposited on nickel ferrite and to study the possibility of using them as electrocatalysts in the model reaction of electrohydrogenation of acetophenone (APh). These studies were prompted by the need to find out the influence of the magnetic component — the carrier — on the electrocatalytic activity of copper nanoparticles in an electrolytic cell, on the outer side of which (under the cathode) there was a magnet holding the ferromagnetic catalyst in the form of powder on the cathode surface. This method was previously developed under the leadership of Professor I.V. Kirilyus using skeletal catalysts, which showed high electrocatalytic activity in the electrohydrogenation of many organic compounds [14–16]. Copper nanoparticles do not have magnetic properties and, when hydrogen is released at the cathode, they begin to periodically rise and fall back to the cathode surface, shortening the duration of their contact with the electrode, necessary to obtain a charge. This is thought to decrease their electrocatalytic activity. At the same time, copper particles show quite high activity in some processes of electrocatalytic hydrogenation of organic compounds comparable to magnetic nickel particles [17]. A detailed review of copper nanoparticles without and with deposition on supports of various nature (carbon materials, metal oxides, polymers, silica, oxides with a delafossite structure, etc.), as well as their use in catalytic reactions of organic transformations has been given in the recent paper [18].

Our previous research [19] found that nickel (II) ferrite, $NiFe_2O_4$, prepared by the co-precipitation method, unlike copper (II) ferrite [20], is not reduced in the electrochemical system and retains its stability in the alkaline medium of the catholyte, and does not show any catalytic effect in the electrohydrogenation reactions of organic compounds. Therefore, it can be used as a magnetic carrier for electrocatalytically active catalyst particles.

Experimental

Materials

Nickel nitrate $Ni(NO_3)_2 \cdot 6H_2O$, ferric nitrate ($Fe(NO_3)_3 \cdot 9H_2O$), sodium hydroxide (NaOH), copper nitrate ($Cu(NO_3)_2 \cdot 3H_2O$), hydrazine hydrate (N_2H_5OH, 64 %) and ethylene glycol ($C_2H_6O_2$, analytical grade) were purchased from "Ridder" LLP (Karaganda, Kazakhstan) and used without further purification. Polyvinyl alcohol (PVA) (Mw = 9,000–10,000 $g \cdot mol^{-1}$) and polyvinylpyrrolidone (PVP) (Mw = 10,000 $g \cdot mol^{-1}$) were purchased from Sigma-Aldrich. Distilled water and medical grade ethyl alcohol (96 %) were used to prepare the required solutions and wash the prepared particles.

Nickel (II) Ferrite Preparation

Nickel (II) ferrite ($NiFe_2O_4$) was synthesized by the co-precipitation method according to the procedure described in [18]. Nickel nitrate (0.06 mol) and ferric nitrate (0.12 mol) were dissolved in 300 ml of distilled water. Then, a 2M NaOH solution was added to pH = 12. The resulting mixture was stirred at 40 °C for 1 h. It was filtered and washed thoroughly with hot distilled water to pH 7. The precipitate was dried at 80 °C. Equal amounts of the resulting powder were thermally treated at 500 °C and 700 °C for 2 h under conditions with limited oxygen access (in crucibles with closed lids). The powders were then ground in an electric mill.

Synthesis of Cu Nanoparticles

Copper (II) nitrate (0.025 mol) was dissolved in a solution of 200 ml of ethylene glycol and 200 ml of distilled water. An aqueous solution of 1 M NaOH was then slowly added to the reaction mixture until pH = 12. Subsequently, hydrazine hydrate (1 mol) was added dropwise. The reaction mixture was kept at 60 °C for 1 h. During the vigorous reaction, the formation of red-brown copper particles was observed. The resulting Cu particles were separated by centrifugation, washed with 100 ml of distilled water and ethyl alcohol heated to 30 °C. Then, they were dried under vacuum at 80 °C. Cu nanoparticles were also prepared using a similar procedure with the reduction of the metal salt in the presence of polymer particle stabilizers (PVA and PVP).

Synthesis of Cu(x)/$NiFe_2O_4$(y) Composites

Ethylene glycol (200 ml) was added to the selected amount of $NiFe_2O_4$ (500 °C). The mixture was subjected to ultrasonic treatment for 30 minutes. Then, 200 ml of an aqueous solution containing the required amount of copper nitrate was added and stirred for 30 min. The pH was then adjusted to 12 using 1 M NaOH solution. The required amount of hydrazine hydrate was then added dropwise to reduce copper, keeping the molar ratio $Cu(NO_3)_2/N_2H_4$ = 1:40. The reaction mixture was kept at a temperature of 60 °C. The resulting particles were separated by centrifugation and washed with distilled water and ethyl alcohol heated to 30 °C. Then, they were dried under vacuum at 80 °C to a constant weight. Thus, Cu(x)/$NiFe_2O_4$(y) composites were

obtained with different percentage ratios of copper to nickel ferrite: x:y = 80:20; 70:30; 60:40; 50:50; 40:60; 30:70; 20:80. The Cu(50)/ $NiFe_2O_4$ (50) + PVA/PVP composites were also prepared by adding copper nitrate to a 3 % polymer (PVA or PVP) aqueous solution and subsequent reduction using the similar procedure.

The metal content in the filtrates after the synthesis of nickel ferrite and Cu(x)/$NiFe_2O_4$(y) composites was determined by selective complexometric titration methods [17, 21]. Based on the titration results, it was established that there were no copper and nickel cations in the resulting transparent filtrates.

Study of the Electrocatalytic Activity of Cu(x)/$NiFe_2O_4$(y) Composites

The electrocatalytic activity of the obtained supported Cu(x)/$NiFe_2O_4$(y) composites as catalysts was studied in the electrohydrogenation of an aromatic ketone, acetophenone: C_6H_5–C(O)–CH_3 → C_6H_5–CH(OH)–CH_3. The experiments were carried out in a diaphragm electrochemical cell in an aqueous-alkaline solution (the initial NaOH concentration was 2 %) at a current of 2.5 A and a temperature of 30 °C. The powder of the prepared catalysts weighing 1 g was deposited on a horizontally located copper cathode (with an area of 0.09 dm^2) tightly adjacent to the bottom of the electrolytic cell. The catalysts with magnetic properties were held on the cathode by an external magnet placed outside the electrolyzer. The magnetic induction of the magnetic field generated was 0.05 T. A platinum grid served as the anode. Electrocatalytic hydrogenation of APh (with an initial concentration in the catholyte of 0.137 mol/L) was also carried out in an aqueous-alkaline solution of the catholyte at a current of 2.5 A, and a temperature of 30 °C.

Characterization

The structural phase characteristics of the synthesized nickel ferrite and composites of copper particles deposited on nickel ferrite were studied on a D8 ADVANCE ECO diffractometer (Bruker, Germany) using CuKα radiation in the angular range (2θ) 15–90°. The morphological characteristics of heat-treated samples of nickel ferrites and Cu(x)/$NiFe_2O_4$(y) composites were studied on a TESCAN MIRA 3 scanning electron microscope (SEM) (Czech Republic) using secondary (SE) and backscattered (BSE) electron detectors. The samples were analyzed with a conductive carbon layer deposited on them. Elemental microanalysis of the composites was performed using an X-Act energy dispersive detector (Oxford Instruments). Photographs of the deposited Cu catalyst particles were taken on a Levenhuk DTX 90 digital USB microscope (Russia). The specific surface area (SSA) of nickel ferrite particles was determined from nitrogen adsorption data obtained on a Sorbi-MS instrument (Russia) using the BET (Brunauer, Emmett and Teller) method, and the pore size distributions were established using the statistical thickness surface area (STSA) method.

Results and Discussion

According to the XRD analyses, the composition of the copper nanoparticles reduced separately by hydrazine hydrate in a water + EG medium contains, in addition to the crystalline phases of copper, oxides copper (CuO, Cu_2O) phases (Fig. 1, a). The content of these phases in the sample after synthesis is as follows: 81.6 % Cu, 9.4 % Cu_2O, and 9.0 % CuO. After electrochemical experiments, the copper and Cu_2O contents in the composition of these particles increase to 88.2 % and 11.8 %, respectively, while the CuO phases disappear (Fig. 1, b). Obviously, in the electrochemical system, copper cations are reduced from CuO oxide with the formation of copper in the zero-valent state, and Cu_2O is additionally formed. The size of Cu particles after synthesis, calculated using diffractometer software, is 44 nm (for the crystalline phase (111) at an angle of 2θ = 43.03°), and increases to 52 nm after the electrochemical experiments.

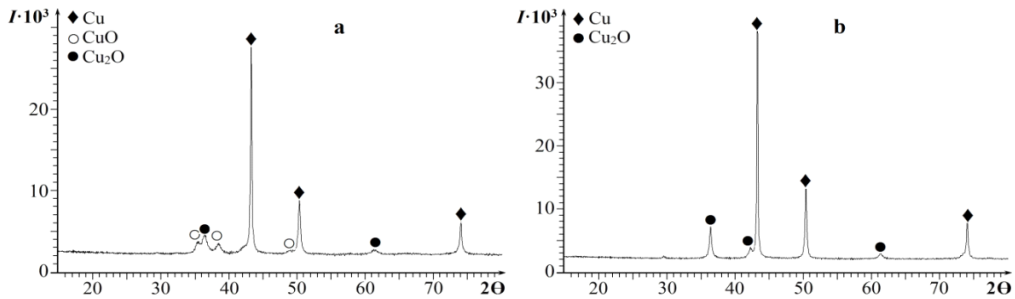

Figure 1. XRD patterns of Cu nanoparticles before (*a*) and after (*b*) electrohydrogenation of APh

Micrographs of the synthesized Cu particles (Fig. 2) show that they have the shape of short nanorods or nanotubes (~30–60 nm in diameter), some of which are pointed. These nanorods assemble chaotically into

spiny little balls ("hedgehogs") of different sizes (~100–500 nm) forming a loose mass. An elemental analysis by energy dispersive X-ray spectroscopy (EDS) (spectrum 2) shows the presence of Cu with a small amount of oxygen. It is interesting to note that when the synthesis of copper nanoparticles is carried out only in an aqueous medium without a stabilizer, and hydrazine hydrate is also used for the reduction, then the particles have a layered structure with an approximately round shape and sizes of 100–400 nm [22]. The use of stabilizers such as PVP, polyethylene glycol, and starch contributes to a decrease in the size of copper nanoparticles to 70–100, 30–50 and 50–70 nm, respectively.

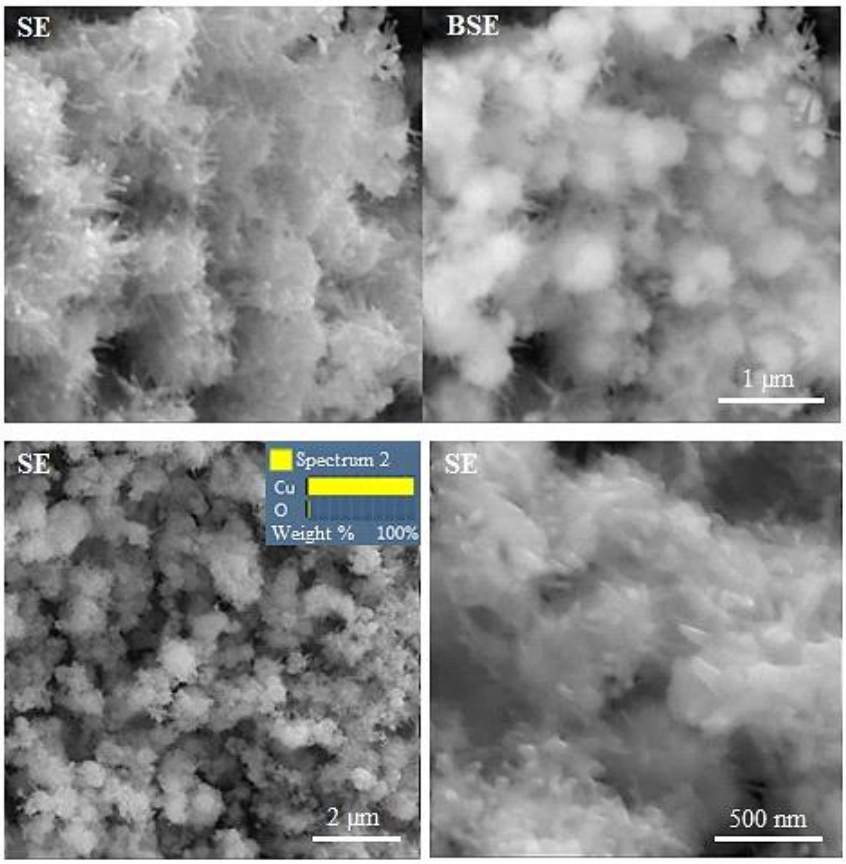

Figure 2. SEM images of Cu nanoparticles after synthesis in different scanning scales

Nickel (II) ferrite was prepared by the co-precipitation method followed by heat treatment at 500 °C and 700 °C. The phase composition of both heat-treated samples is represented by crystalline phases of nickel ferrite $NiFe_2O_4$ of cubic structure and hematite phases (α-Fe_2O_3) in small quantities (Fig. 3). The particle sizes in these nickel ferrite samples, according to the X-ray diffraction data, are 14 and 25 nm (for the (311) phase at a diffraction angle of 2θ = 35.7–35.6°), i.e. the size of the nickel ferrite nanoparticles increases with increasing temperature.

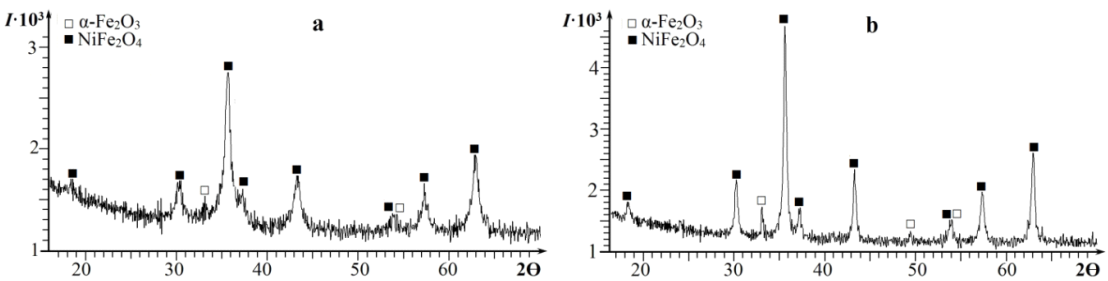

Figure 3. XRD patterns of $NiFe_2O_4$ (500 °C) (*a*) and $NiFe_2O_4$ (700 °C) (*b*) samples

Micrographs of nickel ferrite (Fig. 4) show that the particles in both samples are round in shape and vary slightly in size (~35–80 nm). At the same time, the somewhat amorphous particles of the $NiFe_2O_4$ (500 °C) sample are pressed together more tightly than the particles of the $NiFe_2O_4$ (700 °C) sample, which are grouped into cluster structures resembling a torus (donut) shape. Both nickel ferrite samples have magnetic properties, confirming magnetism studies carried out on nickel ferrite nanoparticles fabricated under similar conditions by the co-precipitation method [23]. For example, for $NiFe_2O_4$ nanoparticles with an average size of 28 nm, the saturation magnetization (M_S) at room temperature was ~40.5 emu/g, which is lower than that of a bulk sample of this ferrite (56 emu/g). For comparison, the M_S value for magnetite (Fe_3O_4) nanoparticles with sizes of ~20 nm at room temperature is 75.3 emu/g [24]. The given M_S values show that the magnetic properties of nickel ferrite are somewhat weaker than those of magnetite.

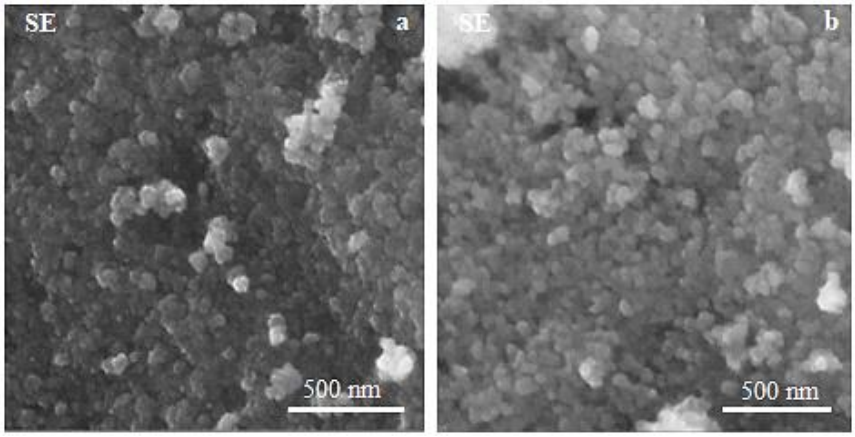

Figure 4. SEM images of $NiFe_2O_4$ (500 °C) (*a*) and $NiFe_2O_4$ (700 °C) (*b*)

In order to select one of the two nickel ferrite samples as a carrier for catalytically active copper nanoparticles, their specific surface area (SSA) was measured using the nitrogen adsorption-desorption isotherm in the BET method following the STSA calculations for the pore size distribution (Table 1).

Table 1

Specific surface area and porosity data for $NiFe_2O_4$ samples

Nickel ferrite sample	SSA, m^2/g	$V_{\Sigma\ pores}$, cm^3/g	Pore size distribution, %	
			mesopores	macropores
$NiFe_2O_4$ (500 °C)	72.7±1.4	0.135	45.0	55.0
$NiFe_2O_4$ (700 °C)	22.8±0.4	0.069	32.3	67.7

It is known that in solid materials, including powders, the pores present are classified according to their size into micropores (< 2 nm), mesopores (2–50 nm) and macropores (> 50 nm) [25]. In the both samples, the average pore sizes are 3–15, 56 and 80 nm, but with different volume ratios. According to Table 1, the total pore volume in the $NiFe_2O_4$ (500 °C) sample is larger than in the $NiFe_2O_4$ sample treated at 700 °C. Moreover, in the second sample, the volume of macropores relative to the total pore volume ($V_{\Sigma\ pores}$) exceeds the volume of mesopores by more than two times, which is apparently due to a greater degree of particle aggregation in this sample and the larger sizes of the aggregates formed. The specific surface area of particles in the $NiFe_2O_4$ (500 °C) sample is also significantly larger than in the $NiFe_2O_4$ (700 °C) sample. Since the best values for supporting catalyst particles are higher values of these structural characteristics, the nickel ferrite sample with heat treatment at 500 °C was chosen to create catalytic systems with supported copper particles.

Syntheses of supported Cu(*x*)/$NiFe_2O_4$ (500 °C)(*y*) composites were carried out with different ratios of copper particles and nickel ferrite (see synthesis procedure). Figure 5 shows the X-ray diffraction patterns for the Cu(50)/$NiFe_2O_4$(50) sample after synthesis and after electrocatalytic hydrogenation of acetophenone.

In the XRD patterns of the Cu(50)/$NiFe_2O_4$(50) sample, the intensity of the peaks of the crystalline phases of copper is significantly higher than the intensity of the nickel ferrite peaks, which corresponds to their values in the XRD patterns of individual components (Figures 1 and 3). In the constitution of this com-

posite after its use as a catalyst in the electrohydrogenation of APh, the crystalline phases of copper and nickel ferrite remain and the phases of copper (I) oxide appear in small amounts (Figure 5, *b*).

Micrographs of the synthesized Cu(50)/$NiFe_2O_4$(50) composite (Figure 6, *a*) show that copper particles in the form of rounded formations of different sizes (~100–800 nm) (highlighted in white) are located on the surface of nickel ferrite and some of them are also found among the nickel ferrite particles. There are also separate clusters of round copper particles connected to each other.

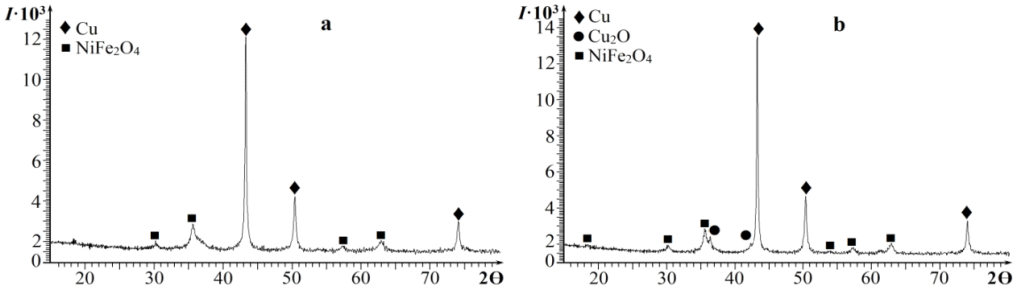

Figure 5. XRD patterns of Cu(50)/$NiFe_2O_4$(50) sample after synthesis (*a*) and after electrocatalytic hydrogenation of APh (*b*)

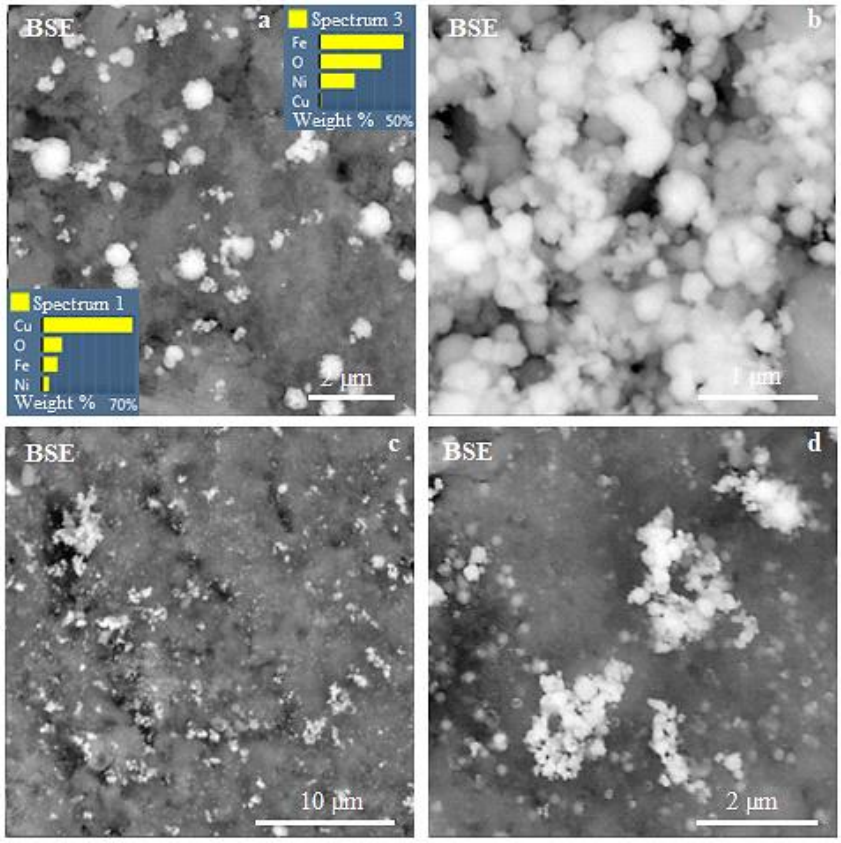

Figure 6. SEM images of Cu(50)/$NiFe_2O_4$(50) composite after synthesis (*a*, *b*) and after electrocatalytic hydrogenation of APh (*c*, *d*)

The shape of the copper particles in the Cu(50)/$NiFe_2O_4$(50) composite differs from the copper balls consisting of nanorods in the case of individual reduction under the same conditions (Fig. 2). It is possible that during the synthesis of the composite, small particles of nickel ferrite serve as initial grains for the formation of copper particles, which then take a rounded shape to form core-in-shell particles. After electrocatalytic application, the structure of this catalyst remains practically unchanged (Fig. 6, *c* and *d*).

The presence of magnetic properties in the synthesized Cu(50)/$NiFe_2O_4$(50) composite is demonstrated by the photographs in Figure 7. Without applying a magnet (Fig. 7, *a*), all particles simply lie on the glass

surface and are visible as particles with a metallic sheen — these are obviously nickel ferrite and red-brown particles of copper itself and copper on the support. In the presence of a magnet (Fig. 7, *b*), all particles are arranged in the form of fir trees perpendicular to the surface.

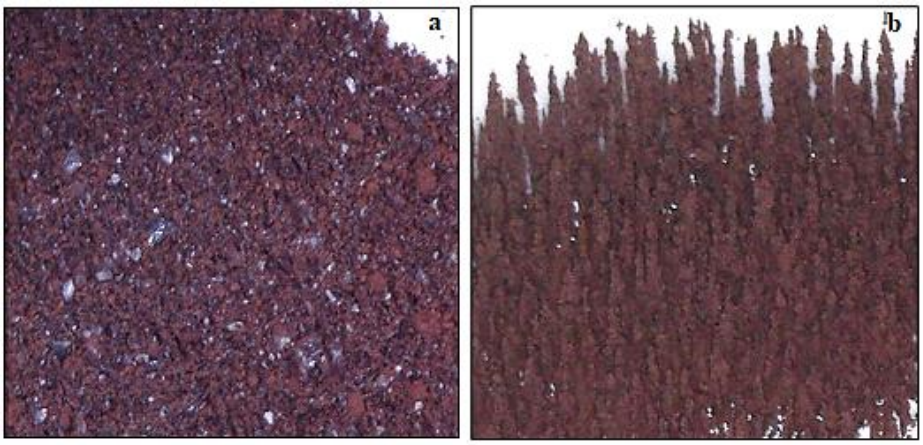

Figure 7. Photographs of Cu(50)/$NiFe_2O_4$(50) composite without (*a*) and with magnet (*b*)

All synthesized Cu(*x*)/$NiFe_2O_4$(500 °C)(*y*) composites with different percentages ratios of copper particles and carrier were deposited on the surface of a copper cathode, on the outer side of which a magnet was placed, in a diaphragm cell in an aqueous-alkaline catholyte solution. As the measurements of the gases released (hydrogen and oxygen) showed, the electrolysis of a NaOH aqueous solution was accompanied by an additional release of oxygen (V_{O_2} values in Table 2).

Table 2

Results of electrocatalytic hydrogenation of acetophenone on Cu particles and Cu/$NiFe_2O_4$ catalysts

Catalyst	Copper content in 1 g of catalyst, g	Electrochemical reduction of copper oxides		Electrocatalytic hydrogenation of acetophenone				
		τ, min	V_{O_2}, ml	*W*, ml H_2/min (α = 0.25)	η, %	α, %	Composition of extracts, %	
							1-PhE	APh
Cu cathode	–	–	0.0	9.6	56.7	95.5	90.80	4.93
Cu (0.5 g)	0.47	30	47.7	13.5	77.5	99.0	99.78	0.22
Cu + PVA (0.5 g)	0.49	20	31.2	13.4	75.0	100.0	99.77	0.23
Cu + PVP (0.5 g)	0.49	20	31.0	13.3	75.0	100.0	99.83	0.17
Cu(20) / $NiFe_2O_4$(80)	0.20	30	21.2	7.6	45.0	99.8	99.76	0.24
Cu(30) / $NiFe_2O_4$(70)	0.30	40	29.7	7.8	45.8	100.0	99.54	0.46
Cu(40) / $NiFe_2O_4$(60)	0.40	30	28.8	10.5	60.0	100.0	99.85	0.15
Cu(50) / $NiFe_2O_4$(50)	0.51	30	26.0	11.5	66.3	100.0	99.82	0.18
Cu(50)/$NiFe_2O_4$(50) + PVA	0.49	20	35.3	10.6	60.0	100.0	99.75	0.25
Cu(50)/$NiFe_2O_4$(50) + PVP	0.49	20	35.3	11.1	62.5	100.0	99.23	0.77
Cu(60) / $NiFe_2O_4$(40)	0.60	30	25.4	12.3	72.5	100.0	99.86	0.14
Cu(70) / $NiFe_2O_4$(30)	0.69	30	55.5	12.4	72.5	100.0	99.89	0.11
Cu(80) / $NiFe_2O_4$(20)	0.79	30	55.5	12.4	72.5	100.0	99.88	0.12
$NiFe_2O_4$ (500 °C)	–	0	0.0	–	–	–	–	–
$NiFe_2O_4$ (700 °C)	–	0	0.0	–	–	–	–	–

This indicates the occurrence of electrochemical reduction of copper cations from its existing oxides in the composites deposited on the cathode:

Cu cathode: $CuO + 2e^- + H_2O \rightarrow Cu^0 + 2OH^-$

$2H_2O + 2e^- \rightarrow H_2 + 2OH^-$

Pt anode: $4OH^- \rightarrow O_2 + 2H_2O + 4e^-$

The V_{O_2} values given in Table 2 can be used to assess the content of copper oxides in the composition of copper particles deposited on nickel ferrite. These data indicate that copper oxides are present in almost all copper particles reduced in the presence of a carrier, polymer particle stabilizers and without any additives to the reaction medium of their synthesis (Table 2). Perhaps partial oxidation of copper occurs when its particles are washed after synthesis and dried.

After completion of the electrochemical reduction of copper oxides (when the release of additional volumes of oxygen was terminated), an organic substance was introduced into the catholyte to carry out its electrocatalytic hydrogenation in the presence of Cu(x)/$NiFe_2O_4$(500 °C)(y) catalysts held on the cathode by an external magnet. The results obtained are presented in Table 2, which lists such characteristics as: V_{O_2} is the volume of additionally released oxygen as a result of the electrochemical reduction of copper oxides contained in its particles; τ is the process duration; W is the average rate of APh hydrogenation over a period equal to $\alpha = 0.25$; η is the hydrogen utilization coefficient at the same value of α, and α is the APh conversion. The same Table shows that samples of nickel ferrite with heat treatment at 500 and 700 °C are not reduced in the electrochemical system under the given conditions and do not exhibit electrocatalytic activity in the electrohydrogenation of acetophenone.

For comparison, Table 2 shows the results of the electrochemical reduction of APh on a Cu cathode (without a catalyst) and its electrocatalytic hydrogenation on copper nanoparticles synthesized without and in the presence of polymer stabilizers. These data show that the rate of electrochemical reduction of APh under the given conditions is quite high (9.6 ml H_2/min), but the process does not proceed to completion and with the formation of a small amount of by-products. The electrocatalytic hydrogenation of APh on copper particles and on Cu(x)/$NiFe_2O_4$(y) supported catalysts was carried out almost completely and without by-products, which was confirmed by chromatographic analyzes (Table 2). At the same time, the highest rates of APh hydrogenation were observed in processes using Cu particles (13.3–13.5 ml H_2/min).

For processes on supported catalysts, the rate of hydrogenation depends on the content of copper particles in their composition: the more there are, the higher is the rate of APh hydrogenation, and starting from the ratio x:y = 60:40 it almost does not change. Therefore, this percentage ratio of copper particles to nickel ferrite can be considered as optimal for this catalyst. However, it should be noted that the rate of APh hydrogenation on catalysts with the particle content $x > 60$ % is lower than that on copper nanoparticles (Table 2). It can be assumed that nickel ferrite, which has poor electrical conductivity, slows down the transfer of charge from the cathode to catalytically active copper particles, which is also reflected in the rate of electrocatalytic hydrogenation of the organic compound. In general, Cu(x)/$NiFe_2O_4$(y) supported catalysts, starting from the ratio x:y = 40:60, exhibit electrocatalytic activity in the studied process of electrohydrogenation of acetophenone with the selective formation of 1-phenylethanol, a fragrant substance with the hyacinth odor.

Conclusions

Magnetic composites of Cu nanoparticles supported on nickel ferrite with different contents of their components were synthesized by the reduction of copper cations in the presence of $NiFe_2O_4$ prepared by the co-precipitation procedure. Their structure, morphological features, and electrocatalytic properties in the electrohydrogenation of acetophenone were studied. It was found that the electrocatalytic activity of the resulting composites was manifested in the process studied starting from the Cu(40 %):$NiFe_2O_4$(60 %) ratio. The rate of APh electrohydrogenation increases compared to its electrochemical reduction on a copper cathode (without a catalyst). Its conversion with the selective formation of 1-phenylethanol reaches maximum values. It was suggested that the slightly lower rate of APh electrohydrogenation on Cu/$NiFe_2O_4$ composite-catalysts compared to Cu particles is due to the known poor electrical conductivity of nickel ferrite, which slows down the charge transfer from the cathode to the catalytically active copper particles.

Funding

This research was funded by the Science Committee of the Ministry of Science and Higher Education of the Republic of Kazakhstan (Program No. BR24992921).

*Author Information**

**The authors' names are presented in the following order: First Name, Middle Name and Last Name*

Nina Mikhailovna Ivanova (*corresponding author*) — Doctor of Chemical Sciences, Full Professor, Head of the Laboratory of Electrocatalysis and Quantum-chemical Research, LLP "Institute of Organic Synthesis and Coal Chemistry of the Republic of Kazakhstan", Alikhanov Street, 1, 100000, Karaganda, Kazakhstan; e-mail: nmiva@mail.ru; https://orcid.org/0000-0001-8564-8006

Yakha Amkhadovna Vissurkhanova — Researcher, Laboratory of Electrocatalysis and Quantum-chemical Research, LLP "Institute of Organic Synthesis and Coal Chemistry of the Republic of Kazakhstan", Alikhanov Street, 1, 100000, Karaganda, Kazakhstan; Teacher, Department of Physical and Analytical Chemistry, Karaganda Buketov University, Universitetskaya street, 28, 100024, Karaganda, Kazakhstan; e-mail: yakhavisurkhanova@bk.ru; https://orcid.org/0000-0001-7279-1145

Yelena Anatol'evna Soboleva — Candidate of Chemical Sciences, Leading researcher, Laboratory of Electrocatalysis and Quantum-chemical Research, LLP "Institute of Organic Synthesis and Coal Chemistry of the Republic of Kazakhstan", Alikhanov Street, 1, 100000, Karaganda, Kazakhstan; e-mail: esoboleva-kz@mail.ru; https://orcid.org/0000-0002-1089-367X

Saule Orynbaevna Kenzhetaeva — Candidate of Chemical Sciences, Professor, Department of Organic Chemistry and Polymers, Karaganda Buketov University, Universitetskaya street, 28, 100024, Karaganda, Kazakhstan; e-mail: kenzhetaeva58@mail.ru; https://orcid.org/0000-0003-1891-5236

Author Contributions

The manuscript was written through contributions of all authors. All authors have given approval to the final version of the manuscript. CRediT: **Nina Mikhailovna Ivanova** conceptualization, writing-original draft, methodology, validation, visualization, funding acquisition, writing-review & editing; **Yakha Amkhadovna Vissurkhanova** investigation, methodology, data curation, Figures design, visualization; **Yelena Anatol'evna Soboleva** investigation, data curation, resources, visualization; **Saule Orynbaevna Kenzhetaeva**, investigation, data curation, formal analysis, validation.

Conflicts of Interest

The authors declare no conflict of interest.

References

1 Rossi, L.M., Costa, N.J.S., Silva, F.P., & Goncalves, R.V. (2013). Magnetic nanocatalysts: supported metal nanoparticles for catalytic applications. *Nanotechnol. Rev.*, *2*(5), 597–614. https://doi.org/10.1515/ntrev-2013-0021

2 Rossi, L.M., Ferraz, C.P., Fiorio, J.L., & Vono, L.L.R. (2021). Magnetically Recoverable Nanoparticle Catalysts. *Nanoparticles in Catalysis*, 159–181. Portico. https://doi.org/10.1002/9783527821761.ch8

3 Wu, W., Wu, Z., Yu, T., Jiang, C., & Kim, W.-S. (2015). Recent progress on magnetic iron oxide nanoparticles: synthesis, surface functional strategies and biomedical applications. *Sci. Technol. Adv. Mater.*, *16*, 023501, 43. https://doi.org/10.1088/1468-6996/16/2/023501

4 Liu, M., Ye, Y., Ye, J., Gao, T., Wang, D., Chen, G., & Song, Z. (2023). Recent advances of magnetite (Fe_3O_4)-based magnetic materials in catalytic applications. *Magnetochem.*, *9*(4), 110. https://doi.org/10.3390/magnetochemistry9040110

5 Pham, V.L., Kim, D.-G., & Ko,S.-O. (2018). Oxidative degradation of the antibiotic oxytetracycline by Cu@Fe_3O_4 core-shell nanoparticles. *Science of the Total Environment*., *631-632*, 608–618. https://doi.org/10.1016/j.scitotenv.2018.03.067

6 Zhao, Z., Cai, Z., Yang, L., Hu, Z., Zhang, Y., Peng, X., Wang, Q., Yuan, X., & Li, G. (2018). Ternary magnetic Ag–Cu/Fe_3O_4/rGO composite as an efficient photocatalyst for degradation of malachite green. *J. Mater. Sci: Mater. Electron*., *29*, 17743–17749. https://doi.org/10.1007/s10854-018-9881-7

7 Zhang, Y., Yan, W., Sun, Z., Li, X., & Gao, J. (2014). Fabrication of magnetically recyclable Ag/Cu@Fe_3O_4 nanoparticles with excellent catalytic activity for *p*-nitrophenol reduction. *RSC Advances*, *4*(72), 38040–38047. https://doi.org/ HYPERLINK "http://dx.doi.org/10.1039/C4RA05514D"10.1039/C4RA05514D

8 Senapati, K.K., Roy, S., Borgohain, C., & Phukan, P. (2012). Palladium nanoparticle supported on cobalt ferrite: An efficient magnetically separable catalyst for ligand free Suzuki coupling. *J. Mol. Catal. A: Chem.*, *352*, 128–134. https://doi.org/10.1016/j.molcata.2011.10.022

9 Singh, A.S., Patil, U.B., & Nagarkar, J.M. (2013). Palladium supported on zinc ferrite: A highly active, magnetically separable catalyst for ligand free Suzuki and Herck coupling. *Catal. Commun.*, *35*, 11–16. https://doi.org/10.1016/j.catcom.2013.02.003

10 Guin, D., Baruwati, B., & Manorama, S.V. (2007). Pd on amine-terminated ferrite nanoparticles: A complete magnetically recoverable facile catalyst for hydrogenation reactions. *Organic Letters*, *9*(7), 1419–1421. https://doi.org/10.1021/ol070290p

11 Zeynizadeh, B., Mohammadzadeh, I., Shokri, Z., & Hosseini, S.A. (2017). Synthesis and characterization of $NiFe_2O_4$@Cu nanoparticles as a magnetically recoverable catalyst for reduction of nitroarenes to arylamines with $NaBH_4$. *J. Colloid. Interface Sci.*, 500, 285–293. https://doi.org/10.1016/j.jcis.2017.03.030

12 Saykova, D., Saikova, S., Mikhlin, Yu., Panteleeva, M., Ivantsov, R., & Belova, E. (2020). Synthesis and characterization of core-shell magnetic nanoparticles $NiFe_2O_4$@Au. *Metals*, *10*(8), 1075. https://doi.org/ HYPERLINK "https://doi.org/%2010.3390/met10081075" HYPERLINK "https://doi.org/%2010.3390/met10081075"10.3390/met10081075

13 Blanco-Esqueda, I. G., Ortega-Zarzosa, G., Martínez, J. R., & Guerrero, A. L. (2015). Preparation and Characterization of Nickel Ferrite-SiO_2/Ag Core/Shell Nanocomposites. *Advances in Materials Science and Engineering*, *2015*, 1–7. https://doi.org/10.1155/2015/678739

14 Kirilyus, I.V. (1981). *Elektrokataliticheskoe gidrirovanie [Electrocatalytic hydrogenation]*. Alma-Ata: Nauka KazSSR [in Russian].

15 Kirilyus, I.V., Muldakhmetov, M.Z., Filimonova, V.I., & Bekenova, U.B (1997). *Elektrokataliticheskoe gidrirovanie atsetilenovykh spirtov [Electrocatalytic hydrogenation of acetylene alcohols]*. Almaty: «Gylym» [in Russian].

16 Ivanova, N.M., Soboleva, Ye.A., & Kulakova, Ye.V. (2019). *Elektrokataliticheskoe gidrirovanie azotistykh geterotsiklov [Electrocatalytic hydrogenation of nitrogen heterocycles]*. Karaganda: «Glasir» [in Russian].

17 Soboleva, E.A., Visurkhanova, Ya.A., Ivanova, N.M., Beisenbekova, M.E., & Kenzhetaeva, S.O. (2021). Ultrafine copper and nickel powders in the electrocatalytic hydrogenation of organic compounds. *Chem. J. Kazakhstan*, No 2, 32–48. https://doi.org/10.51580/2021-1/2710-1185.26

18 Gawande, M.B. Goswami, A., Felpin, F.-X., Asefa, T., Huang, X., Silva, R, Zou, X., Zboril, R., & Varma R.S. (2016). Cu and Cu-Based Nanoparticles: Synthesis and Applications in Catalysis. *Chem. Rev.*, 116, 3722–3811. https://doi.org/10.1021/acs.chemrev.5b00482

19 Vissurkhanova, Ya.A., Soboleva, E.A., Ivanova, N.M., & Muldakhmetov, Z.M. (2020). Thermal and electrochemical reduction of nickel (II) ferrite under the influence of polymer stabilizers. *Bulletin of the Karaganda University. Chemistry Series*, *98* (2), 42–50. https://doi.org/10.31489/2020ch2/42-50

20 Ivanova, N.M., Soboleva, E.A., Visurkhanova, Ya.A., & Muldakhmetov, Z. (2020). Electrochemical synthesis of Fe–Cu composites based on copper(II) ferrite and their electrocatalytic properties. *Russ. J. Electrochem.*, *56*(7), 533–543. http://doi.org/ HYPERLINK "http://doi.org/10.1134/S1023193520070034"10.1134/S1023193520070034

21 Vasil'ev, V.P., Morozova, R.P., & Kochergina, L.A. (2000*). Praktikum po analiticheskoi khimii [Workshop on analytical chemistry]*. Moscow: Khimiia [in Russian].

22 Olad, A., Alipour, M., & Nosrati, R. (2017). The use of biodegradable polymers for the stabilization of copper nanoparticles synthesized by chemical reduction method. *Bull. Mater. Sci.*, *40*(5), 1013-1020. https://doi.org/10.1007/s12034-017-1432-y

23 Maaz, K., Karim, S., Mumtaz, A., Hasanain, S.K., Liu, J., & Duan, J.L. (2009). Synthesis and magnetic characterization of nickel ferrite nanoparticles prepared by co-precipitation. *J. Magn. Magn. Mater.*, *321*(12), 1838–1842. https://doi.org/10.1016/j.jmmm.2008.11.098

24 Hu, P., Kang, L., Chang, T., Yang, F., Wang, H., Zhang, Y., Yang, J., Wang, K., Du, J., & Yang, Z. (2017). High saturation magnetization Fe_3O_4 nanoparticles prepared by one-step reduction method in autoclave. *J. Alloy. Compd.*, *728*, 88–92. https://doi.org/10.1016/j.jallcom.2017.08.290

25 Inagaki, M. (2009). Pores in carbon materials — importance of their control. *New Carbon Materials*, *24*(3), 193–232. https://doi.org/10.1016/S1872-5805(08)60048-7

How to Cite: Maksotova, K.S., Akbayeva, D.N., Bakirova, B.S., Serikkyzy, A., Lesbek, B.M., Tatykhanova, G.S. & Kudaibegenov, S.E. (2024) Preparation and Characterization of Copper Nanoparticles Stabilized by Poly(vinyl alcohol) for Catalytic Oxidation of 1-Propanol. *Eurasian Journal of Chemistry, 29, 3(115), 119-129.* https://doi.org/10.31489/2959-0663/3-24-4

Article

Received: 1 June 2024 | Revised: 29 July 2024 |
Accepted: 31 July 2024 | Published online: 19 August 2024

UDC 541.64+544.47

https://doi.org/10.31489/2959-0663/3-24-4

Kuralay S. Maksotova[1,2], Dina N. Akbayeva[1,2*], Botagoz S. Bakirova[1,2], Akerke Serikkyzy[2], Bexultan M. Lesbek[2], Gulnur S. Tatykhanova[3], Sarkyt E. Kudaibergenov[1]

[1]*Institute of Polymer Materials and Technology, Almaty, Kazakhstan;*
[2]*Al-Farabi Kazakh National University, Almaty, Kazakhstan;*
[3]*Satbayev University, Almaty, Kazakhstan*
*(*Corresponding author's e-mail: dina.akbayeva@bk.ru)*

Preparation and Characterization of Copper Nanoparticles Stabilized by Poly(vinyl alcohol) for Catalytic Oxidation of 1-Propanol

The aqueous solution of copper (II) complex of poly(vinyl alcohol) (PVA-Cu(II)) was characterized by conductimetric titration, UV-Vis spectroscopy and FTIR. The molar composition of the PVA-Cu(II) complex was determined to be equimolar. Subsequently, the PVA-Cu(II) complex was reduced by sodium borohydride to prepare copper nanoparticles (CuNPs) stabilized by PVA (PVA-CuNPs). According to DLS measurements in aqueous solution the average size of PVA-CuNPs was varied from 10 to 25 nm depending on the amount of sodium borohydride used for reduction. The optimal volume of sodium borohydride to obtain 96 % PVA-CuNPs with 10 nm size was found to be 3 mL of $NaBH_4$ (0.5 mol·L^{-1}). The PVA-CuNPs were then deposited onto SiO_2 support to obtain SiO_2/PVA-CuNPs nanocatalyst for the oxidation of 1-propanol. The SEM image and XRD spectrum of SiO_2/PVA-CuNPs nanocatalyst showed the deposition of PVA-CuNPs on the surface of SiO_2. The resulting SiO_2/PVA-CuNPs nanocatalyst was used for the oxidation of 1-propanol to propionaldehyde by molecular oxygen in a batch-type catalytic reactor at 20°C and atmospheric pressure. The optimum catalyst mass and reaction time were found for the conversion of 1-propanol to propionaldehyde with yields ranging from 61.4 % to 87.8 %. Criteria of hydrodynamic and diffusive similarity (Re, Pr', Sh), overall volumetric mass transfer coefficient ($k_L a$), and economic metric (STY) were evaluated. 1-Propanol reacted with the decomposed atomically adsorbed oxygen atoms on the Cu(111), (220) surfaces to form propionaldehyde and water.

Keywords: copper nanoparticles, polyvinyl alcohol, metal-polymer complex, oxidation, 1-propanol, oxygen, heterogeneous catalysis, silica.

Introduction

The catalytic oxidation of alcohols plays an important role among organic transformations and continues to attract great attention [1]. The resulting carbonyl-containing compounds, such as aldehydes, can participate in further reactions important for fine chemical synthesis. Inexpensive air [2, 3], oxygen [4], hydrogen peroxide [5], and ozone [6] are commonly used as a source of oxygen atoms in the oxidation of 1-propanol to propionaldehyde and propionic acid. The ability of copper to adsorb, activate O_2 and generate copper-oxygen species in heterogeneous catalysts can explain their involvement in the four-electron processes in which O_2 and H_2O are interconverted [7, 8]. Copper nanoparticles are cost effective in comparison to noble d-metals such as Ag, Au and Pt. They are widely applied as catalysts in the coupling reactions, C–H bond activation reactions, oxidation and reduction reactions, and multicomponent reactions [9].

The two-phase (liquid-solid) and three-phase (gas-liquid-solid) stirred tank reactors, as a major class of multiphase reactors, are widely used in the chemical industry due to their operational reliability, flexibility and improved mass transfer. Three-phase systems are more complex than two-phase systems because the presence of the third phase affects the flow behavior existing in two-phase systems [10]. Three-phase stirred tank reactors are widely used in catalytic hydrogenation, oxidation, ammonolysis, fermentation, and wastewater treatment [11]. However, relatively little information is available on mixing in mechanically stirred three-phase gas-liquid-solid tank reactors [12, 13].

The combination of primary alcohols with environmentally friendly oxidants such as oxygen, air and hydrogen peroxide allows the production of carbonyl compounds mainly in continuous flow packed bed reactor systems. Control of the temperature of the oxidation reactions, minimization of the potential explosion

zone inside the reactors and easy purification of the products are the main obvious advantages of continuous flow technology [14]. The liquid phase oxidation of aliphatic alcohols to aldehydes over heterogeneous catalysts is a well-known test reaction for multiphase reactors. When selecting a reaction system, mild operating conditions, high reaction rate, low cost and safety of reactants are key factors [15].

While two-phase processes can only be carried out in a flow-through reactor, three-phase processes can also be carried out in a batch-type reactor. The choice of reactor often depends on the type of oxidizing agent and its aggregate state. Two-phase liquid-solid systems are well known for the hydrogenation of organic substrates in the presence of immobilized metal nanoparticles [16–18]. Oxidation of various substrates in a conventional laboratory batch reactor is possible for both two-phase and three-phase systems. It was used as a two-phase liquid-gas or liquid-solid laboratory reactor for P-O coupling of yellow phosphorus with alcohols [19, 20], oxidation of octene-1 [21] and alcohols [22]. Selective oxidation of ethanol into acetaldehyde under mild conditions using a biocatalytic system based on cryogel-entrapped catalase can be an example of three-phase system (O_2-EtOH-cryogel) in batch-type reactor [23].

The aim of this work is preparation of copper nanoparticles stabilized by PVA followed by the deposition of CuNPs onto SiO_2 and evaluation of the catalytic activity of the SiO_2/PVA-CuNPs nanocatalyst in the oxidation of 1-propanol to propionaldehyde with a high yield.

Experimental

Materials

Chemically pure reagents $Cu(NO_3)_2{\cdot}2.5{\cdot}H_2O$ (98 %), $NaBH_4$ (99 %), polyvinyl alcohol (PVA, Mw = 47000), silicon dioxide, 1-propanol (99.5 %), and hexane (99 %) were purchased from Sigma-Aldrich and used as received. Deionized water was used to prepare the solutions.

Methods

The pH-metric titration was performed on a pH-meter Bante-210 (China) with an accuracy of 0.02 pH units. The conductometric titration was carried out on the 856 Conductivity Module by Metrohm (Switzerland). FTIR spectra were recorded using Cary 660 spectroscopy (Agilent, USA) at room temperature within the 500–4500 cm^{-1} wavenumber range. UV–Visible spectra of the solutions were recorded using a UV–Vis spectrophotometer (Specord 210 plus BU, Germany). The average hydrodynamic size of the CuNPs was measured with a dynamic light scattering (DLS) instrument, Malvern Zetasizer Nano ZS90 (UK). PXRD patterns were collected on a Siemens/Brucker D5005 powder diffractometer using CuKα radiation in the 2θ range between 4° and 80° with a step width of 2θ = 0.04° and a collection time of 10 s/step. Gas-liquid chromatographic analysis was performed on a DANI Master GC (Cologno Monzese, Italy). An Agilent 6890 N/5973 N gas chromatograph-mass spectrometer (Santa Clara, CA, USA) was used for the identification of the products. The morphology of CuNPs supported on SiO_2 was imaged using a SEM JSM-6390 LV (JEOL, Tokyo, Japan).

Preparation of Copper Nanoparticles

The nanosized CuNPs stabilized with PVA were prepared by the known procedure [24]. First, the PVA-Cu(II) complex was obtained in aqueous solution. Aqueous solutions of 0.25M $Cu(NO_3)_2$ (10 mL) and 0.5M PVA (Mw = 47,000) (10 mL) were mixed in the equimolar ratio [PVA]:[$Cu(NO_3)_2$] = 1:1. The resulting mixture was stirred for 5 min. Freshly prepared 0.5 M $NaBH_4$ (3 mL) was added dropwise to the light blue aqueous solution of PVA–Cu(II) and stirred for 1 h at room temperature. As a result, the turbid brownish-yellow solution of CuNPs stabilized with PVA (PVA–CuNPs) was prepared as shown in Figure 1 and then dialyzed for 24 h. After dialysis, the color of aqueous solution became transparent.

Depositing Copper Nanoparticles on Silicon Dioxide

PVA–CuNPs were deposited on SiO_2 by the impregnation method. For this 0.2 g of SiO_2 was added to 5 mL solution containing PVA–CuNPs and stirred for 5 hours. The precipitate was separated by preparative centrifugation using an “Eppendorf 5810R” (Germany) at $10{\times}10^3$ rpm. It was then washed by distilled water (150 mL×5) and filtered. The resulting amorphous mass was dried in a muffle furnace at 400–500°C for 60 min to completely burn off the organic components (Fig. 1).

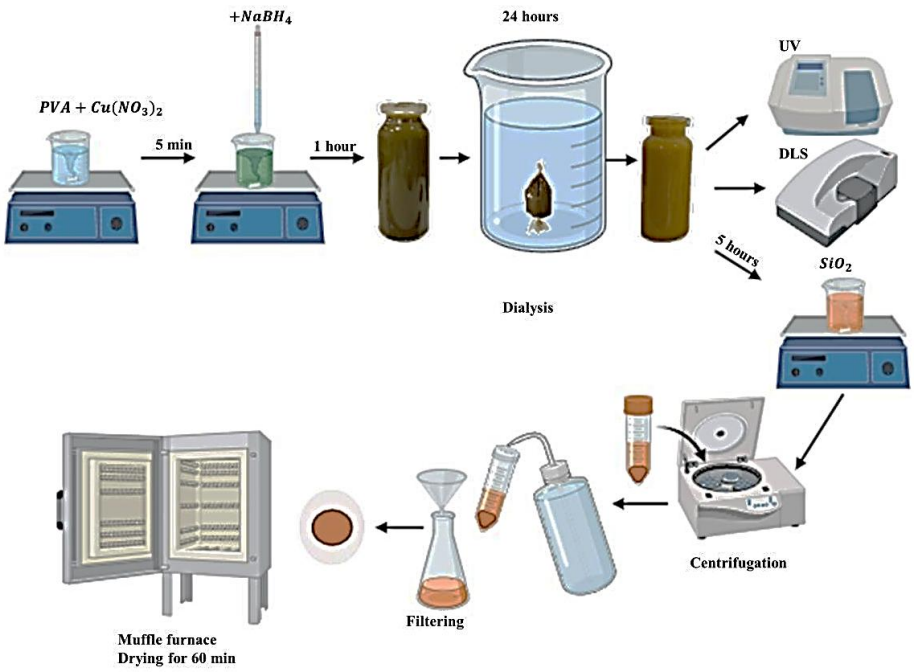

Figure 1. Preparation of CuNPs/PVA deposited on SiO_2

Oxidation of 1-Propanol in a Batch-Type Catalytic Reactor

The oxidation of 1-propanol was carried out in a thermostated glass batch reactor with a total volume of 150 mL (also called a catalytic "duck") by molecular oxygen under aerobic conditions (Fig. 2). The kinetic reaction regime was achieved by shaking the reactor at a frequency of about 250–300 swingings/min. Dried copper nanoparticles in amounts of 0.1, 0.2, 0.3 and 0.5 mg were placed into the reactor. Then, 5 mL of 1-propanol and 5 mL of hexane were added to the reactor and thoroughly purged with oxygen for 5 minutes. The hexane was added to maintain the total solution volume at 10 mL and to use it as an extraction solvent to prevent moisture from entering the chromatography column. The experiment lasted 2–9 hours. The formation and accumulation of the product were monitored by checking its composition by GC analysis.

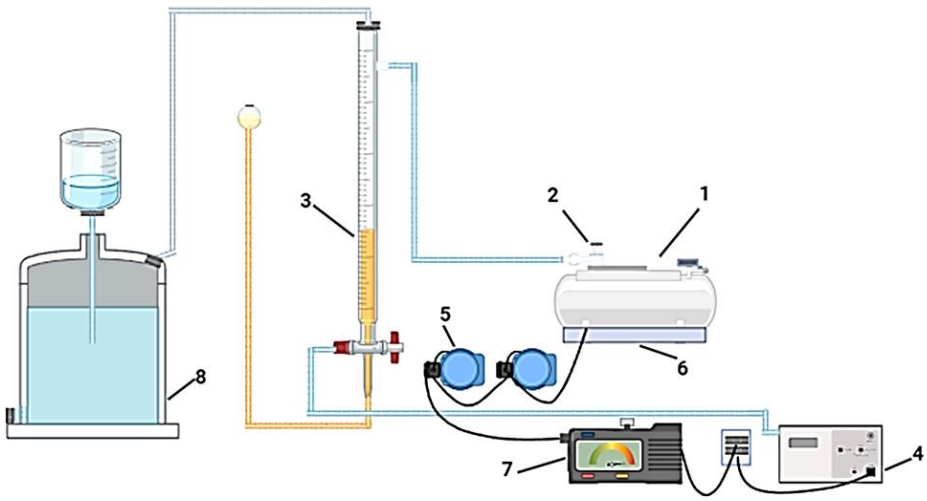

1 — catalytic "duck", *2* — valve for catalyst and 1-propanol insertion, *3* — thermostated burette with dioxygen, 4 — thermostat, *5* — electric motor, *6* — shaker, *7* — laboratory autotransformer, *8* — Berzelius laboratory gasholder

Figure 2. Schematic view of a batch-type catalytic reactor setup for the catalytic oxidation of 1-propanol by molecular oxygen

Results and Discussion

UV-Vis Spectra and Conductimetric Titration

Figures 3 and 4 show the UV–V is spectra and the conductometric titration curve of the PVA-Cu(II) system. The appearance of absorption peak at λ = 800 nm for isomolar series of the mixtures of PVA and Cu(II) confirms the formation of coordination bonds between hydroxyl groups of PVA and copper(II) ions [25, 26]. According to the conductimetric titration curve, the composition of the PVA-Cu(II) complex is equimolar 1:1.

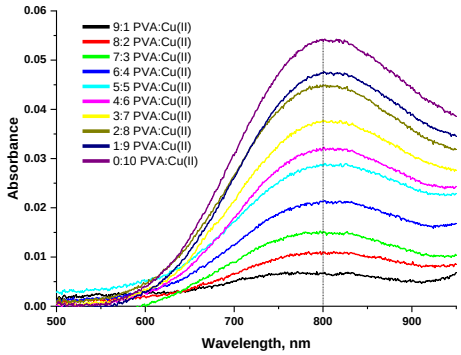

Figure 3. UV–Vis spectra of isomolar series of the mixtures of PVA and Cu(II). [PVA] = $1\cdot10^{-3}$ mol·L^{-1}; [Cu(II)] = $1\cdot10^{-3}$ mol·L^{-1}. V_{total} = 10 mL

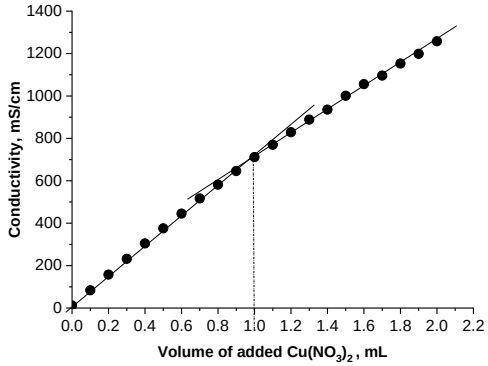

Figure 4. Conductimetric titration of PVA by Cu(II) in water. [PVA] = $1\cdot10^{-3}$ mol·L^{-1}; V_{PVA} = 10 mL; [Cu(II)] = $1\cdot10^{-2}$ mol·L^{-1}

FTIR spectra of the PVA and PVA–Cu(II) complex are shown in Figure 5. The broad peak at 3335 cm^{-1} corresponds to hydrogen bonded OH groups of PVA [27]. The band at 2937 cm^{-1} is related to CH stretching vibrations of macromolecular chain. The sharp band at 1091 cm^{-1} is attributed to the stretching mode of C–C groups, while two strong bands observed at 1456 and 864 cm^{-1} may be attributed to bending and stretching modes of CH_2 group, respectively. The broadening and shifting of the O–H stretching from 3335 cm^{-1} to 3381 cm^{-1} indicates the interaction of hydroxyl groups of PVA with copper ions.

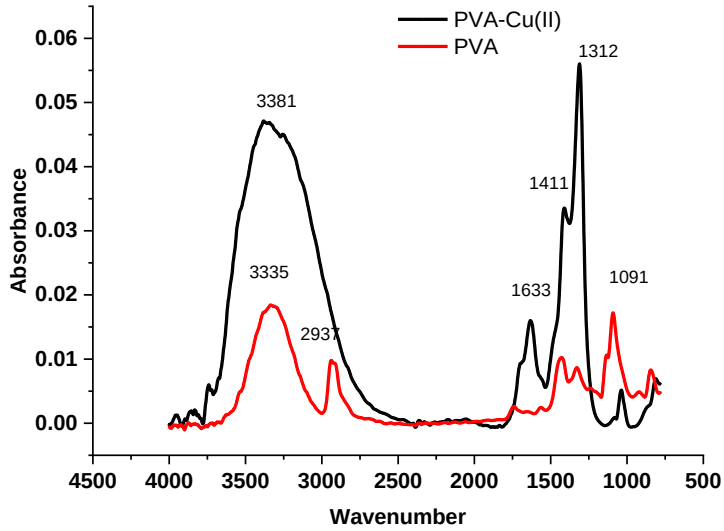

Figure 5. FTIR spectra of the PVA and PVA-Cu(II) complex

Reduction of Cu(II) to CuNPs by Sodium Borohydride

Sodium borohydride is a highly effective reductant with a standard reduction potential of E^o = –1.24 V [28].

$$NaBH_4 + 8OH^- \rightarrow NaBO_2 + 6H_2O + 8e^-;\ -1.24\left(E^0/V\right). \quad (1)$$

In regard to the reduction potential difference between sodium borohydride and Cu(II), it has been demonstrated that sodium borohydride is capable of reducing Cu(II) to Cu(0) [29].

$$\mathrm{Cu(II)}(aq)+2e^{-}\rightarrow \mathrm{Cu}(s);\quad 0.34\left(E^{0}/V\right), \tag{2}$$

Cu nanoparticles were prepared by reducing Cu(II) ions with sodium borohydride ($NaBH_4$). The following reaction takes place in aqueous solution [30]:

$$4\mathrm{Cu(II)}+\mathrm{BH}_4^{-}+8\mathrm{OH}^{-}=4\mathrm{Cu}+\mathrm{B(OH)}_4^{-}+4\mathrm{H}_2\mathrm{O}, \tag{3}$$

Characterization of CuNPs by DLS

The average hydrodynamic sizes of CuNPs in aqueous solution vary from 10 to 25 nm (Fig. 6). In this case, particles with a size of 10 nm predominate, representing 96 % of the total. This value is between those of Cu MVS (Cu atoms obtained by metal vapor synthesis) and Cu bronze powders [31].

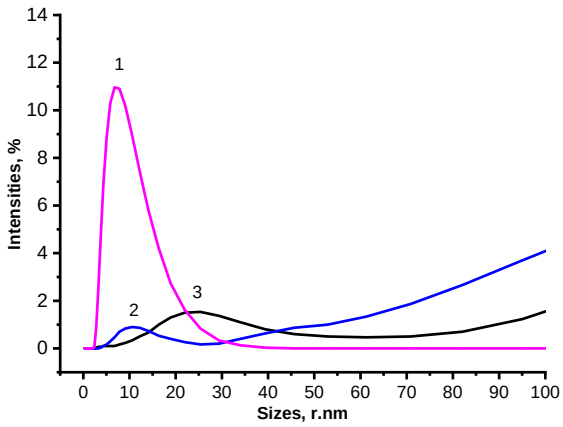

Figure 6. The average hydrodynamic sizes of PVA-CuNPs obtained by reduction of PVA-Cu(II) with 3 mL (1), 0.5 (2) and 0.25 mL (3) of $NaBH_4$ (0.5 mol·L^{-1})

Characterization of CuNPs by SEM and XRD

The surface morphology of the CuNPs deposited on SiO_2 is shown in Figure 7a. It can be seen that the CuNPs cover the surface of micron-sized SiO_2 [32].

The XRD pattern of CuNPs-SiO_2 is presented in Figure 7b. The diffraction patterns show the distinct peaks of two phases, namely crystalline copper metal (cubic) and Cu_2O (cubic), indicating the chemical reduction of Cu(II) ions to Cu and Cu(I). There are four peaks positioned at 2θ ~23°, 36.5°, 42.4° and 61.5°, which correspond well with (110), (111), (200) and (220) planes of the standard data for the face-centered cubic (FCC) structure of Cu_2O [33]. The XRD patterns also show the peaks for Cu at 2θ ~43.4° (111) and 74.3° (220). All peaks can be attributed to the cubic form of metallic copper [34, 35]. These peaks were remarkably close to those provided by JCPDS data of XRD for Cu_2O (JCPDS: 34-1354) and Cu (JCPDS: 04-0836).

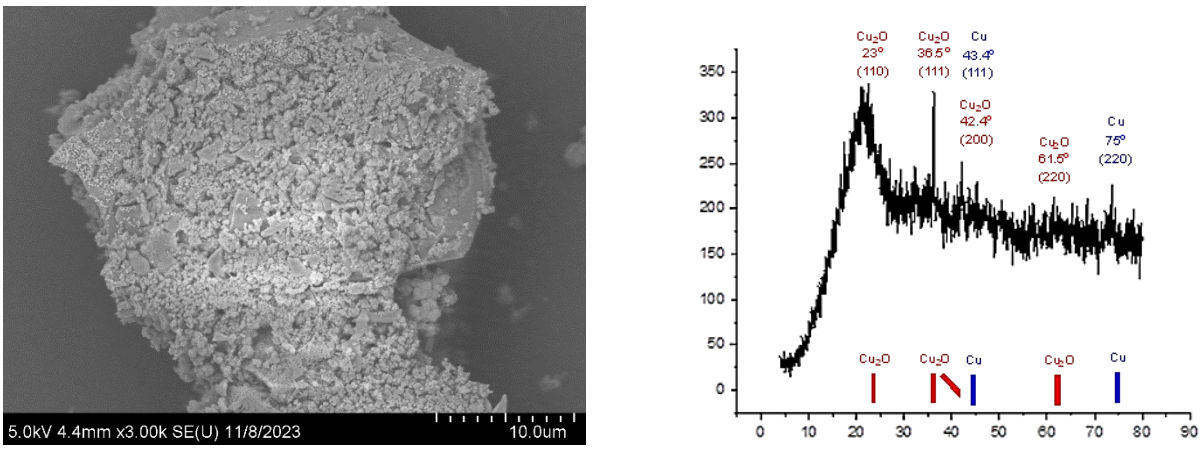

Figure 7. SEM micrograph (*a*) and XRD pattern (*b*) of CuNPs supported on SiO_2

The Oxidation of 1-Propanol

Copper nanoparticles prepared according to Figure 1 were used as a catalyst for the oxidation of 1-propanol with oxygen at 20°C and atmospheric pressure (Fig. 8).

$$\underset{\text{(liquid reactant)}}{\text{1-Propanol}} + \underset{\text{(gas reactant)}}{\text{Oxygen}} \xrightarrow[\text{CuNPs (solid)}]{20^{o}\text{C}} \text{Propionaldehyde} + \text{Water}, \quad (4)$$

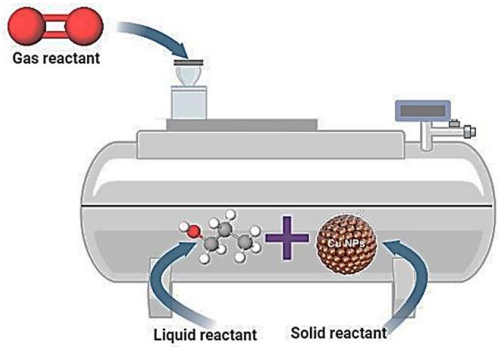

Figure 8. Three-phase system O_2–1-propanol–CuNPs

An increase in the mass of the catalyst (from 0.1 to 0.5 g) resulted in a notable enhancement in the conversion of 1-propanol, rising from 61.4 % to 87.8 % (Fig. 9). The conversion of 1-propanol exhibited a consistent trend over the course of the reaction, maintaining a constant level between 3 and 9 hours. After this period, a gradual decline was observed.

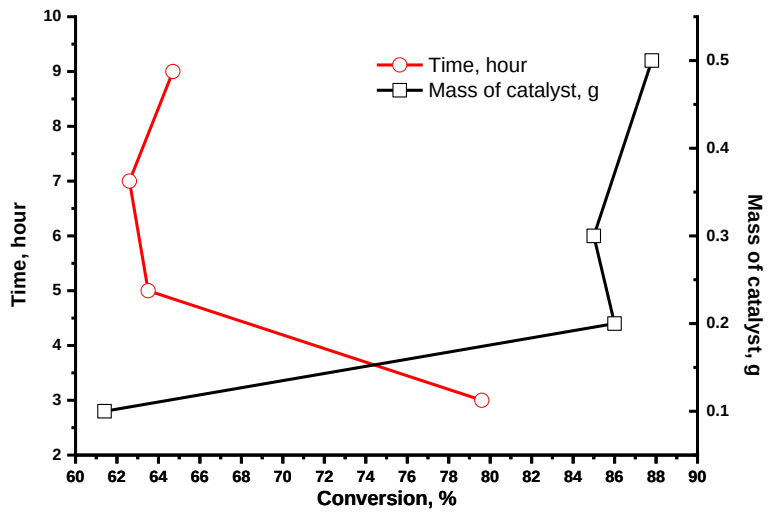

Figure 9. Mass- and time-dependent conversion of 1-propanol

The batch-type catalytic reactor containing the copper nanoparticles has a total volume of 150 mL and is composed of a glass cylinder with an internal diameter of 30 mm and a height of 132 mm. The reactor was equipped with a thermostatic jacket to maintain a constant temperature. The reactor performs a linear reciprocating movement and shakes at a frequency of approximately 250–300 swingings/min.

The Reynolds number in the shaking reactor was determined as Re = 5318, corresponding to turbulent flow (Table) [36, 37]. Shaking diameter of 25 and 50 mm had no significant influence on the mixing time [37]. After 3 hours of shaking the 1-propanol conversion decreased from 87.8 % to 61.5 % and did not change after 5, 7 and 9 hours. The results were mostly within a standard deviation of ±30 %. Using the equation for a Sherwood number ($Sh = 0.53Re^{0.54}(Pr')^{0.33}$) for mass exchange, proceeding with solid phase, and a value for D_e found for the 1-propanol–hexane binary system was equal to $4.8 \cdot 10^{-8}$ $m^2 \cdot s^{-1}$, the mass transport coefficient (($\beta = 2.2 \cdot 10^{-4} \cdot s^{-1}$) was calculated as a function of the diameter of the shaking reactor.

In aerated bioreactors for gas–liquid–solid systems, the critical limiting factor for providing the optimal environment is the oxygen transfer rate (OTR). In shaking flask scale, oxygen transport is accomplished by the rotary or reciprocating action of a shaker apparatus [38]. Oxygen transfer (OTR, mmol·L^{-1}·h^{-1}) is most commonly characterized by the total volumetric mass transfer coefficient ($k_L a$, m·h^{-1}), which is the product of the liquid side mass transfer coefficient (k_L, m·h^{-1}) and the specific interfacial area of mass transfer (a, m^3·m^{-3}) [39]. The k_L value can be approximated by the Higby penetration mass transfer model [38].

Table

Engineering parameters of a batch-type catalytic reactor (V_{total} = 150 mL) for 1-propanol oxidation

Metric	Value
$Re = \frac{wd_{reactor} \cdot \overset{20oC}{\underset{mix\ PrOH-hexane}{}}}{\overset{20oC}{\underset{mix\ PrOH-hexane}{}}}$	5319
$Pr' = \frac{\overset{20oC}{\underset{mix\ PrOH-hexane}{}}}{D_{L\,\overset{20oC}{\underset{mix\ PrOH-hexane}{}}}}$	16.2
$D_L = \frac{110^{-6}}{AB\sqrt{\mu}\left(v_A^{1/3}+v_B^{1/3}\right)^2}\sqrt{\frac{1}{M_A}+\frac{1}{M_B}}$, m^2·s^{-1}	4.8·10^{-8}
$Pe' = RePr'$	86168
$Sh = 0,53Re^{0.54}\left(Pr'\right)^{0.33}$	137
$= \frac{Sh\left(Nu'\right)D}{d_{reactor}}$, s^{-1}	2.1·10^{-4}
$k_L a$, s^{-1}	2.4
$OTR = k_L a\left(C^* - C\right)$, mmol·L^{-1}·h^{-1}	1.5·10^{-3}

Space–time–yield (STY, g·L^{-1} ·h^{-1}) is the key performance indicator for a batch-type catalytic reactor [40]:

$$STY = \frac{[P]f}{R_v} = \frac{3.3410^2\ 0.00053}{0.01} = 0.17710^2 = 17.7\,g\,L^{-1}\,h^{-1},$$

where [P] is the concentration of product leaving the reactor in g·L^{-1}.

As can be seen from the SEM results, the size of the CuNPs supported on SiO_2 decreases from 200 to 85,8 μm (Fig. 10). The main changes are size reduction by abrasion and degradation after prolonged agitation [41]. By reducing the particle size of a catalyst, its surface area increases and the reaction rate in the three-phase system is faster.

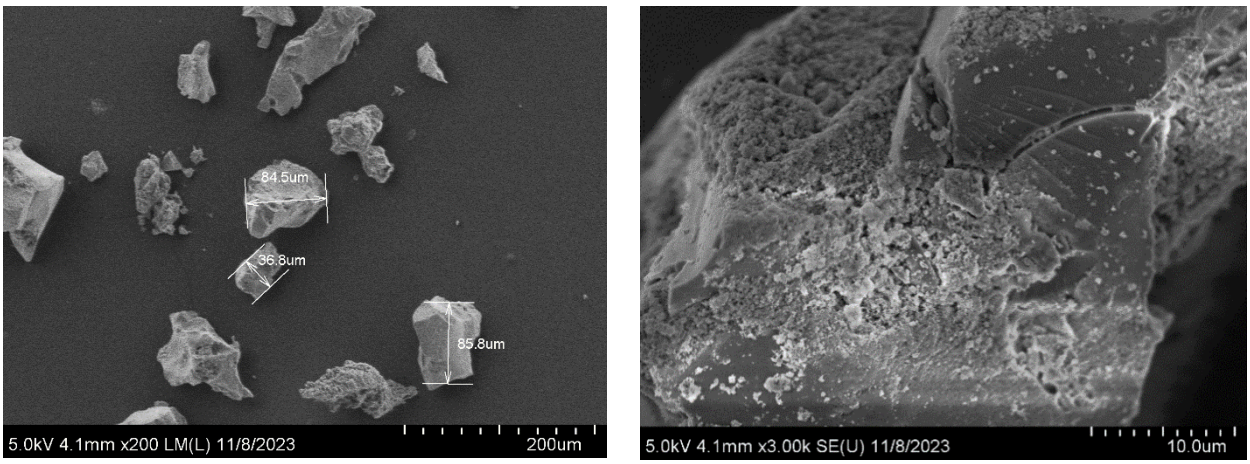

Figure 10. SEM micrographs of CuNPs supported on SiO_2 after 9 hours of oxidation process

Oxygen molecules adsorb and dissociate on the Cu(111),(220) surfaces to form an initial layer of atomic oxygen [42]. XRD data indicate the interaction between copper(111),(220) and dioxygen. Atomically adsorbed oxygen oxidizes 1-propanol on the Cu(111),(220) surface forming propionaldehyde and water. 1-Propanol reacts with the decomposed oxygen atoms on the Cu(111),(220) surfaces, forming water as following:

$$C_2H_5CH_2OH + 2O + Cu(111),(220) \rightarrow C_2H_5CHO + H_2O + O + Cu(111),(220). \quad (5)$$

Conclusions

The ratio of PVA to bivalent copper ions was determined to be equimolar by the conductimetric titration. The formation of the PVA-Cu(II) complex was confirmed by UV-Vis and FTIR spectral methods. Copper nanoparticles stabilized by PVA were impregnated on the surface of SiO_2 using a "one-pot" method. The morphology of the nanoparticles was identified by SEM and XRD, demonstrating an amorphous structure. The average size of CuNPs stabilized by PVP varied from 10 to 25 nm. Preliminary experiments indicate that the Cu powder derived from PVA-CuNPs acts as a catalytic precursor for the oxidation of 1-propanol. The oxidation of 1-propanol with oxygen in the presence of a copper catalyst leads to the formation of the key product — propionaldehyde, with yields ranging from 61.4 % to 87.8 % and depending on the mass of catalyst and the process duration. It was shown that a batch-type laboratory catalytic reactor with a total volume of 150 mL can serve as a three-phase (gas-liquid-solid) stirred laboratory tank reactor and evaluated by following different parameters (Re, Pr', Sh, $k_L a$, STY).

Funding

This research was funded by the Science Committee of the Ministry of Science and Higher Education of the Republic of Kazakhstan (Grant No. AP14869287).

*Author Information**

**The authors' names are presented in the following order: First Name, Middle Name and Last Name*

Kuralay Sakenkyzy Maksotova — 2nd year PhD Student, Faculty of Chemistry and Chemical Technology, Al-Farabi Kazakh National University, Al-Farabi avenue, 71, Almaty 050040, Kazakhstan; e-mail: maksotovak@yandex.kz; https://orcid.org/0000-0001-8606-5005

Dina Nauryzbaevna Akbayeva (*corresponding author*) — Doctor of Chemical Sciences, Chief Researcher, Institute of Polymer Materials and Technology, Microregion "Atyrau 1", Building 3/1, office 110, 050019, Almaty, Kazakhstan; Associated Professor, Faculty of Chemistry and Chemical Technology, Al-Farabi Kazakh National University, Al-Farabi avenue, 71, 050040, Almaty, Kazakhstan; e-mail: *dina.akbayeva@bk.ru*; https://orcid.org/0000-0001-9101-2418

Botagoz Sanatkyzy Bakirova — PhD, Faculty of Chemistry and Chemical Technology, Al-Farabi Kazakh National University, Al-Farabi avenue, 71, 050040, Almaty, Kazakhstan; e-mail: botik_botakan_91@mail.ru; https://orcid.org/0000-0003-1268-3550

Akerke Serikkyzy — 1st year Master Student, Faculty of Chemistry and Chemical Technology, Al-Farabi Kazakh National University, Al-Farabi avenue, 71, 050040, Almaty, Kazakhstan; e-mail: erkeshka.serikovna@gmail.com; https://orcid.org/0009-0009-5013-2478

Bexultan Mekenbayuly Lesbek — 3rd year Bachelor Student, Faculty of Chemistry and Chemical Technology, Al-Farabi Kazakh National University, Al-Farabi avenue, 71, 050040, Almaty, Kazakhstan; e-mail: beksultanlesbek17@gmail.com

Gulnur Sairanovna Tatykhanova — Candidate of Chemical Sciences, Associated professor, Laboratory of Engineering Profile, Satbayev University, 050013, Almaty Kazakhstan; e-mail: gulnurts81@yandex.kz; https://orcid.org/0000-0003-4457-1705

Sarkyt Elekenovich Kudaibergenov — Doctor of Chemical Sciences, Professor, Chief Researcher, Director of the Institute of Polymer Materials and Technology, Microregion "Atyrau 1", Building 3/1, office 110, 050019, Almaty, Kazakhstan; e-mail: skudai@mail.ru; https://orcid.org/0000-0002-1166-7826

Author Contributions

The manuscript was written through contributions of all authors. All authors have given approval to the final version of the manuscript. CRediT: **Kuralay Sakenkyzy Maksotova** — methodology, investigation; **Dina Nauryzbaevna Akbayeva** — conceptualization, methodology, validation, visualization, original draft preparation, writing-review & editing, supervision, funding acquisition; **Botagoz Sanatkyzy Bakirova** — methodology, validation, investigation; **Akerke Serikkyzy** — methodology, validation, investigation; **Bexultan Mekenbayuly Lesbek** — methodology, validation, investigation; **Gulnur Sairanovna Tatykhanova** — methodology, validation, investigation, supervision; **Sarkyt Elekenovich Kudaibergenov** — conceptualization; methodology, validation, investigation, supervision, funding acquisition.

Acknowledgments

Authors thank Rheinland-Pfalzische Technical University Kaiserslautern-Landau (Germany) for access to laboratory facilities.

Conflicts of Interest

The authors declare no conflict of interest.

References

1 Kopylovich, M.N., Ribeiro, A.P.C., Alegria, E.C.B.A., Martins, N.M.R., Martins, L.M.D.R.S., & Pombeiro, A.J.L. (2015). Catalytic oxidation of alcohols: Recent advances. In *Advances in Organometallic Chemistry*. Elsevier: Amsterdam, The Netherlands; *63*(3), 1–157. https://doi.org//10.1016/bs.adomc.2015.02.004

2 Day, A.R., & Eisner, A. (1931). Catalytic Oxidation of n-Propyl Alcohol. *J. Phys. Chem.*, *36*(7), 1912–1915. https://doi.org//10.1021/j150337a004

3 Mongkhonsi, T., Pimanmas, P., & Praserthdam, P. (2000). Selective Oxidation of Ethanol and 1-Propanol over V–Mg–O/TiO_2 Catalyst. *Chem. Lett.*, *29*(8), 968–969. https://doi.org//10.1246/cl.2000.968

4 Minachev, K.M., Antoshin, G.V., Klissurski, D.G., Guin, N.K., & Abadzhijeva, N.T. (1979). Oxidation of n-propanol over vanadium oxide catalysts. *React. Kinet. Catal. Lett*., *10*(2), 163–167. https://doi.org//10.1007/BF02075986

5 Liu, M., Yu, F., Yuan, B., Xie, C. & Yu, S. (2021). Oxidation of 1‑propanol to propionic acid with hydrogen peroxide catalysed by heteropolyoxometalates. *BMC Chem.*, *15*(1), Article 23. https://doi.org//10.1186/s13065-021-00750-5

6 Reisz, E., Tekle-Röttering, A., Naumov, S., Schmidt, W., & Schmidt, T.C. (2019). Reaction of 1-propanol with Ozone in Aqueous Media. *Int. J. Mol. Sci*., *20*, Article 4165. https://doi.org//10.3390/ijms20174165

7 Elwell, C.E., Gagnon, N.L., Neisen, B.D., Dhar, D., Spaeth, A.D., Yee, G.M., & Tolman, W.B. (2017). Copper–Oxygen Complexes Revisited: Structures, Spectroscopy, and Reactivity. *Chem. Rev.*, *117(3)*, 2059–2107. https://doi.org//10.1021/acs.chemrev.6b00636

8 Kang, L., Wang, B., Bing, Q., Zalibera, M., Büchel, R., Xu, R., Wang, Q., Liu, Y., Gianolio, D., Tang, C.C., Gibson, E.K., Danaie, M., Allen, C., Wu, K., Marlow, S., Sun, L., He, Q., Guan, S., Savitsky, A., Velasco-Vélez, J.J., Callison, J., Kay, C.W.M., Pratsinis, S.E., Lubitz, W., Liu, J., & Wang, F.R. (2020). Adsorption and activation of molecular oxygen over atomic copper(I/II) site on ceria. *Nat. Commun.*, *11*, 4008. https://doi.org//10.1038/s41467-020-17852-8

9 Ojha, N.K., Zyryanov, G.V., Majee, A., Charushin, V.N., Chupakhin, O.N., & Santra, S. (2017). Copper nanoparticles as inexpensive and efficient catalyst: A valuable contribution in organic synthesis. *Coord. Chem. Rev.*, *353*, 1–57. https://doi.org//10.1016/j.ccr.2017.10.004

10 Kushalkar, K.B., & Pangarkar, V.G. (1995). Particle-Liquid Mass Transfer in Three-Phase Mechanically Agitated Contactors: Power Law Fluids. *Ind. Eng. Chem. Res.*, *34*(7), 2485–2492. https://doi.org//10.1021/ie00046a033

11 Pangarkar, V.G., Yawalkar, A.A., Sharma, M.M., & Beenackers, A.A.C.M. (2002). Particle−Liquid Mass Transfer Coefficient in Two-/Three-Phase Stirred Tank Reactors. *Ind. Eng. Chem. Res.*, *41*(17), 4141–4167. https://doi.org//10.1021/ie010933j

12 Kawase, Y., Shimizu, K., Araki, T., & Shimodaira, T. (1997). Hydrodynamics in Three-Phase Stirred Tank Reactors with Non-Newtonian Fluids. *Ind. Eng. Chem. Res.*, *36*(1), 270–276. https://doi.org//10.1021/ie960452d

13 Tschentscher, R., Spijkers, R.J.P., Nijhuis, T.A., van der Schaaf, J., & Schouten, J.C. (2010). Liquid−Solid Mass Transfer in Agitated Slurry Reactors and Rotating Solid Foam Reactors. *Ind. Eng. Chem. Res.*, *49*(21), 10758–10766. https://doi.org//10.1021/ie100385n

14 Masuda, K., Ichitsuka, T., Koumura, N., Sato, K., & Kobayashi, S. (2018). Flow fine synthesis with heterogeneous catalysts. *Tetrahedron*, *74*(15), 1705–1730. https://doi.org//10.1016/j.tet.2018.02.006

15 Mazzarino, I., Santos, A., & Baldi, G. (1994). Catalytic oxidation of n-propanol in a multiphase upflow reactor: surface tension effects. *Chem. Eng. Sci.*, *49*(24), 5699–5707. https://doi.org//10.1016/0009-2509(94)00311-4

16 Kudaibergenov, S.E. (2019). Physicochemical complexation and catalytic properties of polyampholyte cryogels. *Gels*, *5*, Article 8. https://doi.org//10.3390/gels5010008

17 Kudaibergenov, S.E., & Dzhardimalieva, G.I. (2000). Flow-through catalytic reactors based on metal nanoparticles immobilized within porous polymeric gels and surfaces/hollows of polymeric membranes. *Polymers*, *12*, Article 572. https://doi.org//10.3390/polym12030572

18 Dzhardimalieva, G.I., Zharmagambetova, A.K., Kudaibergenov, S.E., & Uflyand, I.E. (2020). Polymer-immobilized clusters and metal nanoparticles in catalysis. *Kinet. Catal. 61*, 198–223. https://doi.org//10.1134/S0023158420020044

19 Dorfman, Y.A., Abdreimova, R.R., & Akbayeva, D.N. (1995). Kinetika i mekhanizm okislitelnogo alkoksilirovaniya tetrafosfora v prisutstvii sulfatov i karboksilatov Cu(II) [Kinetics and mechanism of oxidative alkoxylation of tetraphosphorus in the presence of Cu(II) sulfates and carboxylates]. *Kinetika i kataliz — Kinetics and catalysis*, *36*(1), 103–110 [in Russian].

20 Akbayeva, D.N., Faizova, F.C., Abdreimova, R.R., & Peruzzini, M. (2007). Oxidation of white phosphorus by peroxides in aqueous and alcoholic solutions: Mechanistic aspects and catalytic studies. *J. Mol. Catal. A Chem.*, *267*, 181–193. https://doi.org//10.1016/j.molcata.2006.11.046

21 Akbayeva, D.N., Bakirova, B.S., Seilkhanova, G.A., & Sitzmann, H. (2018). Oxidation of octene-1 in the presence of palladium-polyvinylpyrrolidone complex. *Bull. Chem. React. Eng. Catal.*, *13*, 560–572. https://doi.org//10.9767/bcrec.13.3.1980.560-572

22 Smagulova, I., Tatykhanova, G., Shakhvorostov, A., Akbayeva, D., & Kudaibergenov, S. (2021). Oxidation of *iso*-propanol and *n*-butanol by catalase encapsulated within macroporous polyampholyte cryogel matrix. *Polym. Adv. Technol.*, *32*, 3817–3826. https://doi.org//10.1002/pat.5396

23 Akbayeva, D.N., Smagulova, I.A., Maksotova, K.S., Bakirova, B.S., Tatykhanova, G.S., & Kudaibergenov, S.E. (2023). In Situ Entrapment of Catalase within Macroporous Cryogel Matrix for Ethanol Oxidation: Flow-through Mode versus Batch Reactor. *Catalysts*, *13(7)*, Article 1075. https://doi.org//10.3390/catal13071075

24 Selenova, B.S., Ayazbayeva, A.Ye., Shakhvorostov, A.V., Kabdrakhmanova, S.K., Nauryzova, S.Z., & Kudaibergenov, S.E. (2021). Preparation and study of the physicochemical characteristics of multilayer polymer composites based on poly(ethyleneimine)- stabilized copper nanoparticles and poly(sodium 2-acrylamide-2-methyl-1-propanesulfonate. *Chem. Bull. Kaz.*, *102*(3), 22–31. https://doi.org//10.15328/cb1235

25 Ustyakina, D.R., Chevtaev, A.S., Tabunshchikov, A.I., Ozerin, A.S., Radchenko, F.S., & Novakov, I.A. (2019). Complexes of polyethyleneimine with Cu^{2+} ions in aqueous solutions as precursors for obtaining nanosized copper particles. *Highmol. Comp. Ser. B*, *61*(3), 179–183. https://doi.org//10.1134/S1560090419030151

26 Mohanapriya, S., Mumjitha, M., PurnaSai, K. & Raj, V. (2016). Fabrication and characterization of poly(vinyl alcohol)-TiO_2 nanocomposite films for orthopedic applications. *J. Mech. Behav. Biomed. Mater.*, *63*, 141–156. https://doi.org//10.1016/j.jmbbm.2016.06.009

27 Vimala, K., Samba Sivudu, K., Murali Mohan, Y., Sreedhar, B., & Mohana Raju, K. (2009). Controlled silver nanoparticles synthesis in semi — hydrogel networks of poly (acrylamide) and carbohydrate: a rational methodology for antibacterial application. *Carbohydr. Polym.*, *75*(3), 463–471. https://doi.org//10.1016/j.carbpol.2008.08.009

28 Colominas, S., McLafferty, J., & Macdonald, D.D. (2009). Electrochemical studies of sodium borohydride in alkaline aqueous solutions using a gold electrode. *Electrochim. Acta*, *54*(13), 3575–3579. https://doi.org//10.1016/j.electacta.2009.01.021

29 Hong, H.-J., & Ryu, J. (2021). Synthesis of Copper Nanoparticles from Cu^{2+}-Spiked Wastewater via Adsorptive Separation and Subsequent Chemical Reduction. *Nanomaterials*, *11*, Article 2051. https://doi.org//10.3390/nano11082051

30 Liu, Q., Zhou, D., Yamamoto, Y., Ichino, R., & Okido, M. (2012). Preparation of Cu nanoparticles with $NaBH_4$ by aqueous reduction method. *T. Nonferrous Metal Soc.*, *22*(1), 117–123. https://doi.org//10.1016/s1003-6326(11)61149-7

31 Vitulli, G., Bernini, M., Bertozzi, S., Pitzalis, E., Salvadori, P., Coluccia, S., & Martra, G. (2002). Nanoscale Copper Particles Derived from Solvated Cu Atoms in the Activation of Molecular Oxygen. *Chem. Mater.*, *14*(3), 1183–1186. https://doi.org//10.1021/cm011199x

32 Vdovina, S.N., & Ferapantov, N.B. (2011). Rol' svoystv polimernoy matritsy v khimicheskom osazhdenii metalla v polimernom gele [The role of the polymer matrices properties in the chemical metal deposition in polymer gel]. *Sorbtsionnye i khromatograficheskie protsessy — Sorption and chromatographic processes*, *11*(1), 132–138 [in Russian].

33 Sawant, S.S., Bhagwat, A.D., & Mahajan, C.M. (2016). Novel Facile Technique for Synthesis of Stable Cuprous Oxide (Cu_2O) Nanoparticles — an Ageing Effect. *J. Nano Elec. Phys.*, *8*(1), Article 01036. https://doi.org//10.21272/jnep.8(1).01036

34 Biçer, M., & Şişman İ. (2010). Controlled synthesis of copper nano/microstructures using ascorbic acid in aqueous CTAB solution. *Powder Technol.*, *198*(2), 279–284. https://doi.org//10.1016/j.powtec.2009.11.022

35 Ngoc, D.T. B., Duy, D.B., Tuan, L.N.A., Thach, B.D., Tho, T.P., & Phu, D.V. (2021). Effect of copper ions concentration on the particle size of alginate-stabilized Cu_2O-Cu nanocolloids and its antibacterial activity against rice bacterial leaf blight (Xanthomonas oryzae pv. Oryzae). *Adv. Nat. Sci: Nanosci. Nanotechnol.*, *12*(1), Article 013001. https://doi.org//10.1088/2043-6262/abebd6

36 Büchs, J. (2001). Introduction to advantages and problems of shaken cultures. *Biochem. Eng. J.*, *7(2)*, 91–98. https://doi.org//10.1016/s1369-703x(00)00106-6

37 Tan, R. -K., Eberhard, W., & Büchs, J. (2011). Measurement and characterization of mixing time in shake flasks. *Chem. Eng. Sci.*, *66*(3), 440–447. https://doi.org//10.1016/j.ces.2010.11.001

38 Garcia-Ochoa, F., & Gomez, E. (2010). Oxygen Transfer Rate Determination: Chemical, Physical and Biological Methods. *Encyclopedia of Industrial Biotechnology*. Wiley online library. https://doi.org//10.1002/9780470054581.eib467

39 Löffelholz, C., Kaiser, S. C., Kraume, M., Eibl, R., & Eibl, D. (2013). Dynamic Single-Use Bioreactors Used in Modern Liter- and m3- Scale Biotechnological Processes: Engineering Characteristics and Scaling Up. *Adv. Biochem. Engin./Biotechnol.*, 1–44. https://doi.org//10.1007/10_2013_187

40 Coloma, J., Guiavarc'h, Y., Hagedoorn, P.L., & Hanefeld, U. (2021). Immobilisation and flow chemistry: Tools for implementing biocatalysis. *Chem. Commun*., *57*, 11416–11428. https://doi.org//10.1039/D1CC04315C

41 Gubiani, P.I., De Almeida, T.A., Mulazzani, R.P., De Araújo Pedron F., Sanches Suzuki, L.E.A., & Pereira, C.A. Shaking settings to reduce the breakdown of Entisol fragile particles in texture analysis (2021). *Rev. Bras. Cienc. Solo*, *45*, Article e0210066. https://doi.org//10.36783/18069657rbcs20210066

42 Gargano, M., Ravasio, N., Rossi, M., Tiripicchio, A., & Camellini, M.T. (1989). Reactivity of metallic copper with acidic organic compounds in the presence of molecular oxygen. Crystal structure of $[\{Cu(NCO)(py)_2\}_2]\cdot H_2O$. *J. Chem. Soc., Dalton Trans.*, *5*, 921–925. https://doi.org//10.1039/dt9890000921

How to Cite: Sidorov, V.L., Baimuratova, R.K., Korchagin, D.V., Ivanov, A.V., Kydralieva, K.A., & Dzhardimalieva, G.I. (2024). Magnetically Separable Fe_3O_4/γ-Fe_2O_3@MIL-88b(Fe) and Fe_3O_4/γ-Fe_2O_3@NH_2-MIL-88b(Fe) Composites for the Photocatalytic Degradation of Congo Red Dye. *Eurasian Journal of Chemistry, 29, 3(115), 130-147.* https://doi.org/10.31489/2959-0663/3-24-5

Article

Received: 8 June 2024 | Revised: 24 July 2024 |
Accepted: 31 July 2024 | Published online: 19 August 2024

UDC 541.145+ 544.47

https://doi.org/10.31489/2959-0663/3-24-5

Vladislav L. Sidorov[1,2], Rose K. Baimuratova[1*], Denis V. Korchagin[1], Andrey V. Ivanov[1], Kamila A. Kydralieva[3], Gulzhian Dzhardimalieva[1,3]

[1]Federal Research Center of Problems of Chemical Physics and Medicinal Chemistry, Russian Academy of Sciences; Chernogolovka, Moscow region, Russia;
[2]Lomonosov Moscow State University, Moscow, Russia;
[3]Moscow Aviation Institute (National Research University), Moscow, Russia
*(*Corresponding author's e-mail: Roz_Baz@mail.ru)*

Magnetically Separable Fe_3O_4/γ-Fe_2O_3@MIL-88b(Fe) and Fe_3O_4/γ-Fe_2O_3@NH_2-MIL-88b(Fe) Composites for the Photocatalytic Degradation of Congo Red Dye

Industry-wide applications of synthetic dyes produce large amounts of dye wastewater that requires treatment. Advanced oxidation processes are considered promising, since they incorporate highly reactive hydroxyl radicals capable of oxidizing most organic pollutants, including most commonly used azo dyes, into carbon dioxide and water. In this regard, iron-based metal-organic frameworks are effective heterogeneous photocatalysts for the generation hydroxyl radicals via Fenton reaction. In this study, Fe_3O_4/Fe_2O_3@MIL-88b(Fe) and Fe_3O_4/γ-Fe_2O_3@NH_2-MIL-88b(Fe) composites were obtained, where Fe_3O_4/γ-Fe_2O_3 particles enabled magnetic separation, and Fe-metal-organic frameworks (MOF) coating exhibited photocatalytic activity. These composites were characterized by elemental analysis, FTIR spectra, XRD patterns, magnetization curves, TGA profiles, nitrogen adsorption-desorption isotherms. Using ultraviolet-visible spectroscopy and Congo Red anionic azo dye (CR) as organic pollutant, composites' adsorption kinetics were observed and their photocatalytic activities were studied. As a result, Fe_3O_4/γ-Fe_2O_3@MIL-88b(Fe) and Fe_3O_4/γ-Fe_2O_3@NH_2-MIL-88b(Fe) were both capable photocatalysts for generating hydroxyl radicals from hydrogen peroxide (H_2O_2) through Fenton-like reaction with removal efficiencies of CR dye approaching 89 % and 95 %, respectively. Moreover, a higher photocatalytic activity was observed for Fe_3O_4/γ-Fe_2O_3@NH_2-MIL-88b(Fe), supposedly, due to -NH_2 group increasing the electron density on the aryl ring, which stabilized hole localization at the organic linker, increased photoexcited state lifetime and promoted electron transfer onto metal center in Fe_3-μ_3-O cluster.

Keywords: Heterogeneous Fenton-like catalysts, MIL-88b(Fe), NH_2-MIL-88b(Fe), Iron-based MOFs, Photocatalysis, magnetic composites, adsorption kinetics, organic pollutants degradation.

Introduction

Synthetic dyes are extensively utilized in textile, printing, pharmaceutical, cosmetic, food and beverage industries [1–3]. In particular, azo dyes remain as the most commonly implemented dyes due to their superior stability upon being subjected to light irradiation, acidic and basic solutions, oxidation [4]. Estimates suggest that staggering 280,000 tons of untreated dye wastewater are annually discharged into the environment [5].

Organic pollutant removal can be achieved in a number of ways including physical adsorption [6], biological treatment [7] and advanced oxidation processes (AOPs) which incorporate highly reactive hydroxyl radicals (·OH) [8]. While physical adsorption is an inherently simple process, utilized adsorbent gradually turns into solid waste and subsequently requires laborious regeneration [9]. Biological treatment methods are scalable, yet they tend to lose their efficiency when employed for azo dyes degradation [10]. Finally, AOPs are considered promising, since hydroxyl radicals are capable of oxidizing most organic pollutants, including azo dyes, into carbon dioxide (CO_2) and water (H_2O) [11].

Generally speaking, methods for hydroxyl radicals' generation in wastewater include ozonation, ultrasonication, ultraviolet (UV) irradiation, incorporation of oxidizing agents such as hydrogen peroxide (H_2O_2) and various combinations of these processes [12]. Ozonation is mainly encumbered by ozone's limited solubility in water, therefore propagating increased energy and time requirements for treatment[13]. Furthermore, ultrasonication process also specifies high energy consumption [12]. In case of a standalone UV

irradiation organic pollutants tend to partially decompose, leaving harmful intermediates present in water [12]. In this regard, numerous catalysts are being considered to enhance decomposition process, including silver nanoparticles (Ag NPs) [14], various semiconductors [15], such as titanium dioxide (TiO_2), zinc oxide (ZnO), gallium arsenide (GaAs), tungsten trioxide (VI) (WO_3), gallium phosphide (GaP), cadmium sulfide (CdS) [7]), systems with presence of divalent ferrous ions (Fe^{2+}) [12] for a Fenton reaction [16]. Though Ag NPs demonstrate high catalytic activity, they need to be initially activated via complex procedure [15]. Semiconductor materials often possess a large band gap similar to TiO_2 (3.2 eV) which prevents them from fully absorbing solar spectrum energy. Additionally, rapid recombination of photogenerated electron/hole pairs in these materials further diminishes quantum efficiency [17]. While Fenton reaction is feasible in the absence of light and demonstrates remarkable efficiency at generating hydroxyl radicals, it traditionally necessitates highly acidic pH (2-3) and implements homogeneous ferrous catalyst, that requires subsequent laborious extraction [12]. Nevertheless, Fenton reaction process can be improved upon by introducing external ultraviolet-visible (UV-Vis) irradiation [18] and simultaneously utilizing heterogeneous ferrous photocatalyst. Moreover, a priority is set on the development of new heterogeneous ferrous photocatalyst materials that initiate Fenton reaction at slightly acidic or neutral pH.

Metal-organic frameworks (MOFs) are porous two- or three-dimensional coordination polymers constructed via self-assembly of inorganic nodes (metal ions or clusters) and organic linkers (bridging ligands) [19]. Owing to the huge number of currently available inorganic nodes and organic linkers MOFs demonstrate an astonishing structure variety, adjustable pore volume and high specific surface area, all of which encourages their use for gas separation and detection, drug delivery, hydrogen storage, adsorption and catalysis [20–22].

Implementation of inorganic nodes with d-block transition metals produces Ti-MOFs, Zr-MOFs [23], Fe-MOFs [20, 24] and Cu-MOFs [25] that possess an optimal bandgap for solar spectrum absorption and can be potentially utilized as UV-Vis photocatalysts for degradation of organic pollutants [18]. It is believed that organic linkers promote charge separation and electron transfer onto metal centers, while also enhancing electron-hole pair transport towards MOF's surface for better performance in redox reactions [20]. Additionally, weak coordination between d-block transition metals and non-bridging ligands propagates the formation of coordination vacancies, resulting in metal centers behavior similar to Lewis acid catalytic sites [18]. Lastly, organic linkers possessing dissimilar double bond conjugation architecture may be used to further improve MOF's photocatalytic properties and its ability for absorbing solar spectrum [18, 20].

One of the most commonly used inorganic nodes in Fe-MOFs (such as MIL-88b(Fe), MIL-101(Fe) and MIL-100(Fe)) is a trinuclear oxo-centered iron (Fe_3-μ_3-O) cluster [26, 27] with octahedral metal centers. In presence of a visible light irradiation Fe_3-μ_3-O cluster undergoes excitation and a subsequent electron transfer from O^{2-} to Fe^{3+}, forcing metal center reduction [20], while Fe-MOF's porous structure ensures sufficient diffusion of reagents towards reduced metal centers. Evidently, nonbridging ligands in metal center's coordination sphere are easily substituted for Lewis bases. In this regard, MIL-88b(Fe), being a highly flexible Fe-MOF with 1,4-benzenedicarboxylates (BDC) as organic linkers bridging together Fe_3-μ_3-O clusters, possesses high photocatalytic activity and is therefore considered as a promising heterogeneous Fenton catalyst [24, 28, 29]. As a Lewis base, H_2O_2 easily adsorbs onto Fe_3-μ_3-O clusters, while electron-rich benzenedicarboxylate (BDC) linkers promote photoinduced reduction of Fe^{3+} into Fe^{2+}, which initiates Fenton reaction. Despite MIL-88b(Fe)'s flexibility in presence of polar solvents such as water (H_2O), its topology remains the same, yet its pore volume alters, potentially further enhancing reagents' diffusion towards metal centers. In contrast to homogenous Fe^{2+}/Fe^{3+} catalyst, heterogeneous MIL-88b(Fe) is capable of initiating Fenton reaction at less acidic pH (4-6) [28]. It is worth noting that at pH from 4 to 5 a miniscule amount of ferrous ions is released into solution; however they do not exhibit noticeable catalytic activity, since homogeneous Fenton requires higher acidity [28]. At basic pH (10) MIL-88b(Fe)'s adsorption capacity and photocatalytic activity diminish quickly, which may be linked to compromised integrity of the porous structure [28, 29]. Otherwise, MIL-88b(Fe) retains its performance over a wide range of pH (4-8) [28].

MOF's adsorption and photocatalytic performance can be enhanced by implementing organic linkers with additional functional groups [30]. Namely, insertion of 2-amino-1,4-benzenedicarboxylate (NH_2-BDC) linkers between Fe_3-μ_3-O clusters produces NH_2-MIL-88b(Fe) that inherits MIL-88b(Fe)'s original structure. Amino groups enable additional mechanisms for sorbate-sorbent interaction, including emergence of covalent bonds with an electron-deficient sorbate [30], hydrogen bonds [31], electrostatic and ionic interactions [32], chelation [33]. When determining optimal pH one should also consider potential electrostatic and ionic repulsion between protonated amino group and different ionic forms of sorbate molecules [32, 34, 35].

Another important aspect of MOF is its ability to retain adsorption and photocatalytic performance over repeated use cycles. In this regard, both MIL-88b(Fe) [26] and NH_2-MIL-88b(Fe) [35] exhibit good long-term stability with little decrease in photocatalytic activity after several successive cycles of organic pollutants decomposition. Significant loss of photocatalytic activity only occurs at prolonged irradiation intervals (more than 400 hours), when almost all organic linkers undergo decarboxylation [36].

To improve MOF's practical reusability, it can be applied as a coating on the magnetic particle's surface, enabling magnetic separation of MOF from aqueous medium. Compared with conventional filtration and centrifugation processes, removal of heterogeneous catalysts via magnetic separation is considered promising since it reduces solvents and auxiliaries use, as well as financial and time expenses [37]. Magnetite (Fe_3O_4) and maghemite (γ-Fe_2O_3) particles are generally chosen as magnetic carriers due to their environmental friendliness, straightforward synthesis and sufficient saturation magnetization values. Standalone iron oxide particles also catalyze the decomposition of organic pollutants [38, 39], yet they possess high surface energy, which often causes their aggregation, leading to an overall decrease in catalytic activity [40]. Nevertheless, Fe_3O_4 particles coated with MIL-100(Fe) photocatalyst result in a Fe_3O_4@MIL-100(Fe) composite, which decomposes methylene blue more efficiently than TiO_2 and is easily removed from solution with a strong magnet [41].

While numerous evidences prove MIL-88b(Fe)'s and NH_2-MIL-88b(Fe)'s acceptable adsorption and photocatalytic performance, few studies implement magnetic separation of Fe-MOFs from aqueous medium and examine their ability to decompose azo dyes. Therefore, this study primarily focuses on the synthesis of Fe_3O_4/γ-Fe_2O_3@MIL-88b(Fe) and Fe_3O_4/γ-Fe_2O_3@NH_2-MIL-88b(Fe) composites, where Fe_3O_4/γ-Fe_2O_3 particles enable magnetic separation, and Fe-MOF coating exhibits photocatalytic activity [40]. Fe-MOFs were constructed through rational approach of utilizing pre-synthesized Fe_3-μ_3-O acetate clusters as secondary building units [42–45]. Essentially, Fe_3-μ_3-O clusters' geometry strictly determined the coordination of organic linkers, which produced isoreticular Fe-MOFs with desired topology. Finally, Fe_3O_4/γ-Fe_2O_3@MIL-88b(Fe) and Fe_3O_4/γ-Fe_2O_3@NH_2-MIL-88b(Fe) were both capable photocatalysts for generating hydroxyl radicals from H_2O_2 through Fenton-like reaction with removal efficiencies of Congo Red dye approaching 89 % and 95 %, respectively.

Experimental

Starting Materials

Ferric chloride hexahydrate ($FeCl_3 \cdot 6H_2O$, puriss.), ferrous chloride tetrahydrate ($FeCl_2 \cdot 4H_2O$, puriss.), sodium acetate trihydrate ($CH_3COONa \cdot 3H_2O$, puriss.), ethanol (C_2H_5OH, 96,5 %, pur.), aqueous ammonia (NH_4OH, 25 %, pur.), hydrogen peroxide (H_2O_2, 30 %, pur.), glacial acetic acid (CH_3COOH, 99,8 %, puriss.), potassium hydroxide (KOH, puriss.) were supplied by Ruskhim chemical company, while 1,4-benzenedicarboxylic (terephthalic) acid (BDCa, $C_8H_6O_4$, 98 %) and 2-amino-1,4-benzenedicarboxylic (2-aminoterephthalic) acid (NH_2-BDCa, $C_8H_7NO_4$, 99 %) were purchased from Sigma-Aldrich.

Preparation of Oxo-Centered Iron Acetate Cluster

To synthesize oxo-centered iron acetate ($[Fe_3(\mu_3\text{-}O)(CH_3COO)_6(H_2O)_3]Cl \cdot 6H_2O$) cluster, preheated (50 °C) aqueous solutions of 3M $FeCl_3 \cdot 6H_2O$ (127.22 g, 150 mL) and 6M $CH_3COONa \cdot 3H_2O$ (122.42 g, 150 mL) were poured in 600 mL beaker and magnetically stirred (500 rpm) at 50 °C for 30 minutes [45]:

$$3FeCl_3 \cdot 6H_2O + 6CH_3COONa \cdot 3H_2O \rightarrow$$
$$\rightarrow [Fe_3(\mu_3\text{-}O)(CH_3COO)_6(H_2O)_3]Cl \cdot 6H_2O + 6NaCl + 2HCl + 26H_2O \quad (1)$$

The reaction mixture was then poured in 150 mm × 75 mm crystallizing dish and left to cool down overnight. In the following days water was allowed to slowly evaporate. The resulting precipitate was filtered in a Buchner funnel and washed with cold ethanol (–18 °C). After that, the precipitate was dried in a vacuum (10^{-3} Torr, 40 °C, 10 h). Yield: 88.77 g (80 %). Found (wt. %): C, 19.7±0.13; H, 5.2±0.05; Fe, 22.9±0.5. Calculated for ($[Fe_3(\mu_3\text{-}O)(CH_3COO)_6(H_2O)_3]Cl \cdot 6H_2O$) (wt. %): C, 19.60; H, 4.93; Fe, 22.78; Cl, 4.82. FTIR (KBr, vmax/cm-1): 3523 ν(O-H); 2929 ν(C-H); 1601 vas(COO-), 1520 vas(COO-), 1444 νs(COO-); 665 ν(Fe-O).

Preparation of Fe_3O_4/γ-Fe_2O_3@Fe-MOF Composites

To obtain each Fe_3O_4/γ-Fe_2O_3@Fe-MOF composite a two-stage process was implemented. At the first stage, Fe_3O_4/γ-Fe_2O_3 particles were synthesized through Elmore's approach [46]. Namely, in presence of argon atmosphere 10.1 g of $FeCl_3 \cdot 6H_2O$, 3.71 g of $FeCl_2 \cdot 4H_2O$ and 250 mL of deionized water were added into 500 mL three neck round bottom flask and vigorously mixed with mechanical stirrer (2000 rpm) until

complete dissolution. While maintaining mechanical stirrer speed and argon flow to the flask, 22.5 mL of NH_4OH (25 %) were added drop-wise to cause precipitation:

$$2FeCl_3 + FeCl_2 + 8NH_4OH \rightarrow Fe_3O_4\downarrow + 8NH_4Cl + 4\,H_2O \quad (2)$$

Despite argon atmosphere inside the flask, Fe_3O_4 still underwent partial oxidation into $\gamma\text{-}Fe_2O_3$, thus producing $Fe_3O_4/\gamma\text{-}Fe_2O_3$ particles. At the second stage, $Fe_3O_4/\gamma\text{-}Fe_2O_3$ particles were coated with Fe-MOF through rational approach of utilizing pre-synthesized $[Fe_3(\mu_3\text{-}O)(CH_3COO)_6(H_2O)_3]Cl\cdot 6H_2O$ clusters as secondary building units [42]. To obtain $Fe_3O_4/\gamma\text{-}Fe_2O_3$@MIL-88b(Fe) composite, 8.48 g of BDCa were added to reaction mixture in the flask while stirring speed further remained the same. After the dissolution of BDCa, 12.4 g of $[Fe_3(\mu_3\text{-}O)(CH_3COO)_6(H_2O)_3]Cl\cdot 6H_2O$ were finally added for an exchange reaction to occur, which resulted in nonbridging acetate ligands being substituted with BDCa linkers, thus producing desired MIL-88b(Fe) coating (Scheme). To obtain $Fe_3O_4/\gamma\text{-}Fe_2O_3$@$NH_2$-MIL-88b(Fe) composite same steps were carried out with 9.10 g of NH_2-BDCa. Finally, each composite precipitate was filtered in a Buchner funnel and washed with warm (65 °C) deionized water. After that, precipitates were dried in a vacuum (10^{-3} Torr, 50 °C, 5 h). Yield: 17.06 g (98 %) and 12.35 g (72 %) for $Fe_3O_4/\gamma\text{-}Fe_2O_3$@MIL-88b(Fe) and $Fe_3O_4/\gamma\text{-}Fe_2O_3$@$NH_2$-MIL-88b(Fe), respectively.

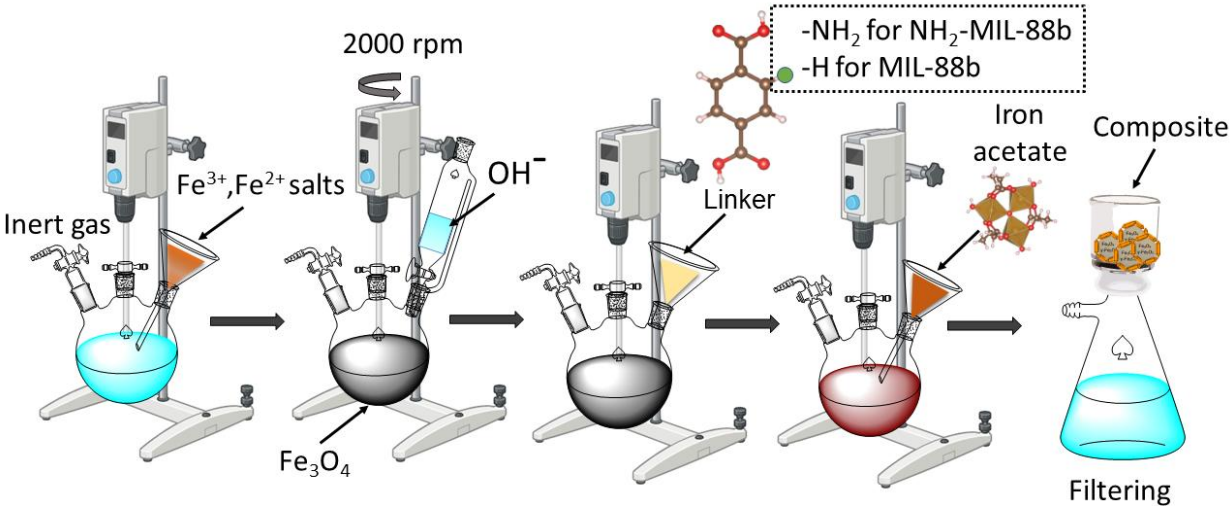

Scheme. Schematic representation of the $Fe_3O_4/\gamma\text{-}Fe_2O_3$@MOF composites' synthesis process

General Methods

C, H, N contents were determined through combustion analysis (Elementar vario MICRO cube, Germany), while Fe content was measured using atomic absorption spectroscopy (AAS) (Carl Zeiss AAS-3, Germany). Oxygen content was subsequently calculated via the equation: O (wt. %) = 100 − (C + H + N + Fe). Fourier-transform infrared (FTIR) spectra of the composites were recorded in the range of 4000–500 cm^{-1} (PerkinElmer Spectrum 100, USA) using attenuated total reflection (ATR) technique. To further evaluate composites' structure and quantify Fe_3O_4 and $\gamma\text{-}Fe_2O_3$ phases, powder X-ray diffraction (XRD) analysis was conducted under Cu-Kα radiation (λ = 1.5406 Å) (Aeris Benchtop, Malvern PANalytical, the Netherlands). The magnetization curves of the composites were recorded at room temperature (25 °C) with field ranging from –10 kOe to 10 kOe on a vibrating sample magnetometer (VSM) (CFMS, Cryogenic Ltd, Japan). To study composites' thermal stability thermogravimetric analysis (TGA) was conducted (Mettler Toledo TGA/SDTA851e, Switzerland) from 25 to 550 °C at a heating rate of 10 °C/min in nitrogen atmosphere. Nitrogen adsorption-desorption isotherms were obtained at -196 °C (Quantachrome Autosorb-1, USA) and subsequently used to determine Brunauer–Emmett–Teller (BET) surface area and average pore diameter of each composite. Sample pretreatment was performed at the absorber degassing station by purging the sample with helium and then evacuating to 10^{-5} Torr at 423 K.

Adsorption Studies

Prior to exploring photocatalytic activity of composites, their adsorption capacity was carefully examined. Namely, adsorption experiments implemented Congo Red anionic azo dye (CR) (Fig. S1*a*) as an organic pollutant which had to be removed from aqueous solution. While CR can exist both in protonated (below

the pH of 3.0, blue-colored solution) and unprotonated (above the pH of 5.2, red-colored solution) forms, the latter one exhibits ultraviolet-visible (UV-Vis) spectrum with a distinct -N=N- group peak at 498 nm. Therefore, a height of this peak was used to specifically monitor CR concentration in a solution with accordingly adjusted pH (above 6.0) via UV-V is spectrophotometer (Speks SSP-705, Spektroskopicheskie sistemy, Russian Federation). Before measuring UV-Vis spectra, each CR solution sample/aliquot was centrifuged at 11000 rpm for 4 minutes to isolate it from the composite particles. In case of kinetic observations magnetic separation of composites via strong neodymium magnet was preliminarily implemented. Finally, CR removal efficiency Re (%) and adsorption capacity q (mg/g) were denoted as follows:

$$Re = \frac{(C_0 - C)}{C_0} \times 100\%,$$

$$q = \frac{(C_0 - C)V}{m},$$

where C_0 (mg/L) is the initial CR concentration; C (mg/L) is CR concentration at a given time; V (L) is solution's volume and m (g) is composite's mass.

Effect of Composite Dosage

In a typical experiment, 10 mL of CR solution (60 mg/L, 25 °C), a specific dosage of selected composite (5, 10, 15, 20, 25, 30 mg) and a drop of 1M KOH solution (approx. 0.1 mL) were added into 50 mL conical flask, which was then placed on a reciprocating laboratory shaker PE-6500 (ECROSKHIM) for 45 minutes, after which samples of CR solution were taken. Throughout these experiments an optimal concentration of composite for subsequent studies was determined.

Effect of pH

Each experiment was started with 50 mL of CR solution (60 mg/L, 25 °C) and 100 mg of selected composite (2 g/L) being added to a 100 mL conical flask. Immediately after that, the conical flask was placed on the reciprocating laboratory shaker PE-6500 (ECROSKHIM) for 45 minutes, while CR solution's pH was adjusted and maintained accordingly by a drop-wise addition of 0.1M KOH solution. For pH readout a digital pH-meter pH-410 (AKVILON) with a combination pH electrode (Ag/AgCl reference system) was implemented. After 45 minutes had passed, samples of CR solution were taken. Ultimately, each composite's maximum adsorption capacity was evaluated.

Adsorption Kinetics

To observe adsorption kinetics a following adsorption experiment was conducted for each composite. Firstly, 50 mL of CR solution (60 mg/L, 25 °C) were poured into 150 mL (75×45 mm) crystallizing dish and a stir bar (ferrite rod in a glass ampule) was added. Magnetic stirrer MSH 300 (BioSan) was turned on and its speed was set at approximately 500 rpm. After that, 0.04 mL of glacial acetic acid was added into CR solution. According to the digital pH-meter pH-410 (AKVILON) with the combination pH electrode (Ag/AgCl reference system) a pH value of 3.5 was reached. In fact, this exact pH was subsequently used in photocatalytic degradation experiments, since it provided an optimal Fe^{2+}/Fe^{3+} ratio for Fenton reaction [47]. Lastly, 100 mg of selected composite (2 g/L) were added to CR solution, which marked experiment's starting point. Throughout the experiment, which lasted for 150 minutes, the crystallizing dish was covered with a hood that blocked off any incident light, thus excluding photocatalytic degradation as a contributing factor towards CR removal efficiency. Every 15 minutes, composite was mostly gathered at crystallizing dish's bottom via strong neodymium magnet and 2.5 mL aliquot was taken from CR solution. To separate the remaining small composite particles, this aliquot was centrifuged, and 2.0 mL of supernatant CR solution were carefully transferred into a separate test tube. After that, precisely 1 drop of 1M KOH solution was added to raise the pH above 6.0 and convert CR back into its unprotonated form for subsequent UV-Vis spectra measurement.

Photocatalytic Activity Study

The experiment to study the photocatalytic activity of each composite started with the same procedure used for observing adsorption kinetics. Namely, 50 mL of CR solution (60 mg/L, 25°C), 0.04 mL of glacial acetic acid and the stir bar were added into 150 mL (75×45 mm) crystallizing dish. The magnetic stirrer's speed was set at approximately 500 rpm and remained the same throughout whole experiment. The experiment's starting point was marked when 100 mg of selected composite (2 g/L) were added to the solution. In the first 45 minutes of the experiment the crystallizing dish was covered with a hood that blocked off any incident light. After 45 minutes had passed, the hood was removed and 1 mL of H_2O_2 30 % (176 mM) was

added to the solution. At the same time a 26W UV lamp (Camelion, 365 nm) was turned on and placed directly above the solution's surface at a distance of 1–2 cm. The experiment lasted a total time of 150 minutes, during which every 15 minutes 2.5 mL aliquots of CR solution were taken and treated identically to ones in observing adsorption kinetics. Finally, a control experiment was conducted using the same procedure but without the composite.

Results and Discussion

Characterization of Fe_3O_4/γ-Fe_2O_3@Fe-MOF Composites

Design Approach

Currently, there are four main techniques of obtaining composites which combine MOFs with magnetic particles (MPs): mixing pre-synthesized MPs with MOF, embedding MPs into MOF's pores, encapsulation of MP with an interface material that promotes MOF application, layer-by-layer growth of MOF coating directly on MP's surface [48]. In this study, the latter technique was implemented to obtain Fe_3O_4/γ-Fe_2O_3@MIL-88b(Fe) and Fe_3O_4/γ-Fe_2O_3@NH_2-MIL-88b(Fe) composites, where Fe_3O_4/γ-Fe_2O_3 particles enable magnetic separation, and Fe-MOF coating exhibits photocatalytic activity. Since BDCa and NH_2-BDCa were added before $[Fe_3(\mu_3\text{-}O)(CH_3COO)_6(H_2O)_3]Cl\cdot 6H_2O$ cluster, they effectively functionalized Fe_3O_4/γ-Fe_2O_3 particles' surface, enabling subsequent layer-by-layer growth of MOF coating [48].

Usually, a standard technique for MOF creation utilizes metal salts to generate inorganic nodes during MOF's self-assembly process. However, if MOF incorporates Fe_3-μ_3-O or similar clusters as inorganic nodes, they may not be generated sufficiently, thus altering MOF's structure [49] and producing polycrystalline and amorphous structures [50]. Therefore, in this study Fe-MOFs were constructed by a rational approach of using pre-synthesized Fe_3-μ_3-O acetate clusters as secondary building units [42–45]. Moreover, Fe_3-μ_3-O clusters' geometry strictly determined the coordination of BDC or NH_2-BDC linkers, which produced isoreticular Fe-MOFs with desired topology [51, 52].

Elemental analysis

The total composition of the synthesized composites was determined by elemental analysis (Table 1).

Table 1

C, H, N, Fe, O contents (wt. %) of Fe-MOFs and synthesized composites

Sample	C	H	N	Fe	O
MIL-88b(Fe)[53]	36.4	5.6	–	21.3	36.6
MIL-88b(Fe)[42]	38.5	2.6	–	22.3	36.6
NH_2-MIL-88b(Fe)[42]	36.6	3.0	4.6	22.3	33.5
Fe_3O_4/γ-Fe_2O_3@MIL-88b(Fe)	21.1	3.0	–	33.9	41.4
Fe_3O_4/γ-Fe_2O_3@NH_2-MIL-88b(Fe)	14.1	2.4	1.3	39.6	42.6

In contrast with isolated MIL-88b(Fe) [53] and NH_2-MIL-88b(Fe) [42], carbon content has decreased to 14.1–21.1 wt. % and iron content has increased to 33.9–39.6 wt. %, which confirms the presence of both Fe_3O_4/γ-Fe_2O_3 particles and Fe-MOFs in composites' structure. According to carbon content data, the mass fraction of Fe-MOF coating amounted to 57.8±1.5 % in Fe_3O_4/γ-Fe_2O_3@MIL-88b(Fe) composite, which was approximately 20 % more than in the Fe_3O_4/γ-Fe_2O_3@NH_2-MIL-88b(Fe) (38.5±1.5 %).

FTIR Spectra

To further confirm composites' structure, FTIR spectra of Fe_3O_4/γ-Fe_2O_3@MIL-88b(Fe) (Fig. 1*a*) and Fe_3O_4/γ-Fe_2O_3@NH_2-MIL-88b(Fe) (Fig. 1*b*) were compared with ones of Fe_3O_4, Fe-MOFs and organic linkers. The bands at 1542–1561 cm-1 and 1376–1407 cm-1 corresponded to asymmetric and symmetric stretching vibrations of Fe-bound carboxylate groups in Fe-MOFs, respectively. Additionally, C-H stretching and bending vibrations in aromatic rings of organic linkers were represented by the bands at 2928–2933 cm-1 and 728–768 cm^{-1}, respectively. The band at 555–564 cm^{-1} was ascribed to Fe-O stretching vibrations both in Fe_3O_4 and Fe-MOFs. For NH_2-MIL-88b(Fe) (Figure 1b) symmetric and asymmetric stretching vibrations of the -NH_2 group were represented by the two bands at 3455 cm-1 and 3373 cm-1, respectively, while the band at 1249 cm-1 was due to C-N stretching vibration [54]. These characteristic bands of Fe_3O_4 and Fe-MOFs were also inherent in composites, which ultimately confirmed their structure.

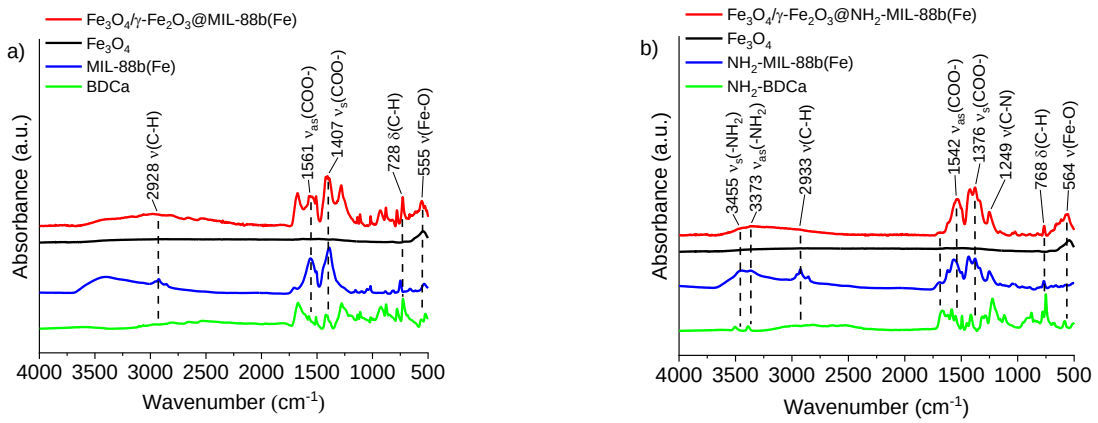

Figure 1. FTIR spectra of $Fe_3O_4/\gamma\text{-}Fe_2O_3$@MIL-88b(Fe) (*a*) and $Fe_3O_4/\gamma\text{-}Fe_2O_3$@$NH_2$-MIL-88b(Fe) (*b*), Fe_3O_4, Fe-MOFs and organic linkers

XRD patterns

Since Fe_3O_4 underwent partial oxidation into $\gamma\text{-}Fe_2O_3$ during composite synthesis, XRD patterns were recorded (Fig. 2) to determine the actual ratio of Fe(II) and Fe(III) (i.e. x = Fe(II)/Fe(III)) in $Fe_3O_4/\gamma\text{-}Fe_2O_3$ particles. Both of Fe_3O_4 and $\gamma\text{-}Fe_2O_3$ are inherently cubic phases with identical (311), (400), (422), (511), (440) reflections and slightly different unit cell length a values [55, 56]. As a consequence, there is a little offset between Fe_3O_4 and $\gamma\text{-}Fe_2O_3$ reflection peaks. In case of $Fe_3O_4/\gamma\text{-}Fe_2O_3$ particles, this offset can be exploited for determining the average a value:

$$a = \frac{\lambda}{2*\sin\left(\frac{2\theta}{2}\right)}\sqrt{\left(h^2+k^2+l^2\right)}, \tag{5}$$

where λ is radiation source wavelength; h, k, l are Miller indices. Using known values of x = 0.5, a = 8.335–8.340 Å for Fe_3O_4 (ICDD–PDF 19-629) and x = 0, a = 8.396–8.400 Å for $\gamma\text{-}Fe_2O_3$ (ICDD–PDF 39-1346), the average a was converted into the actual Fe(II)/Fe(III) ratio in $Fe_3O_4/\gamma\text{-}Fe_2O_3$ particles of $Fe_3O_4/\gamma\text{-}Fe_2O_3$@MIL-88b(Fe) and $Fe_3O_4/\gamma\text{-}Fe_2O_3$@$NH_2$-MIL-88b(Fe) composites (Table 2). Finally, the Fe_3O_4 content was 22.7 wt. % and 72.2 wt. % for $Fe_3O_4/\gamma\text{-}Fe_2O_3$ particles in $Fe_3O_4/\gamma\text{-}Fe_2O_3$@MIL-88b(Fe) and $Fe_3O_4/\gamma\text{-}Fe_2O_3$@$NH_2$-MIL-88b(Fe), respectively.

Table 2

Average unit cell length *a* (Å), Fe(II)/Fe(III) *x* ratio and Fe_3O_4 content (wt. %) for $Fe_3O_4/\gamma\text{-}Fe_2O_3$ particles in the composites

Sample	*a*	*x*	Fe_3O_4
$Fe_3O_4/\gamma\text{-}Fe_2O_3$@MIL-88b(Fe)	8.346	0.094	22.7
$Fe_3O_4/\gamma\text{-}Fe_2O_3$@$NH_2$-MIL-88b(Fe)	8.375	0.332	72.2

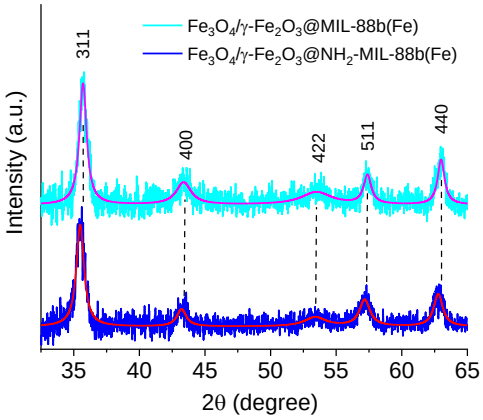

Figure 2. XRD patterns of $Fe_3O_4/\gamma\text{-}Fe_2O_3$@MIL-88b(Fe) and $Fe_3O_4/\gamma\text{-}Fe_2O_3$@$NH_2$-MIL-88b(Fe) composites

It should be noted that reflections intrinsic to MIL-88b(Fe) and NH_2-MIL-88b(Fe) (Fig. S2) were not present in the 5–30° range of the recorded XRD patterns. Supposedly, guest-responsive structural flexibility [57–59] induces Fe-MOFs' breathing phenomenon [53, 60, 61], which ultimately alters unit cell volume of Fe-MOFs during solvation and desolvation processes. Therefore, it was proposed that MIL-88b(Fe) and NH_2-MIL-88b(Fe) reflections have shifted towards unrecorded small angles. Previously, it was shown for MIL-88b(Fe) that water molecules cause reorientation of Fe_3-μ_3-O clusters and BDC linkers via rotation about the O-O axis in carboxylate groups [62]. In this regard, MIL-88B(Fe)/Fe_3S_4 [63] and MIL-88b/nanorods [53] composites exhibit similar behavior.

Magnetization Curves

To study the effect of Fe-MOF coating on $Fe_3O_4/\gamma\text{-}Fe_2O_3$ particles' magnetic properties, magnetization curves for $Fe_3O_4/\gamma\text{-}Fe_2O_3$@MIL-88b(Fe) and $Fe_3O_4/\gamma\text{-}Fe_2O_3$@$NH_2$-MIL-88b(Fe) composites were recorded (Fig. 3).

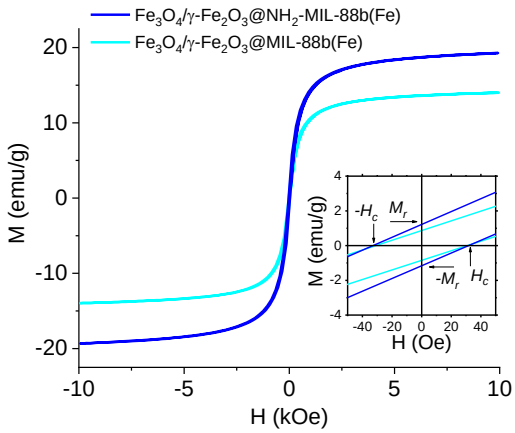

Figure 3. Magnetization curves of $Fe_3O_4/\gamma\text{-}Fe_2O_3$@MIL-88b(Fe) and $Fe_3O_4/\gamma\text{-}Fe_2O_3$@$NH_2$-MIL-88b(Fe) composites at room temperature (25 °C)

As expected [64–66], magnetic hysteresis was retained for ferromagnetic $Fe_3O_4/\gamma\text{-}Fe_2O_3$ particles in both composites. For quantitative analysis saturation magnetization Ms, remanent magnetization Mr and coercivity Hc were extracted from composite magnetization curves (Table 3). In contrast with isolated Fe_3O_4 and $\gamma\text{-}Fe_2O_3$ particles saturation magnetization has decreased to 14-19 emu/g as a result of non-magnetic Fe-MOF coating being present. Since Ms value of $Fe_3O_4/\gamma\text{-}Fe_2O_3$@MIL-88b(Fe) composite was approximately 25 % smaller than that of $Fe_3O_4/\gamma\text{-}Fe_2O_3$@$NH_2$-MIL-88b(Fe), an inverse correlation between saturation magnetization and Fe-MOF's mass fraction has been established by elemental analysis. Similarly, remanent magnetization values were 0.9 and 1.2 emu/g for $Fe_3O_4/\gamma\text{-}Fe_2O_3$@MIL-88b(Fe) and $Fe_3O_4/\gamma\text{-}Fe_2O_3$@$NH_2$-MIL-88b(Fe), respectively. Both composites exhibited identical reduced coercivity of 33 Oe. Finally, saturation magnetization values were sufficient to perform magnetic separation of composites from aqueous solution using a strong neodymium magnet.

Table 3

Saturation magnetization M_s (emu/g), remanent magnetization M_r (emu/g) and coercivity H_c (Oe) of Fe_3O_4, $\gamma\text{-}Fe_2O_3$ and synthesized composites

Sample	M_s	M_r	H_c
Fe_3O_4 [64,65]	70-80	4-7	70
$\gamma\text{-}Fe_2O_3$ [65,66]	50-70	4-7	50
$Fe_3O_4/\gamma\text{-}Fe_2O_3$@MIL-88b(Fe)	14	0.9	33
$Fe_3O_4/\gamma\text{-}Fe_2O_3$@$NH_2$-MIL-88b(Fe)	19	1.2	33

TGA Profiles

Thermostability of Fe_3O_4/Fe_2O_3@MIL-88b(Fe) and $Fe_3O_4/\gamma\text{-}Fe_2O_3$@$NH_2$-MIL-88b(Fe) was assessed using TGA profiles (Fig. 4a). Both composites exhibited similar TGA profiles with three main weight loss steps. The high-volatility first step (up to 220-230 °C) was due to guest water molecules being released from

Fe-MOF coating. The second step (up to 384-406 °C) was assumed to represent the decarboxylation of -COO- groups in organic linkers [34]. The third step lasted up to 525 °C and was associated with irreversible degradation of Fe-MOFs' structure. To further quantify composite thermostability, TGA derivative (dTGA) profiles were plotted (Fig. 4b) to determine the temperatures of maximum weight loss rates T_{max1}, T_{max2} (above 300 °C), T_{max3} (above 440 °C) for each TGA step (Table 4). In contrast to Fe_3O_4/Fe_2O_3@MIL-88b(Fe), a slight increase in T_{max2} value was observed for Fe_3O_4/γ-Fe_2O_3@NH_2-MIL-88b(Fe), which may be attributed to $–NH_2$ group engagement in electrostatic and hydrogen bond interactions. In fact, NH_2-MIL-88b(Fe) also possessed a higher T_{max2} value than MIL-88b(Fe). After TGA completion a larger final weight was observed for Fe_3O_4/γ-Fe_2O_3@NH_2-MIL-88b(Fe) composite (Table 4), which could be partially related to the smaller mass fraction of Fe-MOF coating.

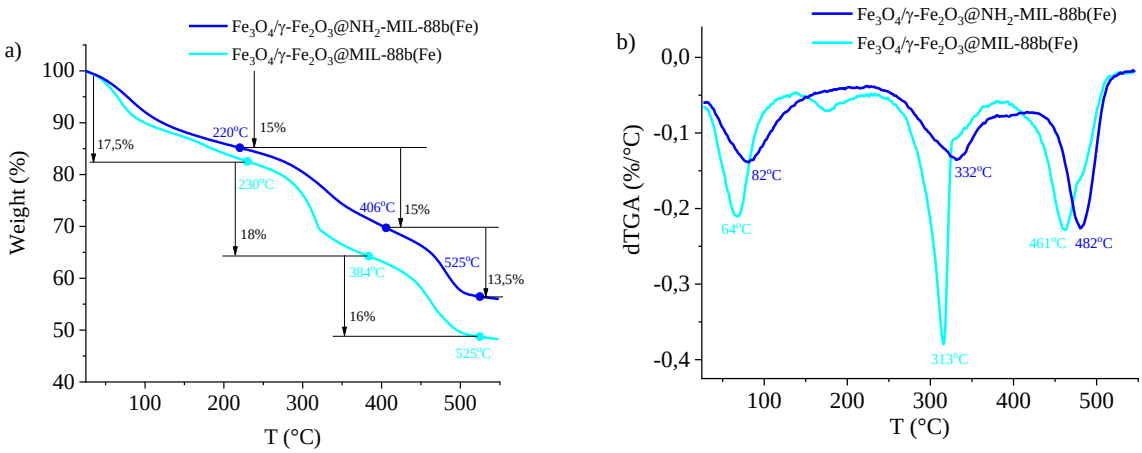

Figure 4. TGA (*a*) and dTGA (*b*) profiles of Fe_3O_4/γ-Fe_2O_3@MIL-88b(Fe) and Fe_3O_4/γ-Fe_2O_3@NH_2-MIL-88b(Fe) composites at a heating rate of 10 °C/min

Table 4

Temperatures of maximum weight loss rates T_{max1}, T_{max2}, T_{max3} (°C) and final weight FW (%) of Fe-MOFs and synthesized composites

Sample	T_{max1}	T_{max2}	T_{max3}	*FW*
MIL-88b(Fe) [42]	60	328	462	49
NH_2-MIL-88b(Fe) [42]	61	346	450	56
Fe_3O_4/γ-Fe_2O_3@MIL-88b(Fe)	64	313	461	48
Fe_3O_4/γ-Fe_2O_3@NH_2-MIL-88b(Fe)	82	332	482	56

Nitrogen Adsorption-Desorption Isotherms

To study composite porosity, nitrogen adsorption-desorption isotherms were obtained for Fe_3O_4/γ-Fe_2O_3@MIL-88b(Fe) and Fe_3O_4/γ-Fe_2O_3@NH_2-MIL-88b(Fe) at –196 °C (Fig. 5). Before the measurement of nitrogen adsorption-desorption isotherm, each composite was pretreated at 150 °C for 2 hours. According to IUPAC classification the composites exhibited type IV nitrogen adsorption-desorption isotherms, suggesting Fe-MOF mesoporous structure. The hysteresis loop, specific for capillary condensation in the mesopores, was apparent for both Fe_3O_4/γ-Fe_2O_3@MIL-88b(Fe) and Fe_3O_4/γ-Fe_2O_3@NH_2-MIL-88b(Fe).

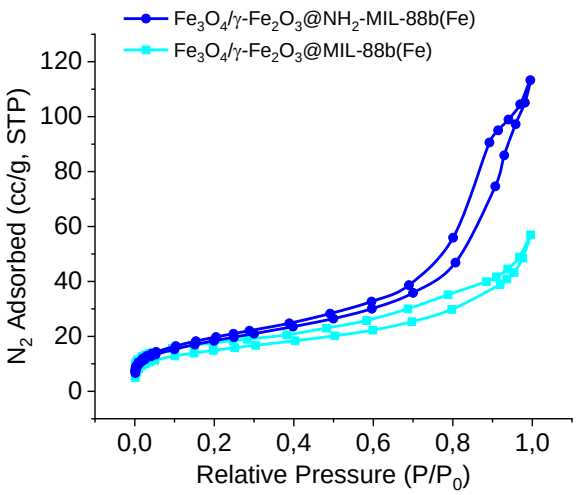

Figure 5. Nitrogen adsorption-desorption isotherms of Fe_3O_4/γ-Fe_2O_3@MIL-88b(Fe) and Fe_3O_4/γ-Fe_2O_3@NH_2-MIL-88b(Fe) composites at -196 °C

Ultimately, the composite BET surface area S_{BET}, as well as Barret-Joyner-Halenda (BJH) pore volume V and average diameter d were determined (Table 5). Additionally, t-plot method was implemented to assess micropore volume V_{micro} and surface area S_{micro} (Table 5). The S_{BET} values of Fe_3O_4/γ-Fe_2O_3@MIL-88b(Fe) and Fe_3O_4/γ-Fe_2O_3@NH_2-MIL-88b(Fe) were 54 and 68 m^2/g, respectively. Depending on synthesis methodology MIL-88b(Fe) and NH_2-MIL-88b(Fe) BET surface can range from 14 to 303 m^2/g [26, 42, 67]. In comparison with isolated Fe-MOFs, reduced S_{BET} values of the composites may be attributed to partial encapsulation of Fe_3O_4/γ-Fe_2O_3 particles inside Fe-MOFs' pores during synthesis. Nevertheless, Fe_3O_4/γ-Fe_2O_3@NH_2-MIL-88b(Fe) expectably possessed slightly increased S_{BET}, V, d values than those of Fe_3O_4/γ-Fe_2O_3@MIL-88b(Fe) [68].

Table 5

BET surface area S_{BET} (m^2/g), BJH pore volume V (cm^3/g) and diameter d (nm), t-plot micropore volume V_{micro} (cm^3/g) and surface area S_{micro} (m^2/g) of Fe-MOFs and synthesized composites

Sample	S_{BET}	V	d	V_{micro}	S_{micro}
MIL-88b(Fe) [26]	165	0.2	-	-	-
MIL-88b(Fe) [42]	303	0.34	2.6	-	-
NH_2-MIL-88b(Fe) [42]	191	0.65	6.77	-	-
NH_2-MIL-88b(Fe) [67]	14	-	-	-	-
Fe_3O_4/γ-Fe_2O_3@MIL-88b(Fe)	54	0.07	3.5	0.003	7.3
Fe_3O_4/γ-Fe_2O_3@NH_2-MIL-88b(Fe)	68	0.17	8.8	0.001	5.7

Adsorption and Photocatalytic Degradation

Effects of Composite Dosage and pH

To determine the optimal composite concentration for subsequent studies, the CR removal efficiency Re was initially monitored at different Fe3O4/γ-Fe_2O_3@MIL-88b(Fe) and Fe_3O_4/γ-Fe_2O_3@NH_2-MIL-88b(Fe) dosages (Fig. 6). As expected, with increasing dosage a gradual rise in CR removal efficiency was observed with an inflection point present at around 15–20 mg for both composites. More importantly, lower dosages increased an error margin for Re values, while elevated Re values at higher dosages limited further assessment of photocatalytic activity. Therefore, an optimal concentration of composite was determined to be 2 g/L, during which a moderate 40–60 % CR removal efficiency was observed.

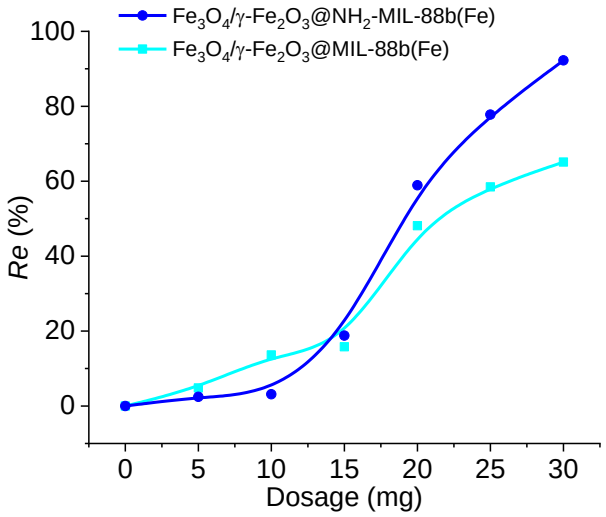

Figure 6. The effect of composite dosage on the CR removal efficiency *Re* for Fe_3O_4/γ-Fe_2O_3@MIL-88b(Fe) and Fe_3O_4/γ-Fe_2O_3@NH_2-MIL-88b(Fe) composites

To evaluate each composite maximum adsorption capacity *q*, CR removal efficiency *Re* was monitored in the pH range of 5 to 12 for Fe_3O_4/γ-Fe_2O_3@MIL-88b(Fe) and Fe_3O_4/γ-Fe_2O_3@NH_2-MIL-88b(Fe) (Fig. 7). In contrast with Fe_3O_4/γ-Fe_2O_3@MIL-88b(Fe), higher *Re* values were generally observed for Fe_3O_4/γ-Fe_2O_3@NH_2-MIL-88b(Fe), porous structure of which supposedly exhibited better stability due to dispersion interactions between -NH_2 groups and was therefore more accessible [69].

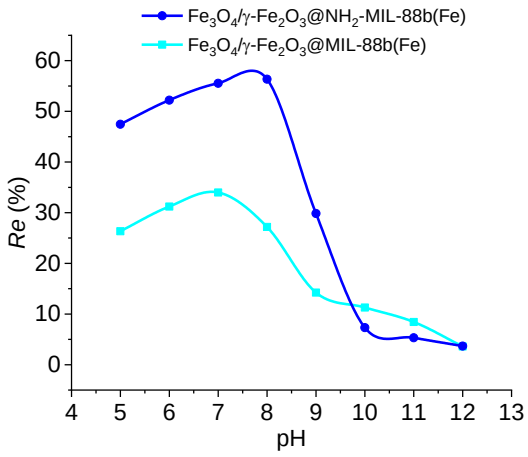

Figure 7. The effect of solution pH on the CR removal efficiency *Re* for Fe_3O_4/γ-Fe_2O_3@MIL-88b(Fe) and Fe_3O_4/γ-Fe_2O_3@NH_2-MIL-88b(Fe) composites

Additionally, Fe_3O_4/γ-Fe_2O_3@MIL-88b(Fe) and Fe_3O_4/γ-Fe_2O_3@NH_2-MIL-88b(Fe) adsorption capacities peaked at 10.2 mg/g with pH of 7 and 16.9 mg/g with pH of 8, respectively. These maxima occurrence can be explained by composite surface Zeta potential. Reportedly, Zhao X. and colleagues have evaluated that the point of zero charge *pzc* for NH_2-MIL-101(Cr) (which partially resembles MIL-88b(Fe) and NH_2-MIL-88b(Fe) structures) occurs at slightly basic pH (7.8), whereas at lower pH its surface charges positively [70]. Assuming that *pzc* for Fe_3O_4/γ-Fe_2O_3@MIL-88b(Fe) also occurs at slightly basic pH (8), a pH of 7 positively charges composite surface [71], which then electrostatically attracts CR molecules via negatively charged -SO_3^- groups, thus a peak *Re* value is reached. A decrease in *Re* values at acidic pH may be caused by neutral or repelling interactions between positively charged composite surface and CR zwitterions [72] or CR protonated molecules, respectively. Lastly, *Re* values dropped significantly at basic pH possibly due to electrostatic repulsion between negatively charged -SO_3^- groups of CR molecules and -COO^- groups in BDC linkers. Similar assumptions can be made for Fe_3O_4/γ-Fe_2O_3@NH_2-MIL-88b(Fe) with *pzc* at pH of

9. However, at basic pH donor mesomeric effect, inherent in -NH_2 groups, causes *Re* values to diminish faster.

Adsorption Kinetics and Photocatalytic Activity

To observe adsorption kinetics and study photocatalytic activity of the composites, a change in CR normalized concentration C/C_0 over time t was monitored during photodegradation via H_2O_2 and UV irradiation (H_2O_2+UV), isolated adsorption (composite) and photocatalytic degradation (composite+H_2O_2+UV) for Fe_3O_4/γ-Fe_2O_3@MIL-88b(Fe) and Fe_3O_4/γ-Fe_2O_3@NH_2-MIL-88b(Fe) (Fig. 8). The H_2O_2+UV system was the least effective since its removal efficiency Re peaked at 15 %. During isolated adsorption Fe_3O_4/γ-Fe_2O_3@MIL-88b(Fe) and Fe_3O_4/γ-Fe_2O_3@NH_2-MIL-88b(Fe) performed almost identically with Re values reaching 38-44 %. Nevertheless, when each composite, H_2O_2 and UV irradiation were utilized simultaneously, Fenton-like reaction occurred [34], which generated highly reactive hydroxyl radicals for CR degradation. As a result, during CR photocatalytic degradation both composite+H_2O_2+UV systems demonstrated even higher Re values of 89 % and 95 % for Fe_3O_4/γ-Fe_2O_3@MIL-88b(Fe) and Fe_3O_4/γ-Fe_2O_3@NH_2-MIL-88b(Fe), respectively. Moreover, a higher photocatalytic activity was observed for Fe_3O_4/γ-Fe_2O_3@NH_2-MIL-88b(Fe) with a Re value reaching 88 % in 15 minutes, whereas Fe_3O_4/γ-Fe_2O_3@MIL-88b(Fe) required more than 1.5 hours for Re value to reach 89 %. Supposedly, -NH_2 group increases the electron density on the aryl ring, which stabilizes hole localization at the organic linker, increases photoexcited state lifetime and promotes electron transfer onto metal center in Fe_3-μ_3-O cluster [73]. Therefore, Fe_3O_4/γ-Fe_2O_3@NH_2-MIL-88b(Fe) generated more hydroxyl radicals and degraded CR faster, than Fe_3O_4/γ-Fe_2O_3@MIL-88b(Fe).

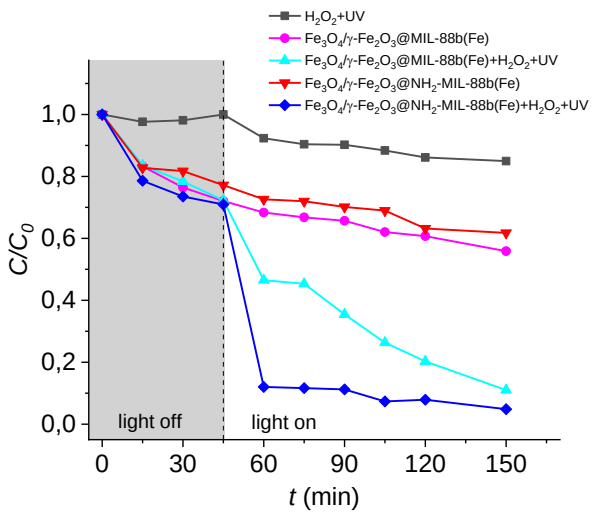

Figure 8. Adsorption kinetics and photocatalytic activity of Fe_3O_4/γ-Fe_2O_3@MIL-88b(Fe) and Fe_3O_4/γ-Fe_2O_3@NH_2-MIL-88b(Fe) composites

To quantify photocatalytic degradation kinetics, the pseudo-first-order model can be implemented:

$$\ln\left(\frac{C}{C_0}\right) = -k \cdot t, \tag{6}$$

where *k* is photodegradation rate constant. The resulting *k* values for Fe_3O_4/γ-Fe_2O_3@MIL-88b(Fe) and Fe_3O_4/γ-Fe_2O_3@NH_2-MIL-88b(Fe) were 0.013±0.001 min^{-1} and 0.023±0.002 min^{-1}, respectively. According to previous studies, *k* value depends not only on the type of photocatalyst used, but is also highly reliant on the incident photon energy from particular irradiation source. For example, if Rhodamine B was degraded under visible light in presence of MIL-88A(Fe)[74], MIL-88A@GO and MIL-88A@polyacrylate composites [75], the resulting *k* values were 0.0793 min^{-1} (natural sunlight), 0.0645 min^{-1} and 0.0726 min^{-1} (500W Xe lamp with UV cutoff filter) (Table S1), respectively. When visible light was replaced by UV irradiation, the *k* value for MIL-88A(Fe) quadrupled [76], reaching 0.461 min^{-1} (9W UVA lamp). Therefore, in comparison with homogeneous Fenton [77] and heterogeneous SnO_2–Fe_3O_4 [78] and $MgFe_2O_4$ [79] systems with UV irradiation (Table S1), Fe_3O_4/γ-Fe_2O_3@MIL-88b(Fe) and Fe_3O_4/γ-Fe_2O_3@NH_2-MIL-88b(Fe) were acceptable photocatalysts, since they exhibited similar rate constants and higher *Re* values.

Cyclability of Composites

To analyze the possibility of Fe-MOF coating peeling off from Fe_3O_4/γ-Fe_2O_3 particles surface, we decided to carry out three consecutive photocatalysis cycles in the same conditions (Fig. 9). After first and second photocatalysis cycles each composite was magnetically separated from the solution, washed with distilled water (200 mL) and dried in a vacuum (10^{-3} Torr, 50 °C. 5 h). As a result, Fe_3O_4/γ-Fe_2O_3@MIL-88b(Fe) demonstrated poor stability since *Re* decreased from 89 % in first cycle to 29 % in third cycle (Fig. 9). In contrast with Fe_3O_4/γ-Fe_2O_3@MIL-88b(Fe), a smaller drop in photocatalytic activity was observed for Fe_3O_4/γ-Fe_2O_3@NH_2-MIL-88b(Fe) composite, which resulted in Re decreasing from 95 % in first cycle to 69 % in third cycle (Fig. 9), suggesting slower peeling of NH_2-MIL-88b(Fe). This observation was additionally confirmed by comparing FTIR spectra of dried composites before each cycle, where a drop in Fe-bound carboxylate group bands (1376-1561 cm^{-1}) intensity for Fe_3O_4/γ-Fe_2O_3@MIL-88b(Fe) composite (Fig. S3a) was more rapid than that of Fe_3O_4/γ-Fe_2O_3@NH_2-MIL-88b(Fe) (Fig. S3b). Ultimately, Fe_3O_4/γ-Fe_2O_3@NH_2-MIL-88b(Fe) composite has demonstrated better cyclability than Fe_3O_4/γ-Fe_2O_3@MIL-88b(Fe).

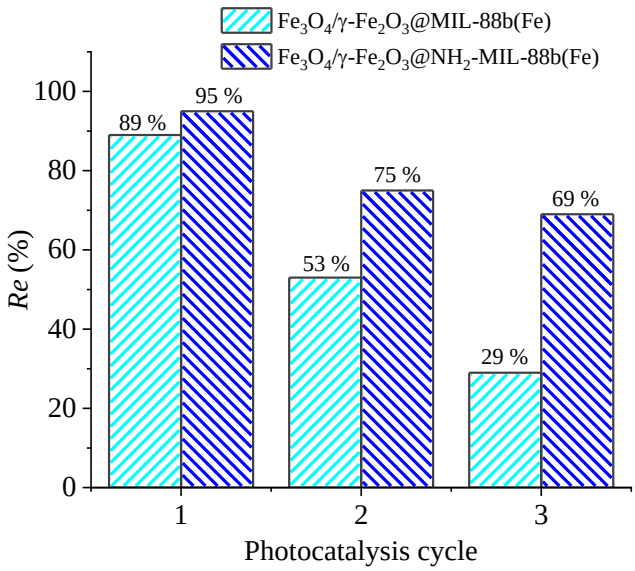

Figure 9. Removal efficiency Re of CR dye for Fe_3O_4/γ-Fe_2O_3@MIL-88b(Fe) and Fe_3O_4/γ-Fe_2O_3@NH_2-MIL-88b(Fe) composites during three consecutive photocatalysis cycles

Conclusions

In this study, Fe_3O_4/Fe_2O_3@MIL-88b(Fe) and Fe_3O_4/γ-Fe_2O_3@NH_2-MIL-88b(Fe) composites were obtained, where Fe_3O_4/γ-Fe_2O_3 particles enabled magnetic separation, and Fe-MOF coating exhibited photocatalytic activity. Fe-MOFs were constructed through rational approach of utilizing pre-synthesized Fe_3-μ_3-O acetate clusters as secondary building units, geometry of which strictly determined the coordination of BDC or NH_2-BDC linkers. The elemental analysis and FTIR spectra confirmed the presence of both Fe_3O_4/γ-Fe_2O_3 particles and Fe-MOFs in composites structure. Using composites XRD patterns, the Fe_3O_4 content was determined to be 22.7 wt. % and 72.2 wt. % for Fe_3O_4/γ-Fe_2O_3 particles in Fe_3O_4/γ-Fe_2O_3@MIL-88b(Fe) and Fe_3O_4/γ-Fe_2O_3@NH_2-MIL-88b(Fe), respectively. Magnetization curves of Fe_3O_4/γ-Fe_2O_3@MIL-88b(Fe) and Fe_3O_4/γ-Fe_2O_3@NH_2-MIL-88b(Fe) specified saturation magnetization M_s of 14–19 emu/g, remanent magnetization M_r of 0.9-1.2 emu/g and coercivity H_c of 33 Oe. All these values were lower than those of isolated Fe_3O_4 and γ-Fe_2O_3 particles, but the M_s composites values were sufficient for magnetic separation. TGA profiles for Fe_3O_4/γ-Fe_2O_3@MIL-88b(Fe) and Fe_3O_4/γ-Fe_2O_3@NH_2-MIL-88b(Fe) exhibited three main weight loss steps, where every second step had the maximum weight loss rate above 300 °C and was attributed to the decarboxylation of -COO^- groups in organic linkers. Both Fe_3O_4/γ-Fe_2O_3@MIL-88b(Fe) and Fe_3O_4/γ-Fe_2O_3@NH_2-MIL-88b(Fe) exhibited type IV nitrogen adsorption-desorption isotherms, suggesting Fe-MOFs mesoporous structure, and their S_{BET} values were 54 and 68 m^2/g, respectively. In contrast with Fe_3O_4/γ-Fe_2O_3@MIL-88b(Fe), higher Re values were generally observed for Fe_3O_4/γ-Fe_2O_3@NH_2-MIL-88b(Fe), porous structure of which supposedly exhibited better stability due to

dispersion interactions between -NH_2 groups and was therefore more accessible. Additionally, Fe_3O_4/γ-Fe_2O_3@MIL-88b(Fe) and Fe_3O_4/γ-Fe_2O_3@NH_2-MIL-88b(Fe) adsorption capacities peaked at 10.2 mg/g with pH of 7 and 16.9 mg/g with pH of 8, respectively. When each composite, H_2O_2 and UV irradiation were utilized simultaneously, Fenton-like reaction occurred, which generated highly reactive hydroxyl radicals for CR degradation. As a result, during CR photocatalytic degradation high *Re* values of 89 % and 95 % were achieved for Fe_3O_4/γ-Fe_2O_3@MIL-88b(Fe) and Fe_3O_4/γ-Fe_2O_3@NH_2-MIL-88b(Fe), respectively. Moreover, a higher photocatalytic activity was observed for Fe_3O_4/γ-Fe_2O_3@NH_2-MIL-88b(Fe), supposedly, due to -NH_2 group increasing the electron density on the aryl ring, which stabilized hole localization at the organic linker, increased photoexcited state lifetime and promoted electron transfer onto metal center in Fe_3-μ_3-O cluster. Therefore, Fe_3O_4/γ-Fe_2O_3@NH_2-MIL-88b(Fe) generated more hydroxyl radicals and degraded CR faster, than Fe_3O_4/γ-Fe_2O_3@MIL-88b(Fe). Finally, when compared to homogeneous Fenton and SnO_2–Fe_3O_4 and $MgFe_2O_4$ heterogeneous systems, Fe_3O_4/γ-Fe_2O_3@MIL-88b(Fe) and Fe_3O_4/γ-Fe_2O_3@NH_2-MIL-88b(Fe) exhibited similar rate constants and higher Re values. Ultimately, Fe_3O_4/γ-Fe_2O_3@NH_2-MIL-88b(Fe) composite has demonstrated better cyclability than Fe_3O_4/γ-Fe_2O_3@MIL-88b(Fe).

Supporting Information

The Supporting Information is available free at https://ejc.buketov.edu.kz/index.php/ejc/article/view/130/93

Funding

This work has been carried out in accordance with the state tasks, state registration 124013100858-3, 124013000757-0 and 124020800013-7 using the equipment of the Multi-User Analytical Center of FRC PCP and MC RAS.

*Author Information**

**The authors' names are presented in the following order: First Name, Middle Name and Last Name*

Vladislav Lvovich Sidorov — Graduate student of Department of Fundamental Physical and Chemical Engineering, Lomonosov Moscow State University, 119991, Moscow, Russia; Laboratory Assistant, Federal Research Center of Problems of Chemical Physics and Medicinal Chemistry, Russian Academy of Sciences, 142432, Chernogolovka, Moscow region, Russia; e-mail: bobik_132@mail.ru

Rose Kurmangalievna Baimuratova *(corresponding author)* — Candidate of Chemical Sciences, Junior Researcher, Federal Research Center of Problems of Chemical Physics and Medicinal Chemistry, Russian Academy of Sciences, 142432, Chernogolovka, Moscow region, Russia; e-mail: roz_baz@mail.ru; https://orcid.org/0000-0002-8389-6871

Denis Vladimirovich Korchagin — Candidate of Chemical Sciences, Leading Researcher, Federal Research Center of Problems of Chemical Physics and Medicinal Chemistry, Russian Academy of Sciences, 142432, Chernogolovka, Moscow region, Russia; e-mail: korden@icp.ac.ru; https://orcid.org/0000-0002-0199-1382

Andrey Vladimirovich Ivanov — Candidate of Chemical Sciences, Senior Researcher, Federal Research Center of Problems of Chemical Physics and Medicinal Chemistry, Russian Academy of Sciences, 142432, Chernogolovka, Moscow region, Russia; e-mail: dzhardim@icp.ac.ru

Kamila Asylbekovna Kydralieva — Doctor of Chemical Sciences, Professor Employment, Moscow Aviation Institute (National Research University), 125993, Moscow, Russia; e-mail: kydralievaka@mai.ru; https://orcid.org/0000-0002-4596-4140

Gulzhian Iskakovna Dzhardimalieva — Doctor of Chemical Sciences, Head of Laboratory of Metallopolymers, Federal Research Center of Problems of Chemical Physics and Medicinal Chemistry, Russian Academy of Sciences, 142432, Chernogolovka, Moscow region, Russia; e-mail: g_dzhardim@mail.ru; https://orcid.org/0000-0002-4727-8910

Author Contributions

The manuscript was written through contributions of all authors. All authors have given approval to the final version of the manuscript. CRediT: **Vladislav Lvovich Sidorov**: investigation, methodology, visualiza-

tion, writing — original draft, formal analyses; **Rose Kurmangalievna Baimuratova**: investigation, conceptualization, validation, writing — original draft; **Denis Vladimirovich Korchagin**: investigation, software, formal analyses; **Andrey Vladimirovich Ivanov**: investigation, methodology, data curation; **Kamila Asylbekovna Kydralieva**: methodology, data curation; **Gulzhian Iskakovna Dzhardimalieva**: conceptualization, methodology, writing — review & editing, supervision.

Conflicts of Interest

All authors declare that they have no conflicts of interest.

References

1 Ihmels, H. (2019). Dyes in modern organic chemistry. *Beilstein Journal of Organic Chemistry*, *15*, 2798–2800. https://doi.org/10.3762/bjoc.15.272

2 Qadri, R., & Faiq, M. A. (2020). Freshwater Pollution: Effects on Aquatic Life and Human Health. In: Qadri, H., Bhat, R., Mehmood, M., Dar, G. (eds). *Fresh Water Pollution Dynamics and Remediation* (Pp. 15–26). Springer Singapore. https://doi.org/10.1007/978-981-13-8277-2_2

3 Pizzicato, B., Pacifico, S., Cayuela, D., Mijas, G., & Riba-Moliner, M. (2023). Advancements in Sustainable Natural Dyes for Textile Applications: A Review. *Molecules*, *28*(16), 5954. https://doi.org/10.3390/molecules28165954

4 Murcia, M. D., Gómez, M., Gómez, E., Gómez, J. L., & Christofi, N. (2011). Photodegradation of congo red using XeBr, KrCl and Cl2 barrier discharge excilamps: A kinetics study. *Desalination*, *281*, 364–371. https://doi.org/10.1016/j.desal.2011.08.011

5 Jin, X.-C., Liu, G.-Q., Xu, Z.-H., & Tao, W.-Y. (2007). Decolorization of a dye industry effluent by Aspergillus fumigatus XC6. *Applied Microbiology and Biotechnology*, *74*(1), 239–243. https://doi.org/10.1007/s00253-006-0658-1

6 Swan, N. B., & Zaini, M. A. A. (2019). Adsorption of Malachite Green and Congo Red Dyes from Water: Recent Progress and Future Outlook. *Ecological Chemistry and Engineering S*, *26*(1), 119–132. https://doi.org/10.1515/eces-2019-0009

7 Hanafi, M. F., & Sapawe, N. (2020). A review on the current techniques and technologies of organic pollutants removal from water/wastewater. *Materials Today: Proceedings*, *31*, A158–A165. https://doi.org/10.1016/j.matpr.2021.01.265

8 Kokkinos, P., Venieri, D., & Mantzavinos, D. (2021). Advanced Oxidation Processes for Water and Wastewater Viral Disinfection. A Systematic Review. *Food and Environmental Virology*, *13*(3), 283–302. https://doi.org/10.1007/s12560-021-09481-1

9 Mahmoodi, N. M., Arami, M., Limaee, N. Y., & Tabrizi, N. S. (2006). Kinetics of heterogeneous photocatalytic degradation of reactive dyes in an immobilized TiO2 photocatalytic reactor. *Journal of Colloid and Interface Science*, *295*(1), 159–164. https://doi.org/10.1016/j.jcis.2005.08.007

10 Holkar, C. R., Jadhav, A. J., Pinjari, D. V., Mahamuni, N. M., & Pandit, A. B. (2016). A critical review on textile wastewater treatments: Possible approaches. *Journal of Environmental Management*, *182*, 351–366. https://doi.org/10.1016/j.jenvman.2016.07.090

11 Perazolli, L., Nuñez, L., Silva, M. R. A. D., Pegler, G. F., Costalonga, A. G. C., Gimenes, R., Kondo, M. M., & Bertochi, M. A. Z. (2011). TiO< sub>2</sub>/CuO Films Obtained by Citrate Precursor Method for Photocatalytic Application. *Materials Sciences and Applications*, *02*(06), 564–571. https://doi.org/10.4236/msa.2011.26075

12 Mishra, N., Reddy, R., Kuila, A., Rani, A., Nawaz, A., & Pichiah, S. (2017). A Review on Advanced Oxidation Processes for Effective Water Treatment. *Current World Environment*, *12*(3), 469–489. https://doi.org/10.12944/CWE.12.3.02

13 Wang, L., Yun, J., Zhang, H., Si, J., Fang, X., & Shao, L. (2021). Degradation of Bisphenol A by ozonation in rotating packed bed: Effects of operational parameters and co-existing chemicals. *Chemosphere*, *274*, 129769. https://doi.org/10.1016/j.chemosphere.2021.129769

14 Pędziwiatr, P., Mikołajczyk, F., Zawadzki, D., Mikołajczyk, K., & Bedka, A. (2018). Decomposition of hydrogen peroxide—Kinetics and review of chosen catalysts. *Acta Innovations*, *26*, 45–52. https://doi.org/10.32933/ActaInnovations.26.5

15 Liu, B., Chen, B., & Zhang, B. (2017). Oily Wastewater Treatment by Nano-TiO_2 -Induced Photocatalysis: Seeking more efficient and feasible solutions. *IEEE Nanotechnology Magazine*, *11*(3), 4–15. https://doi.org/10.1109/MNANO.2017.2708818

16 O'Dowd, K., & Pillai, S. C. (2020). Photo-Fenton disinfection at near neutral pH: Process, parameter optimization and recent advances. *Journal of Environmental Chemical Engineering*, *8*(5), 104063. https://doi.org/10.1016/j.jece.2020.104063

17 Gupta, S. M., & Tripathi, M. (2011). A review of TiO_2 nanoparticles. *Chinese Science Bulletin*, *56*(16), 1639–1657. https://doi.org/10.1007/s11434-011-4476-1

18 López, Y. C., Viltres, H., Gupta, N. K., Acevedo-Peña, P., Leyva, C., Ghaffari, Y., Gupta, A., Kim, S., Bae, J., & Kim, K. S. (2021). Transition metal-based metal–organic frameworks for environmental applications: A review. *Environmental Chemistry Letters*, *19*(2), 1295–1334. https://doi.org/10.1007/s10311-020-01119-1

19 Batten, S. R., Champness, N. R., Chen, X. -M., Garcia-Martinez, J., Kitagawa, S., Öhrström, L., O'Keeffe, M., Paik Suh, M., & Reedijk, J. (2013). Terminology of metal–organic frameworks and coordination polymers (IUPAC Recommendations 2013). *Pure and Applied Chemistry*, *85*(8), 1715–1724. https://doi.org/10.1351/PAC-REC-12-11-20

20 Wang, D., Huang, R., Liu, W., Sun, D., & Li, Z. (2014). Fe-Based MOFs for Photocatalytic CO_2 Reduction: Role of Coordination Unsaturated Sites and Dual Excitation Pathways. *ACS Catalysis*, *4*(12), 4254–4260. https://doi.org/10.1021/cs501169t

21 Shanmugam, M., Agamendran, N., Sekar, K., & Natarajan, T. S. (2023). Metal–organic frameworks (MOFs) for energy production and gaseous fuel and electrochemical energy storage applications. *Physical Chemistry Chemical Physics*, *25*(44), 30116–30144. https://doi.org/10.1039/D3CP04297A

22 Park, J., Agrawal, M., Sava Gallis, D. F., Harvey, J. A., Greathouse, J. A., & Sholl, D. S. (2020). Impact of intrinsic framework flexibility for selective adsorption of sarin in non-aqueous solvents using metal–organic frameworks. *Physical Chemistry Chemical Physics*, *22*(11), 6441–6448. https://doi.org/10.1039/C9CP06788D

23 Shi, L., Wang, T., Zhang, H., Chang, K., & Ye, J. (2015). Electrostatic Self-Assembly of Nanosized Carbon Nitride Nanosheet onto a Zirconium Metal–Organic Framework for Enhanced Photocatalytic CO_2 Reduction. *Advanced Functional Materials*, *25*(33), 5360–5367. https://doi.org/10.1002/adfm.201502253

24 Ma, Y., Lu, Y., Hai, G., Dong, W., Li, R., Liu, J., & Wang, G. (2020). Bidentate carboxylate linked TiO2 with NH_2-MIL-101(Fe) photocatalyst: A conjugation effect platform for high photocatalytic activity under visible light irradiation. *Science Bulletin*, *65*(8), 658–669. https://doi.org/10.1016/j.scib.2020.02.001

25 Liu, Y., Yang, Y., Sun, Q., Wang, Z., Huang, B., Dai, Y., Qin, X., & Zhang, X. (2013). Chemical Adsorption Enhanced CO_2 Capture and Photoreduction over a Copper Porphyrin Based Metal Organic Framework. *ACS Applied Materials & Interfaces*, *5*(15), 7654–7658. https://doi.org/10.1021/am4019675

26 Gao, C., Chen, S., Quan, X., Yu, H., & Zhang, Y. (2017). Enhanced Fenton-like catalysis by iron-based metal organic frameworks for degradation of organic pollutants. *Journal of Catalysis*, *356*, 125–132. https://doi.org/10.1016/j.jcat.2017.09.015

27 Laurier, K. G. M., Vermoortele, F., Ameloot, R., De Vos, D. E., Hofkens, J., & Roeffaers, M. B. J. (2013). Iron(III)-Based Metal–Organic Frameworks As Visible Light Photocatalysts. *Journal of the American Chemical Society*, *135*(39), 14488–14491. https://doi.org/10.1021/ja405086e

28 Hou, S., Wu, Y., Feng, L., Chen, W., Wang, Y., Morlay, C., & Li, F. (2018). Green synthesis and evaluation of an iron-based metal–organic framework MIL-88B for efficient decontamination of arsenate from water. *Dalton Transactions*, *47*(7), 2222–2231. https://doi.org/10.1039/C7DT03775A

29 Yue, X., Guo, W., Li, X., Gao, X., & Zhang, G. (2017). Preparation of Efficient BiOBr/MIL-88B(Fe) Composites with Enhanced Photocatalytic Activities. *Water Environment Research*, *89*(7), 614–621. https://doi.org/10.2175/106143017X14839994522821

30 Gecgel, C., Simsek, U. B., Gozmen, B., & Turabik, M. (2019). Comparison of MIL-101(Fe) and amine-functionalized MIL-101(Fe) as photocatalysts for the removal of imidacloprid in aqueous solution. *Journal of the Iranian Chemical Society*, *16*(8), 1735–1748. https://doi.org/10.1007/s13738-019-01647-w

31 Guo, H., Niu, B., Wu, X., Zhang, Y., & Ying, S. (2019). Effective removal of 2,4,6-trinitrophenol over hexagonal metal–organic framework NH_2-MIL-88B(Fe). *Applied Organometallic Chemistry*, *33*(1), e4580. https://doi.org/10.1002/aoc.4580

32 Alluhaybi, A. A., Alharbi, A., Alshammari, K. F., & El-Desouky, M. G. (2023). Efficient Adsorption and Removal of the Herbicide 2,4-Dichlorophenylacetic Acid from Aqueous Solutions Using MIL-88(Fe)-NH_2. *ACS Omega*, *8*(43), 40775–40784. https://doi.org/10.1021/acsomega.3c05818

33 Howarth, A. J., Liu, Y., Li, P., Li, Z., Wang, T. C., Hupp, J. T., & Farha, O. K. (2016). Chemical, thermal and mechanical stabilities of metal–organic frameworks. *Nature Reviews Materials*, *1*(3), 15018. https://doi.org/10.1038/natrevmats.2015.18

34 Chen, M.-L., Lu, T.-H., Long, L.-L., Xu, Z., Ding, L., & Cheng, Y.-H. (2021). NH_2-Fe-MILs for effective adsorption and Fenton-like degradation of imidacloprid: Removal performance and mechanism investigation. *Environmental Engineering Research*, *27*(2), 200702–0. https://doi.org/10.4491/eer.2020.702

35 Li, Y., Jiang, J., Fang, Y., Cao, Z., Chen, D., Li, N., Xu, Q., & Lu, J. (2018). TiO_2 Nanoparticles Anchored onto the Metal–Organic Framework NH_2-MIL-88B(Fe) as an Adsorptive Photocatalyst with Enhanced Fenton-like Degradation of Organic Pollutants under Visible Light Irradiation. *ACS Sustainable Chemistry & Engineering*, *6*(12), 16186–16197. https://doi.org/10.1021/acssuschemeng.8b02968

36 Mateo, D., Santiago-Portillo, A., Albero, J., Navalón, S., Alvaro, M., & García, H. (2019). Long-Term Photostability in Terephthalate Metal–Organic Frameworks. *Angewandte Chemie International Edition*, *58*(49), 17843–17848. https://doi.org/10.1002/anie.201911600

37 Peralta, M. E., Ocampo, S., Funes, I. G., Onaga Medina, F., Parolo, M. E., & Carlos, L. (2020). Nanomaterials with Tailored Magnetic Properties as Adsorbents of Organic Pollutants from Wastewaters. *Inorganics*, *8*(4), 24. https://doi.org/10.3390/inorganics8040024

38 Hernandez, J. S. T., Aragón-Muriel, A., Corrales Quintero, W., Castro Velásquez, J. C., Salazar-Camacho, N. A., Pérez Alcázar, G. A., & Tabares, J. A. (2022). Characterization of Fe3O4 Nanoparticles for Applications in Catalytic Activity in the Adsorption/Degradation of Methylene Blue and Esterification. *Molecules*, *27*(24), 8976. https://doi.org/10.3390/molecules27248976

39 Hermanek, M., Zboril, R., Medrik, I., Pechousek, J., & Gregor, C. (2019). Retraction of "Catalytic Efficiency of Iron(III) Oxides in Decomposition of Hydrogen Peroxide: Competition between the Surface Area and Crystallinity of Nanoparticles". *Journal of the American Chemical Society*, *141*(51), 20566–20566. https://doi.org/10.1021/jacs.9b03677

40 Liu, M., Ye, Y., Ye, J., Gao, T., Wang, D., Chen, G., & Song, Z. (2023). Recent Advances of Magnetite (Fe3O4)-Based Magnetic Materials in Catalytic Applications. *Magnetochemistry*, *9*(4), 110. https://doi.org/10.3390/magnetochemistry9040110

41 Zhang, C.-F., Qiu, L.-G., Ke, F., Zhu, Y.-J., Yuan, Y.-P., Xu, G.-S., & Jiang, X. (2013). A novel magnetic recyclable photocatalyst based on a core–shell metal–organic framework Fe_3O_4@MIL-100(Fe) for the decolorization of methylene blue dye. *Journal of Materials Chemistry A*, *1*(45), 14329. https://doi.org/10.1039/c3ta13030d

42 Baimuratova, R. K., Zhinzhilo, V. A., Uflyand, I. E., Dmitriev, A. I., Zhidkov, M. V., Ovanesyan, N. S., Kugabaeva, G. D., & Dzhardimalieva, G. I. (2023). Low-Temperature Synthesis of Metal–Organic Coordination Polymers Based on Oxo-centered Iron Complexes: Magnetic and Adsorption Properties. *Russian Journal of Physical Chemistry A*, *97*(4), 735–748. https://doi.org/10.1134/S0036024423040064

43 Sapianik, A. A., Kiskin, M. A., Kovalenko, K. A., Samsonenko, D. G., Dybtsev, D. N., Audebrand, N., Sun, Y., & Fedin, V. P. (2019). Rational synthesis and dimensionality tuning of MOFs from preorganized heterometallic molecular complexes. *Dalton Trans.*, *48*(11), 3676–3686. https://doi.org/10.1039/C8DT05136D

44 Wongsakulphasatch, S., Nouar, F., Rodriguez, J., Scott, L., Le Guillouzer, C., Devic, T., Horcajada, P., Grenèche, J. -M., Llewellyn, P. L., Vimont, A., Clet, G., Daturi, M., & Serre, C. (2015). Direct accessibility of mixed-metal (III / II) acid sites through the rational synthesis of porous metal carboxylates. *Chemical Communications*, *51*(50), 10194–10197. https://doi.org/10.1039/C5CC02550H

45 Peng, L., Asgari, M., Mieville, P., Schouwink, P., Bulut, S., Sun, D. T., Zhou, Z., Pattison, P., van Beek, W., & Queen, W. L. (2017). Using Predefined M_3 (μ_3-O) Clusters as Building Blocks for an Isostructural Series of Metal–Organic Frameworks. *ACS Applied Materials & Interfaces*, *9*(28), 23957–23966. https://doi.org/10.1021/acsami.7b06041

46 Elmore, W. C. (1938). Ferromagnetic Colloid for Studying Magnetic Structures. *Physical Review*, *54*(4), 309–310. https://doi.org/10.1103/PhysRev.54.309

47 Devi, L., Kumar, S., & Reddy, K. (2009). Photo fenton like process Fe3+/(NH4)2S2O8/UV for the degradation of Di azo dye congo red using low iron concentration. *Open Chemistry*, *7*(3), 468–477. https://doi.org/10.2478/s11532-009-0036-9

48 Yadav, S., Dixit, R., Sharma, S., Dutta, S., Solanki, K., & Sharma, R. K. (2021). Magnetic metal–organic framework composites: Structurally advanced catalytic materials for organic transformations. *Materials Advances*, *2*(7), 2153–2187. https://doi.org/10.1039/D0MA00982B

49 Huang, L. (2003). Synthesis, morphology control, and properties of porous metal–organic coordination polymers. *Microporous and Mesoporous Materials*, *58*(2), 105–114. https://doi.org/10.1016/S1387-1811(02)00609-1

50 Bennett, T. D., & Cheetham, A. K. (2014). Amorphous Metal–Organic Frameworks. *Accounts of Chemical Research*, *47*(5), 1555–1562. https://doi.org/10.1021/ar5000314

51 Yaghi, O. M., O'Keeffe, M., Ockwig, N. W., Chae, H. K., Eddaoudi, M., & Kim, J. (2003). Reticular synthesis and the design of new materials. *Nature*, *423*(6941), 705–714.

52 Ockwig, N. W., Delgado-Friedrichs, O., O'Keeffe, M., & Yaghi, O. M. (2005). Reticular Chemistry: Occurrence and Taxonomy of Nets and Grammar for the Design of Frameworks. *Accounts of Chemical Research*, *38*(3), 176–182. https://doi.org/10.1021/ar020022l

53 Zhang, S., Zhuo, Y., Ezugwu, C. I., Wang, C., Li, C., & Liu, S. (2021). Synergetic Molecular Oxygen Activation and Catalytic Oxidation of Formaldehyde over Defective MIL-88B(Fe) Nanorods at Room Temperature. *Environmental Science & Technology*, *55*(12), 8341–8350. https://doi.org/10.1021/acs.est.1c01277

54 Nakamoto, K. (2009). *Infrared and Raman spectra of inorganic and coordination compounds* (6th ed). Wiley.

55 Batista, M. A., Costa, A. C. S. D., Souza Junior, I. G. D., & Bigham, J. M. (2008). Cristallochemical characterization of synthetic Zn-substituted maghemites (g-Fe2-xZn xO3). *Revista Brasileira de Ciência do Solo*, *32*(2), 561–568. https://doi.org/10.1590/S0100-06832008000200011

56 Gorski, C. A., & Scherer, M. M. (2010). Determination of nanoparticulate magnetite stoichiometry by Mossbauer spectroscopy, acidic dissolution, and powder X-ray diffraction: A critical review. *American Mineralogist*, *95*(7), 1017–1026. https://doi.org/10.2138/am.2010.3435

57 Pallach, R., Keupp, J., Terlinden, K., Frentzel-Beyme, L., Kloß, M., Machalica, A., Kotschy, J., Vasa, S. K., Chater, P. A., Sternemann, C., Wharmby, M. T., Linser, R., Schmid, R., & Henke, S. (2021). Frustrated flexibility in metal-organic frameworks. *Nature Communications*, *12*(1), 4097. https://doi.org/10.1038/s41467-021-24188-4

58 Horcajada, P., Serre, C., Maurin, G., Ramsahye, N. A., Balas, F., Vallet-Regí, M., Sebban, M., Taulelle, F., & Férey, G. (2008). Flexible Porous Metal-Organic Frameworks for a Controlled Drug Delivery. *Journal of the American Chemical Society*, *130*(21), 6774–6780. https://doi.org/10.1021/ja710973k

59 Schneemann, A., Bon, V., Schwedler, I., Senkovska, I., Kaskel, S., & Fischer, R. A. (2014). Flexible metal–organic frameworks. *Chem. Soc. Rev.*, *43*(16), 6062–6096. https://doi.org/10.1039/C4CS00101J

60 Pham, M.-H., Vuong, G.-T., Vu, A.-T., & Do, T.-O. (2011). Novel Route to Size-Controlled Fe–MIL-88B–NH_2 Metal–Organic Framework Nanocrystals. *Langmuir*, *27*(24), 15261–15267. https://doi.org/10.1021/la203570h

61 Ma, M., Bétard, A., Weber, I., Al-Hokbany, N. S., Fischer, R. A., & Metzler-Nolte, N. (2013). Iron-Based Metal–Organic Frameworks MIL-88B and NH_2-MIL-88B: High Quality Microwave Synthesis and Solvent-Induced Lattice "Breathing". *Crystal Growth & Design*, *13*(6), 2286–2291. https://doi.org/10.1021/cg301738p

62 Mellot-Draznieks, C., Serre, C., Surblé, S., Audebrand, N., & Férey, G. (2005). Very Large Swelling in Hybrid Frameworks: A Combined Computational and Powder Diffraction Study. *Journal of the American Chemical Society*, *127*(46), 16273–16278. https://doi.org/10.1021/ja054900x

63 Ye, Z., Zhang, W., Lanzalaco, S., Zhao, L., Sirés, I., Xia, P., Zhai, J., & He, Q. (2023). Ultra-uniform MIL-88B(Fe)/Fe3S4 hybrids engineered by partial sulfidation to boost catalysis in electro-Fenton treatment of micropollutants: Experimental and mechanistic insights. *Chemical Engineering Journal*, *455*, 140757. https://doi.org/10.1016/j.cej.2022.140757

64 Kicheeva, A. G., Sushko, E. S., Bondarenko, L. S., Kydralieva, K. A., Pankratov, D. A., Tropskaya, N. S., Dzeranov, A. A., Dzhardimalieva, G. I., Zarrelli, M., & Kudryasheva, N. S. (2023). Functionalized Magnetite Nanoparticles: Characterization, Bioef-

fects, and Role of Reactive Oxygen Species in Unicellular and Enzymatic Systems. *International Journal of Molecular Sciences*, *24*(2), 1133. https://doi.org/10.3390/ijms24021133

65 Schwaminger, S. P., Bauer, D., Fraga-García, P., Wagner, F. E., & Berensmeier, S. (2017). Oxidation of magnetite nanoparticles: Impact on surface and crystal properties. *CrystEngComm*, *19*(2), 246–255. https://doi.org/10.1039/C6CE02421A

66 Shokrollahi, H. (2017). A review of the magnetic properties, synthesis methods and applications of maghemite. *Journal of Magnetism and Magnetic Materials*, *426*, 74–81. https://doi.org/10.1016/j.jmmm.2016.11.033

67 Tran, L. T., Dang, H. T. M., Tran, H. V., Hoang, G. T. L., & Huynh, C. D. (2023). MIL-88B(Fe)-NH_2: An amine-functionalized metal–organic framework for application in a sensitive electrochemical sensor for Cd^{2+}, Pb^{2+}, and Cu^{2+} ion detection. *RSC Advances*, *13*(32), 21861–21872. https://doi.org/10.1039/D3RA02828C

68 Zhao, Q., Zhang, L., Wang, X., Jia, X., Xu, P., Zhao, M., & Dai, R. (2019). Simultaneous efficient adsorption and photocatalytic degradation of methylene blue over iron(III)-based metal–organic frameworks: A comparative study. *Transition Metal Chemistry*, *44*(8), 789–797. https://doi.org/10.1007/s11243-019-00349-9

69 Rodenas, T., Van Dalen, M., García-Pérez, E., Serra-Crespo, P., Zornoza, B., Kapteijn, F., & Gascon, J. (2014). Visualizing MOF Mixed Matrix Membranes at the Nanoscale: Towards Structure-Performance Relationships in CO_2/CH_4 Separation Over NH_2-MIL-53(Al)@PI. *Advanced Functional Materials*, *24*(2), 249–256. https://doi.org/10.1002/adfm.201203462

70 Zhao, X., Zheng, M., Gao, X., Gao, Z., & Huang, H. (2020). Construction of an anionic porous framework via a post-synthesis strategy to regulate the adsorption behavior of organic pollutants. *Journal of Materials Science*, *55*(30), 14751–14760. https://doi.org/10.1007/s10853-020-05043-1

71 Taherzade, S. D., Abbasichaleshtori, M., & Soleimannejad, J. (2022). Efficient and ecofriendly cellulose-supported MIL-100(Fe) for wastewater treatment. *RSC Advances*, *12*(15), 9023–9035. https://doi.org/10.1039/D1RA08949H

72 Fu, Y., & Viraraghavan, T. (2002). Removal of Congo Red from an aqueous solution by fungus Aspergillus niger. *Advances in Environmental Research*, *7*(1), 239–247. https://doi.org/10.1016/S1093-0191(01)00123-X

73 Andrade, P. H. M., Ahouari, H., Volkringer, C., Loiseau, T., Vezin, H., Hureau, M., & Moissette, A. (2023). Electron-Donor Functional Groups, Band Gap Tailoring, and Efficient Charge Separation: Three Keys To Improve the Gaseous Iodine Uptake in MOF Materials. *ACS Applied Materials & Interfaces*, *15*(25), 31032–31048. https://doi.org/10.1021/acsami.3c04955

74 Viswanathan, V. P., Mathew, S. V., Dubal, D. P., Adarsh, N. N., & Mathew, S. (2020). Exploring the Effect of Morphologies of Fe(III) Metal-Organic Framework MIL-88A(Fe) on the Photocatalytic Degradation of Rhodamine B. *ChemistrySelect*, *5*(25), 7534–7542. https://doi.org/10.1002/slct.202001670

75 Xue, B., Du, L., Jin, J., Meng, H., & Mi, J. (2021). In situ growth of MIL-88A into polyacrylate and its application in highly efficient photocatalytic degradation of organic pollutants in water. *Applied Surface Science*, *564*, 150404. https://doi.org/10.1016/j.apsusc.2021.150404

76 Andrew Lin, K.-Y., Chang, H.-A., & Hsu, C.-J. (2015). Iron-based metal organic framework, MIL-88A, as a heterogeneous persulfate catalyst for decolorization of Rhodamine B in water. *RSC Advances*, *5*(41), 32520–32530. https://doi.org/10.1039/C5RA01447F

77 Tama, J., Riyani, K., & Setyaningtyas, T. (2020). Effect of ultraviolet and visible lights on degradation of congo red dye using Fe^{2+}/H_2O_2. *Journal of Physics: Conference Series*, *1494*(1), 012029. https://doi.org/10.1088/1742-6596/1494/1/012029

78 Said, M., Rizki, W. T., Asri, W. R., Desnelli, D., Rachmat, A., & Hariani, P. L. (2022). SnO2–Fe3O4 nanocomposites for the photodegradation of the Congo red dye. *Heliyon*, *8*(4), e09204. https://doi.org/10.1016/j.heliyon.2022.e09204

79 Shahid, M., Jingling, L., Ali, Z., Shakir, I., Warsi, M. F., Parveen, R., & Nadeem, M. (2013). Photocatalytic degradation of methylene blue on magnetically separable MgFe2O4 under visible light irradiation. *Materials Chemistry and Physics*, *139*(2–3), 566–571. https://doi.org/10.1016/j.matchemphys.2013.01.058

How to Cite: Burkeyeva, G.K., Kovaleva, A.K., Ibadullaeva, M.N., Ubaydullauly, M., Plocek, J. & Sergaziyeva, K.E. (2024). Synthesis and Investigation of Catalytic Properties of Metal and Polymer Nanocomposites Based on Unsaturated Polyester Resins. *Eurasian Journal of Chemistry, 29, 3(115), 148-159.* https://doi.org/10.31489/2959-0663/3-24-7

Article

Received: 19 June 2024 | Revised: 9 September 2024 |
Accepted: 16 September 2024 | Published online: 23 September 2024

UDC 541.057.17

https://doi.org/10.31489/2959-0663/3-24-7

Gulsym K. Burkeyeva[1], Anna K. Kovaleva[2*], Madinabonu N. Ibadullaeva[1], Magzhan Ubaydullauly[1], Jiri Plocek[3], Kamila E. Sergaziyeva[1]

[1]*Department of Organic Chemistry and Polymers, Karaganda Buketov University, Karaganda, Kazakhstan;*
[2]*Research Institute of Chemical Problems, Karaganda Buketov University, Karaganda, Kazakhstan;*
[3]*Institute of Inorganic Chemistry of the Czech Academy of Sciences, Husinec-Rez, Czech Republic;*
*(*Corresponding author`s e-mail: cherry-girl1899@mail.ru)*

Synthesis and Investigation of Catalytic Properties of Metal-Polymer Nanocomposites Based on Unsaturated Polyester Resins

This paper focuses on the hydrogenation process in metal-polymer complexes based on copolymers of polypropylene glycol fumarate phthalate and polypropylene glycol maleate phthalate, using acrylic acid and immobilized cobalt metal particles as catalysts. A classical reaction of the electrocatalytic hydrogenation of pyridine to piperidine was applied. SEM and dynamic light scattering were utilized to investigate the average size and dispersity of cobalt metal nanoparticles. The experimental findings show that the efficiency of hydrogenation can be improved by increasing the temperature from 25 to 40 °C and the current to 2 A. More specifically, increasing the temperature to 40 °C promotes swelling of the polymer and its transition from a globular collapsed state to an open one, which leads to an increase in the number of active catalytic centers and, as a consequence, acceleration of the hydrogenation process. Increasing the current strength to 2 A also helps to increase the rate of the hydrogenation process. Further increasing the current to 3 A is undesirable due to an increase in the yield of by-products and a decrease in the yield of the target product, piperidine. Based on a comparative analysis, it was established that the use of a copolymer of polypropylene glycol maleate phthalate with acrylic acid as the polymer matrix base is the most preferable for obtaining polymer-metal complexes with nanosized cobalt.

Keywords: nanocatalytic systems, nanocatalysts, catalytic activity, electrocatalytic hydrogenation, metal-polymer complex, nanoparticles, unsaturated polyesters, polypropylene glycol maleate phthalate, polypropylene glycol fumarate phthalate.

Introduction

Most organic molecules are produced on an industrial scale using catalytic processes. Due to successful application and commercialization, the search and development of novel heterogeneous nanocatalytic systems is currently one of the most sought-after areas in nanoscience [1]. Metal nanoparticles have been utilized as active catalytic centers in numerous chemical processes for more than a century [2]. This is explained by the high catalytic activity of nanoparticles, which is determined by their enormous specific surface area to volume. Advances in materials science over the past few decades have had a direct impact on the development of nanocatalysis [3–5].

Technological aspects of constructing nanosystems have undergone significant development under the influence of advances in nanotechnology. Catalysts can be tailored to specific industrial processes by precisely controlling of nanoparticle dispersity, shape, content, and spatial distribution of the constituents of nanostructured catalytic systems. Improving the catalytic activity of novel nanocatalysts while simultaneously exploring their stability and selectivity against catalytic poisons is a crucial path in this area. The fact that nanocatalysts can be regenerated and reused is another factor contributing to their widespread use.

New routes to synthesize nanoscale catalysts have become possible thanks to technological developments, especially in the field of nanotechnology-based advanced catalysis [6–8]. Nowadays, nanocatalysis is widely used in the chemical industry due to its ease of use, environmental friendliness and efficiency in carrying out processes of hydrogenation and oxidation of organic compounds. In this context, special attention is paid to metal-polymer complexes (MPC) with immobilized nanosized metals. These next generation nanocatalysts exhibit enzyme-like activity at room temperature and atmospheric pressure. Therefore, the creation of MPCs based on available polymer compounds with immobilized metal nanoparticles is a relevant direction in nanoscience.

Unsaturated polyesters are promising coreactants for the synthesis of the polymer base of nanocatalysts due to their functionality and reactivity. High resistance to external factors, ease of production, convenience in use in combination with availability, low cost and environmental friendliness significantly increase interest in unsaturated polyesters as co-reactants for obtaining new functional polymer materials [9–11]. The ability of unsaturated polyesters to cure in the presence of vinyl monomers results in the formation of a polymer compound with a cross-linked structure [12, 13]. This property makes the finished product useful as a polymer base, a matrix that effectively immobilizes nanosized metal particles to create effective nanocatalytic systems.

Previously, copolymers of unsaturated polyesters polyethylene (propylene) glycol maleates with acrylic acid and nanometric cobalt, nickel, and silver metals were used to create mono- and bimetallic metal-polymer nanocomposite composites. It has been shown that these copolymers can be used as a polymer matrix to create efficient hydrogenation catalysts. The examined metal-polymer complexes were found to contain discrete cobalt and nickel nanoparticles with a diameter of 30–120 nm, which are uniformly dispersed throughout the polymer matrix and have a predominantly spherical shape [14, 15].

The purpose of this work is to study the electrocatalytic activity and physicochemical characteristics of nanocomposites based on acrylic acid and metallic cobalt (Co) in a polymer matrix of polypropylene glycol fumarate phthalate (p-PGFPh) and polypropylene glycol maleate phthalate (p-PGMPh).

Experimental

Propylene glycol, maleic and phthalic anhydrides, acrylic acid, benzoyl peroxide, pyridine (Sigma-Aldrich), fumaric acid, diethyl ether (Vekon), zinc and cobalt chlorides, and sodium hypophosphite (Reakhim) are among the reagents employed in the study. None of the reagents required additional purification.

The initial unsaturated polyesters — polypropylene glycol maleate phthalate and polypropylene glycol fumarate phthalate — were obtained using polycondensation reactions of propylene glycol with maleic anhydride (or fumaric acid, respectively) and phthalic anhydride. The ratio of acidic reagents (maleic anhydride or fumaric acid to phthalic anhydride) was 0.7:0.3 moles. The reaction was carried out at temperatures from 423 to 433 K with zinc chloride as a catalyst [16, 17]. The molecular weights of the obtained compounds were calculated using gel permeation chromatography and were approximately ~2350 Da (p-PGMPh) and ~2500 Da (p-PGFPh).

The curing of the synthesized p-PGMPh and p-PGFPh was carried out with acrylic acid (AA) at a temperature of 333 K in the presence of benzoyl peroxide as a radical initiator (1 mass.% of the mass of the initial reaction mixture).

The scheme of synthesis of copolymers of p-PGMF and p-PGFF with AA is presented in Figure 1 (*a*, *b*).

Using the residual principle, the mother solutions in dioxane were analyzed by HPLC method on a Shimadzu HPLC 20 chromatograph (Japan) to determine the copolymer composition. After removing the unreacted amount, the p-PGMPh–AA and p-PGFPh–AA copolymers were dried until their mass remained constant.

The use of copolymers of p-PGMPh and p-PGFPh with AA as a polymer base for the production of nanocomposites is due to their stimulus sensitivity depending on varying environmental factors. In particular, the behavior of these copolymers under the influence of increasing temperature and alkalinity was previously studied [18]. It was established that an increase in temperature promotes the transition of the polymer network to a swollen state. This is explained by the occurrence of a mixed-type volume-phase transition ("swelling–collapse–swelling"), which polymer matrices based on p-PGMPh–AA and p-PGFPh–AA undergo. Thus, samples at room temperature (20 °C) initially increase to a certain size. Next, with an increase in temperature (up to 30 °C), a predominance of hydrophobic interactions is observed, as a result of which the polymer network decreases in size and is collapsed. Further heating of the external solution (over 30 °C) leads to an increase in the role of hydrogen bonds, which significantly weaken with rising temperature. This promotes an increase in the size of the polymer network, i.e. the polymer swells. Accordingly, the specific contact area of immobilized cobalt with pyridine increases, which enhances the efficiency of the process of electrocatalytic hydrogenation of organic compounds.

The rise of the medium alkalinity is a favorable factor for the unfolding of the polymer network. The explanation for this is the presence of ionized carboxyl groups in the microchains, which are attached to the main chain by covalent bonds. As a result, the electrostatic repulsion of like-charged carboxyl groups plays a decisive role in the behavior of gels. The resulting increase in the degree of dissociation of the above carboxyl groups, accompanied by a shift to the region of high pH values, leads to an increase in their electrostatic

repulsion. A shift towards increasing the alkalinity of the medium promotes the unfolding of the globular structure of the polymer network (in the case of an acidic medium), which leads to swelling of the gel. This is explained both by more complete dissociation as a result of the formation of salt molecules in the solution, and by the weakening of the dominance of hydrogen bonds that cause the collapse of the gel. The hydrophobic interactions that take place are not capable to have a significant effect on the processes of attraction between the links of the polymer network.

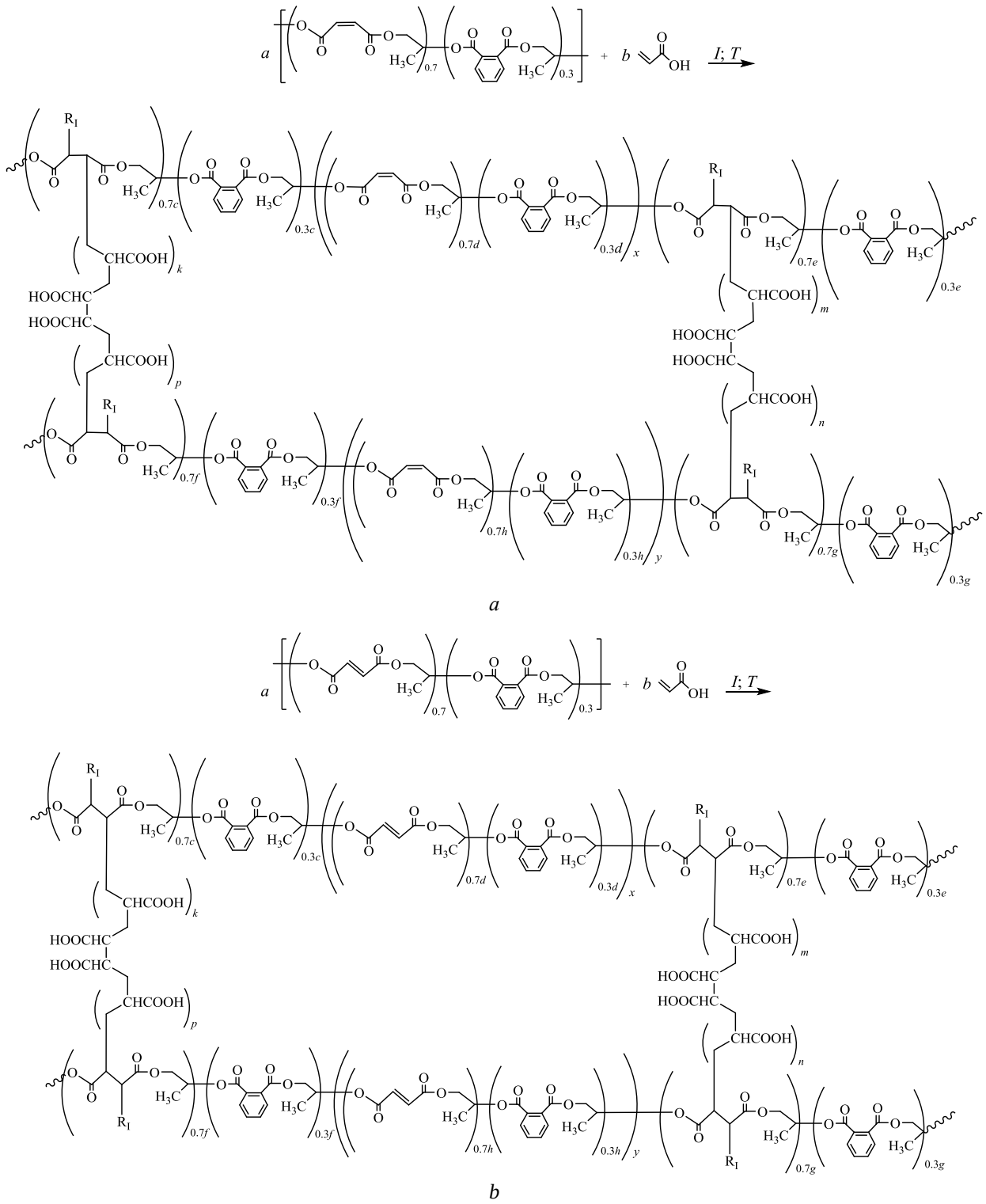

Figure 1. Scheme of radical copolymerization of p-PGMPh and p-PGFPh with AA

It is worth noting that such a course of the swelling curve depending on the change in the acidity/alkalinity of the medium indicates the typical polyelectrolyte behavior of the gels we synthesized based on p-PGMPh and p-PGFPh with AA.

Thus, the use of the presented copolymers as a polymer matrix for the immobilization of metal cobalt nanoparticles into it in order to get nanocatalysts for electrocatalytic hydrogenation in an alkaline medium at elevated temperatures is promising.

In order to immobilize cobalt particles in polymer matrices, p-PGMPh–AA and p-PGFPh–AA copolymers with compositions of 13.1:86.9 mass.% and 14.2:85.8 mass.%, respectively, were kept in a 0.1 N solution of cobalt chloride for 6 hours, after which the Co^{2+} ions were reduced to Co^0 using a 0.2 N solution of sodium hypophosphite NaH_2PO_2 in the presence of an ammonia solution of silver chloride (0.2 N) as a catalyst. Schematically the reaction is as follows:

$$7Co^{2+} + 2H_2PO^{2-} + 6H_2O \rightarrow 7Co^0 \downarrow + 2PO_4^{3-} + 16H^+$$

It's important to note that the obtained MPC's properties with reduced Co^0 are practically independent of the AgCl concentration in the silver chloride ammonia solution.

There are multiple steps involved in the reduction of Co^{+2} to Co^0 in the volume of the p-PGMPh-AA and p-PGFPh-AA polymers. First, Co^{2+} ions are added to the matrix of polymers. Subsequently, reagent diffusion occurs inside the polymer volume. At the final phase, cobalt chloride ($CoCl_2$) and sodium hypophosphite (NaH_2PO_2) are mixed, causing direct reduction from Co^{2+} to Co^0 [19].

At T = 293K the reduction process lasted for two hours. After washing with distilled water, the resulting metal-polymer composites were dried in a vacuum oven until their mass remained constant. The immobilization of cobalt particles into the polymer matrix was confirmed by visual inspection, which showed a color change from white (empty p-PGMPh–AA and p-PGFPh–AA polymer matrices) to gray in the studied samples.

Identification of MPCs was carried out using infrared spectroscopy on an FSM 1201 IR spectrometer. The surface morphology of the polymer matrix with immobilized cobalt metal nanoparticles was studied using scanning electron microscopy on a MIRA 3 TESCAN instrument at an accelerating voltage of 5 kV. The nanoparticle size distribution was determined by photon correlation spectroscopy using a Zetasizer Nano S90 instrument from Malvern Instruments. The metallic cobalt content in the composites was determined by energy-dispersive analysis using a 4210 MP-AES instrument from Agilent Technologies Bayan Lepas Free.

To evaluate the effectiveness of the obtained MPCs in comparison with the skeletal cobalt catalyst, a model reaction of pyridine hydrogenation to piperidine was carried out in an electrochemical system, yielding the dipiridyl as a by-product. Additionally, the effect of temperature and current on the yield of the target product (piperidine) and by-product (dipiridyl) in the pyridine hydrogenation reaction was investigated.

The pyridine hydrogenation process was carried out using a diaphragm electrocatalytic thermostat cell composed of Pyrex glass. A 3 MK-40 membrane diaphragm served as the barrier between the anodic (platinum mesh) and cathodic (copper plate with $S_{surface}$ = 0,048 dm^2) compartments in this cell. This two-chamber diaphragm cell, as well as the parameters and conditions of hydrogenation were developed by Doctor of Chemical Sciences, Professor Kirilyus I.V. [20]. The cell's airtightness was ensured by fittings attached to "masts" located in the anode and cathode spaces of the electrolyzer. The evolved gases (hydrogen and oxygen) were vented through a nozzle, and their volume was monitored using burette scales [21, 22].

The pyridine electrocatalytic hydrogenation process was carried out while varying the current (from 1 A to 3 A) and temperature (from 20 °C to 40 °C) to evaluate the yield of piperidine and dipiridyl. Initially, solutions of the anolyte and catholyte (20 % and 5 % sodium hydroxide solutions, respectively) were introduced into the electrocatalytic thermostat cell, and the reaction conditions were adjusted. After establishing the desired reaction conditions, saturation of the MPCs with electrocatalytic hydrogen was carried out in the cathode part of the electrocatalytic thermostat cell. The mass of metal-polymer composites introduced into the cathode part of the electrocatalytic cell was 1 g ± 0.1 %. The cobalt content in MPC based on p-PGMPh–AA was 0.87 g, and 0.9 g in MPC based on p-PGFPh–AA. To get comparable experimental results, skeletal cobalt of similar mass was taken (0.87 g ± 0.1 % — for comparison with the effectiveness of MPC based on p-PGMPh–AA and 0.9 g ± 0.1 % — for comparison with MPC based on p-PGFPh–AA). This process lasted for about 30 minutes and ended when the ratio of the volumes of hydrogen and oxygen released in the burettes reached 2:1. Subsequently, the pyridine hydrogenation process was directly conducted by introducing a pyridine ($V_{pyr.}$ = 1 ml) into the cathodic part of the electrocatalytic cell, and the volume of evolved gases H_2 и O_2 in the burettes was recorded every 2 minutes. The reaction concluded once the volume of hydrogen

ceased to change, indicating the cessation of its absorption by the substrate (pyridine). Following this, the reaction rate of electrocatalytic hydrogenation W ($mol \cdot L^{-1} \cdot s^{-1}$) was determined

The target and by-products of pyridine hydrogenation received on the cathode were analyzed by gas chromatography on an Agilent 7890A/5975C chromatograph equipped with a mass spectrometric detector. The analysis was carried out after their extraction with diethyl ether (mass ratio 1:1).

Results and Discussion

Electrocatalytic hydrogenation is one of the most common industrial methods for the synthesis of new chemical products. Transition metals, their alloys, or oxides are typically used as catalysts in such reactions [23]. However, as follows from the experience gained in the electrocatalytic hydrogenation of unsaturated organic compounds, transition metal oxides do not exhibit catalytic properties in such processes [21, 22]. Due to their greater functionality, efficiency and lower cost, increasing attention is being paid to the use of MPCs obtained by immobilizing nanoscale catalytically active metals within a polymer matrix. Previously, polymer matrices based on unsaturated polyesters were synthesized from polyglycol maleinates with some vinyl-type ionogenic monomers, followed by immobilization of nickel, cobalt, and silver nanoparticles in them. The obtained metal-polymer composite catalysts showed excellent catalytic properties [24].

In continuation of studies on the possibility of using unsaturated polyester resins as a polymer matrix for the production of metal-polymer composite catalysts, we immobilized cobalt nanoparticles into copolymers of p-PGMPh–AA and p-PGFPh–AA with a composition of 13.1:86.9 mass.% and 14.2:85.8 mass.%, respectively. The surface morphology of the copolymer samples was examined using scanning electron microscopy (Figure 2) with subsequent processing of the obtained results. As a result of the analysis, the average pore size of the three-dimensional polymer network was found to be no more than 0.5 μm, which meets the requirements for polymers used as the polymer matrix base for nanocatalysts [25].

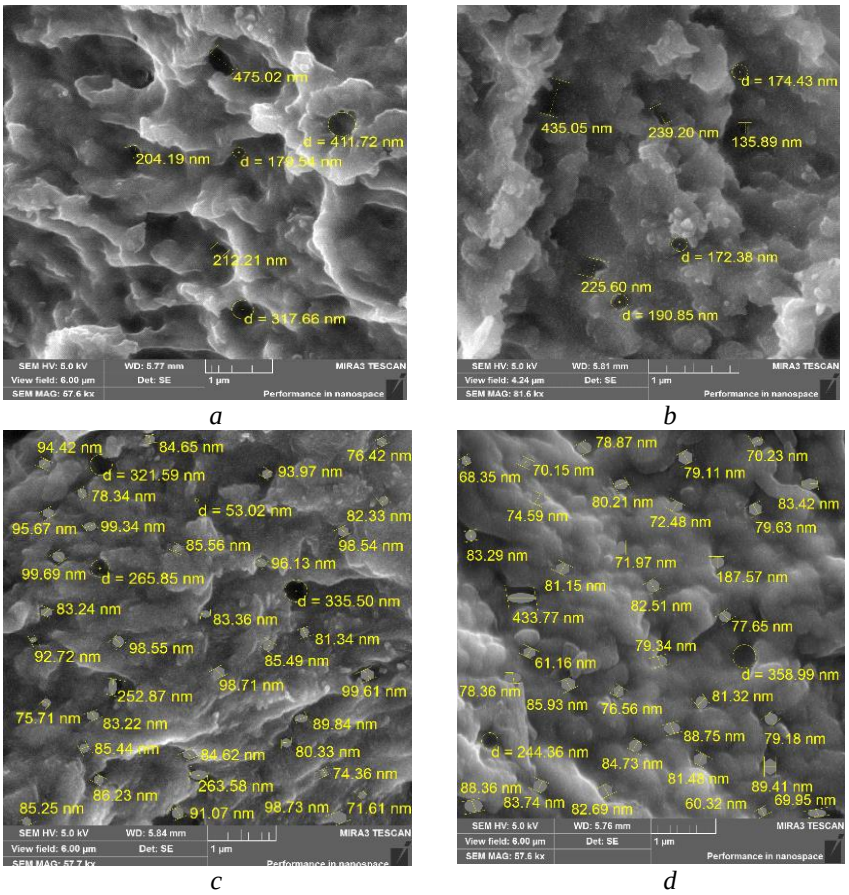

a — p-PGMPh–AA (13.1:86.9 mass.%); *b* — p-PGFPh–AA (14.2:85.8 mass.%);
c — p-PGMPh–AA–Co^0; *d* — p-PGFPh–AA–Co^0

Figure 2. Surface morphology of the polymers and MPCs

As a continuation of our work, we also studied the effect of the concentration of $CoCl_2$ solution on the size and polydispersity of immobilized nanoscale cobalt in the polymer matrix. Specifically, photon correlation spectroscopy with the help of a Zetasizer Nano S90 device from Malvern Instruments was used to evaluate the cobalt dispersion in the metal-polymer composite. Table 1 presents the findings.

Table 1

Effect of $CoCl_2$ concentration on the size and polydispersity of metallic nanoparticles

Copolymer	Concentration of $CoCl_2$, N	Concentration of ammoniacal solution of AgCl, N	Nanoparticle yield, %	Average particle size, nm	Polydispersity
p-PGMPh	0.01	0.2	92.5±1.9	42	0.136
	0.05		91.4±1.8	51	0.144
	0.1		88.9±1.8	88	0.198
	0.2		62.8±1.3	167	0.743
p-PGFPh	0.01		87.8±1.8	35	0.129
	0.05		86.2±1.7	48	0.134
	0.1		82.6±1.7	76	0.187
	0.2		55.2±1.1	159	0.734

As can be seen in Table 1, the average size and polydispersity of Co^0 nanoparticles rise with increasing concentration of the cobalt salt solution, but their yield decreases. Based on this, it was determined that 0.1 N was the optimum concentration of cobalt chloride to achieve a suitable balance of metal particle yield, size and polydispersity.

Figure 3 presents the diagram illustrating the distribution of cobalt particles within the volume of the p-PGMPh–AA polymeric matrix when using a 0.1 N $CoCl_2$ solution.

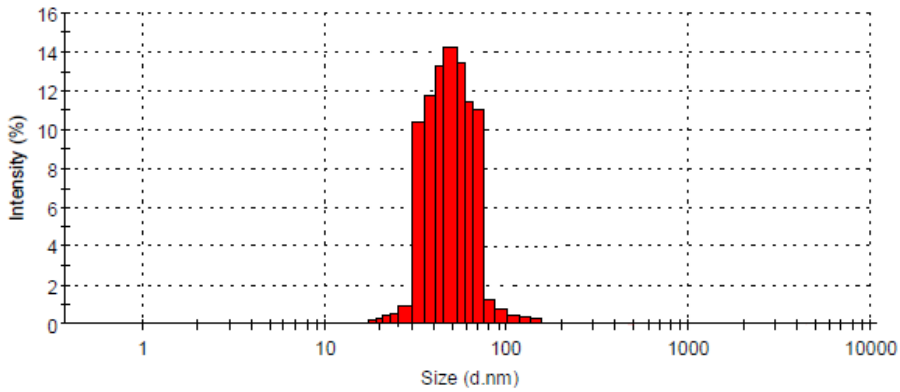

Figure 3. Distribution diagram of cobalt particles within the volume of the p-PGMPh–AA polymer matrix when using a 0.1 N solution of $CoCl_2$

Analyzing the data presented in Figure 3, it can be noted that most nanoparticles have sizes from 53 to 100 nm. The agglomerates (clusters of small particles) observed on the surface of the polymer network do not exceed 260 nm in size.

Similar results were obtained for the composite with the p-PGFPh–AA polymeric matrix (Table 1). As mentioned earlier, changing the AgCl ammonia solution concentration did not have a noticeable effect on the dispersion of nanoparticles within the polymer matrix volume.

The concentration of metallic cobalt in the metal-polymer composite was quantitatively determined using energy dispersive spectroscopy. Figure 4 (*a*, *b*) presents energy-dispersive spectroscopy results for the metal-polymer composites based on p-PGMPh and p-PGFPh with AA and 0.1 N cobalt chloride.

Distinct peaks in the 1570–1590 cm^{-1} range were observed when the polymer matrices including immobilized cobalt particles were subjected to infrared spectroscopy. These peaks correspond to the unsaturated double bonds observed in p-PGMP and p-PGFP. Furthermore, bands of absorption were detected in the range of 2860–2885 cm^{-1}, which is associated with the unsaturated polyesters $–CH_3$ methyl group.

–CH_2–CO– groups are characterized by the emergence of strong thin bands in the 1400–1440 см$^{-1}$ region. The presence of the complex –COOC=C– ether group is confirmed by peaks at 1778 cm^{-1} and 1792 cm^{-1}. The peaks at 1722 cm^{-1} in the IR spectrum of the p-PGMPh–AA copolymer, as well as peaks at 1706 cm^{-1} and 1729 cm^{-1} in the spectrum of the p-PGFPh–AA copolymer, confirm the presence of –COOH carboxyl groups, while the peaks at 2854 cm^{-1} and 2921 cm^{-1} characterize the –CH_2– methylene groups of acrylic acid.

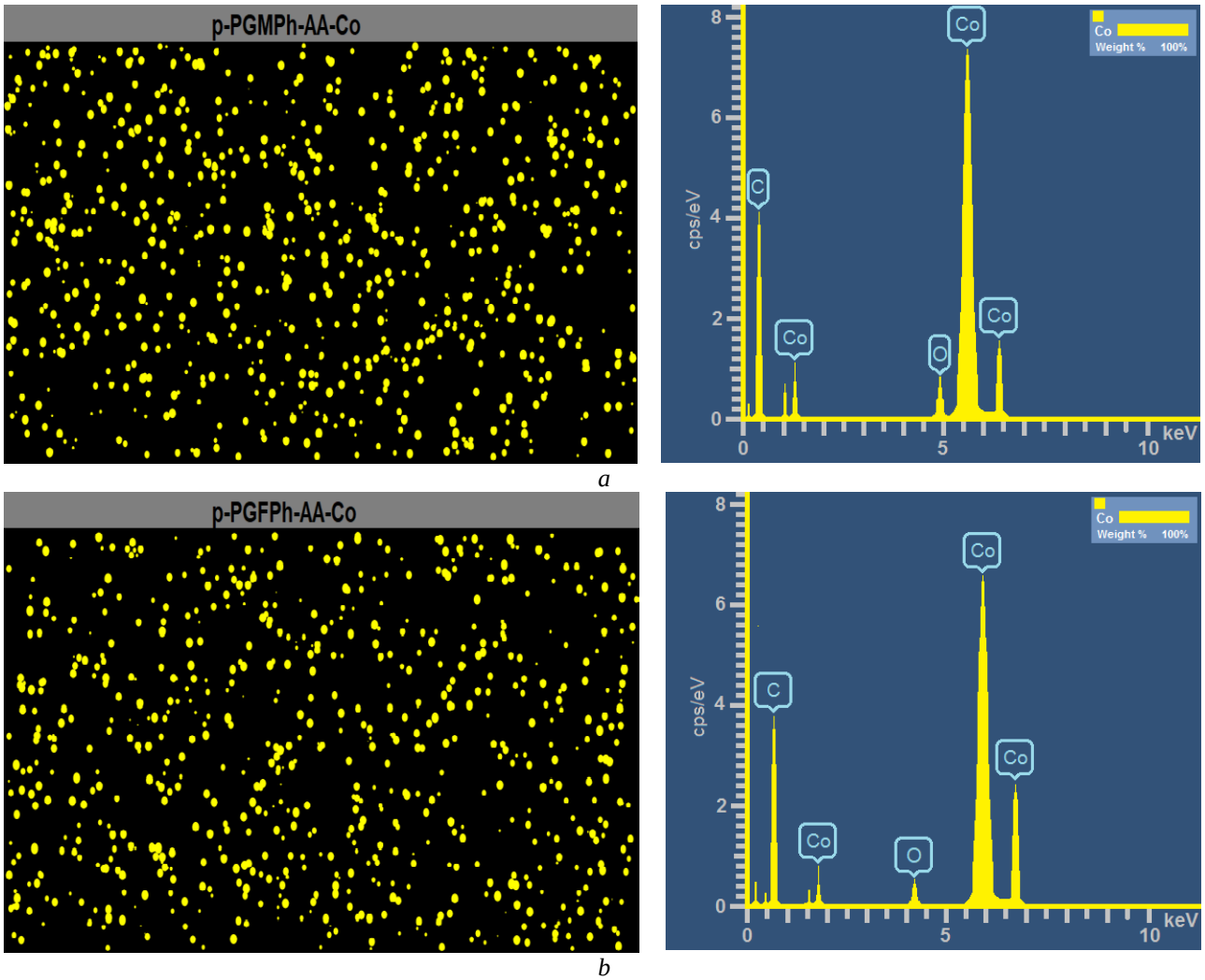

a — p-PGMPh–AA–Co^0; *b* — p-PGFPh–AA–Co^0

Figure 4. Micrographs of the distribution of Co^0 particles in the metal-polymer composites

Peaks in the 600–800 cm^{-1} range indicate that metallic cobalt particles have been mechanically included (immobilized) into the polymer matrix. The dispersion of the nanoparticles affects the intensity of these bands [26].

The study examined the possibility of using cobalt nanoparticles as electrocatalysts. These metal nanoparticles were immobilized into p-PGMPh–AA and p-PGFPh–AA polymer matrices.

The efficiency of electrocatalytic hydrogenation depends greatly on the process conditions, in particular on the current and temperature. It has been established that increasing the current contributes to the acceleration of the hydrogenation rate of unsaturated and cyclic compounds. Electrolysis carried out in a galvanostatic mode demonstrates an inverse relationship between the process time and the current. As a result, the electrolysis duration decreases as current increases. On the other hand, increasing the current may have adverse effects such as triggering side reactions and reducing the yield of the target product [27]. As a result, determining the ideal ratio of current to process time is critical to achieving maximum efficiency.

The reaction was carried out in the presence of p-PGMPh–AA–Co^0 and p-PGFPh–AA–Co^0 metal-polymer composites at a temperature of 20 °C while adjusting the current in the range of 1 to 3 A in order to identify the ideal conditions for catalytic hydrogenation of pyridine. Table 2 presents the achieved results.

Table 2

Effect of current on the yield of the target product (piperidine)

Current, A	Current density, A/dm²	Time, min		Yield of piperidine, %	
		p-PGMPh–AA–Co^0	p-PGFPh–AA–Co^0	p-PGMPh–AA–Co^0	p-PGFPh–AA–Co^0
1	21	88	92	78	72
2	42	67	75	71	66
3	63	41	49	61	53

According to Table 2, an increase in current from 1 to 3 A (cathode — copper plate with $S_{surf.}$ = 0.048 dm^2) results in a significant decrease in the yield of the target product due to the occurrence of side reactions and, consequently, an increase in the yield of by-products. Therefore, increasing the current to 3 A in order to reduce the hydrogenation time is undesirable. Analyzing the yield of piperidine at current of 1 A and 2 A, it is important to note their close values, while the process duration is significantly reduced, indicating greater efficiency of hydrogenation at a current of 2 A.

Figures 5 (*a*, *b*) presents the pyridine hydrogenation curves in the absence of a catalyst (1), with a skeletal Co-catalyst (2), and for metal-polymer composites based on p-PGMPh–AA–Co^0 and p-PGFPh–AA–Co^0 at a temperature T = 298 K and current I = 2 A.

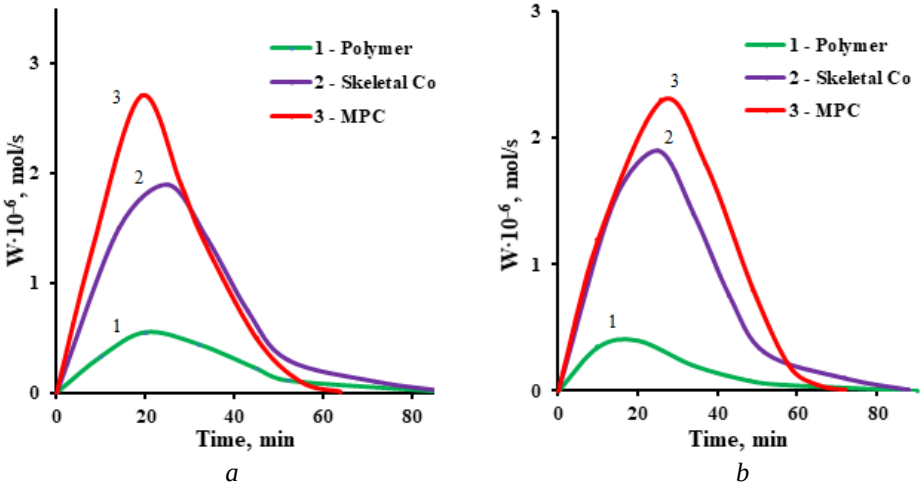

Figure 5. Change in the rate of pyridine electrohydrogenation in the absence of a catalyst (1), in the presence of skeletal Co catalyst (2), and in the presence of metal-polymer composite (MPC) based on p-PGMPh–AA–Co^0 (3, *a*) and p-PGFPh–AA–Co^0 (3, b) (I = 2 A, T = 298 K)

Analyzing curve (1) in Figure 5, which corresponds to hydrogenation without a catalyst, it is notable its subdued nature, although a small absorption of H_2 is observed. This circumstance can be explained by the partial saturation of the double bonds present in the structure of the copolymers. This assumption is confirmed by the bromide-bromate method, as a result of which it was found that before the start of the hydrogenation process, the content of unsaturated double bonds for the p-PGMPh–AA copolymer (13.1:86.9 mass.%) was 14 %, after hydrogenation this figure decreased to 9 %. Similarly, for the p-PGFPh–AA copolymer (14.2:85.8 mass.%), the degree of unsaturation was 17 % and 11 %, respectively. Curve (2) in Figure 5, on the other hand, demonstrates a pronounced character, indicating catalytic hydrogenation of pyridine with the formation of both target and by-products. Compared to the hydrogenation process with a skeletal cobalt catalyst (2), curve (3) in the presence of metal-polymer composites based on polymer matrices with immobilized nanoscale Co^0 particles shows a more extreme character. This suggests a more intense hydrogenation process of pyridine, with a high rate of H_2 absorption. The maximum rate of the electrocatalytic hydrogenation process is reached at approximately 19–26 minutes (Figure 5 *a*, *b*). After reaching the maximum, there is a sharp decrease in the reaction rate, attributed to the consumption of some of the substrate

(pyridine) undergoing hydrogenation to piperidine and by-products such as tetrahydropyridine (less than 1 %) and dipiperidyl (from 4 % to 9 %). No further significant changes in the hydrogen absorption curve are observed, indicating the completion of the hydrogenation process.

Previous studies have demonstrated that the first binary systems, p-PGMPh–AA and p-PGFPh–AA, are "smart" polymers due to their sensitivity to various variables such as temperature changes. In particular, polymers undergo a volume-phase transition of the "swelling-collapse-swelling" type with increasing temperature, the minimum of which is observed at 30 °C. The behavior of the metal-polymer composites (MPCs) containing immobilized Co particles is comparable. As a result, additional studies of pyridine hydrogenation in the presence of these MPCs were carried out with temperature variations of up to 5 °C between 25 °C and 40 °C. The obtained data are presented in Table 3 and Figure 6 (*a*, *b*).

Table 3

Effect of temperature on the yield of the target product (piperidine) and by-product (dipyridyl) of pyridine hydrogenation

Catalyst	Temperature, °C	Time, min	Yield of products, %		Pyridine, %
			Piperidine	Dipyridyl	
Skeletal Co	25	88	60.51	4.1	35.39
	30	80	66.24	5.4	28.36
	35	72	73.91	6.8	19.29
	40	58	79.03	8.8	12.17
p-PGMPh–AA–Co^0	25	64	71.28	3.9	24.82
	30	70	72.12	4.9	22.98
	35	61	86.71	6.5	6.79
	40	48	89.64	7.6	2.76
p-PGFPh–AA–Co^0	25	72	67.15	5.2	27.65
	30	80	69.07	6.0	24.93
	35	69	83.29	6.8	9.91
	40	55	85.83	8.9	5.27

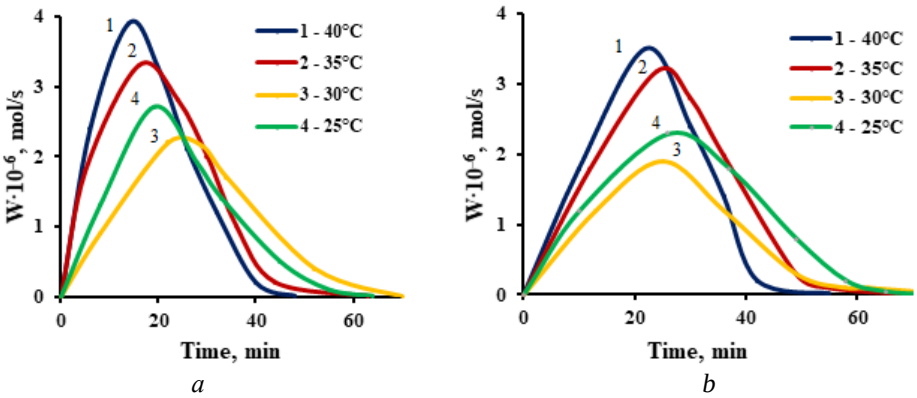

Figure 6. Hydrogenation of pyridine in the presence of MPC based on (*a*) p-PGMPh–AA–Co^0 and (*b*) p-PGFPh–AA–Co^0 at various temperatures and current I = 2 A

As can be seen from Table 3, increasing the temperature to 40 °C stimulates the expansion of the polymer matrix, which significantly increases the specific surface area of the MPC. As a result, the hydrogenation reaction rate accelerates (Fig. 6*a*, *b*). A decrease in the selectivity of the target products yield, associated with the activation of side reactions and, as a consequence, an increase in the yield of side products, makes it undesirable to increase the temperature to 40 °C. In terms of p-PGMPh–AA–Co^0 and p-PGFPh–AA–Co^0, the ideal temperature for the hydrogenation process in the presence of MPC is 35 °C.

It is important to note the higher efficiency of MPC based on p-PGMPh–AA–Co^0 when comparing the catalytic activity of MPCs based on p-PGMPh and p-PGFPh with AA and immobilized Co^0 nanoparticles, taking into account the duration of the hydrogenation process and the target product yield. The physicochemical characteristics of the original p-PGMPh–AA polymer matrix are responsible for this. These characteristics include a higher sorption capacity, sensitivity to external factors (such as fluctuations in temperature and

current), and a more porous structure within the polymer network. MPCs based on p-PGMPh–AA–Co^0 and p-PGFPh–AA–Co^0 demonstrated a preference for the skeletal cobalt catalyst due to their greater dispersity.

Conclusions

Heterogeneous catalysis involves the reaction occurring at the interface of different phases, where one of the determining factors is the larger specific surface area of the catalyst. Therefore, an increase in the system dispersity leads to an increase in the contact area (interaction) between the reactant and the catalyst. Particle size is also of great importance. Specifically, with a decrease in particle size, the number of catalytically active surface centers per unit area of the polymer matrix increases. This results in an increase in the rate of hydrogenation.

Consequently, the results of the studies indicate high catalytic activity of MPCs based on p-PGMPh–AA–Co^0 and p-PGFPh–AA–Co^0. The production of nanoscale cobalt metal particles and their immobilization within the volume of the polymer matrix contributes to an increase in the specific contact surface area of the MPCs with the reaction medium, which leads to enhanced hydrogenation efficiency. Immobilization of cobalt particles in a polymer matrix prevents their coagulation and oxidation. The obtained SEM images demonstrate a uniform distribution of predominantly isolated spherical Co^0 nanoparticles in the volume of the studied MPC polymer matrices. The presence of aggregates formed by nanoparticle agglomeration, with sizes exceeding 280 nm, is observed on the surface of the polymer mesh. In the presence of created MFCs, the hydrogenation proceeds faster than when using a skeletal cobalt catalyst for all the reasons described earlier. Furthermore, the use of MFCs obtained from p-PGMPh–AA–Co^0 and p-PGFPh–AA–Co^0 improves the selectivity of the target product yield.

The obtained research results indicate the prospects for developing new nanocatalysts based on p-PGMPh and p-PGFPh with AA polymer systems with subsequent immobilization of catalytically active nanoscale transition metals within the polymer matrix.

*Author Information**

**The authors' names are presented in the following order: First Name, Middle Name and Last Name*

Gulsym Kabayevna Burkeyeva — PhD, Associate Professor of Chemical Sciences, Karaganda Buketov University, Universitetskaya street, 28, 100024, Karaganda, Kazakhstan; e-mail: guls_b@mail.ru; https://orcid.org/0000-0003-1993-7648

Anna Konstantinovna Kovaleva (*corresponding author*) — PhD, Senior Researcher, Karaganda Buketov University, Universitetskaya street, 28, 100024, Karaganda, Kazakhstan; e-mail: cherry-girl1899@mail.ru; https://orcid.org/0000-0001-9758-648X

Madinabonu Nabizhon kizi Ibadullayeva — Master Student, Karaganda Buketov University, Universitetskaya street, 28, 100024, Karaganda, Kazakhstan; e-mail: madinabanu02ibadullaeva@mail.ru; https://orcid.org/0009-0005-0709-9191

Magzhan Ubaydullauly — Master Student, Karaganda Buketov University, Universitetskaya street, 28, 100024, Karaganda, Kazakhstan; e-mail: ubaidullamagzhan@gmail.com

Jiri Plocek — PhD, CSc., Institute of Inorganic Chemistry of the Czech Academy of Sciences, Husinec-Rez 1001 25068 Rez, Czech Republic; e-mail: plocek@iic.cas.cz; https://orcid.org/0000-0001-6082-5766

Kamila Erdaurenkyzy Sergaziyeva — Student, Karaganda Buketov University, Universitetskaya street, 28, 100024, Karaganda, Kazakhstan; e-mail: sergazievakamila72@gmail.com

Author Contributions

The manuscript was written through contributions of all authors. All authors have given approval to the final version of the manuscript. CRediT: **Gulsym Kabayevna Burkeyeva** conceptualization, validation, visualization, supervision & editing; **Anna Konstantinovna Kovaleva** conceptualization, data curation, methodology, validation, visualization, writing-original draft, writing-review & editing; **Madinabonu Nabizhon kizi Ibadullayeva** data curation & methodology; **Magzhan Ubaydullauly** data curation & investigation; **Jiri Plocek** supervision & editing; **Kamila Erdaurenkyzy Sergaziyeva** data curation & investigation.

Acknowledgments

Authors thank Karaganda Buketov University for access to library facilities.

Conflicts of Interest

The authors declare no conflict of interest.

References

1 Zheng, N.F. (2018). Selective Nanocatalysis. *ChemNanoMat, 4*(5), 431. https://doi.org//10.1002/cnma.201800159

2 Gellman, A.J. & Shukla, N. (2009). Nanocatalysis — More than speed. *Nat. Mat., 8*(2), 87-88. https://doi.org/10.1038/nmat2363

3 Gai, P.L.,Roper, R. & White, M.G. (2002). Recent advances in nanocatalysis research. *Cur. Opin. in Solid State & Mat. Sci., 6*(5), 401–406. https://doi.org/10.1016/S1359-0286(02)00109-2

4 Kang, S. & Lee, J.C. (2022). Nanocatalysis — A Trending Tool in Organic Reactions. *Let. in Org. Chem., 19*(4), 257–258.

5 Vinod, C.P. (2010). Surface science as a tool for probing nanocatalysis phenomena. *Catalysis Today, 154*(1-2), 113–117. https://doi.org/10.1016/j.cattod.2010.03.018

6 Martins, L.M.D.R.S. (2021). Highlights of the Nanocatalysis in Organic Chemistry. *Catalysts, 11*(2), No. 213. https://doi.org/10.3390/catal11020213

7 Kalidindi, S.B. & Jagirdar, B.R. (2012). Nanocatalysis and Prospects of Green Chemistry. *ChemSuSChem, 5*(1), 65–75. https://doi.org/10.1002/cssc.201100377

8 Xu, Q.E. Song, Y.H. Lui, Zh. & Lui, Y.H. (2016). Nanocatalysis for Organic Chemistry. *Curr. Org. Chem., 20*(19), 2013–2021. https://doi.org/10.2174/1385272820666160215235505

9 Burkeev, M.Zh. javascript:void(0);Kovaleva, A.K., javascript:void(0);Tazhbaev, E.M., javascript:void(0);Burkeeva, G.K., javascript:void(0);Davrenbekov, S.Zh., javascript:void(0);Kopbosynova, A.A., javascript:void(0);Omasheva, A.V. & javascript:void(0);Mataev, M.M. (2015). Nanocatalytic systems based on poly(ethylene glycol maleate)-acrylamide copolymers. *Russian J. of Appl. Chem., 88*(2), 314–319. https://doi.org/10.1134/S1070427215020202

10 Burkeyev, M.Z., Kovaleva, A.K., Plocek, J., Tazhbayev, E.M., Burkeyeva, G.K., Bolatbai, A.N. & Davrenbekov, S.Z. (2018). Synthesis and Properties of Poly(Propylene Glycol Maleate Phthalate)–Styrene Copolymers as a Base of Composite Materials. *Russian J. of Appl. Chem., 91*(11), 1742–1749. https://doi.org/10.1134/S1070427218110022

11 Burkeyeva, G.K., Kovaleva, A.K., Tazhbayev, Ye.M., Ibrayeva, Zh.M., & Plocek, J. (2023). Development of Energy Efficient "Cold" Curing Method for Polypropylene Glycol Fumarate Using an Optimized Initiating System. *Eurasian J. of Chem. 109*(1), 68-77. https://doi.org/10.31489/2959-0663/1-23-10

12 Burkeyeva G.K., Kovaleva A.K., Tazhbayev Ye.M., Ibrayeva Zh.M. & Zhaparova L.Zh. (2023). Investigation of Curing Process and Thermal Behavior of Copolymers Based on Polypropylene Glycol Fumarate and Acrylic Acid Using the Methods of DSC and TGA. *Polymers, 15*, No. 3753. https://doi.org/10.3390/polym15183753

13 Burkeev M.Zh., Khamitova T.O., Havlicek D., Bakibaev A.A., Tazhbaev E.M., Davrenbekov S.Zh. & Kozhabekova G.E. (2018). *Catal. in Ind., 10*(4), 270–278. https://doi.org/10.1134/S2070050418040037

14 Burkeyev, M.Zh. & Tazhbayev, Ye.M. (2018). Pat. No. 33266 RK. Publ. C08G63/00 [in Russian]

15 Fung, V. Hu, G.X., Wu, Z.L. & Jiang, D.E. (2020). Hydrogen in Nanocatalysis. *J. Phys. Chem. Let., 11*(17), 7049-7057. https://doi.org/10.1021/acs.jpclett.0c01783

16 Geonmonond, R.S., Anderson, G.M. & javascript:void(0);https://www.webofscience.com/wos/author/record/1168294Camargo, P.H.C. (2018). Controlled synthesis of noble metal nanomaterials: motivation, principles, and opportunities in nanocatalysis. *Anais da Academia Brasileira De Ciencias, 90*(1), 719–744. https://doi.org/10.1590/0001-3765201820170561

17 Piccolo, L. (2021). Restructuring effects of the chemical environment in metal nanocatalysis and single-atom catalysis. *Catalysis Today, 373*, 80–97. https://doi.org/10.1016/j.cattod.2020.03.052

18 Burkeyev, M.Zh., Tazhbayev, Ye.M., Zhakupbekova, E.Zh., Kovaleva, A.K. & Kopbosynova A.A. (2015). Synthesis and study of properties of copolymers based on polypropylene glycol maleate phthalate with acrylic acid. *Bulletin of the Karaganda University. Ser. Chem. 1*(77), 31–36. [in Russian]

19 Jiang X-h., Wang, R-q, Wei W-x, Lu, L-d. & Chujko, S.V. (2009). Synthesis, morphology and catalytic properties of cobalt nanoparticles. *Chem. Phys. and Mesoscopy. 11*(3), 315–321. [in Russian]

20 Kirilyus I.V. (1990). *Electrocatalytic hydrogenation of organic compounds.* Science Kaz.SSR.

21 Ivanova, N.M., Soboleva, E.A., Visurkhanova, Ya. A. & Kirilyus, I.V. (2015). Electrocatalytic activity of polyaniline-copper composites of p-nitroaniline. *Rus. J. of Electrochem., 51*(2), 166–172. https://doi.org/10.1134/S1023193515020056

22 Ivanova, N.M., Soboleva, E.A., Visurkhanova, Ya.A. & Lazareva, E.S. (2018). Structure-Phase Changes in Polymer Composites Doped with Silver Nitrate and Their Electrocatalytic Activity. *Rus. J. of Electrochem., 54*(11), 999–1005. https://doi.org/10.1134/S1023193518130207.

23 Mahmood, A., javascript:void(0);Guo, W.H., Guo, W., javascript:void(0);Tabassum, H. Hassina javascript:void(0);Z., Zou R.Q. (2016). Metal-Organic Framework-Based Nanomaterials for Electrocatalysis. *Adv. En. Mat.*, *6*(17), SI. https://doi.org/10.1002/aenm.201600423

24 Burkeev, M.Zh., Shibayeva, S.R., Khamitova, T.O., Plocek, J., Tazhbayev, Y.M., Davrenbekov, S.Zh., Nurmaganbetova, M.T., Kazhmuratova, A.T., Zhumagalieva, T.S. & Kezdikbayeva A.T. (2021). Synthesis and Catalytic Properties of New Polymeric Monometallic Composites Based on Copolymers of Polypropylene Glycol Maleate Phthalate with Acrylic Acid. *Polym., 13, 4369.* https://doi.org/10.3390/polym13244369

25 Tarasevich, M.R., Orlov, S.B., Shkol`nikov, Ye.I., Toroptseva, T.N. & Basova, I.G. (1990). *Electrochemistry of polymers.* Science.

26 Tarasevich, B.N. (2012). *IR spectra of the main classes of organics connections.* (Ref. mater.). MSU.

27 Sharma, S., Kumari, M. & Sharma D.K. (2009). Electroreduction of 4-nitrobenzaldehyde in basic medium at Different Electrodes. *Nat. Sci.*, *7*(3), 84–98.

How to Cite: Liu, X., Bekchanov, D., Baikenov, M.I., & Su, X. (2024) Construction of Ag/AgCl@MIL-53(Fe): Achieving Efficient Photocatalytic Water Oxidation via the Plasma-Phase Silver and Heterojunction Synergistic Effect. *Eurasian Journal of Chemistry, 29, 3(115), 160-170.* https://doi.org/10.31489/2959-0663/3-24-14

Article

Received: 2 July 2024 | Revised: 22 August 2024 |
Accepted: 9 September 2024 | Published online: 23 September 2024

UDC 544.47+542.943

https://doi.org/10.31489/2959-0663/3-24-14

Xiaofei Liu[1], Davronbek Bekchanov[2], Murzabek I.Baikenov[3], Xintai Su[4]*

[1]*College of Chemistry and Chemical Engneering, Xinjiang Agricultural University, Urumqi, China;*
[2]*Faculty of Chemistry, Department of Polymer Chemistry, National University of Uzbekistan, Tashkent, Uzbekistan;*
[3]*Karaganda Buketov University, Karaganda, Kazakhstan;*
[4]*School of Environment and Energy, Guangdong Provincial Key Laboratory of Solid Wastes Pollution Control and Recycling, South China University of Technology, Guangzhou, Guangdong, China*
*(*Corresponding author's e-mail: suxintai@scut.edu.cn)*

Construction of Ag/AgCl@MIL-53(Fe): Achieving Efficient Photocatalytic Water Oxidation via the Plasma-Phase Silver and Heterojunction Synergistic Effect

The development of highly efficient water oxidation catalysts is a bottleneck in achieving artificial photosynthesis, as water oxidation is a complex process involving multiple electron and proton transfers. To further improve the photocatalytic water oxidation performance of MIL-53(Fe), a series of Ag/AgCl@MIL-53(Fe) samples with different Fe:Ag ratios were synthesized by hydrothermal methods and used in the photocatalytic water oxidation reactions. XRD characterization showed the successful preparation of Ag/AgCl@MIL-53(Fe) heterostructure catalysts. The reaction results showed that sample AAM-2 (Fe:Ag=5:1) had the best photocatalytic water oxidation performance, with the highest TOF value of 0.14 mmol/(g·s) and quantum efficiency of 39.0 % under the conditions of catalyst mass of 1 mg and pH=9.0 for boric acid-borax buffer solution. Measurements of photocurrent indicated that the AAM-2 samples doped with Ag/AgCl had higher photocurrent densities, thus improving the photocatalytic performance. This provides new insights for constructing highly efficient porous MOFs catalysts.

Keywords: Metal organic framework (MOFs); hydrothermal method; MIL-53(Fe); Ag/AgCl@MIL 53(Fe); surface plasma resonance; heterojunction; photocatalysis of water oxidation; photocurrent densities.

Introduction

Photocatalytic water splitting, as an advanced technology, has a very broad application prospect in the field of energy. Its core value is that it can efficiently convert sunlight into chemical energy, thus realizing the direct decomposition of water and producing clean hydrogen and oxygen [1]. This catalytic process can not only reduce the dependence on fossil fuels and reduce environmental pollution, but also has far-reaching significance in promoting the sustainable development of energy. It consists of two half-reactions: the oxidation of water to O_2 and the reduction of hydrogen ions to H_2. Compared with the reduction of water with two electrons transferred, the oxidation of water is more difficult to occur because it involves the transfer of four electrons and the formation of an O–O bond [2]. Therefore, the water oxidation reaction process is more complex and challenging than the water reduction reaction.

Previous studies have explored metal oxides, metal sulfides, and other materials as photocatalysts for water oxidation [3–4]. However, the application of Metal-Organic Frameworks (MOFs) in this respect is less common, mainly because most MOFs cannot withstand the harsh conditions of water oxidation. Lin et al. reported the three UiO-67 catalysts doped with Ir, which showed high water oxidation activity [5]. However, due to the extreme conditions of water oxidation, the MOFs catalysts were unstable, which led to the partial decomposition of Ir complexes. Moreover, the Ir based composites are neither economical. It is worthwhile to explore the development of stable, cost-effective MOFs as photocatalysts for water oxidation. Iron is a resource-rich element, and many MOFs materials containing iron MOFs, such as MIL-53(Fe) and MIL-88 (Fe), have specific structures and uniform sizes. In previous studies, the iron oxygen clusters Fe-O within iron-based MOFs could be excited under visible light, leading to their visible light response characteristics [6]. Therefore, many iron-based MOFs have been used in photocatalytic reactions. Kholdeeva et al. investigated the capability of iron-based metal-organic frameworks MIL-100 and MIL-101 for carbon-hydrogen oxide formations [7]. Wang et al. have synthesized both MIL-100(Fe) and MIL-68(Fe), and found that they can achieve selective hydroxylation of benzene to phenol with high selectivity [8].

Introducing another metal ion to prepare bimetallic MOFs is one of the modification methods to improve the performance of single-metal MOFs [9]. Due to the significant amplified absorbance of the surface plasma resonance (SPR) of noble metal nanoparticles in the visible light region, it is possible to modify the photocatalyst [10]. Particularly, Ag/AgX (X = Cl, Br), a type of composite plasma photocatalyst, can generate highly active photo-excited carriers under visible light irradiation to achieve the rapid degradation of various organic pollutants [11–12]. Additionally, Ag/AgX modification has significantly enhanced the photocatalytic reaction activity of traditional semiconductor photocatalysts such as TiO_2, $BiVO_4$, Bi_2WO_4 and C_3N_4 [14]. Since the silver nanoparticles exhibit a plasma resonance effect that can introduce a new light absorption source and possesses an energy-matched band structure, it can improve the efficiency of carrier separation.

However, whether the additive Ag/AgX can enhance the photocatalytic performance of MOFs and whether the role of Ag/AgCl in photocatalytic reactions based on MOFs systems is similar to that previously reported in inorganic semiconductor systems is still an open question. Therefore, the study of the photocatalytic process of Ag/AgX@MOFs is of great significance. Previous studies have shown that MIL-53(Fe) can improve its photocatalytic water oxidation performance by doping metal ions. In this article, the effective combination of the plasma Ag/AgCl with MIL-53(Fe) has improved the photocatalytic water oxidation performance of MIL-53(Fe) through the heterojunction mechanism. This structure is conducive to the synergistic transfer of photogenerated electrons and holes in the catalyst. The research results on photocatalytic water oxidation by Ag/AgCl@MIL-53(Fe) will provide new ideas for the design and development of high-efficiency MOFs-based photocatalysts.

Experimental

Preparation of Ag/AgCl@MIL-53(Fe) Catalysts

Different samples with varying Fe/Ag molar ratios were prepared using a hydrothermal method. A mixture of 10 mmol of 1,4-H_2BDC (AR), an appropriate amount of $FeCl_3 \cdot 6H_2O$ (AR) and $AgNO_3$ (AR), and 50 mL of DMF (SP) solution was prepared, and the mixture was stirred at room temperature for 30 min. The obtained precipitates were then transferred into a sealed 100 mL autoclave, and the system was heated at 150 °C for 12 h. After the reaction, the autoclave was allowed to cool to room temperature naturally, and the obtained precipitates were washed with DMF three times, followed by water washing three times, and further dried under vacuum at 80 °C for 12 h to obtain the final Ag/AgCl@MIL-53(Fe) photocatalyst. The molar ratio of Fe to Ag was varied, while maintaining the total molar ratio of metal ions to ligand as 1:1. Based on the molar ratio compositions, the resulting samples were labeled as AAM-0 (Fe:Ag = 1:0), AAM-1 (Fe:Ag = 7:1), AAM-2 (Fe:Ag = 5:1), and AAM-3 (Fe:Ag = 2:1).

Catalyst Characterization

X-ray diffraction patterns (XRD) were determined on a Bruker AXS D8 Focus diffractometer (operated at 40 kV and 30 mA) using Cu Kα irradiation.

N_2-BET was performed using a ST-08B physical-sorption instrument at 77 K.

Fourier transform infrared (FT-IR) spectra were recorded on an Equinox55 spectrometer (Bruker, Germany) by means of the KBr pellet technique.

Scanning electron microscope (SEM) images of the typical samples were recorded on a SU8010 model supplied by Hitachi Ltd. of Japan. Before conducting the SEM test, a layer of Au was sprayed onto the surface of the sample to enhance its conductivity. When performing mapping tests, the solid sample was dispersed in anhydrous ethanol and ultrasonically dispersed before being evenly dripped onto a silicon wafer on an optical surface for testing.

Synthesis of the Photosensitiser $[Ru(bpy)_3](ClO_4)_2$

Studies have shown that in a photocatalytic water oxidation system using $[Ru(bpy)_3]^{2+}$ as the photosensitizer, $[Ru(bpy)_3](ClO_4)_2$ is more conducive to the photocatalytic water oxidation reaction than $[Ru(bpy)_3]Cl_2$. Therefore, configuring the original photosensitiser $[Ru(bpy)_3]Cl_2$ into $[Ru(bpy)_3](ClO_4)_2$ is beneficial for enhancing the photocatalytic oxygen production performance of the catalyst.The specific steps are as follows: Dissolve 400 mg of $[Ru(bpy)_3]Cl_2$ in a small amount of distilled water to ensure complete dissolution, transfer to a 50 mL opaque reaction flask, and then add 4 M $HClO_4$ acid solution dropwise under magnetic stirring until no more white precipitate is formed. The solution is filtered and washed three times with ether to remove H^+ ions and water from the precipitate, which is then dried in the dark at room temperature for 12 h. And storing the obtained final product $[Ru(bpy)_3](ClO_4)_2$ orange powder in the dark at low temperature.

Evaluation of Photocatalytic Oxygen Production Performance

In the non-homogeneous system for photocatalytic water oxidation experiments, the synthesized samples were used as photocatalysts for water oxidation (0–2 mg), with $[Ru(bpy)_3](ClO_4)_2$ serving as the photosensitiser (1.0 mM, 8.76 mg), and $Na_2S_2O_8$ as the electron sacrificial agent (40 mM, 95.2 mg). The reactions were carried out in a borax-borate buffer solution (80 mM, pH = 8.0–10.0). The specific steps were as follows: first, a certain amount of catalyst, photosensitiser, and electron sacrificial agent were weighed in the dark, and then added separately to the reactor, followed by the addition of a 10 mL of buffer solution using a pipette gun. The sampling bottle was sealed and subjected to gas displacement treatment. The photocatalytic reaction was carried out using PLS-SXE xenon lamp (300 W) produced by Porfilet as the light source. Before beginning the use of the xenon lamp (with a 420 nm filter), use a power meter to set the light power density of the xenon lamp to 100 mW/cm^2 (simulating the solar irradiance). Place the sampling bottle that has been air-exhausted under the adjusted xenon lamp, and perform magnetic stirring simultaneously. Every two minutes, a gas sampling needle with a capacity of 250 μL is used to withdraw 100 μL of the gas from the sampling bottle and inject it into the GC-2014C gas chromatography produced by Shimadzu, Japan. To detect the oxygen content generated within the bottle, O_2 (99.99 %) is used as the standard sample for quantification, and the oxygen production is calculated based on the peak area of oxygen measured each time. In this experiment, sampling continues until 10 minutes, until the peak area of oxygen no longer increases. Additionally, use a pH meter to measure the pH value of the solution after the complete reaction.

Photoelectrochemical Performance Test

The preparation steps for the electrode are as follows: Take 8 mg of the catalyst, disperse it in approximately 1 mL of ethanol, add 40 μL of Nafion solution, and sonicate to form a paste. The paste is then spin-coated uniformly on a 1 cm × 1 cm FTO conductive glass sheet, and dried in a vacuum at 110 °C for 12 h to prepare the working electrode. After that, platinum wire is used as the counter electrode, and Sure enough electrode is used as the reference electrode, with 80 mM $Na_2S_2O_8$ solution as the electrolyte. Photocurrent measurements are performed using a 300W xenon lamp as the light source. The current response changes of different samples under illumination/non-illumination conditions are achieved through intermittent illumination over a fixed time.

Results and Discussion

X-ray diffraction (XRD) was used to analyze the phase composition of the Ag/AgCl@ MIL-53(Fe)(AAM) sample. As shown in Figure 1, the characteristic peaks of the pure phase AAM-0 appeared at 9.4°, 12.7°, 17.6°, and 25.4°, which matched the XRD patterns of the simulated crystal of MIL-53(Fe) reported previously. The XRD spectrum of the AAM-2 sample, which had been doped with Ag/AgCl, was mainly dominated by the characteristic peaks of MIL-53(Fe). In addition, the diffraction peaks corresponding to the cubic phase AgCl (111), (200), and (220) faces were observed, located at 27.8°, 32.3°, and 46.3°, respectively. A weak peak was also observed at 38.2° in the XRD spectrum of AAM-2, corresponding to the (111) plane of the cubic phase metallic Ag [14]. This indicates that the Ag/AgCl heterojunction structure was successfully introduced. It is noteworthy that the position of the characteristic diffraction peaks of MIL-53(Fe) in the AAM-2 spectrum did not change significantly, indicating that doping with Ag/AgCl would not destroy the crystal structure of MIL-53(Fe).

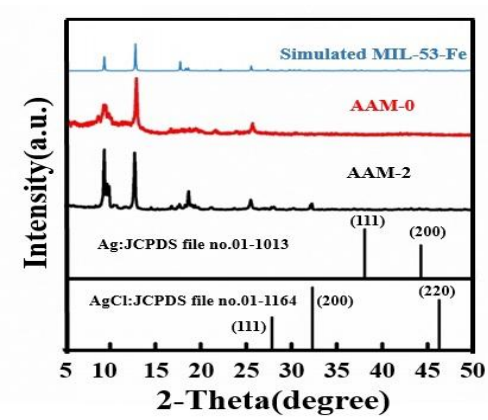

Figure 1. XRD patterns of AAM-0 and AAM-2

The BET-BJH method was used to analyze the specific surface area, pore volume, and pore diameter of the AAM-0 and AAM-2 catalysts, with the results listed in Table 1. The synthesized AAM-0 and AAM-2 samples had specific surface areas of 52 and 28 m^2/g, respectively. After doping with Ag/AgCl, the specific surface area decreased, suggesting that Ag/AgCl may block the pores of the MIL-53(Fe). The adsorption isotherms are shown in Fig. 2, where both the AAM-0 and AAM-2 catalysts exhibit IV-type isotherms and H3-type hysteresis loops. Additionally, with an average particle size of 3.0 nm for AAM-0 and 3.3 nm for AAM-2. According to the IUPAC classification of pores, it is evident that they predominantly consist of mesopores, which are generated by the agglomeration of particles. The average pore diameter of the AAM-2 sample with Ag/AgCl doping is smaller than that of the AAM-0 sample.

Table 1

Textural properties of the catalysts

Sample	Specific surface area (m^2/g) [a]	Average pore volume ($cm^3\ g^{-1}$)[b]	Average pore size (nm) [c]
AAM-0	52	0.09	3.0
AAM-2	28	0.06	3.3

[a]Calculated by the BET method. [b] BJH desorption pore volume. [c] BJH desorption average pore diameter.

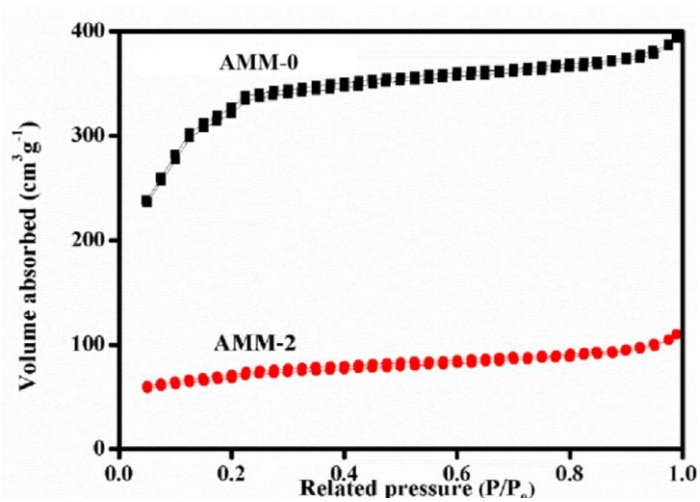

Figure 2. Adsorption curves of AAM-0 and AAM-2

The nanocrystalline structure of AAM was further determined by scanning electron microscopy (SEM). Fig. 3 shows the SEM morphologies of the AAM-0 and AAM-2 catalysts, where the pure phase AAM-0 appears to have a tetragonal structure, indicating the successful synthesis of MIL-53(Fe), which is consistent with the XRD results. Additionally, it was observed that the AAM-2 samples doped with Ag/AgCl still maintained a framework structure. However, in comparison to the tetragonal structure of AAM-0, there is a noticeable change in the microscopic structure, with the framework structure appearing less clear and distinct.

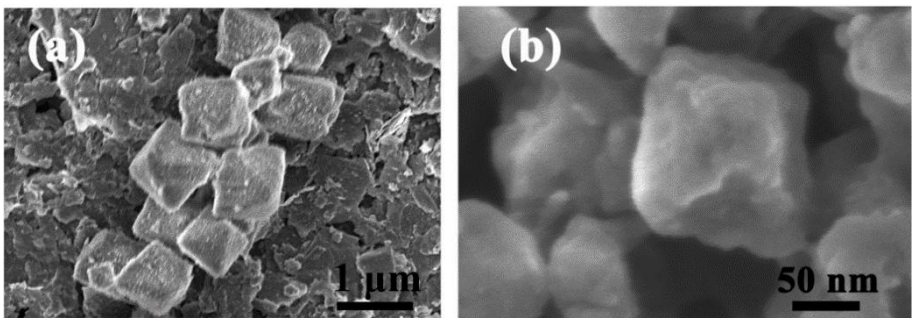

Figure 3. SEM images of (a) AAM-0 (b) AAM-2

Furthermore, the molecular structure of the AAM-0 and AAM-2 catalysts was investigated using infrared spectroscopy (Fig. 4). It was found that the infrared spectra of the AAM-2 sample were very similar to those of the AAM-0 sample. The characteristic absorption peaks at 1536 and 1392 cm^{-1} were attributed to the asymmetric stretching vibration of the carboxyl group (υ_{as} (C-O)) and the symmetric stretching vibration (υ_s (C-O)) [15], respectively, indicating the presence of dicarboxylate linkers in the framework. The characteristic absorption bands of the benzene ring were observed at 1629 cm^{-1} (C=C) and 756 cm^{-1} (C-H) [16]. Additionally, the band at 542 cm^{-1} in the low-frequency region also confirmed the typical Fe-O stretching vibration found in the framework [17].

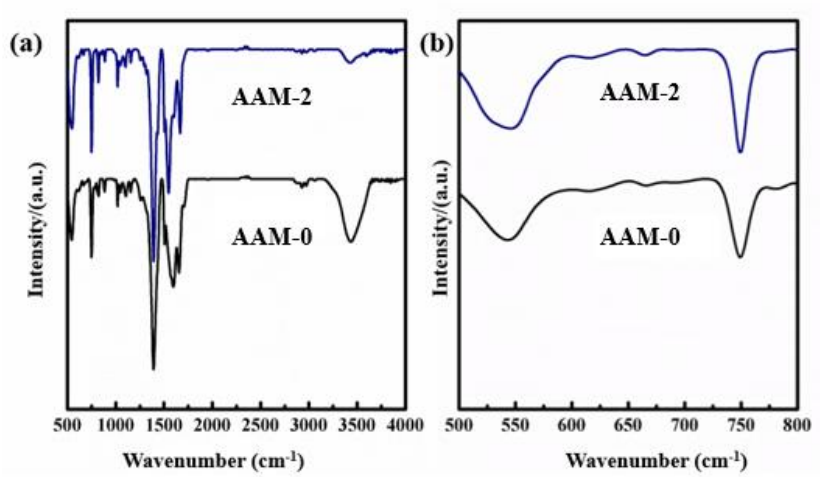

Figure 4. FT-IR spectra of as-prepared AAM-0 and AAM-2 samples

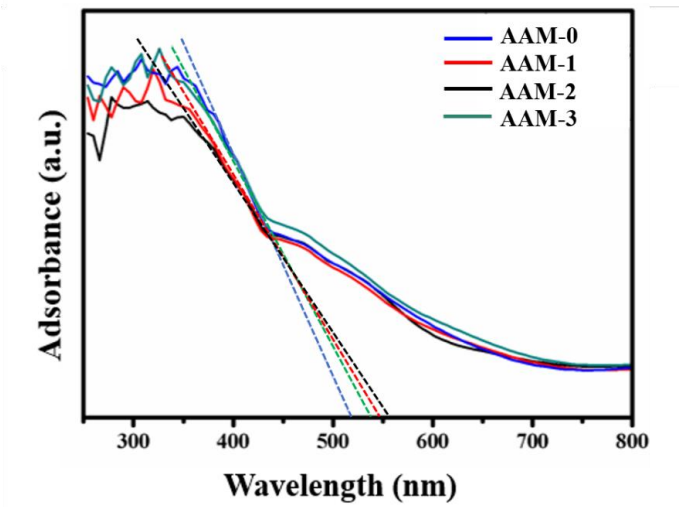

Figure 5. UV-vis diffuse reflectance spectra of AAM-0, AAM-1, AAM-2 and AAM-3 samples

The spectral absorption capability of the catalysts for visible light has been investigated through the determination of the ultraviolet-visible diffuse reflection spectra (URS) of the samples. As shown in Fig. 5, the absorption onset for Fe-MIL 53 is approximately 517 nm. As the amount of Ag/AgCl doping increases, the absorbance in the visible light region (>400 nm) is enhanced compared to Fe-MIL 53, with the maximum absorption intensity achieved when the Fe:Ag ratio is 5:1 (AAM-2). An increase in the absorbance in the visible light region implies a higher utilization efficiency of solar energy. Therefore, incorporating Ag/AgCl into Fe-MIL 53 particles can enhance its photocatalytic water oxidation performance.

To compare the influence of the loading of Ag/AgCl on photocatalytic activity, we performed tests on the oxygen production activity of AAM-0, AAM-1, AAM-2 and AAM-3 catalysts under the same conditions of water photolysis. First, a control experiment was conducted under conditions without light or catalyst, and no O_2 was detected, indicating that the O_2 came from the photo-oxidation of water. The curves of oxygen

production versus time for the four photocatalysts, AAM-0, AAM-1, AAM-2, and AAM-3, under visible light are shown in Fig. 6. All four samples exhibited photocatalytic activity for water oxidation, with the AAM-0 catalyst producing 20.16 μmol of oxygen in 10 min. The oxygen production of the AAM photocatalysts was improved, with AAM-2 (Fe:Ag = 5:1) producing 45.86 μmol of oxygen in 10 min, which is 2.27 times that of MIL-53(Fe). This result indicates that under the same preparation conditions, the loading of Ag/AgCl effectively improves the photocatalytic activity of MIL-53(Fe).

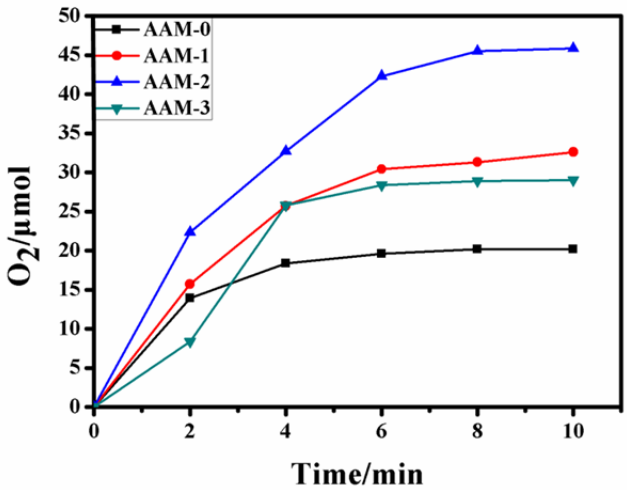

Figure 6. Kinetics of oxygen generation of the photocatalytic system
with different loads of Ag/ AgCl based MIL-53(Fe)

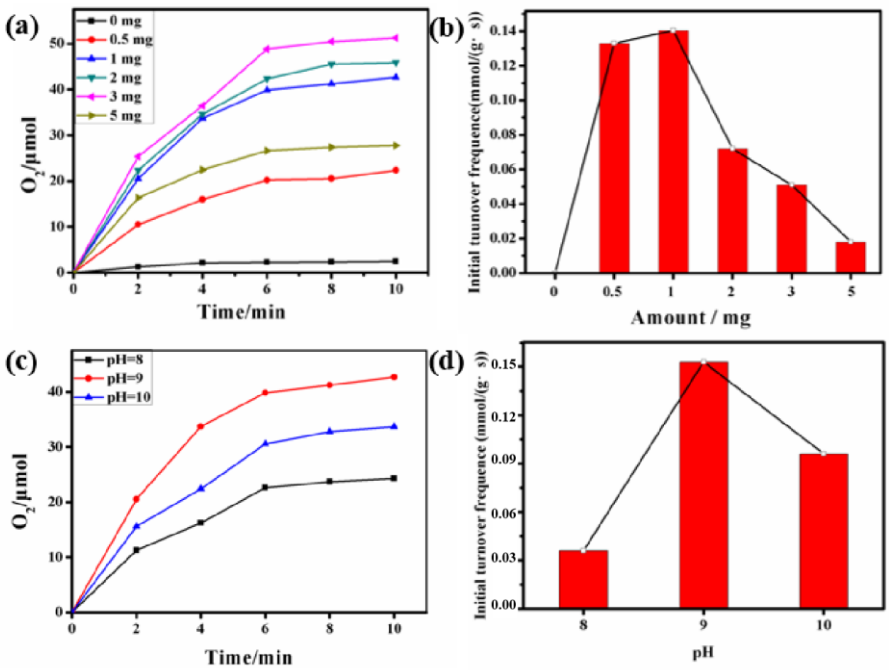

Figure 7. Kinetics of O_2 evolution of the photocatalytic system using AAM-1(Fe:Ag=5:1).
(*a*) using different amountof AAM-2, (*b*) initial turnover frequencies of AMM-1 using different amount,
(*c*) at different pH, (*d*) initial turnover frequencies at different pH

To further screen the conditions of the photocatalytic water oxidation system, the selected AAM-2 (Fe:Ag=5:1) was tested for its photocatalytic water oxidation performance under different conditions. From Fig 7, we can see that under the condition without light or catalyst, there is only a very small amount of oxygen in the system, and no oxygen generation is observed. The experimental results show that the AAM-2 (Fe:Ag=5:1) catalyst plays a major role in the photocatalytic water oxygenation reaction. At a pH of 9.0,

with the increase in the amount of catalyst, the oxygen production also increases, reaching a maximum value of 50.12 μmol when the catalyst reaches 3 mg. However, when the amount of catalyst increases to 5 mg, the oxygen production decreases. This indicates that adding more catalyst does not necessarily mean better performance, as excessive catalyst can adsorb on the surface of the photosensitizer, hindering direct contact between the photosensitizer and light, and also affecting the catalytic activity of the catalyst. At 1 mg of catalyst, the TOF value is 0.14 mmol/(g·s), with the highest oxygen production efficiency, and 1 mg is selected as the optimal amount of catalyst. When further increasing the amount of catalyst, the photocatalytic activity may actually decrease. This could be due to the excessive addition of the catalyst, which may reduce the transparency of the system, inhibit the contact between the photosensitizer and light, and thus lower the catalytic efficiency. After the reaction, the solution color changed from orange-yellow to dark-brown. The pH of the solution was measured, and it was found to have decreased from 9 to 8.5. The rate-controlling step of the photo-catalytic oxygen production reaction is given by formula (1). The accumulation of H^+ leads to a continuous decrease in pH, indicating that $[Ru(bpy)_3]^{3+}$ is not consumed in time. This will cause the reaction solution to change color and terminate the reaction.

$$4[Ru(bpy)_3]^{3+} + 2H_2O \rightarrow 4[Ru(bpy)_3]^{2+} + O_2 + 4H^+ \quad (1)$$

To further screen the optimal conditions, the effects of different pH values of boric acid buffer solutions on the photocatalytic water oxidation performance of AAM-2 catalyst were explored, as shown in Fig. 7(*c*). In alkaline conditions, there is a significant difference in the amount of oxygen released under different pH values. At pH = 8.0, the oxygen production is 19.8 μmol, and at pH = 10.0, the oxygen production is 32.42 μmol. Generally, high pH solutions are favorable for water oxidation because they can remove H^+ generated during the catalytic process [18], as shown in equation (1). This may be due to the structural decomposition of AAM-2 MOFs in strong alkaline solutions. This also indicates that the optimal pH for AAM-2 photocatalytic water oxidation is 9.0.

The initial quantum efficiency of the AAM-2 sample under the optimal reaction conditions was also calculated as follows:

The oxygen production amount in the initial 1 min was: 14.4 μmol

The number of consumed photons $=14.4\times10^{-6}\times6.02\times10^{23}\times4$

$=3.46\times10^{19}$

The optical power measured by the power meter: P=100 mW/cm^2, the diameter of the reaction bottle is 2 cm, The height of the liquid level in the bottle is 3.5 cm.

The light energy per minute: $E = P\times t\times D\times h$

$= 100\times10^{-3}\times60\times2\times3.5$ J

$= 42$ J

The energy of a single photon: $E_{ph} = h\nu = \frac{hc}{\lambda} = \frac{6.34\times10^{-34}\times3\times10^{8}}{420\times10^{-9}}$

$=4.73\times10^{-19}$ J

The total number of photons provided by the light per minute: $= \frac{E}{E_{ph}} = \frac{42}{4.73\times10^{-19}} = 8.88\times10^{19}$

Initial quantum efficiency:

$$\Phi_{QY(initial)} = \frac{\text{The number of photons consumed in the production of oxygen}}{\text{The total number of photons provided by the light per second}}$$

$$= \frac{3.46\times10^{19}}{8.88\times10^{19}}\times100\ \%$$

$= 39.0\ \%$

A cyclic experiment using the catalyst to examine the stability of the catalyst in the photocatalytic water oxidation process (Fig. 8). The AAM-2 catalyst synthesized by the water heat method (Fe:Ag = 5:1) was recycled for testing the catalytic performance of the water oxidation reaction. The recycled catalyst still showed good catalytic activity, but the amount of oxygen produced in the cyclic reaction showed a slight decrease. The possible reason for this result is that the catalyst will be physically lost during the recovery process, which will affect the cycle reaction.

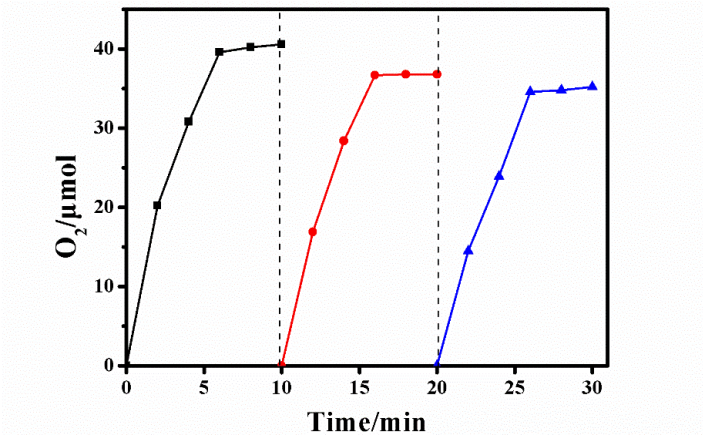

Figure 8. Cyclic behavior of AAM-2 (Fe:Ag=5:1) photocatalystic water oxidation

To further understand the electrochemical performance of the catalyst, the photocurrents of the AAM-0 and AAM-2 samples were measured, as shown in Fig. 9. It can be observed that the photocurrent density of AAM-2 is significantly higher than that of the pure phase AAM-0. This increase in photocurrent density is related to the effective separation of photogenerated electron-hole pairs, indicating that the catalyst doped with Ag/AgCl can enhance its photocurrent density, suggesting a higher efficiency of separation of photogenerated electron-hole pairs and thus improved photoelectrochemical performance.

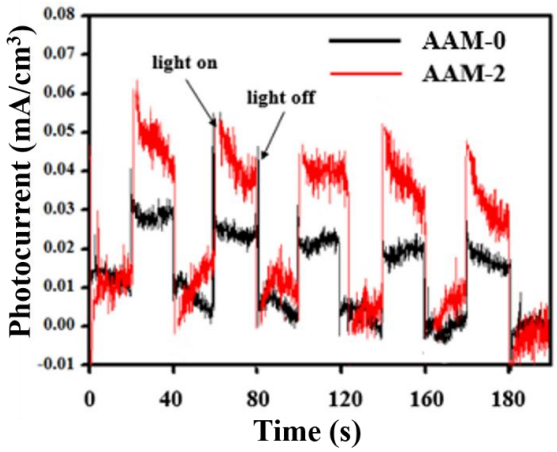

Figure 9. Transient photocurrent response of AAM-0, and AAM-2

Based on the results and discussion above, an hypothesis of the photocatalytic reaction pathway in the Ag/AgCl@MIL-53(Fe) system was proposed (Fig. 10). The conduction band (CB) and valence band (VB) energies of MIL-53(Fe) were 0.50 eV and 2.09 eV, respectively, with a bandgap energy of 2.59 eV, capable of being excited under visible light. Since the VB value of MIL-53(Fe) is higher than that of the water oxidation-reduction potential, MIL-53(Fe) is able to catalyze the water oxidation reaction under visible light irradiation [18]. For Ag/AgCl, due to its larger bandgap of 3.26 eV, AgCl cannot be excited by visible light. Upon irradiation with visible light, the Ag plasmon is excited, transferring the plasmon-induced electrons into the CB of AgCl. The positive charge in the Ag region can recombine with the photogenerated electrons in MIL-53(Fe), effectively promoting the separation of charge carriers in MIL-53(Fe). The oxidation of H_2O on MIL-53(Fe) by photogenerated electrons and holes migrate cooperatively in the Ag/AgCl@MIL-53(Fe) system, ensuring the longevity of the charge carriers and enhancing the photocatalytic activity. Importantly, MIL-53(Fe) as a typical metal-organic framework possesses a large surface area and high porosity. This structural feature endows Ag/AgCl@MIL-53(Fe) with open channels for effective diffusion and regulation of reactants, which is conducive to the photocatalytic reaction.

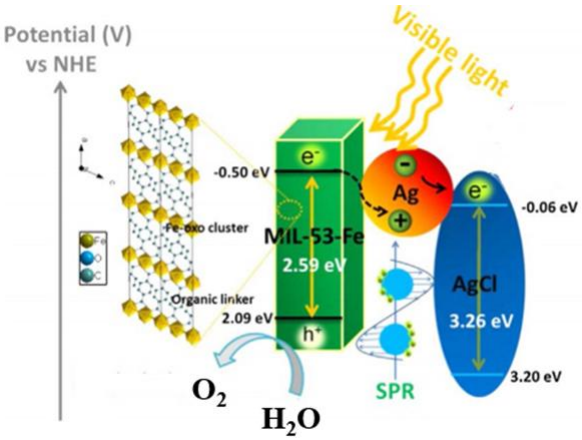

Figure 10. Proposed photocatalytic water oxidation reaction pathway of Ag/AgCl@MIL-53(Fe) under visible light irradiation

Conclusions

Hydrothermal synthesis of Ag/AgCl doped in MIL-53(Fe) for the study of photocatalytic water oxidation. The photocatalytic water oxidation performance was optimized by adjusting the Fe:Ag ratio. XRD results showed the successful preparation of the Ag/AgCl@MIL-53(Fe) heterostructure catalyst. According to the measured photocatalytic water oxidation performance, when the Fe:Ag ratio was 5:1, the photocarrier separation efficiency of sample AAM-2 was the highest, and its corresponding photocatalytic oxygen production performance was also the best among a series of Ag/AgCl@MIL-53(Fe) samples, which showed a clear advantage compared to the oxygen production performance of the pure phase MIL-53(Fe). Moreover, it exhibited good stability. Photocurrent test results indicated that under strong oxidative conditions, the AAM-2 catalyst had structural stability and could maintain a stable internal photoresponse current. The calculated results obtained a quantum efficiency of 39.0 % for AAM-2, with a TOF value of 0.14 mmol/(g·s). This has certain scientific guidance significance for enhancing the MOFs-based catalysts in photocatalytic water oxidation reactions.

Funding

The authors acknowledge deeply the financial supporting by the project of the Xinjiang Science and Technology Department (2022B01042, 2022E01051, 2022E02098), the Yili State Science and Technology Bureau Project (YZ2023A7, YZD2024A16, YZ2023A11), and the Project of Changji Science and Technology Bureau (2023Z04)

*Author Information**

**The authors' names are presented in the following order: First Name, Middle Name and Last Name*

Xiaofei Liu — Associate Processor, College of Chemistry and Chemical Engneering, Xinjiang Agricultural University, 311 East Nongda Road, 830052, Urumqi, China; e-mail: 1136887541@qq.com; https://orcid.org/0009-0000-9199-2989

Davronbek Bekchanov — Doctor of Chemical Sciences, Professor, Faculty of Chemistry, Department of Polymer Chemistry, National University of Uzbekistan, 100174, Tashkent, Uzbekistan; e-mail: bekchanovdj@gmail.com; https://orcid.org/0000-0002-3233-5572

Murzabek Ispolovich Baikenov — Doctor of Chemical Sciences, Professor, Karaganda Buketov University, Universitetskaya street, 28, 100024, Karaganda, Kazakhstan; e-mail: murzabek_b@mail.ru; https://orcid.org/0000-0002-8703-0397

Xintai Su (*corresponding author*) — Professor, School of Environment and Energy, Guangdong Provincial Key Laboratory of Solid Wastes Pollution Control and Recycling, South China University of Technology, 510006, Guangzhou, Guangdong, PR China; e-mail: suxintai@scut.edu.cn; https://orcid.org/0000-0001-6615-5273

Author Contributions

The manuscript was written through contributions of all authors. All authors have given approval to the final version of the manuscript. CRediT: **Xiaofei Liu** data curation, formal analysis, investigation, software, validation and writing — original draft; **Davronbek Bekchanov** software, resources and project administration; **Murzabek Ispolovich Baikenov** data curation, investigation, supervision and validation; **Xintai Su** conceptualization, funding acquisition, investigation, methodology, project administration, resources, supervision, visualization and writing-review and editing.

Conflicts of Interest

The authors declare no conflict of interest.

References

1 Ahmed, M., & Xinxin, G. (2016). A review of metal oxynitrides for photocatalysis. *Inorganic Chemistry Frontiers, 3*(5), 578–590. https://doi.org/10.1039/c5qi00202h

2 Winikoff, S. G., & Cramer, C. J. (2014). Mechanistic analysis of water oxidation catalyzed by mononuclear copper in aqueous bicarbonate solutions. *Catal. Sci. Technol., 4*(8), 2484–2489. https://doi.org/10.1039/c4cy00500g

3 Zhang, X., Jia, X., Duan, P., Xia, R., Zhang, N., Cheng, B., Wang, Z., & Zhang, Y. (2021). V_2O_5/P-g-C_3N_4 Z-scheme enhanced heterogeneous photocatalytic removal of methyl orange from water under visible light irradiation. *Colloids and Surfaces A: Physicochemical and Engineering Aspects, 608*, 125580. https://doi.org/10.1016/j.colsurfa.2020.125580

4 Fazli, S., & Asadpour-Zeynali, K. (2022). Investigation of electrochemical synthesis temperature effect of the binary transition metals sulfide on nickel foam in water oxidation study. *Materials Chemistry and Physics, 291*, 126670. https://doi.org/10.1016/j.matchemphys.2022.126670

5 Wang, C., Xie, Z., deKrafft, K. E., & Lin, W. (2011). Doping Metal–Organic Frameworks for Water Oxidation, Carbon Dioxide Reduction, and Organic Photocatalysis. *Journal of the American Chemical Society, 133*(34), 13445–13454. https://doi.org/10.1021/ja203564w

6 Chi, L., Xu, Q., Liang, X., Wang, J., & Su, X. (2016). Iron-Based Metal–Organic Frameworks as Catalysts for Visible Light-Driven Water Oxidation. *Small, 12*(10), 1351–1358. Portico. https://doi.org/10.1002/smll.201503526

7 Kholdeeva, O. A., Skobelev, I. Y., Ivanchikova, I. D., Kovalenko, K. A., Fedin, V. P., & Sorokin, A. B. (2014). Hydrocarbon oxidation over Fe- and Cr-containing metal-organic frameworks MIL-100 and MIL-101–a comparative study. *Catalysis Today, 238*, 54–61. https://doi.org/10.1016/j.cattod.2014.01.010

8 Wang, D., Wang, M., & Li, Z. (2015). Fe-Based Metal–Organic Frameworks for Highly Selective Photocatalytic Benzene Hydroxylation to Phenol. *ACS Catalysis, 5*(11), 6852–6857. https://doi.org/10.1021/acscatal.5b01949

9 Zhang, X., Luo, J., Wan, K., Plessers, D., Sels, B., Song, J., Chen, L., Zhang, T., Tang, P., Morante, J. R., Arbiol, J., & Fransaer, J. (2019). From rational design of a new bimetallic MOF family with tunable linkers to OER catalysts. *Journal of Materials Chemistry A, 7*(4), 1616–1628. https://doi.org/10.1039/c8ta08508k

10 Vaiano, V., Jaramillo-Paez, C. A., Matarangolo, M., Navío, J. A., & del Carmen Hidalgo, M. (2019). UV and visible-light driven photocatalytic removal of caffeine using ZnO modified with different noble metals (Pt, Ag and Au). *Materials Research Bulletin, 112*, 251–260. https://doi.org/10.1016/j.materresbull.2018.12.034

11 Wang, P., Huang, B., Qin, X., Zhang, X., Dai, Y., Wei, J., & Whangbo, M. (2008). Ag@AgCl: A Highly Efficient and Stable Photocatalyst Active under Visible Light. *Angewandte Chemie International Edition, 47*(41), 7931–7933. Portico. https://doi.org/10.1002/anie.200802483

12 Yan, X., Wang, X., Gu, W., Wu, M., Yan, Y., Hu, B., Che, G., Han, D., Yang, J., Fan, W., & Shi, W. (2015). Single-crystalline $AgIn(MoO_4)_2$ nanosheets grafted Ag/AgBr composites with enhanced plasmonic photocatalytic activity for degradation of tetracycline under visible light. *Applied Catalysis B: Environmental, 164*, 297–304. https://doi.org/10.1016/j.apcatb.2014.09.046

13 Jung, H., Kim, C., Yoo, H.-W., You, J., Kim, J. S., Jamal, A., Gereige, I., Ager, J. W., & Jung, H.-T. (2023). Continuous-flow reactor with superior production rate and stability for CO_2 reduction using semiconductor photocatalysts. *Energy & Environmental Science, 16*(7), 2869–2878. https://doi.org/10.1039/d3ee00507k

14 Ye, L., Liu, J., Gong, C., Tian, L., Peng, T., & Zan, L. (2012). Two Different Roles of Metallic Ag on Ag/AgX/BiOX (X = Cl, Br) Visible Light Photocatalysts: Surface Plasmon Resonance and Z-Scheme Bridge. *ACS Catalysis, 2*(8), 1677–1683. https://doi.org/10.1021/cs300213m

15 Li, Q. F., Lu, K., Zhou, Q., & Baik, D. H. (2006). A study on interfacial mechanisms and structure of poly(ethylene-co-methacrylic acid)/copper with reflection–absorption infrared spectroscopy. *Journal of Materials Science, 41*(24), 8271–8275. https://doi.org/10.1007/s10853-006-1006-7

16 Lyu, W., Shi, Y., Zheng, Y., & Liu, X. (2018). XPS and FTIR studies of fungus-stained Daemonorops margaritae. *Journal of Forestry Research, 30*(2), 739–743. https://doi.org/10.1007/s11676-018-0598-5

17 Somvanshi, A., Ahmad, A., Husain, S., Manzoor, S., Qahtan, A. A. A., Zarrin, N., Fatema, M., & Khan, W. (2021). Structural modifications and enhanced ferroelectric nature of $NdFeO_3$–$PbTiO_3$ composites. *Applied Physics A, 127*(6). https://doi.org/10.1007/s00339-021-04562-1

18 Ling, D., Park, W., Park, S., Lu, Y., Kim, K. S., Hackett, M. J., Kim, B. H., Yim, H., Jeon, Y. S., Na, K., & Hyeon, T. (2014). Multifunctional Tumor pH-Sensitive Self-Assembled Nanoparticles for Bimodal Imaging and Treatment of Resistant Heterogeneous Tumors. *Journal of the American Chemical Society, 136*(15), 5647–5655. https://doi.org/10.1021/ja4108287